

**Determination and Analysis of the Sub-Second Fluctuations in the Ionospheric
Electron Density Using the GPS**

by

Anthony Mark McCaffrey

Master of Science, University of New Brunswick, 2015
Bachelor of Science, University of Prince Edward Island, 2012

A Dissertation Submitted in Partial Fulfillment
of the Requirements for the Degree of

Doctor of Philosophy

in the Graduate Academic Unit of Physics

Supervisors: P. T. Jayachandran, Ph.D., Physics

Examining Board: Zong-Chao Yan, Ph.D., Physics
Viqar Husain, Ph.D., Mathematics and Statistics
Marcelo Santos, Ph.D., Geodesy and Geomatics Engineering

External Examiner: Joran Moen, Ph.D., Physics, University of Oslo

This dissertation is accepted by the
Dean of Graduate Studies

THE UNIVERSITY OF NEW BRUNSWICK

July, 2018

©Anthony Mark McCaffrey, 2018

Abstract

Structures in the high latitude ionospheric density are responsible for variations in the phase and amplitude of trans-ionospheric signals. These include space-based navigation systems like the Global Positioning System (GPS). The ionosphere is dispersive, and the refractive index is dependent on the electron density. Thus, variations in the ionosphere will cause changes in the refractive index of the medium. This will lead directly to fluctuations in the phase of the signal, as observed at ground-based receivers. If the spatial scale of these changes in the electron density is sufficiently small, diffraction can occur. This causes rapid variations in the phase and amplitude of the signal. The study of these refractive and diffractive variations (scintillation) has proven vital in monitoring and studying the ionospheric medium. It is known that the diffractive variations in the signal's amplitude and phase are observed in the high-frequency regime; in the typical modern analysis, the refractive variations are assumed to be of low frequency and thus removed by high pass filtering the received signal. This assumption is based on longstanding low latitude measurements. In the high latitude, these assumptions must be reevaluated because of the increase in ionospheric drift speeds observed in the region. Without careful evaluation, the high-frequency refractive variations can be wrongly classified as diffraction. On the other hand, in studying high-frequency variations in the electron density, diffractive artifacts may appear as refractive. This study verifies the existence of diffractive-like high-frequency refractive variations in the high latitude and outlines methods to determine whether the high-frequency variations observed in the GPS carrier phase observable are purely refractive. These methods rely on recent advances in the GPS satellite and receivers; the advances and their impact on

ionospheric monitoring are discussed. The outlined methods of distinguishing these refractive variations are used to study the high-frequency changes in the ionosphere electron density. Electron precipitation is shown to be a likely cause of the small-scale structures which induce the high-frequency refractive variations in the GPS carrier phase.

Dedication

I would like to dedicate this work to the people who have supported me through my academic career and to those who helped me get through it. Many thanks to my parents, Mark and Hayley McCaffrey, my aunt Christina Pater, my girlfriend Annik Dupuis, and all my friends and family. A special recognition to my instructors who have helped guide me through this process: P. T. Jayachandran, my graduate supervisor, James Polson, my undergraduate supervisor, and Elizabeth MacAulay, my high school physics teacher.

Without the people mentioned here, this work would not have been possible. Thank you all.

Acknowledgements

The work was partially supported by the David M. Armstrong foundation. Data sources used in the study are referenced when first mentioned. Computing resources were provided by ACENET. Many thanks to the current and former members of the CHAIN research team for their help along the way. Thanks to the UNB Physics department faculty members for their input and suggestions towards the overall research project.

Table of Contents

Abstract	ii
Dedication	iv
Acknowledgements	v
Table of Contents	vi
List of Tables.....	x
List of Figures	xi
Abbreviations	xxiv
1 Introduction and Outline	1
1.1 Introduction	1
1.2 Thesis Outline.....	6
2 Ionosphere	12
2.1 Introduction	12
2.2 Ionospheric Layers	15
2.2.1 D Layer.....	15
2.2.2 E layer	16
2.2.3 F layer.....	17
2.3 Regional differences	20

2.4	Radio Wave Propagation.....	29
3	Hardware.....	35
3.1	Introduction	35
3.2	Global Positioning System.....	37
3.3	Canadian High Arctic Ionospheric Network	43
3.4	GPS Observables	48
4	Theory	56
4.1	Introduction	56
4.2	GPS Scintillation	57
4.3	Rapid Refractive Variations in Phase.....	63
4.3.1	Total Electron Content	68
5	Data and Methods	74
5.1	Introduction	74
5.2	Septentrio Binary Format Files	75
5.3	Phase Jumps	77
5.4	Standard Scintillation Analysis Methods	81
5.4.1	Multipath.....	84
5.4.2	Scintillation Indices.....	88
6	Independent L2 Tracking	93
6.1	Introduction	93

6.2	L2 Tracking	96
6.3	Results	99
6.4	Conclusion.....	109
7	Refractive Phase Variations	111
7.1	Introduction	111
7.2	Methods	113
7.3	Results and discussion.....	115
7.3.1	Determining Refractive Variations	115
7.3.2	A Case Study Using Three Carrier Frequencies	143
7.3.3	Total Electron Content Analysis	152
7.3.4	Preliminary Determination of the Noise Floor	159
7.4	Conclusion.....	172
8	High-Frequency TEC.....	176
8.1	Introduction	176
8.2	Data and Methods of Analysis	177
8.2.1	Bounding the Higher Order Terms	179
8.2.2	Receiver Phase Noise.....	182
8.2.3	Constraining to Refractive Variations.....	185
8.3	Results and Discussion.....	190
8.3.1	Generation Mechanisms.....	197

8.4	Conclusion.....	217
9	Conclusion and Future Work	219
9.1	Summary	219
9.2	Major Results	221
9.3	Future Work	222
	Bibliography.....	225
	Curriculum Vitae	

List of Tables

Table 3.1 The CHAIN stations using a Septentrio PolaRxS Pro GPS receiver.....47

Table 3.2 Approximate values for the errors associated with the carrier phase
observable.51

Table 7.1 The cut off and noise floor frequencies obtained for both the L1 and L2
carriers for the two presented examples..... 129

Table 7.2 The Fresnel and noise floor frequencies for the L1, L2, and L5 carriers..... 146

Table 7.3 Colors, satellites, and time ranges for the quiet time carrier phase observable
spectra presented in Figure 7.30. 166

List of Figures

Figure 2.1 Example density profile of the mid-latitude ionosphere, demonstrating the differences between solar minimum (dotted), maximum (solid), nighttime (black), and daytime (red). The layers of the ionosphere are also labelled. The profiles were created using the International Reference Ionosphere 2007 model (Watson, 2011).....	14
Figure 2.2 Illustrative example of the typical electron density in the mid and low latitude regions. The equatorial anomaly is also present, centred near 15 hours local time. The anomaly creates two enhancements in electron density, the pair roughly centred on the geomagnetic equator and settling $10^{\circ} - 15^{\circ}$ to either side of it. Retrieved from https://iono.jpl.nasa.gov/gim.html	21
Figure 2.3 Illustrative example of the variability which can occur in the high latitude regions of the ionosphere. The percent difference between an active ionospheric day's TEC map compared to a representative quiet day is presented. Nearly a 100% increase in TEC is observed in the high latitudes, as well as enhancements and depletions ranging from -60% to 100% difference. Retrieved from https://iono.jpl.nasa.gov/storm_demo.html	23
Figure 2.4 An idealized representation of the twin cell convection pattern observed in the high latitude regions, presented in geomagnetic latitude and local time coordinates (Heelis et al., 1982).	24
Figure 2.5 Illustrative representation of the Earth's magnetic field and the solar wind's interaction with it. The magnetic field is compressed in the dayside (left) and elongated on the night side (right). This is due to the pressure of the solar wind. The solar wind is	

also shown to be deflected away from the Earth due to the magnetic field. Retrieved from <https://www.jpl.nasa.gov/infographics/infographic.view.php?id=10686>.26

Figure 2.6 An image of the auroral oval, as seen from space, superimposed onto a map of the Earth. The image was taken using the Ultraviolet Imager onboard the “Polar” satellite. The red colour represents the brightest portions of the auroral oval while the blue represents the dimmest. Retrieved from http://sd-www.jhuapl.edu/Aurora/UVI_on_Earth.html.....28

Figure 2.7 An illustrative explanation of HF communication using the ionosphere to facilitate over the horizon communication. Since the transmitter and receiver do not have a line of sight to one another due to the curvature of the Earth, communication between the two locations would not be possible without the ionosphere. Retrieved from <https://www.electronics-notes.com/articles/antennas-propagation/ionospheric/hf-propagation-basics.php>.....32

Figure 2.8 A simple illustration demonstrating the refractive effect of a homogenous ionosphere on satellite-based signals. The satellite on the left, which transmits the orange signal, represents no ionosphere. The signal travels directly from the satellite to the ground. The satellite on the right, with the yellow signal, shows the effects of a homogenous ionosphere, where the signal is bent as it enters and exits the ionospheric medium. Retrieved from <https://www.e-education.psu.edu/geog862/node/1715>.....34

Figure 3.1 Simple two-dimensional illustration of the trilateration technique used in GPS positioning. Retrieved from <http://scienceline.org/2016/05/how-does-your-gps-know-where-you-are/>.39

Figure 3.2 Illustrative example of the P-code (first panel), the P-code signal (second panel), the C/A code (third panel), the C/A code signal (fourth panel) and the composite

signal (fifth panel). The P-code signal and the C/A code signal illustrate the modulation of the respective codes to pure signals. The C/A code signal and the P-code signal are in quadrature, allowing for their addition to create the final composite signal.....42

Figure 3.3 The Septentrio PolaRxS Pro GPS receiver. This receiver is used to retrieve all GPS data presented in this study. Each receiver is located at a station in the Canadian high latitude region, all as part of CHAIN. Retrieved from https://www.navtechgps.com/septentrio_polarxs_packaged_receivers/.....45

Figure 3.4 Map of CHAIN, outlining which stations are using the Novatel or Septentrio GPS receivers.46

Figure 3.5 Illustration of the composite GPS signal at a given epoch, represented by plotting the in-phase and quadrature signals' magnitudes in polar form.49

Figure 3.6 An example of the carrier phase observable (black) and the IQ-derived phase (blue). The event has a large portion of quiet time which demonstrates the difference in magnitudes; a significant event is located at roughly 42 minutes (blue) and 47 minutes (black). The IQ-derived phase is shifted negatively by five minutes to better visualize the magnitudes of the event. The IQ-derived phase overestimates the high-frequency noise and underestimates the magnitude of the event.54

Figure 3.7 The spectrum of the IQ-derived phase (blue) and the carrier phase observable (black). Note that the IQ-derived phase has larger magnitude variations in the high frequencies.55

Figure 4.1 Simple illustration of a two-dimensional ionospheric layer, with irregularities scattering a wavefront. The scattered and non-scattered wavefronts will interfere constructively and destructively; this will result in diffractive effects referred to as

scintillation. Note that scattering due to the homogeneous part of the layer is ignored for simplicity.....	59
Figure 4.2 Illustration of the expected spectral behaviour for GPS amplitude and phase scintillation.....	62
Figure 4.3 Illustration of the TEC measurement.....	71
Figure 4.4 An illustrative example of the projection from sTEC to vTEC, using a single thin shell model of the ionosphere. The pierce point of the ray is taken at the assumed height of the shell (h). Retrieved from http://gnss.be/ionosphere_tutorial.php	73
Figure 5.1 Example of a clock jump in the raw carrier phase observable. The uncorrected carrier phase, with the clock jump, is represented by the black curve. The corrected carrier phase observable is represented by the dashed green line.	80
Figure 5.2 Representation of the receiver clock drift (blue). After the clock drifts $500 \mu\text{s}$, it is shifted 1 ms towards the correct value.	83
Figure 5.3 A simple illustration describing multipath. Multiple signals from the same satellite arrive at the antenna with varying path lengths, leading to an interference of the signals.....	85
Figure 5.4 An example of the repetitive nature of multipath. The amplitude (left) and normalized standard deviations over one-minute intervals (right) are presented for three consecutive solar days. Features like the one present at roughly 42 minutes on the first day are seen to repeat each day, shifted negatively by approximately four minutes. This indicates the features repeats on sidereal day intervals.....	87
Figure 5.5 An example of the raw carrier phase observable (top), detrended carrier phase using wavelet detrending and a 0.1 Hz cut-off (middle), and the corresponding scintillation index $\sigma\phi$	90

Figure 5.6 An example of the raw amplitude (top), detrended amplitude using wavelet detrending with a 0.1 Hz cut-off (middle), and the scintillation index S_4 corresponding to the detrended amplitude.91

Figure 6.1 An example of the detrended L1C/A carrier phase (top), detrended L2P(Y) carrier phase (middle left), and detrended L2C carrier phase (middle right) taken from a Septentrio PolaRxS Pro receiver. The linear fit between the L1C/A-L2P(Y) carrier phase pair and the L1C/A-L2C carrier phase pair are presented in the bottom left and right panels respectively.98

Figure 6.2 An example of the detrended L2C carrier phase (top) and the detrended L2P(Y) carrier phase (middle) for the Trimble NetR9 (left) and Septentrio PolaRxS Pro (right) receivers. The difference between the L2P(Y)-L2C carrier phase pair for each receiver are presented in the bottom panels (Trimble on the left, Septentrio on the right).101

Figure 6.3 The detrended signal intensity for the L2C carrier from the Septentrio receiver is presented in the top panel. The L2P(Y)-derived IFLC (middle) and the L2C-derived IFLC (bottom) are presented for each receiver (Trimble on the left, Septentrio on the right).106

Figure 6.4 The L2C-L1C/A and L2P(Y)-L1C/A combination of the carrier phase observables for the Trimble and the Septentrio receivers, where a full-turn rotation of the antenna occurs about 2 seconds into the time series'. This is the effect of phase wind-up incurred by the antenna rotation.108

Figure 7.1 Example carrier phase variation events during DOY 186, 2015. The detrended L1 carrier phase (top left), L2 carrier phase (middle left), and the corresponding IFLC (bottom left) are presented. The red lines indicate the event of

interest, as well as the time window used in calculating the corresponding spectra (panels to the right of the respective datasets).	117
Figure 7.2 Example carrier phase variations event during DOY 218, 2015. The detrended L1 carrier phase (top left), L2 carrier phase (middle left), and the corresponding IFLC (bottom left) are presented. The red lines indicate the event of interest, as well as the time window used in calculating the corresponding spectra (panels to the right of the respective datasets).	118
Figure 7.3 The three spectra presented in Figure 7.1. The L1 spectrum is presented in black, L2 in blue, and the IFLC spectrum in red.	120
Figure 7.4 The three spectra presented in Figure 7.2. The L1 spectrum is presented in black, L2 in blue, and the IFLC spectrum in red.	121
Figure 7.5 L1 amplitude variations for the DOY 186 example. The detrended amplitude is presented in the top panel, with the spectrum, taken over the time interval indicated with the red line, presented in the bottom panel. The fits obtained for the low frequencies, the scintillation frequencies, and the high-frequency noise, are represented by the blue, green, and red lines respectively. The intersection points are indicated by the dashed green lines.	125
Figure 7.6 L2 amplitude variations for the DOY 186 example. The detrended amplitude is presented in the top panel, with the spectrum, taken over the time interval indicated with the red line, presented in the bottom panel. The fits obtained for the low frequencies, the scintillation frequencies, and the high-frequency noise, are represented by the blue, green, and red lines respectively. The intersection points are indicated by the dashed green lines.	126

Figure 7.7 L1 amplitude variations for the DOY 218 example. The detrended amplitude is presented in the top panel, with the spectrum, taken over the time interval indicated with the red line, presented in the bottom panel. The fits obtained for the low frequencies, the scintillation frequencies, and the high-frequency noise, are represented by the blue, green, and red lines respectively. The intersection points are indicated by the dashed green lines. 127

Figure 7.8 L2 amplitude variations for the DOY 218 example. The detrended amplitude is presented in the top panel, with the spectrum, taken over the time interval indicated with the red line, presented in the bottom panel. The fits obtained for the low frequencies, the scintillation frequencies, and the high-frequency noise, are represented by the blue, green, and red lines respectively. The intersection points are indicated by the dashed green lines. 128

Figure 7.9 An example of the refractive variations (top), diffractive variations (middle), and high-frequency noise (bottom) during the DOY 186 example. The L1 carrier phase variations are presented in black, the L2 carrier phase variations are presented in blue. 131

Figure 7.10 An example of the refractive variations (top), diffractive variations (middle), and high-frequency noise (bottom) during the DOY 218 example. The L1 carrier phase variations are presented in black, the L2 carrier phase variations are presented in blue. 132

Figure 7.11 The linear fit between the L1 and L2 carrier phase variations, for the DOY 186 example. The carrier phases' have been bandpass filtered to contain only the refractive variations (top), diffractive variations (middle), and high-frequency noise (bottom). The linear fits are represented by the red lines. 135

Figure 7.12 The linear fit between the L1 and L2 carrier phase variations, for the DOY 218 example. The carrier phases have been bandpass filtered to contain only the refractive variations (top), diffractive variations (middle), and high-frequency noise (bottom). The linear fits are represented by the red lines. 136

Figure 7.13 The surface representing the Fresnel frequency corresponding to given irregularity height and drift velocity pairs (blue) and the place corresponding to the cut off frequency between refractive and diffractive variations determined for the DOY 186 event (red). 138

Figure 7.14 The surface representing the Fresnel frequency corresponding to given irregularity height and drift velocity pairs (blue) and the place corresponding to the cut off frequency between refractive and diffractive variations determined for the DOY 218 event (red). 139

Figure 7.15 The curve representing the intersection between the Fresnel frequency surface and the cut off frequency plane presented in Figure 7.13, corresponding to the DOY 186 example. This presents the irregularity height and drift velocity pairs necessary for a Fresnel frequency equal to the cut off frequency..... 140

Figure 7.16 The curve representing the intersection between the Fresnel frequency surface and the cut off frequency plane presented in Figure 7.14, corresponding to the DOY 218 example. This presents the irregularity height and drift velocity pairs necessary for a Fresnel frequency equal to the cut off frequency. 141

Figure 7.17 The phase variation event for the three carrier frequency example. The detrended L1 carrier phase is presented in the top panel, the L2 carrier in the middle panel, and the L5 carrier in the bottom panel. The red line indicates the event being analyzed..... 145

Figure 7.18 The amplitude spectra corresponding to the phase event. The L1 carrier amplitude spectrum is presented in the top left panel, the L2 carrier spectrum in the top right panel, and the L5 carrier spectrum in the bottom left panel. The blue, green, and red line represent the fits for the zero-slope, low-frequency portion of the spectrum, the scintillation portion, and the high-frequency noise portion, respectively. 146

Figure 7.19 The linear fits between the refractive variations (top panel), diffractive variations (middle panel), and the high-frequency noise (bottom panel) for the L1-L2 carrier phase pair. 149

Figure 7.20 The linear fits between the refractive variations (top panel), diffractive variations (middle panel), and the high-frequency noise (bottom panel) for the L1-L5 carrier phase pair. 150

Figure 7.21 The linear fits between the refractive variations (top panel), diffractive variations (middle panel), and the high-frequency noise (bottom panel) for the L2-L5 carrier phase pair. 151

Figure 7.22 The detrended L1 carrier phase observable (top) and the corresponding raw sTEC (bottom) for the DOY 186 example. 153

Figure 7.23 The detrended L1 carrier phase observable (top) and the corresponding raw sTEC (bottom) for the DOY 218 example. 154

Figure 7.24 The raw sTEC (top) and the filtered sTEC (bottom), which is filtered from the 0.1 Hz low-frequency cut-off to the Fresnel frequency, corresponding to the DOY 186 example. 155

Figure 7.25 The raw sTEC (top) and the filtered sTEC (bottom), which is filtered from the 0.1 Hz low-frequency cut-off to the Fresnel frequency, corresponding to the DOY 218 example. 156

Figure 7.26 The L1 (top left panel) and L2 (top right panel) bandpass filtered carrier phase, filtered from 0.1 Hz to the appropriate Fresnel frequency, the estimated effects of the sTEC (middle panels) on the carrier phase, bandpass filtered to the same frequencies, and the differences between them (bottom panels) corresponding to the DOY 186 example. 158

Figure 7.27 The L1 (top left panel) and L2 (top right panel) bandpass filtered carrier phase, filtered from 0.1 Hz to the appropriate Fresnel frequency, the estimated effects of the sTEC (middle panels) on the carrier phase, bandpass filtered to the same frequencies, and the differences between them (bottom panels) corresponding to the DOY 218 example. 159

Figure 7.28 The comparison of the input modelled scintillation spectrum (*input*, red) to a GPS receiver simulator, the output from the simulator during the modelled scintillation (*iono*, green) and during no scintillation (*no iono*, blue). The simulator uses a 5 Hz bandwidth and a signal to noise ratio of 200 dBHz for this example (Rougerie et al., 2016). 163

Figure 7.29 The comparison of the modelled scintillation spectrum (*input*, red) input provided to a GPS receiver simulator, the output from the simulator during the scintillation variations (*iono*, green) and when no scintillation occurs (*no iono*, blue). In this example, the simulator uses a 10 Hz bandwidth and a signal to noise ratio of 45 dBHz (Rougerie et al., 2016). 165

Figure 7.30 Comparison of four quiet time carrier phase spectra (top) and an ionospheric carrier phase variation event (bottom). The four quiet time spectra are taken from four different satellite, at different times throughout DOY 70. All data is taken from the CHAIN Churchill station. 167

Figure 7.31 The noise floor spectra and event spectrum from Figure 7.30, plotted together to better visualize the comparison..... 169

Figure 7.32 Comparison of the quiet time spectra were taken from the CHUC station (blue), the GRIS station (red) and the FRSC station (green). The CHUC station represents the examples presented in Figure 7.30. The GRIS and FRSC station use the same receiver, relocated from the GRSC station (2015) to the FRSC (2017). 171

Figure 8.1 Example phase variations induced by purely refractive variations based on the established criteria. Data was taken from the CHUC station using satellite PRN 1 during UTC hour 4. The detrended L1 (top left) and L2 (top right) carrier phase observables are presented with the corresponding detrended L1 (middle left) and L2 (middle right) amplitude data. The event takes place at roughly 47 minutes. The corresponding S_4 for each amplitude data set is presented in the bottom panels with the two-sigma rule threshold in red. The S_4 does not exceed the threshold during the phase variation event. 189

Figure 8.2 The linear fit between the detrended L1 and L2 carrier phase observables during the example event. The slope is 1.65, falling within the 1.62 – 1.66 range chosen for the refractive variations criteria. 190

Figure 8.3 A qualitative example of the small amplitude, high-frequency variations in the inactive high-frequency sTEC. The top panel shows a representative example of the 100 Hz sTEC, for one minute. The bottom panel shows a two-second subset of the above sTEC..... 191

Figure 8.4 A representative example of the one-second standard deviations of sTEC used to quantify the sub-second variations in the high-frequency TEC..... 192

Figure 8.5 An example of active sTEC, where larger magnitude sub-second variations are present. The one-second standard deviations in TEC are presented in black, the expected magnitude of the receiver phase jitter in green, and the expected magnitude of the higher order delay terms are in blue..... 196

Figure 8.6 The magnitude of the variations in the geomagnetic field necessary to induce variations in TEC from 0.1 to 3 TECU..... 197

Figure 8.7 An example of significant sub-second sTEC (top) and visually correlating sub-second variations in the geomagnetic field variations (bottom). 199

Figure 8.8 Distribution of the local times corresponding to TEC events, for DOY 91 – 365, 2015.....201

Figure 8.9 Distribution of local times corresponding to geomagnetic field variations events for DOY 91 – 365, 2015.202

Figure 8.10 Comparison of the geomagnetic field variations (top panel) and variations in the sTEC, as seen from three separate GPS satellites (second through fourth panels). The geomagnetic field and sTEC data have been high pass filtered to better visualize to higher frequency variations.....204

Figure 8.11 The track of the DMSP 16 satellite for March 16, 2015 (left) and March 17, 2015 (right), represented by the red line. The Arviat, Gjoa Haven, Rankin Inlet, and Repulse Bay CHAIN station are represented by the black diamonds, with the IPPs of a few satellites of interest represented by the blue lines.....206

Figure 8.12 Electron energy flux for the DMSP 16 satellite pass over the Canadian high latitudes. The passes occur during hour 11 UTC, on March 16, 2015 (left) and March 17, 2015 (right).207

Figure 8.13 The one-second standard deviations for GPS satellite PRNs 5, 7, 15, and 29, as seen from the Arviat, Gjoa Haven, Rankin Inlet, and Repulse Bay stations. Each colour represents a ray path. The left panel shows the data from March 16, 2015, the right panel shows that data from March 17, 2015.....208

Figure 8.14 The horizontal component of the geomagnetic field, high pass filtered, for March 16, 2015 (left) and March 17, 2015 (right).....209

Figure 8.15 The one-second standard deviation in sTEC for all available ray paths during DOY 70, 2015.....210

Figure 8.16 The high pass filtered horizontal component of the magnetic field data. The data was taken from the Churchill station ICM in the CARISMA network during DOY 70, 2015. Significant variations in field data are present during roughly 5 hours UTC to 8 hours UTC, which corresponds to the first sTEC event. Much lower magnitude variations are present in the magnetic field data during the 16.5 hours UTC to 19.5 hours UTC sTEC event.211

Figure 8.17 Illustration of the coverage provided by the GOES-West and GOES-East geostationary satellites. The GOES-East satellite provides coverage of central and eastern Canada and is, therefore, more relevant to this study. Retrieved from <https://www.nesdis.noaa.gov/content/goes-r-has-become-goes-16>.212

Figure 8.18 The electron flux measurements from the GOES-13 during March 10, 2015. The panels are ordered by energy levels, increasing from top to bottom. The blue lines represent the westward facing detector and the black lines represent the eastward facing detector.214

Figure 8.19 TEC along various GPS ray paths during UTC hours 10 through 16, DOY 70, 2015, for six CHAIN stations. Each colour represents a different ray.215

Abbreviations

BPSK - Binary Phase Shift Keying

CARISMA – Canadian Array for Realtime Investigations of Magnetic Activity

CHAIN – Canadian High Arctic Ionospheric Network

DMSP - Defence Meteorological Satellite Program

EUV - Extreme Ultraviolet

FOC - Full Operation Capability

GNSS – Global Navigation Satellite System

GOES - Geostationary Operational Environmental Satellite

GPS - Global Positioning System

HF – High Frequency

ICM – Induction Coil Magnetometer

IFLC – Ionosphere Free Linear Combination

IGS - International GNSS Service

IMF - Interplanetary Magnetic Field

IOC - Initial Operating Capability

ISMR – Ionospheric Scintillation Monitoring Record

MGEX - IGS Multi-GNSS Experiment

OXCO - Oven Controlled Crystal Oscillator

PLL – Phase Lock Loop

PRN - Pseudo Random Noise

RINEX - Receiver Independent Exchange

ROT - Rate Of Change in TEC

ROTI - Rate Of Change of TEC Index

SBF - Septentrio Binary Format

SPS - Standard Positioning Service

sTEC – Slant Total Electron Content

TEC - Total Electron Content

TECU – Total Electron Content Unit

UTC – Coordinated Universal Time

vTEC – Vertical Total Electron Content

1 Introduction and Outline

1.1 Introduction

Space-based navigation, such as the Global Positioning System (GPS), has become ubiquitous through the recent years. Many applications, such as military, marine, and surveying, for example, have become reliant on the accurate performance of GPS. Not only has industry evolved around this tool, but the civilian population has become expectant on the reliability and precision of GPS, specifically in its navigation and positioning capabilities. However, many issues exist that reduce the accuracy in GPS positioning and navigation; these include tropospheric delay, receiver errors, and satellite hardware delays, for example. Many mitigation techniques have been developed and implemented to correct for these errors, however, the most prominent error source, the ionosphere, can produce very large errors in the positioning result and in the most extreme cases can prevent the receiver from obtaining any result, thus making GPS useless.

In ideal situations, the ionosphere is homogenous. This still induces errors in the GPS positioning techniques, but methods of eliminating this error have been well established. Most of the methods exploit the dispersive nature of the medium and the multiple frequencies transmitted by the GPS satellites. However, the ionosphere is rarely this well behaved, especially in active areas like the low and high latitudes. In these regions, structures in the density can cause rapid variations in the amplitude and phase of the

GPS signals. In the best cases, these rapid variations lead to decreases in accuracy and precision of the positioning result. In the extreme cases, the variations in amplitude dip too low, or the magnitude or frequency of the phase variations are too high, and these exceed the receiver's threshold to track the signal (Kaplan and Hegarty, 2005). If this occurs to a sufficient number of satellites in view at a given time, no positioning information would be available. In important applications, such as aviation, this can have very serious consequences. The study of these rapid variations in the amplitude and phase of the signals, and a better understanding of the morphology, climatology, and formation mechanisms of the inhomogeneities that cause them, is an important area of research. Any advances in the area may lead to better mitigation or reduction of the ionospheric errors in GPS and other space-based navigation.

Fortunately, the effects of the ionosphere on the GPS signals can be used to the advantage of those interested in researching and monitoring it. This is typically split into two categories, the study of the low-frequency effects on the signal and the study of the high-frequency effects. The low-frequency effects are caused by very large scale or slow-moving/varying, structures in the density. These can be studied using the dispersive nature of the ionosphere and the multiple frequencies transmitted by the GPS satellites. Using a combination of two frequencies, a measure of the integrated density along the signal's ray path can be obtained. This gives information about the density at a given epoch. Introducing all GPS satellites, and the global network of GPS receivers, very large areas can be studied, observing the morphology of the bulk plasma density. In some cases, nearly global coverage can be obtained.

The study of the high-frequency variations is typically concerned with the smaller scale size or faster moving / varying inhomogeneities in the plasma density. These smaller inhomogeneities can lead to diffraction, causing rapid fluctuations in the amplitude and phase of the signal. These diffractive effects are typically referred to as scintillation. Although these high-frequency variations cannot be related directly to the structures causing them, as can be done in the low-frequency analyses, important information about the distribution of the small-scale inhomogeneities can be determined (Davies, 1990).

Initial studies into these small-scale structures focused on the low and equatorial latitudes and certain assumptions were made based on the discoveries made in this region. However, the characteristics of the ionosphere in this region are very specific, presenting morphology and formation mechanisms not observed elsewhere. Eventually, monitoring hardware was introduced into other regions. This allowed for the study of other areas of the ionosphere, like the high latitude region. The high latitude region, like the equatorial region, is peculiar in its formation mechanisms and morphology. The high latitude ionosphere is intimately connected to the magnetosphere and solar wind, creating a very active ionosphere different from the other regions. Studying the high latitude ionosphere requires care in the methods used in analyzing the data and the assumptions that the methods may be based on. Unfortunately, the methods and assumptions designed using the low latitude results have been commonly used in the high latitude ionosphere, and are now mostly ubiquitous in the field. Since these

assumptions likely will not hold in the high latitude, problems with the analysis methods are likely to occur.

The most prominent issues stem from the detrending frequency. This is the cut-off frequency used in a high-pass filter which is applied to the raw GPS data. As the name suggests, this is meant to remove low-frequency trends in the signal. Based on low latitude studies, a cut-off frequency of 0.1 Hz was chosen (Van Dierendonck et al., 1993). However, it was chosen by suggesting that 0.1 Hz corresponds well to the Fresnel frequency; the Fresnel frequency is the lowest frequency at which scintillation variations should be visible in the amplitude and phase. In short, if the wrong cut-off frequency is used, non-scintillation variations may be present in the detrended signal. The Fresnel frequency is dependent on the drift speed of the ionospheric inhomogeneities. The drift speed has been shown to be much higher in the high latitude ionosphere, suggesting a significant increase in the Fresnel frequencies in the region. Thus, studying the high latitude ionosphere, understanding its differences compared to the other regions, and ensuring the methods being used are valid, are important problems in the field. Recently, work has begun to address and attempt to remedy these issues, for example, see Forte and Radicela (2002), Mushini (2013), and McCaffrey et al. (2018b).

Developing new techniques to further address this issue is important, and as advancements in technology are made, new and more accurate results can be obtained. The Canadian High Arctic Ionospheric Network (CHAIN) (Jayachandran et al., 2009)

has recently expanded to add more GPS-based ionospheric monitoring stations to the Canadian high latitude region. The receivers deployed at these new stations allow for an increased sampling rate of the amplitude and phase of the GPS signal, and tracking techniques of new GPS signals which are more accurate for ionospheric research purposes. This allows for a denser spatial coverage of the ionosphere in the region, monitoring at an increased sampling rate, and most importantly, more accurate measurements of the GPS observables and thus more accurate monitoring of the ionosphere.

We take advantage of these improvements in the instruments and the network to focus on the study of the very small, or very fast moving gradients in the plasma density. These gradients induce high-frequency variations in the GPS carrier phase, with our focus being on the sub-second variations. These variations are purely refractive; this can be shown by taking advantage of the improved accuracy provided by a specific tracking technique used by these receivers. Since the high-frequency variations are typically assumed to be diffractive scintillation, it is important to show that these high-frequency refractive variations can occur in the GPS signal, and methods of isolating them from the diffractive variations are outlined. This is an important result for scintillation research wishing to focus on the diffractive variations alone. However, we choose to focus on the high-frequency refractive variations, focusing on the formation mechanisms of these small-scale or fast drifting structures.

1.2 Thesis Outline

Chapter 2 begins with a brief overview of the ionosphere, focusing on introducing its formation mechanisms. The layers of the ionosphere are then discussed in order of altitude. This begins with the D layer, followed by the E layer, and lastly the F layer and its sublayers: F1 and F2. The main formation mechanisms of these layers, including the main wavelength bands responsible for the ionization of the neutrals, are discussed. Other important mechanisms, including the diffusion of plasma in the F region, and particle precipitation in the lower layers are also introduced. Regional differences in the ionosphere are discussed next, broadly presenting the differences between the mid and low latitude ionosphere. The low latitude ionosphere, specifically the equatorial region is discussed in more depth, focusing on the equatorial anomaly. This is presented in context with the differences in high latitude ionosphere. The high latitude region is of interest for this study and is thus the focus of the section. The effect of the nearly vertical geomagnetic field lines on the high latitude ionosphere is discussed, outlining the auroral and polar cap regions. The chapter is concluded by introducing the ionosphere's effect on radio wave propagation. This begins with its effect on ground-based communication, such as High Frequency (HF) communication. The section ends with a discussion on the effect of the ionosphere on space-based, or trans-ionospheric radio waves, the focus of this study.

Chapter 3 discusses the hardware used for this study. This focuses on the GPS, its satellites, and the receivers which track their signals. The chapter begins with an introduction and brief history of the GPS, and an overview of some of its basic features. This is framed in the context of ionospheric research. The basis behind GPS positioning is also outlined, briefly introducing trilateration, the method used for GPS positioning. The structure of the GPS signals, including the modulation techniques, the carriers, and the legacy and modern codes are discussed. This includes the benefits of the different codes, and how their structure affects their use. CHAIN is discussed in the last section. CHAIN is a network of ground-based equipment in the Canadian high latitude region used primarily for ionospheric research and monitoring. The GPS data for this study is taken almost entirely from CHAIN, and thus the network and the receivers are discussed. Of the receivers available within CHAIN, only the Septentrio PolaRxS Pro is used for this study; the receiver is introduced, and its advantages are discussed.

Chapter 4 covers the background theory relevant to the presented research. This includes the two main effects of the ionosphere on the GPS carrier phase observable: refractive and diffractive effects. Diffractive variations, or scintillation, and the field of scintillation research is discussed. The history of the field is briefly introduced, followed by the diffraction mechanism. The Fresnel scale and Fresnel frequency associated with scintillation are introduced; these are relevant aspects of scintillation theory that will be necessary for discussing later results. The expected spectral behaviour of the amplitude and phase of a GPS signal undergoing the effects of scintillation is also introduced. The purely refractive effects of the ionosphere are introduced next, focusing on the high-

frequency refractive variations induced by inhomogeneities in the ionosphere. This is the main focus of the thesis and is thus discussed in more detail. This includes the derivation of the refractive index of the ionosphere from the Appleton-Hartree equation and its impact on the GPS carrier phase observable. The low-frequency refractive variations are also discussed, introducing the GPS-derived TEC measurement. TEC is a measure of the electron density along the ray path and is a popular and powerful tool in GPS-based ionospheric research and monitoring. Its derivation from the two main GPS carrier phase observables is described.

Chapter 5 outlines the GPS data used in this study, followed by the methods used in analyzing this data. The GPS data, as previously mentioned, comes from the Septentrio receivers of the CHAIN. The data is provided as raw binary files, thus, extensive processing is needed to get the observables of interest. A description of the raw binary files is given, followed by an introduction to the decoding methods used to get the GPS observables. Common receiver effects on these observables, such as clock jumps and cycle slips, are outlined. These are effects that must be removed or mitigated before any of the presented work can be done. The last part of the chapter discusses the methods used in manipulating the raw GPS observables into something more useful for ionospheric research. This includes the prominently used processing methods in the GPS-based ionospheric scintillation research community. The section begins with detrending, the methods used in removing the low-frequency trend from the GPS observables. This is followed by the effects of multipath on the GPS carrier phase and amplitude, and how it can be identified so as not to mistake it with ionospheric-induced

effects. This involves exploiting the repeatability of the GPS orbits and multipath reflectors, as well as the theoretical limit of GPS carrier phase multipath effects. Lastly, the scintillation indices, S_4 and σ_ϕ are introduced and discussed.

Chapter 6 discusses the effects of independent tracking on the GPS observables.

Independent tracking means that each GPS carrier is tracked independently of the others. This is the technique used by the Septentrio PolaRxS Pro receiver. Many other receivers use dependent tracking; this technique assumes that one carrier undergoes nearly identical high-frequency dynamics as another. This leads to a more robust tracking of the carrier but also introduced errors in the high-frequency dynamics. Results are presented demonstrating that the Septentrio receivers do in fact use independent tracking, while others do not. This is done through zero-baseline receiver comparisons and a phase wind-up experiment. The effects of dependent tracking are also presented, demonstrating its impact on the high-frequency dynamics of the signal in regards to ionospheric research.

Chapter 7 introduces the high frequency, purely refractive, variations in the GPS carrier phase. Example ionospheric-induced carrier phase variation events are presented, using several techniques to show that the variations are refractive. This includes a determination of the corresponding Fresnel frequencies and exploiting the deterministic, inverse frequency-squared dependence of the refractive effect of the ionosphere on the phase of the GPS signals. This is first demonstrated using dual frequency results and is

followed by a triple-frequency example, further showing the existence of these refractive variations and how they can be dominant when using the standard scintillation analysis methods. An initial analysis into the TEC of the refractive variations is presented as well, calculating the impact of the TEC on the phase, assuming purely refractive variations are present, and comparing it to the real phase.

Chapter 8 exploits the techniques of the previous chapter to analyze the high frequency, purely refractive variations, of the GPS carrier phase. By using a variation of the methods presented in the previous chapter, the high-frequency GPS-derived TEC can be cleared of diffractive artifacts. The sub-second variations in the auroral region TEC is then analyzed. Both high and low magnitude variations are observed. To determine which variations are relevant, the receiver noise floor and the higher order terms in the refractive index estimation are analyzed. The low magnitude variations are deemed receiver noise; however, the high magnitude variations are likely ionospheric. These sub-second TEC events are shown to correlate moderately well with various events in the magnetic field data, obtained from the Canadian Array for Realtime Investigations of Magnetic Activity (CARISMA). Using particle precipitation data from the Defence Meteorological Satellite Program (DMSP) satellite and the Geostationary Operational Environmental Satellite (GOES) it is shown that increases in electron precipitation coincide with these sub-second TEC variations as well. This is used to suggest that electron precipitation is likely responsible for the sub-second TEC events.

Chapter 9 summarizes the work presented in the thesis and introduces ideas to further the study. The major results include the effects of dependent tracking on GPS-based ionospheric research and the observation of sub-second variations in the density of the ionosphere. The former is important as it indicates that any past high-frequency analysis, if performed using dependent tracking, must be re-evaluated. The latter suggests that very small scale, or very fast moving, irregularities exist in the ionosphere density. These irregularities are unlikely to have been observed in the past, due to hardware limitation, and thus introduce a new area of focus as the GPS hardware improves.

2 Ionosphere

2.1 Introduction

The ionosphere is a section of the Earth's atmosphere where the neutral constituents become ionized creating a layer of plasma. It typically lies within a 60 km - 1000 km altitude above the Earth's surface, however, there are no well-defined boundaries. The neutral constituents of the atmosphere become ionized at these heights predominantly through photo-ionization, although other mechanisms exist with varying contributions to the overall ionization. In the day-side ionosphere (referring to the side of the Earth which is facing the sun), the plasma is in constant flux, where the neutrals are being ionized through photo-ionization while the free electron and ions may recombine. Within the night-side ionosphere, the recombination of the free electrons and the ions dominate, specifically at lower altitudes where the atmospheric neutral density is greater, causing the overall ionization to drop dramatically. The main ionic constituents of the ionosphere are oxygen (O_2^+), diatomic nitrogen (N_2^+), and atomic oxygen (O^+) (Davies, 1990; Hunsucker and Hargreaves, 2007). Due to the varied molecular weights of the constituents, the ionosphere is horizontally stratified. This can be seen in the vertical density profiles of the ionosphere. An example of a mid-latitude ionosphere density profile is presented in Figure 2.1. The four layers of the ionosphere are labelled, the D layer, lying at the lowest altitude, the E layer above it and the F layer above that; The F layer is split into two sublayers, the F1 and F2. Formation of these layers is discussed in more detail in the following section. The difference in the density between the daytime and nighttime ionosphere is also present in the figure. The daytime profiles are presented

in red and the nighttime profiles in black. A clear decrease in ionization during nighttime is observed, most prominently in the lower altitudes due to the increase in molecular density. An increase in the overall density is also observed during solar maximum, represented by the solid lines when compared to the solar minimum profiles presented by the dotted lines. This is due to the increase in solar radiation, causing a direct increase in the ionization of the neutral constituents.

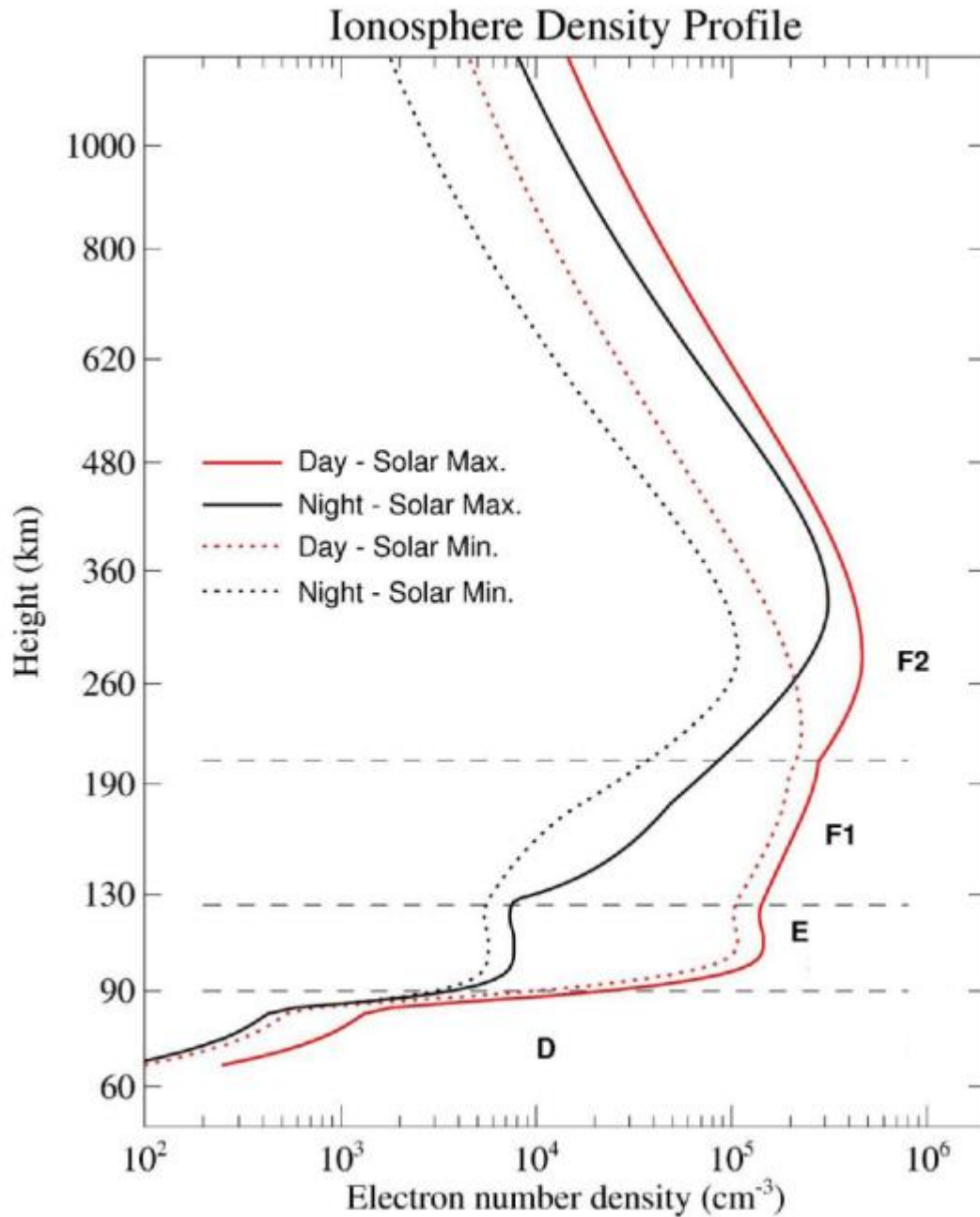


Figure 2.1 Example density profile of the mid-latitude ionosphere, demonstrating the differences between solar minimum (dotted), maximum (solid), nighttime (black), and daytime (red). The layers of the ionosphere are also labelled. The profiles were created using the International Reference Ionosphere 2007 model (Watson, 2011).

2.2 Ionospheric Layers

2.2.1 D Layer

The D layer is the lowest altitude layer of the ionosphere, typically ranging from 60 km to 90 km in height above the Earth's surface. At this low altitude, the main radiation bands capable of penetrating this distance and ionizing the constituents are the Lyman α and hard x-rays. Lyman α radiation has a wavelength of approximately 121.5 nm and can ionize the nitric oxide (NO) molecules. The hard x-rays have wavelengths lying within the 0.1 nm – 1 nm range, and can ionize all constituents (Hunsucker and Hargreaves, 2007). The intensity of the hard x-rays emission from the sun can vary significantly in time, therefore its contribution to the total D region ionization varies as well. A small contribution to the total ionization occurs from Extreme Ultraviolet (EUV) radiation, responsible for ionizing molecular oxygen. The electron affinity of molecular oxygen is small, resulting in the possibility of the removal of an electron by interaction with photons of visible or near-infrared light:



The most popular neutral constituents at the height of the D layer is NO, O₂, and N₂. Since the radiation responsible for ionizing these species are of solar origin, the ionization levels of the D layer increase significantly during the daytime. At night the

overall ionization will decrease significantly since a significant drop in radiation occurs, resulting directly in a decrease in ionization rates. Thus, recombination of the free electrons with the negative ions are the dominant reaction during the night time. Free electrons will also combine with molecular oxygen, creating O_2^- :



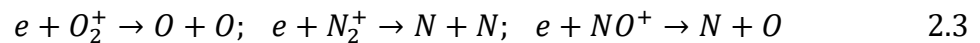
where M is any other molecule, which absorbs excess kinetic energy from the reactants (Davies, 1990; Hunsucker and Hargreaves, 2007). The recombination rates are dominant enough to cause the D layer to mostly disappear at night, reappearing only when the solar radiation begins again after sunrise.

Particle precipitation can be a major contributor the ionization in the D region as well, depending on the geographical region. This is mostly an effect in the high latitude and auroral regions, but in extreme cases can spread to lower latitudes as well. This is due to high energy particles from the solar wind streaming along the Earth's magnetic field lines into the upper atmosphere. These particles may be energetic enough to ionize the neutrals.

2.2.2 E layer

The E layer typically extends from 90 km – 150 km in altitude, with a peak density lying near 110 km. The major contributor to ionization in the E layer is EUV radiation and soft x-rays. The EUV radiation capable of penetrating to the E layer range from 80 nm to 102.7 nm in wavelength. These wavelengths ionize mainly the molecular oxygen present in the layer. The soft x-rays, with wavelengths ranging from 1 nm to 10 nm, can ionize all constituents in the layer, including N₂, O₂, O, and NO (Davies, 1990; Hunsucker and Hargreaves, 2007). The contributions to x-rays come mostly in the form of x-ray flares. The intensity of these flares varies through time, and are particularly low during solar minimum. Therefore, the overall contribution to ionization in the E layer from the soft x-rays is for the most part low, especially during solar minimum. The E layer is also susceptible to ionization due to particle precipitation, like the D layer.

The two dominant sources of recombination in the layer include radiative recombination and dissociative recombination. However, the reaction rate for dissociative recombination is a factor of 10⁵ times faster than radiative recombination, making it the primary reaction. Thus, resulting in the main recombination reactions of



2.2.3 F layer

The F layer begins at about 120 km altitude and extends beyond 1000 km. Most of the total ionospheric plasma resides in the F layer. The F layer is sometimes split into two sub-layers, the F1 layer, and the F2 layer. The F1 layer is not always present, being more likely during summer and during solar minimums. Ionization in the F layer can be due to EUV radiation within the 20 nm to 90 nm wavelength range and x-rays within the 0.1 nm – 10nm wavelength range (Davies, 1990; Hunsucker and Hargreaves, 2007). The F2 layer contains the peak electron density, typically situated between 200 km and 400 km in altitude in the high latitudes. The density of the layer is not predominantly due to photo-ionization, but rather through plasma transport and a decrease in recombination. Thus, the layer remains mostly intact during the nighttime hours, unlike the lower layers.

The primary ions of the F layer are O^+ and N_2^+ , which are most readily created through photoionization with the O and N_2 neutral molecules. The important ions in the recombination reactions are O^+ , NO^+ , and O_2^+ . These are created through the reactions:



The main recombination reaction for the F layer involves a two-step process, outlined by the following sets of equations:



These first reactions create the NO^+ or O_2^+ ions, which are necessary for the second step:



which uses the available free electrons in the region (Rees, 1989; Hunsucker and Hargreaves, 2007). The concentration of the O^+ ion dominates in the upper altitudes of the F layer, with a decrease in the NO^+ and O_2^+ ions. This leads to a decrease in the recombination rates with altitude (Hunsucker and Hargreaves, 2007).

Due to the decrease in atmospheric pressure in the higher altitude F layer, bulk movement of the plasma from the lower layers is an important factor. This diffusion of the lower altitude plasma is partly responsible for the F region persisting through the nighttime hours. This is also why the peak plasma density resides in the F layers, despite the lower density of neutrals. We note as well that plasma transport may dominate the chemical equilibrium of the layer.

2.3 Regional differences

Geographically, the ionosphere is typically split into three areas of interest, the low latitude, mid-latitude, and high latitude regions. Our focus for the presented work will be with the high latitude. To give some context to why the high latitude ionosphere is an important area of research, the low and mid-latitude regions will be briefly discussed before discussing the high latitude regions in more detail.

The mid-latitude ionosphere is mostly homogenous, with increases in the overall electron density observed during the daytime hours and a significant decrease during the nighttime hours. The layers and chemistry of this region are like those discussed above. The low latitude ionosphere differs most substantially in the F region, where the peak electron density can be observed at higher altitudes than typically observed in the other regions (Magdaleno et al., 2011 and references therein). This is observed more prominently during the nighttime hours, where plasma from the lower altitudes diffuses upwards, increasing the peak to altitudes upwards of 500 km. The upwards motion of the plasma is enhanced in the low latitudes due to the Earth's magnetic field orientation and the neutral winds. Near the geomagnetic equator, the magnetic field is horizontal. Neutral winds flow from sunrise to sunset, or west to east, as a result of the dayside heating and nightside cooling. The neutral winds cause the lower altitude plasma to flow along with it, creating an eastward current. This current, in conjunction with the horizontal magnetic field, creates an upwards $\mathbf{E} \times \mathbf{B}$ drift. This drift causes the lower altitude plasma to be transported upwards, to a point where the gravitational force

counteracts the plasma sufficiently to stop it from rising further. At this point the plasma flows to either side of the geomagnetic equator, settling between approximately 10° – 15° latitude to either side of the geomagnetic equator (Hunsucker and Hargreaves, 2007). A representative example of the density in the mid and low latitude regions are illustrated by the Total Electron Content (TEC) map presented in Figure 2.2. TEC is discussed in more detail in Chapter 4; in short, it is a measure of the electron density. Homogenous, low magnitude, TEC values are observed throughout the mid-latitude regions in the figure. The equatorial anomaly is clearly present as well, centred at 15 hours local time. Two distinct enhancements in the electron density can be observed, roughly centred on the geomagnetic equator.

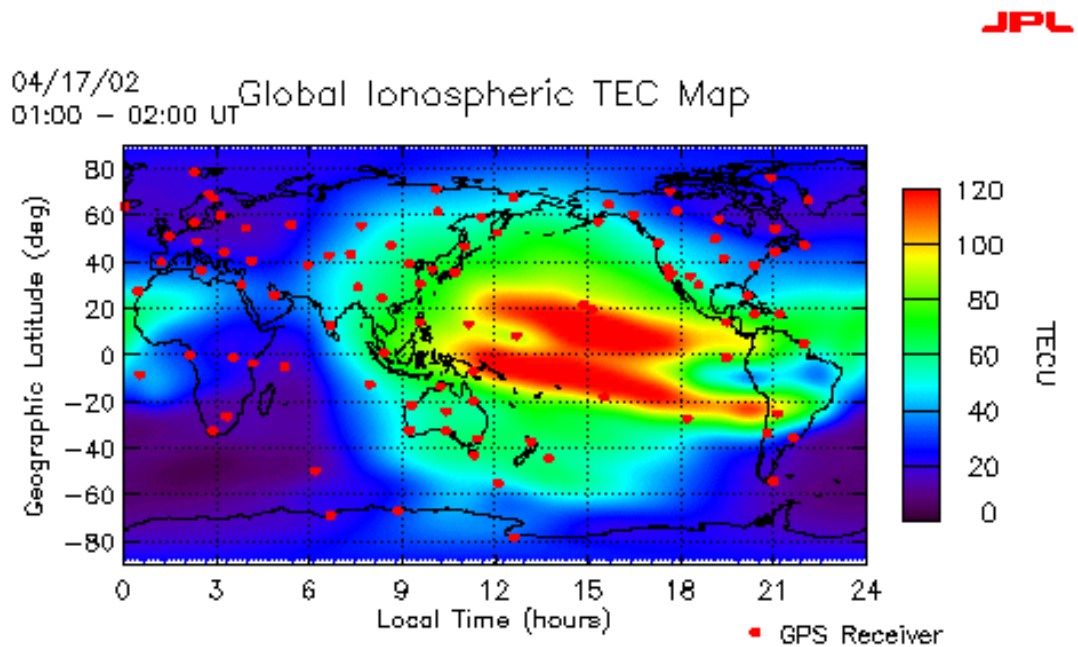


Figure 2.2 Illustrative example of the typical electron density in the mid and low latitude regions. The equatorial anomaly is also present, centred near 15 hours local time. The

anomaly creates two enhancements in electron density, the pair roughly centred on the geomagnetic equator and settling $10^{\circ} - 15^{\circ}$ to either side of it. Retrieved from <https://iono.jpl.nasa.gov/gim.html>.

In the high latitude ionosphere, the geomagnetic field orientation is opposite to the low latitudes; the orientation of the field lines is nearly perpendicular. This creates an ionosphere which is influenced heavily by the solar wind and is therefore very active. An illustrative example of this activity is presented in Figure 2.3; the figure presents a TEC map presenting the percent difference in TEC during an active ionospheric day vs a quiet day. This is obtained by subtracting a representative quiet time map from an active map. The high latitudes show very large percent differences during the active day, with nearly a 100% increase. Variability is also observed, with enhancement and depletions ranging from roughly -60 to 100 percent difference from the quiet times. The high latitude region also commonly exhibits a twin cell convection pattern, contributing to the variability in the region. An idealized picture of this twin cell pattern is presented in Figure 2.4.

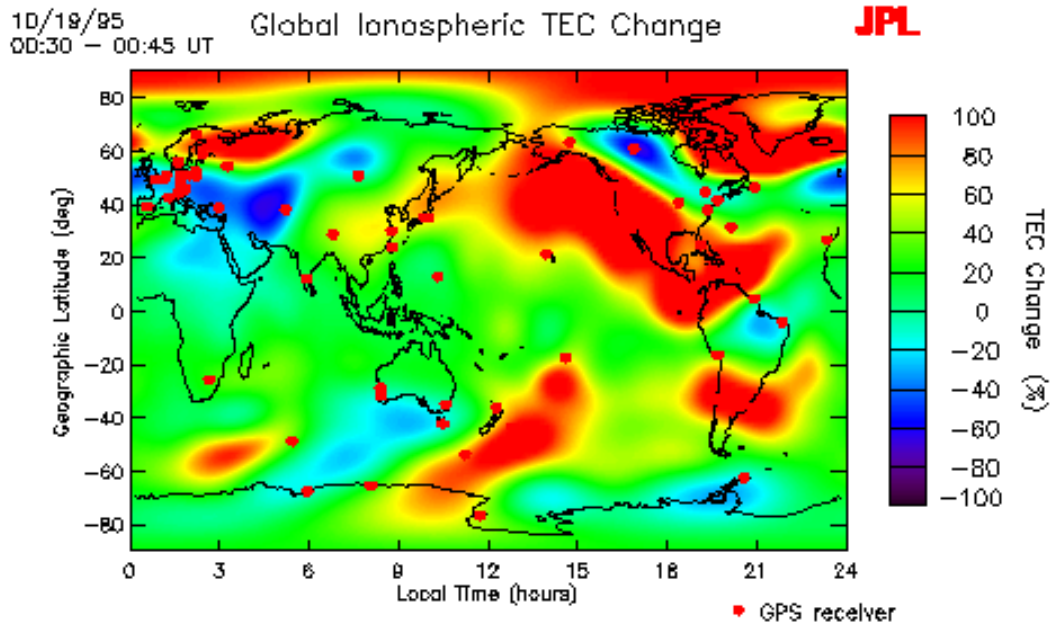


Figure 2.3 Illustrative example of the variability which can occur in the high latitude regions of the ionosphere. The percent difference between an active ionospheric day's TEC map compared to a representative quiet day is presented. Nearly a 100% increase in TEC is observed in the high latitudes, as well as enhancements and depletions ranging from -60% to 100% difference. Retrieved from https://iono.jpl.nasa.gov/storm_demo.html.

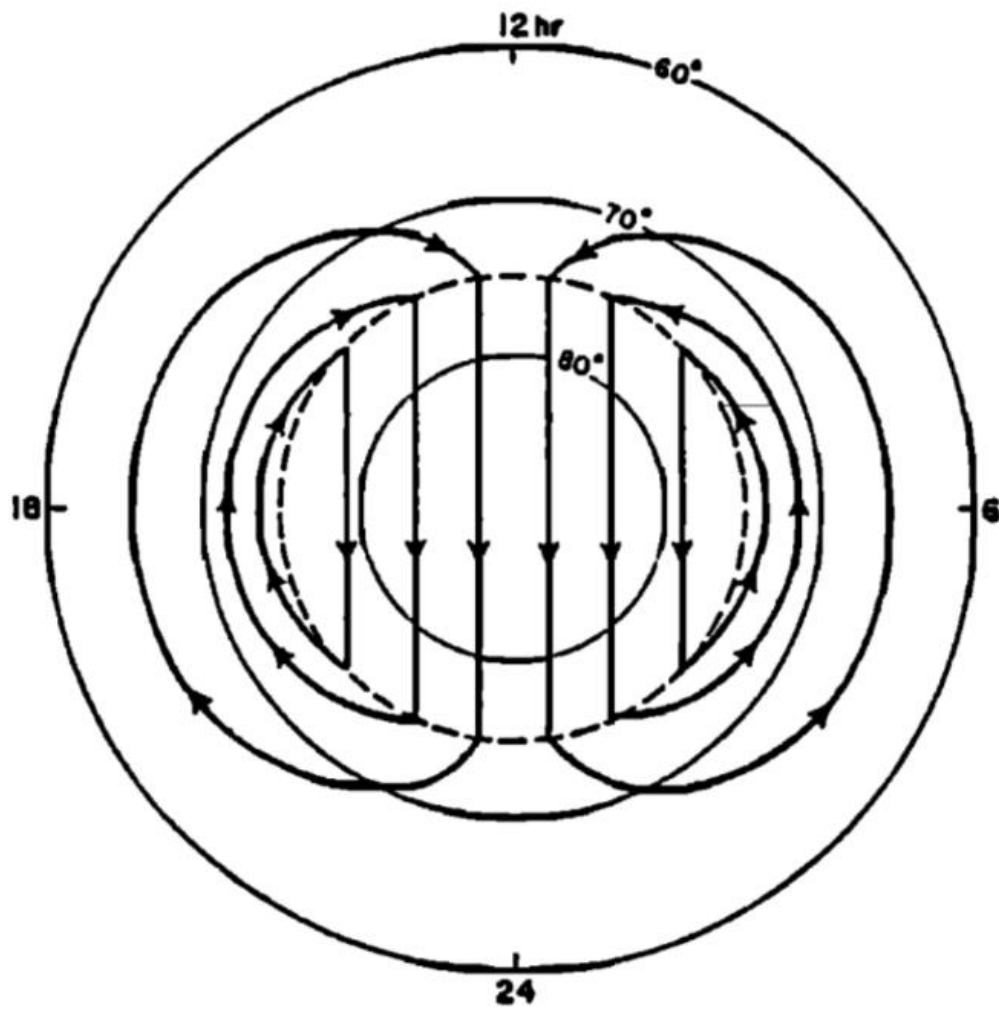


Figure 2.4 An idealized representation of the twin cell convection pattern observed in the high latitude regions, presented in geomagnetic latitude and local time coordinates (Heelis et al., 1982).

The near vertical magnetic field lines, near the geomagnetic pole, can be considered as “open” magnetic field lines. Meaning the field may connect to the magnetic field associated with the solar wind itself. This then allows the solar wind particles to follow

these magnetic field lines down towards the Earth, rather than being deflected. The solar wind is an outflow of solar material driven by the expansion of the solar corona. It is composed mostly of H^+ ions and a nearly equal number of electrons. The solar wind streams towards the Earth at speeds typically within the 200 km/s to 800 km/s range (Davies, 1990; Hunsucker and Hargreaves, 2007). These energetic particles are usually deflected by the Earth's magnetic field, giving the field the compressed shape on the day side and elongated tail on the night side. This is demonstrated in Figure 2.5. The dayside (left side) shows the solar wind compressing the magnetosphere and in turn getting deflected around the Earth.

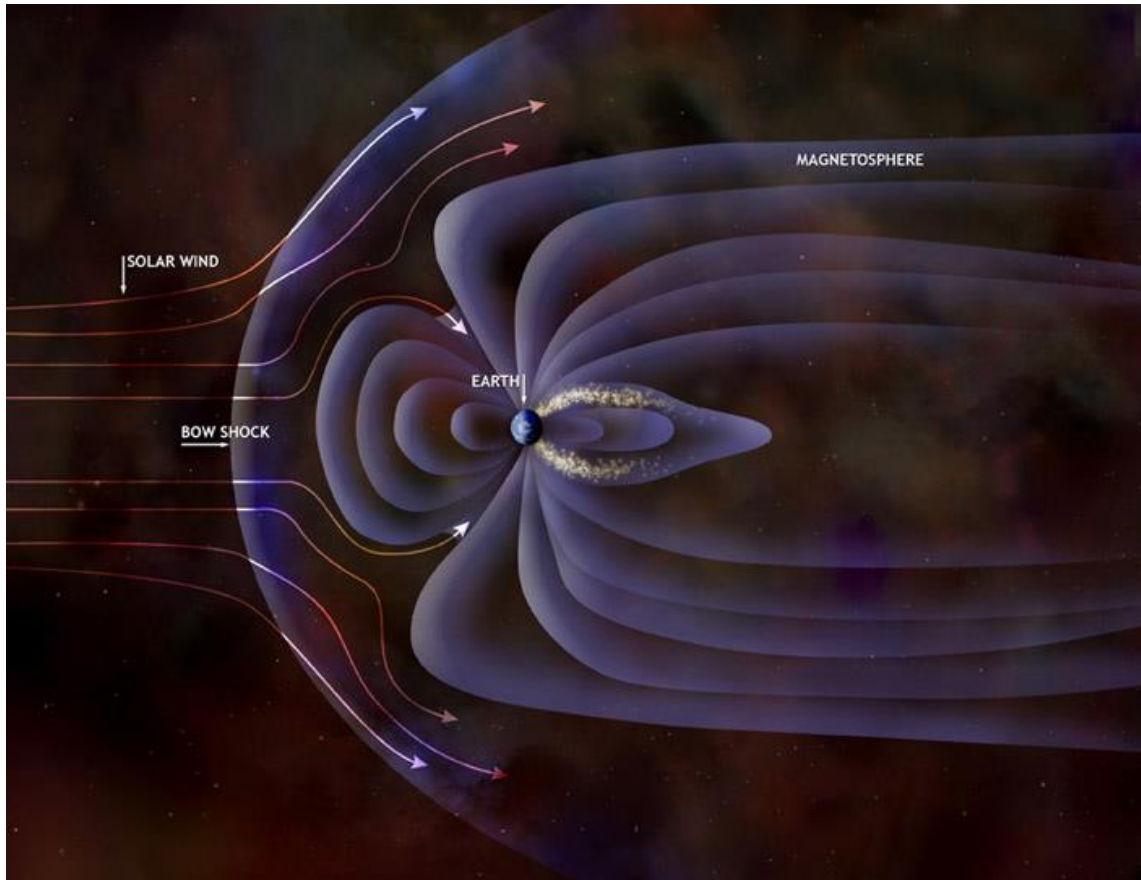


Figure 2.5 Illustrative representation of the Earth's magnetic field and the solar wind's interaction with it. The magnetic field is compressed in the dayside (left) and elongated on the night side (right). This is due to the pressure of the solar wind. The solar wind is also shown to be deflected away from the Earth due to the magnetic field. Retrieved from <https://www.jpl.nasa.gov/infographics/infographic.view.php?id=10686>.

The boundary between the closed and open magnetic field lines represents an important sub-location of the high latitude ionosphere: the auroral oval. A snapshot of the auroral oval, superimposed onto a polar map of the Earth, is presented in Figure 2.6; the data is

obtained from the “Polar” satellite. The red colour represents the most intense portions of the Aurora, the blues represent the least intense. The auroral oval is formed by the boundary between the open and closed field lines; it is a region heavily affected by precipitation of solar wind particles which become trapped on the field lines. These energetic particles flow along the field lines into the atmosphere, ionizing the neutral constituents. This is most likely to occur in the lower layers of the ionosphere, the D and E layers, due to the higher density of neutral constituents. Some constituents may only become excited, rather than becoming ionized. In the subsequent return to the ground state, the molecules will emit photons. Both oxygen and nitrogen emit photons in the visible spectrum. This is also true of nitrogen ions recombining with a free electron. The emission of the visible wavelength photons results in the visible aurora borealis (in the northern hemisphere). The work presented will focus mostly on the high latitude auroral region ionosphere.

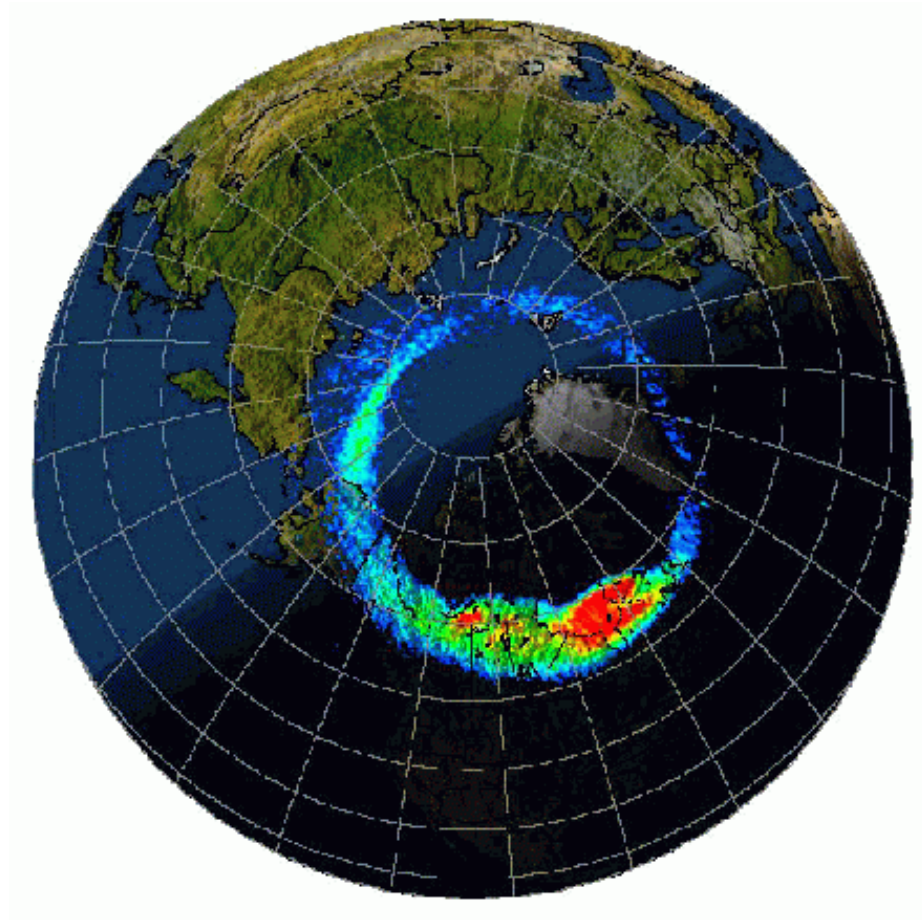


Figure 2.6 An image of the auroral oval, as seen from space, superimposed onto a map of the Earth. The image was taken using the Ultraviolet Imager onboard the “Polar” satellite. The red colour represents the brightest portions of the auroral oval while the blue represents the dimmest. Retrieved from http://sd-www.jhuapl.edu/Aurora/UVI_on_Earth.html.

Above the auroral oval is a region known as the polar cap, the region corresponding to the open magnetic field lines. The “open” end of these field lines are connected to the Interplanetary Magnetic Field (IMF). The IMF is the magnetic field of the solar corona which has been “frozen in” to the solar wind. This is due to the high electrical

conductivity of the solar wind, resulting in a magnetic field which moves with the plasma (as per Alfvén's theorem). As the IMF interacts with the magnetosphere, plasma in the magnetosphere flows through the IMF and its magnetic field. The movement of the electrically charged plasma through a magnetic field creates an electric field. This electric field is mapped to the polar region, pointing in the dawn to dusk direction. The Earth's magnetic field and this electric field will create an $\mathbf{E} \times \mathbf{B}$ drift of the polar cap plasma. This is the major contributor to the bulk plasma motion in the polar cap region. The resulting drift speeds of the plasma range can be as low as 100 m/s, while during days with increases in the IMF magnetic field strength, drift velocities have been known to reach values upwards of 1 - 2 km/s (Davies, 1990; Hunsucker and Hargreaves, 2007).

2.4 Radio Wave Propagation

A defining characteristic of the ionosphere is its effects on electromagnetic waves and impact on radio systems. The first major indication of the existence of an ionized layer of plasma within the Earth's atmosphere came from the famous experiment performed by Guglielmo Marconi (Marconi, 1922). Marconi successfully transmitted a signal from Cornwall, England to St. John's Newfoundland, a separation distance of nearly 3500 km. Due to the curvature of the Earth, it is not possible for the signal to travel directly as there was no direct line of sight. It was concluded that the signal must have reflected off the atmosphere, suggesting the existence of an ionized layer. This forms the basis of the ionosphere's role in HF radio communication; HF refers to the frequency bands from 3 MHz to 30 MHz. Long distance HF communication will transmit signals towards the

ionosphere, using the ionospheric layer to reflect and refract signals back towards the Earth, allowing the signals to travel larger distances. This concept is illustrated in Figure 2.7, showing how the signal is refracted back towards the Earth from the ionosphere, thus allowing the signal to travel from a transmitter to receiver without line of sight. This is possible because the HF frequencies used are below the plasma frequency of the ionosphere. The refractive index of the ionosphere, ignoring collisions and the Earth's magnetic field, can be represented as (Jursa, 1985):

$$n^2 = 1 - X = 1 - \left(\frac{f_n}{f}\right)^2 \quad 2.6$$

$$X = \frac{N_e q^2}{4\pi^2 \epsilon_0 m f^2} \quad 2.7$$

Where f_n is the critical frequency, the frequency below which the medium appears opaque, N_e is the electron density, q is the electron charge (1.602×10^{-19} C), ϵ_0 is the permittivity of free space (8.854×10^{-12} F/m), m is the mass of an electron (9.109×10^{-31} kg), and f is the frequency of the wave (Jursa, 1985). Note that equation 2.7 represents the case of normal incidence. To determine the critical frequency, we set the refractive index to zero, meaning $X = 1$ and

$$f_n = \sqrt{\frac{N_e q^2}{4\pi^2 \epsilon_0 m}} = f \quad 2.8$$

Evaluating equation 2.8 gives the following relationship:

$$f_n = 9.14\sqrt{N_e} \quad 2.9$$

For oblique incidence, we use Snell's law to determine the critical frequency. We state that:

$$n_0 \sin \theta_0 = n_k \sin \theta_k \quad 2.10$$

$$\sin \theta_0 = n_k \quad 2.11$$

where n_0 is the refractive index just before entering the ionosphere (refractive index of the atmosphere), θ_0 is the angle at which the wave enters the ionosphere, n_k is the refractive index at which the wave is initially reflected, and θ_k is the reflection angle.

For the wave to reflect, $\theta_k = 90^\circ$, and noting that $n_0 = 1$, equation 2.10 is simplified to equation 2.11. Substituting equation 2.6 into 2.11 gives:

$$\sin^2 \theta_0 = 1 - \cos^2 \theta_0 = 1 - \left(\frac{f_n}{f}\right)^2 \quad 2.12$$

$$f = f_n \sec \theta_0 \quad 2.13$$

Typical maximum electron density values are within the range of 10^{10} electrons/m³ – 10^{12} electrons/m³, thus resulting in plasma frequencies of approximately 1 MHz - 9 MHz, well within the low end of the HF band. For frequencies greater than the critical frequency, the ionosphere will appear transparent, allowing for transmission of waves through the ionosphere (Hunsucker and Hargreaves, 2007). This is the situation with space-based navigation systems such as the GPS. Note that the refractive index of the ionosphere and its derivation is discussed in more detail in Chapter 4.

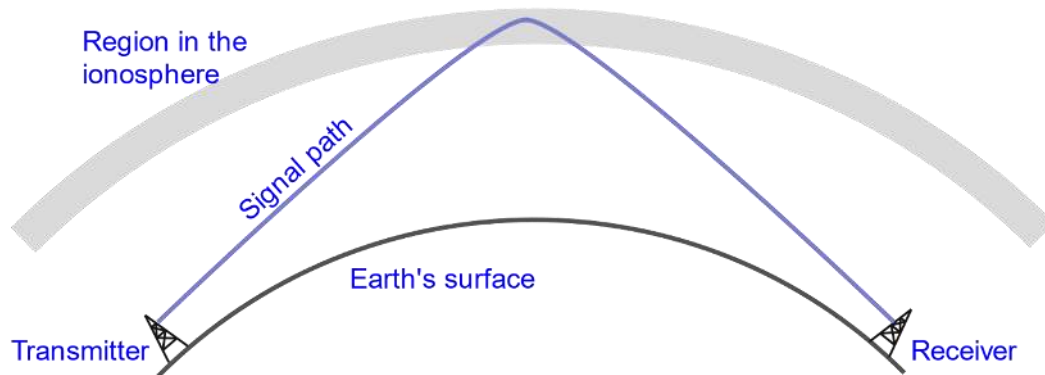


Figure 2.7 An illustrative explanation of HF communication using the ionosphere to facilitate over the horizon communication. Since the transmitter and receiver do not have a line of sight to one another due to the curvature of the Earth, communication between the two locations would not be possible without the ionosphere. Retrieved from <https://www.electronics-notes.com/articles/antennas-propagation/ionospheric/hf-propagation-basics.php>.

The GPS transmits at frequencies in the L band, which applies to frequencies in the range of 0.5 GHz to 2 GHz (Bruder et al., 2003). These frequencies are much greater than the typical plasma frequencies associated with the ionosphere, allowing them to travel through it. In this case, the signal is not reflected totally, but are refracted. Equations 2.6 and 2.7 demonstrate the electron density dependence of the refractive index. Any inhomogeneities in the electron density will result in changes in the refractive index. A simple illustration of the refractive effects of a homogenous ionosphere, compared to no ionosphere, is presented in Figure 2.8. The satellite on the left, transmitting the orange signal, represents the signal's path if no ionosphere were present. The signal is seen to travel directly from the satellite to ground. Note that we are ignoring all other effects along the ray path, like the neutral atmosphere, which will also have a bending effect on the signal's path. For the satellite on the right, transmitting the yellow signal, a homogeneous ionosphere is assumed. In this case, the signal is seen to bend as it enters and exits the ionosphere, due to the refractive properties of the ionosphere. The GPS hardware and the refractive properties of the ionospheric medium are discussed in more detail in Chapters 3 and 4, respectively.

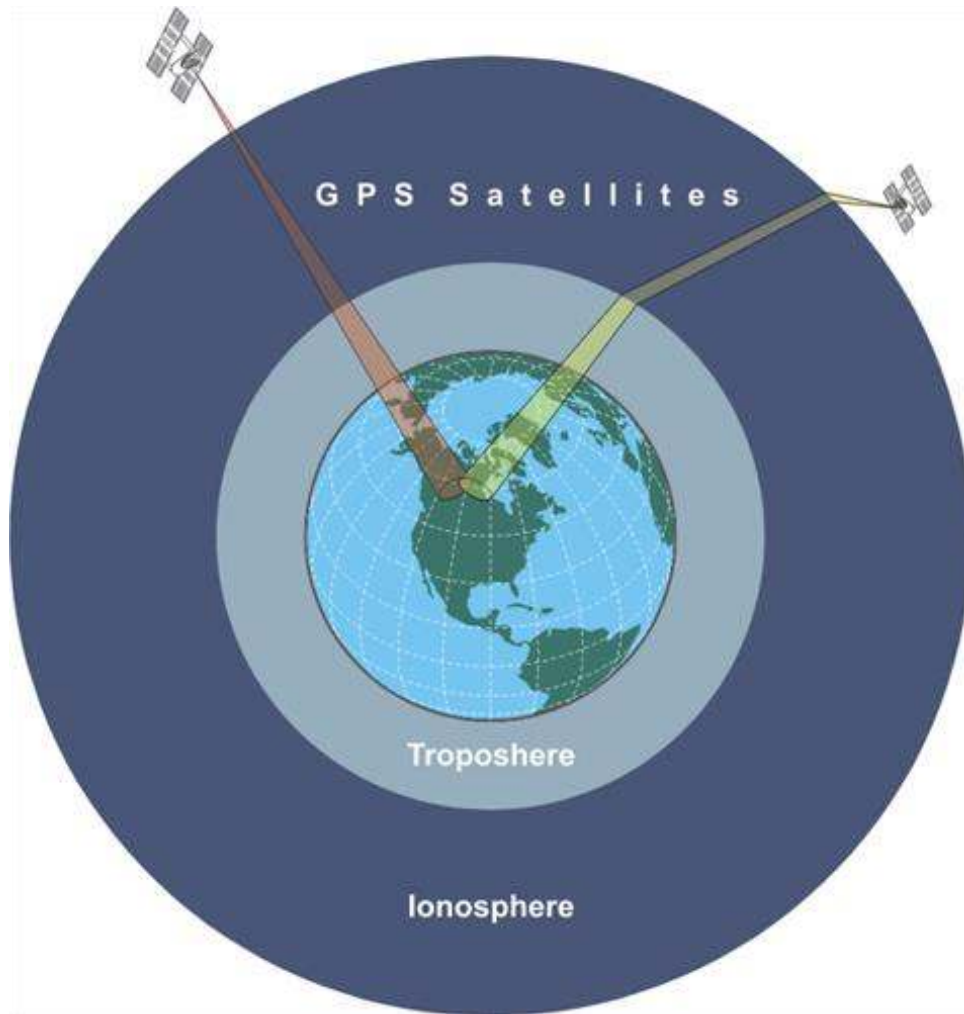


Figure 2.8 A simple illustration demonstrating the refractive effect of a homogenous ionosphere on satellite-based signals. The satellite on the left, which transmits the orange signal, represents no ionosphere. The signal travels directly from the satellite to the ground. The satellite on the right, with the yellow signal, shows the effects of a homogenous ionosphere, where the signal is bent as it enters and exits the ionospheric medium. Retrieved from <https://www.e-education.psu.edu/geog862/node/1715>.

3 Hardware

3.1 Introduction

There are many tools available for ionospheric research and monitoring, each with their advantages and disadvantages. One such tool, which has been proven to be very useful in the field, is GPS. The main advantage that has helped GPS become a very popular tool in ionospheric research and monitoring is its temporal availability. The GPS satellites are transmitting radio signals constantly, with no downtime (excluding hardware malfunctions). This allows researchers to monitor the ionosphere continuously, providing real-time or near real-time data. The GPS constellation has 32+ satellites in orbit (as of 2017), with an orbital inclination angle of 55° . This gives a near global spatial coverage. Combined with the temporal coverage of the constellation, large portions of the ionosphere can be monitored in near-real time. This requires a good global coverage of GPS receivers, tracking the GPS signals. With groups like the International GNSS Service (IGS) and CHAIN, this is possible. The IGS collects GPS data from groups worldwide, in a standardized format, and makes it available publicly. Many other groups have created networks of GPS receivers, some with a focus on ionospheric monitoring, while others not, and many of these groups contribute to the IGS network. This provides a nearly worldwide distribution of GPS receivers outputting publicly available data.

The GPS constellation transmits on a minimum of two carrier frequencies, with more recently deployed satellites transmitting on three carrier frequencies. The carriers are close enough in frequency to assume they follow the same path through the ionosphere, but far enough apart to be treated separately. This allows for research where the varied frequencies can be examined, assuming they encountered the same ionosphere. A popularly used consequence of the two main carrier frequencies is the calculation of the Total Electron Content (TEC), which is a measure of the electron density along the satellite ray paths. This can be used to study changes in the ionospheric electron density in space and time. TEC is discussed in more detail in Chapter 4.

However, a few main disadvantages are present when using GPS for ionospheric research. The main issue arises from the designed purpose of GPS; the GPS system, both the signals and the receivers, are designed with positioning techniques as the focus. This means that some techniques and design choices employed in the GPS hardware are not always ideal for ionospheric monitoring and research. For example, GPS positioning requires very accurate timekeeping. For the sake of keeping the costs low, receiver clocks are poor compared to the satellite clocks. To keep the receiver clock as in-sync as possible with the satellites the receiver clocks are typically steered, which means the clock is constantly adjusted to account for any drifting which occurs. This is detrimental for ionospheric research, where the small adjustments in the receiver clock may manifest themselves in the GPS observables indistinguishable from ionospheric effects. Another example occurs in the tracking methods used in the receivers. In aspects of GPS-based ionospheric research, the differences between the carrier frequencies are very important,

like in the TEC calculation. However, some tracking techniques assume identical dynamics in the carriers. This technique allows a harder to track signal to be tracked more easily, resulting in more robust GPS positioning, but it is detrimental in ionospheric research as it misrepresents the signal dynamics. This is discussed in more detail in Chapter 6.

3.2 Global Positioning System

The GPS is a space-based navigation system, using a constellation of satellites transmitting signals on a minimum of two frequencies. It is one of many Global Navigation Satellite Systems (GNSS) currently in orbit, is maintained by the United States Government, and is provided free of charge to the global public. The main purpose of the GPS is to provide reliable timing, navigation, and positioning to users in both the military and civilian sectors, with a varied degree of accuracy to these respective user types. The first GPS satellite was launched in February of 1989; with Initial Operating Capability (IOC) for the system being obtained in December of 1993. The IOC state consisted of 24 satellites, a combination of prototype and production satellites. The system was deemed to be in the IOC state as it could provide timing and positioning within the specified accuracies of this state. It was not until early 1995 that the GPS was in a Full Operation Capability (FOC) state, with 24 production satellites in orbit and extensive testing of the system having been completed. For civilian use, the system must meet the Standard Positioning Service (SPS) requirements to reach the capability states. The SPS states that the GPS can provide accuracies better than 22 m

and 13 m for the vertical and horizontal planes, respectively. The system must also provide UTC time within an accuracy of 40 ns (Kaplan and Hegarty, 2005). The satellites orbit the earth on orbital planes at an altitude of roughly 20,200 km, with orbital periods of a half sidereal day.

GPS positioning works on the basis of triangulation, or more appropriately, trilateration. An illustration of how this would work in two dimensions is presented in Figure 3.1. In the figure, we see a circle around each satellite, these circles have a radius representative of the distance of the receiver from each satellite, respectively. The intersection point of these three circles is then the receiver's location. Extrapolating Figure 3.1 to three dimensions, each satellite can be surrounded by a sphere with a radius equal to the distance from the respective satellite to the receiver. In three dimensions, and introducing the time dimension, this would require four satellites to pinpoint the receiver's position. Thus, GPS requires four satellites in view to calculate a position.

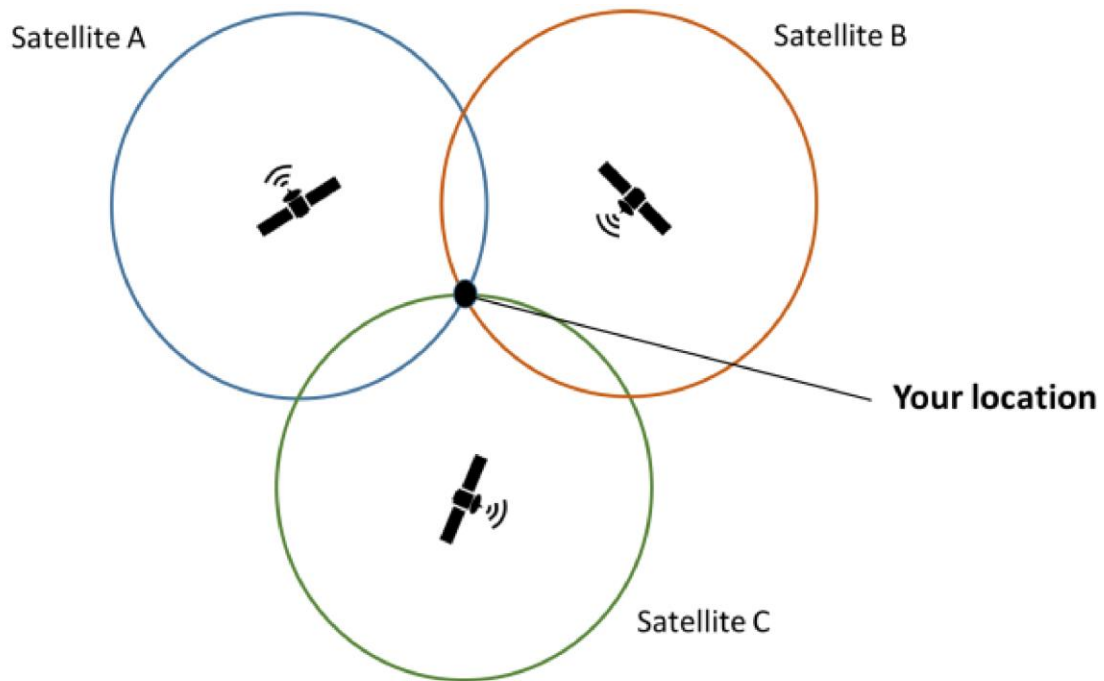


Figure 3.1 Simple two-dimensional illustration of the trilateration technique used in GPS positioning. Retrieved from <http://scienceline.org/2016/05/how-does-your-gps-know-where-you-are/>.

Based on the trilateration technique, the fundamental job of the GPS receiver is to calculate the distance from the satellite to the receiver. This is done by calculating the travel time of a signal transmitted by a satellite. In short, this is done by having the satellite transmit its transmission time for the receiver to compare to its reception time, giving the receiver the total travel time. Assuming a travel speed of the speed of light, the distance over which the signal has travelled from the satellite to the receiver during the time interval can be calculated. The time of transmission is encoded on to the carrier signal by using Binary Phase Shift Keying (BPSK). BPSK is employed by shifting the phase of a signal 180° to represent 1s and 0s of a binary message. When the receivers

encounter this 180° shift in the phase of the signal, it switches the binary bit from 0 to 1 or vice-versa. This technique is used to modulate a navigation message, represented in binary, onto the GPS carriers at 50 bits per second (Kaplan and Hegarty, 2005).

Pseudo Random Noise (PRN) codes are also modulated onto the GPS carriers. In the legacy system, two PRN codes were used: The Course Acquisition (C/A) code, and the Precision (P) code. The P-code was modulated onto both the L1 and L2 carriers, while the C/A code was only available on the L1 carrier. Each of the PRN codes is unique to the satellite, allowing the receiver to know which satellite's signal is being tracked.

Numbering the PRN codes also gives a method of labelling the GPS satellite. We will use this technique throughout the work presented. The modernization of the GPS included the introduction of a Civil (C) code, which is modulated onto the L1 and L2 carriers. There is also a new Military (M) code, and two codes specific to the new L5 carrier. The C/A code is 1023 chips in length with a chipping rate of 1.023 Mbps, meaning the code repeats every millisecond. The P-code, on the other hand, has a length of 6.19×10^{12} chips, with a chipping rate of 10.23 Mbps. This gives the P-code a repeat time of roughly seven days (Kaplan and Hegarty, 2005). By increasing the length of the code and decreasing the chipping rate, the P-code can provide a more accurate distance measurement than the longer chip rate C/A code. Normally, the P code is encrypted, forming the Y code (typically denoted as the P(Y) code). The keys needed to decrypt the P(Y) code are not provided to the public but is reserved for exclusive use with the United States military. This allows the military to gain increased precision using the GPS, taking advantage of the increased chipping rate used in the P(Y) code.

To allow a satellite to transmit multiple codes on a single carrier, like in the L1 case, the two carriers are transmitted in quadrature, 90° out of phase, and added to form a single composite signal. An illustrative example of the modulation of the codes on the signals and the final composite signal are presented in Figure 3.2. The top panel represents the P-code, followed by the modulation of the P-code on to a representative signal. The third panel represents the C/A code, note that it has a longer bit rate than that of the P-code. Below the C/A code is the C/A signal, with the C/A code modulated on it. The P-code signal and the C/A code signal are in quadrature with one another, as observed by the 90° phase shift between them. The final panel shows the composite signal, the addition of the P-code signal and the C/A code signal. Note that this is an illustration and is not to scale with the actual codes and signals.

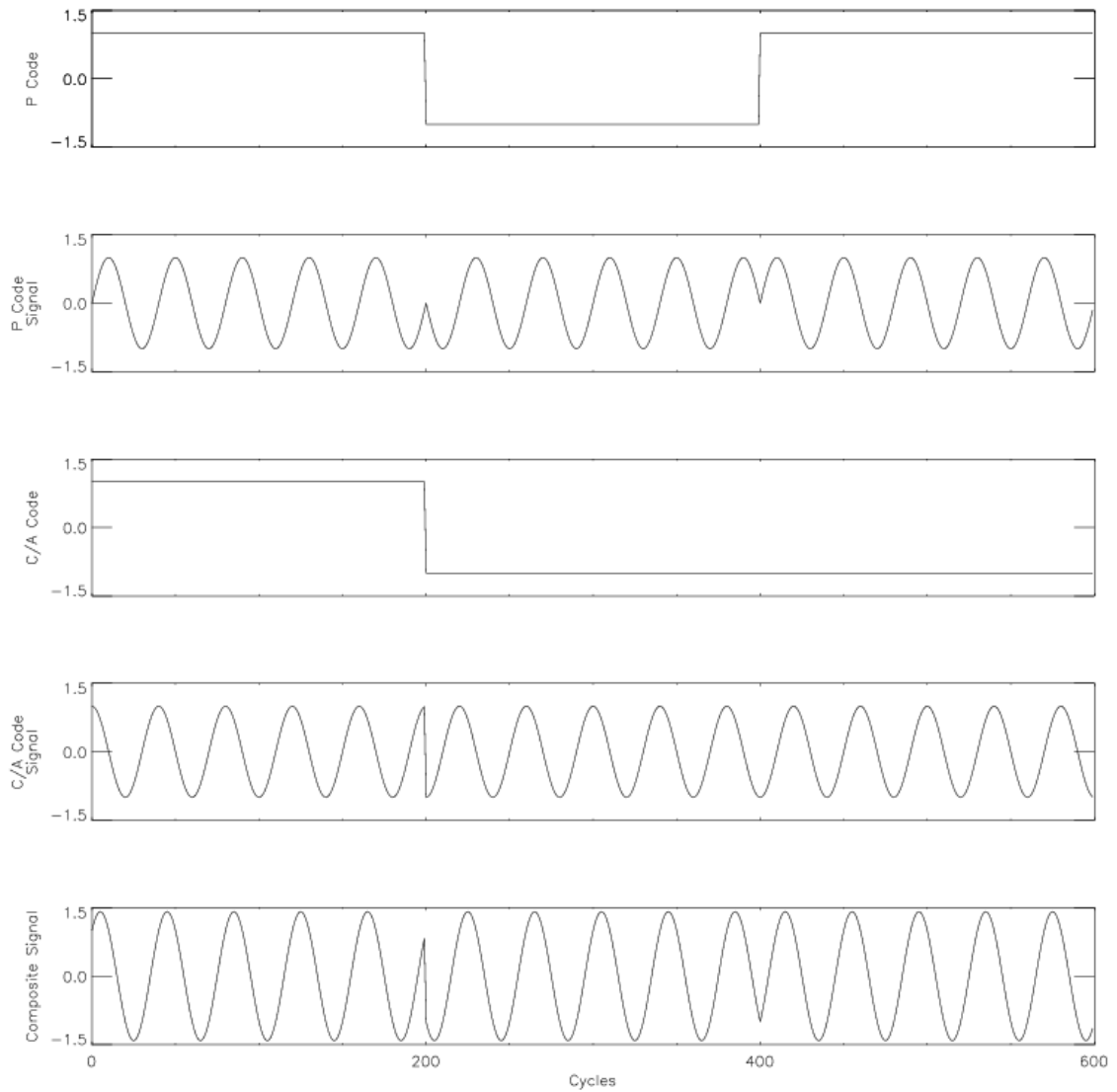


Figure 3.2 Illustrative example of the P-code (first panel), the P-code signal (second panel), the C/A code (third panel), the C/A code signal (fourth panel) and the composite signal (fifth panel). The P-code signal and the C/A code signal illustrate the modulation of the respective codes to pure signals. The C/A code signal and the P-code signal are in quadrature, allowing for their addition to create the final composite signal.

The L2C code is comprised of two ranging codes, Civil Moderate (CM) and Civil Long (CL). As the names suggest, the CL code is longer than the CM code; the CM code is 20 ms in length, with chipped at a rate of 511.5 Kbps, while the CL code is 1.5 s long, also chipped at a rate of 511.5 Kbps (Kaplan and Hegarty, 2005). The CM code is modulated with the navigation message, like the legacy codes, but at half the chipping rate. This was chosen to improve the L2C code in challenging environments. The CL code is not modulated by the navigation message, making it a data-less code. The data-less codes can be tracked more robustly since unknown 180° phase shifts will not occur. The L5 carrier is set up like L2C. The in-phase component and the quadrature component of the L5 carrier both transmit a 10 230-bit code, abbreviated as I5 and Q5 respectively. Like the CM code, the I5 code is modulated with the navigation message, leaving the Q5 data-less (Kaplan and Hegarty, 2005).

The M code is designed to replace the P(Y) code and is therefore intended only for military use. The code will be transmitted on the L1 and L2 carriers, like the P(Y) code. Not much is known about the M code, but is expected to provide improved security, and enhanced data demodulation and tracking (Kaplan and Hegarty, 2005).

3.3 Canadian High Arctic Ionospheric Network

CHAIN is a network of ground-based instruments located in the Canadian high latitude (Jayachandran et al., 2009). This network is dedicated to the monitoring and study of the

high latitude ionosphere. Of the equipment used in CHAIN, the GPS receivers setup throughout the Canadian high latitudes will be used for this study. The network consists of 25 GPS receiver stations, including 9 Novatel GSV4004B receivers, and 16 Septentrio PolaRxS Pro receivers. The Septentrio receiver, the newer of the two, boasts a few advances important for this study. These include an increased sampling rate of the GPS L1 and (most importantly) L2 carrier phase and amplitude, where the Novatel is only capable of sampling the L1 carrier at a high frequency. The Septentrio is capable of sampling observables at a maximum rate of 100 Hz, twice that of the Novatel receiver. Also, the Septentrio receiver samples the L2 carrier phase independently of the L1 carrier phase, allowing for more accurate L2 carrier phase dynamics. For these reasons, data retrieved from the Septentrio receivers are used exclusively in this study. A picture of the receiver is presented in Figure 3.3. A map of the GPS receivers in CHAIN is presented in Figure 3.4, with the stations using the Novatel receivers represented by the blue circles, and the Septentrio stations represented by the red circles. Since only the Septentrio receivers are used in this study, the geographic coordinates, for the Septentrio locations only, are presented in Table 3.1.



Figure 3.3 The Septentrio PolaRxS Pro GPS receiver. This receiver is used to retrieve all GPS data presented in this study. Each receiver is located at a station in the Canadian high latitude region, all as part of CHAIN. Retrieved from https://www.navtechgps.com/septentrio_polarxs_packaged_receivers/.

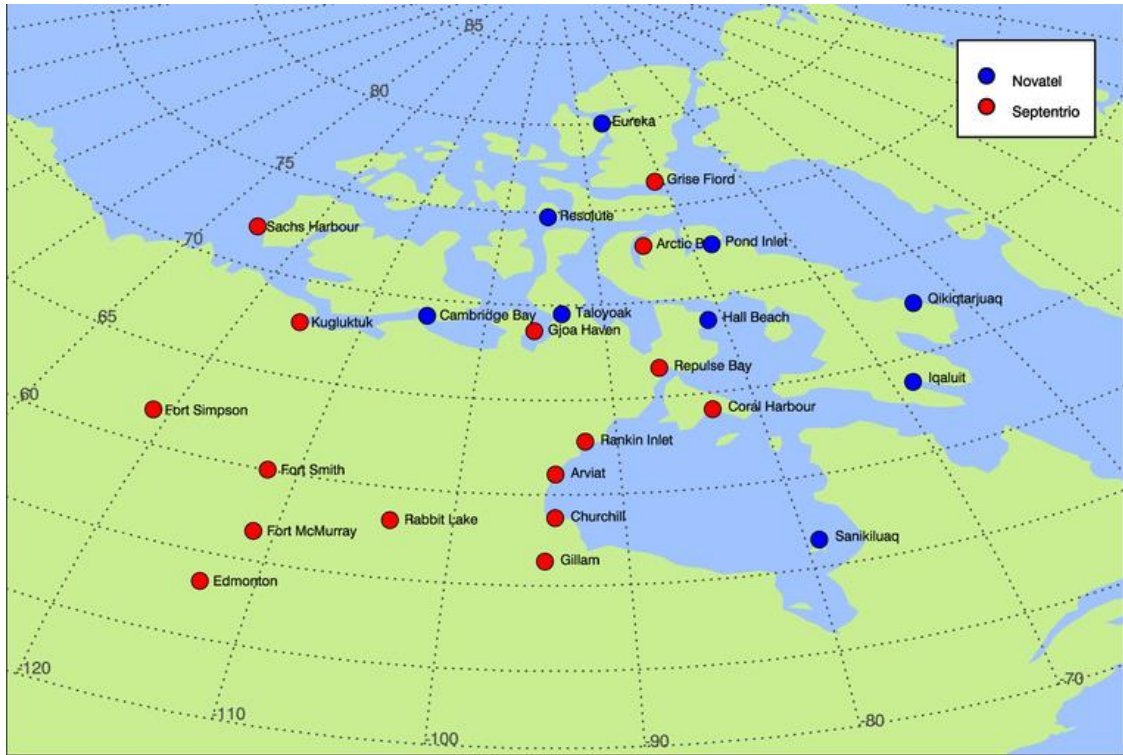


Figure 3.4 Map of CHAIN, outlining which stations are using the Novatel or Septentrio GPS receivers.

Table 3.1 The CHAIN stations using a Septentrio PolaRxS Pro GPS receiver.

Station Name	Station Code	Geographic Latitude (°N)	Geographic longitude (°E)
Arctic Bay	ARCC	73.00	274.97
Arviat	ARVC	61.10	265.93
Churchill	CHUC	58.76	265.91
Coral Harbour	CORC	64.18	276.65
Fort McMurray	MCMC	56.65	248.78
Fort Simpson	FSIC	61.76	238.78
Fort Smith	FSMC	60.03	248.07
Gilliam	GILC	56.38	265.36
Gjoa Haven	GJOC	68.63	264.15
Grise Fjord	GRIC	76.42	277.10
Kulguktuk	KUGC	67.81	244.87
Edmonton	EDMC	53.35	247.03
Rabbit Lake	RABC	58.23	256.32
Rankin Inlet	RANC	62.82	267.89
Repulse Bay	REPC	66.52	273.77
Sach's Harbour	SACC	71.99	234.74

3.4 GPS Observables

From the GPS receivers, a few important observables will be used in this study. The most important to discuss are the amplitude and the phase of the signal. The importance of these observable regarding ionospheric study will be discussed in later chapters. Here we will discuss the observables themselves and how they are obtained from the receiver. The Septentrio receiver provides the in-phase (I) and quadrature (Q) components of the signal. This is used to get the signal intensity. Since the final signal, as transmitted by the GPS satellite and received by the GPS receiver, is the sum of the in-phase and quadrature signals, the amplitude of this wave can be obtained from the amplitude of the in-phase and quadrature components by

$$A = \sqrt{I^2 + Q^2} \quad 3.1$$

where A is the signal amplitude, I is the amplitude of the in-phase component, and Q is the amplitude of the quadrature component. To better illustrate this relationship, we can express the composite signal as a polar plot, plotting the Q signal amplitude against I signal amplitude. This is represented in Figure 3.5. A given point on the composite signal can be plotted as the amplitude of the Q signal at the time versus the amplitude of the I signal at that time. Simple trigonometry then says that the amplitude is the square root of the addition of the I and Q magnitudes squared. We can also get the phase of the signal ϕ again using simple geometry and Figure 3.5:

$$\phi = \text{atan}\left(\frac{Q}{I}\right)$$

3.2

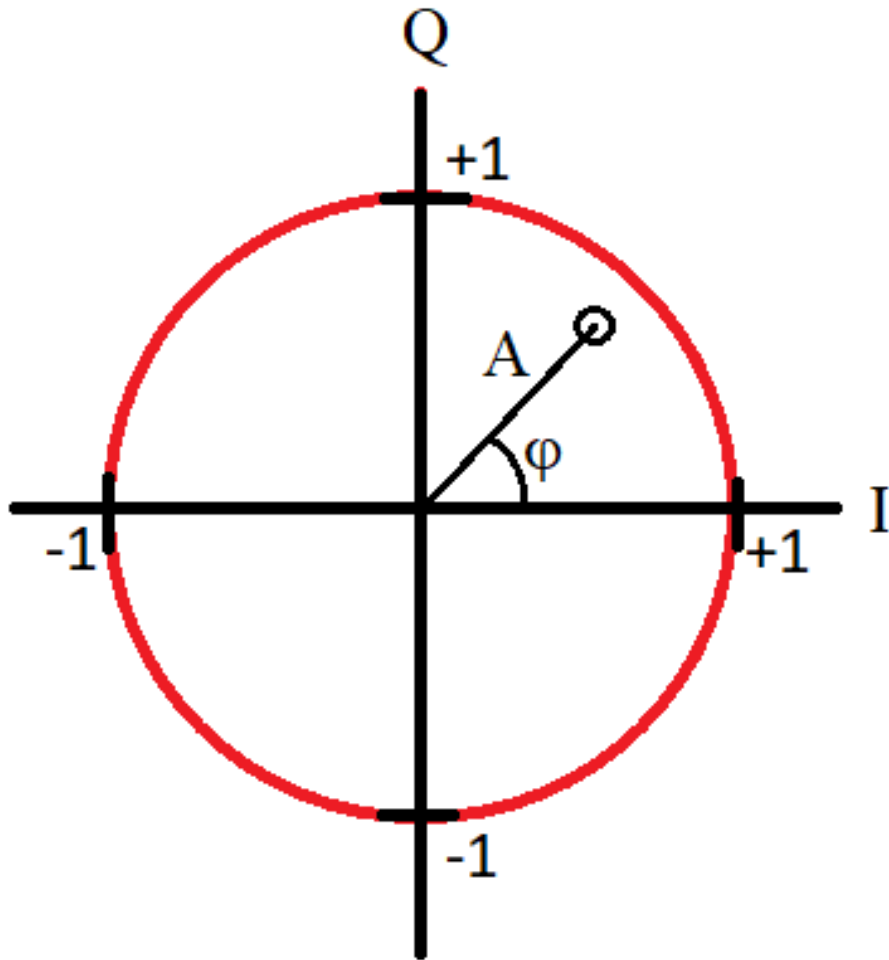


Figure 3.5 Illustration of the composite GPS signal at a given epoch, represented by plotting the in-phase and quadrature signals' magnitudes in polar form.

The GPS receivers also provide an observable known as the carrier phase. This is provided directly but requires modification to get to a useful form for the presented results. The carrier phase observable is a measure of the fractional range between the

satellite and receiver. The receiver determines the frequency of the incoming signal, and in turn then wavelength, and can then estimate the distance the signal has travelled. This, however, requires the receiver to guess the integer number of cycles the signal has undergone between transmission and reception. This is one of a few factors which impact the final carrier phase observable result. The full carrier phase equation can be modelled as (Leick et al., 2015):

$$\Phi_L^{s,r}(t) = \rho^{s,r}(t) + c(dt^s(t) - dt^r(t)) + T^{s,r}(t) - I_L^{s,r}(t) + \lambda_L N_L^{s,r} + \epsilon_L^{s,r}(t) \quad 3.3$$

where $\Phi_L^{s,r}$ represents the carrier phase observable (in meters) for a given satellite (s), receiver (r), and carrier (L) at a given time (t), $\rho^{s,r}$ is the geometric distance from the satellite to the receiver, dt^s and dt^r represent the clock errors associated with the satellite and the receiver respectively, $T^{s,r}$ is the tropospheric delay on the signal's phase, $I_L^{s,r}$ is the ionospheric advance on the phase of the signal, $\lambda_L N_L^{s,r}$ is the wavelength of the signal multiplied by the integer ambiguity, and $\epsilon_L^{s,r}$ is a combination of noise sources, such as multipath or thermal phase jitter, for example. The carrier phase observable, as presented in Equation 3.3 and provided by the GPS receivers, is a distance measurement from the satellite to the receiver. In short, the receiver counts the phase cycles as it tracks the signal, then, knowing the wavelength of the signal, it can calculate a fractional distance between the receiver and satellite. As is seen in Equation 3.3, many factors can impact this distance measurement, causing errors for positioning. The approximate values of these errors are presented in Table 3.2 (Hegarty, 2013). Note

that the integer ambiguity is omitted from the table; this is because the error the integer ambiguity creates can be of any size, dependent on how well the receiver assigns the integer when initially tracking the satellite. The largest error source presented in Table 3.2 is the ionospheric term, $I_L^{s,r}$, which represents changes in the phase of the signal due to changes in the refractive index of the ionosphere. This is the term we are interested in.

Table 3.2 Approximate values for the errors associated with the carrier phase observable.

Error Term	Approximate Error (m)
Clock Errors	0.5 - 1
Troposphere	2 - 3
Ionosphere	3 - 30
Other Sources	<0.5

The methods of isolating the ionospheric term from the carrier phase observable vary depending on the research, but for our results, they will consist of two possibilities. In short, the frequency independent terms can be removed by differencing the carrier phase obtained by two carriers, like L1 and L2 for example, or, the carrier phase can be high pass filtered, removing the low frequency and constant terms from the equation. These methods will be discussed in more detail in Chapter 5.

Since the carrier phase observable clearly requires extra work to get to a form we can use, it may seem more intuitive to use the relationship in equation 3.2. This technique was investigated, but it was decided that using the carrier phase observable better suited the research problem. The reason for this is two-fold: the carrier phase observable is more widely available as a GPS observable, as opposed to the I and Q component values. This allows for future work to more easily replicate the presented work. This also means most past and current work is using the carrier phase observable as well. Therefore, we can use the same techniques as those previously presented. This is very important for the work presented in Chapter 7.

The second reason to use the carrier phase observable is that the high-frequency noise of the phase obtained using the relationship in equation 3.2 is of much larger magnitude than that of the carrier phase observable. A representative example of the carrier phase observable and the IQ-derived phase are presented in Figure 3.6. This example shows a large amount of quiet time data (where no significant variations occur) and an ionospheric induced event, which is centred at approximately 47 minutes for the carrier phase observable curve (black) and the roughly 42 minutes for the IQ-derived phase curve (blue). The IQ-derived phase has been shifted negatively by five minutes. This was done to better show a comparison of the two datasets. Note that both data sets have been high pass filtered with a cut-off of 0.1 Hz to better illustrate the magnitudes of the high-frequency noise. Clearly, the IQ-derived phase has larger amplitude noise since the magnitude of the quiet time variations is larger through the entire presented hour. This is

representative of all times. This can be more accurately visualized in the comparison of the power spectra for this hour. The carrier phase observable spectrum is presented in Figure 3.7 by the black curve, and the IQ-derived phase spectrum represented by the blue curve. Clearly, the higher frequencies of the carrier phase observable are a lower magnitude, with this beginning at frequencies less than 1 Hz. This is relevant since, as we will discuss later, sub-second variations are of major interest in this study. We observe as well that the higher frequencies of the IQ-derived phase appear white, while the carrier phase observable is coloured. Both effects are due to the Phase Lock Loop (PLL). The PLL has an inherent, theoretical, low pass filter applied to the input signal (the composite signal). The resulting carrier phase observable is computed using the results from the PLL, and thus the high-frequency noise is filtered. However, the PLL will create noise, in this case, the noise is coloured. This creates a lower magnitude, but coloured, high-frequency noise for the carrier phase observable. Phase noise is discussed in more detail in Chapter 8.

Also interesting to note is the IQ-derived phase underestimates the magnitude of the ionosphere-induced events compared to the carrier phase observable. This is clearly seen in Figure 3.6. The reason for this is unknown at this point, however, we do suggest that the IQ-derived phase is being high-pass filtered to some extent; this can be seen in the spectral comparison in Figure 3.7. Clearly, higher power is observed in the carrier phase observable in the lower frequencies, and ionospheric-induced variations in the carrier phase typical exhibit a power law behaviour with a negative exponent. Thus, the lowest

frequencies will have the highest power. The spectral characteristics of ionosphere-induced carrier phase variations are discussed in more detail in the following chapter.

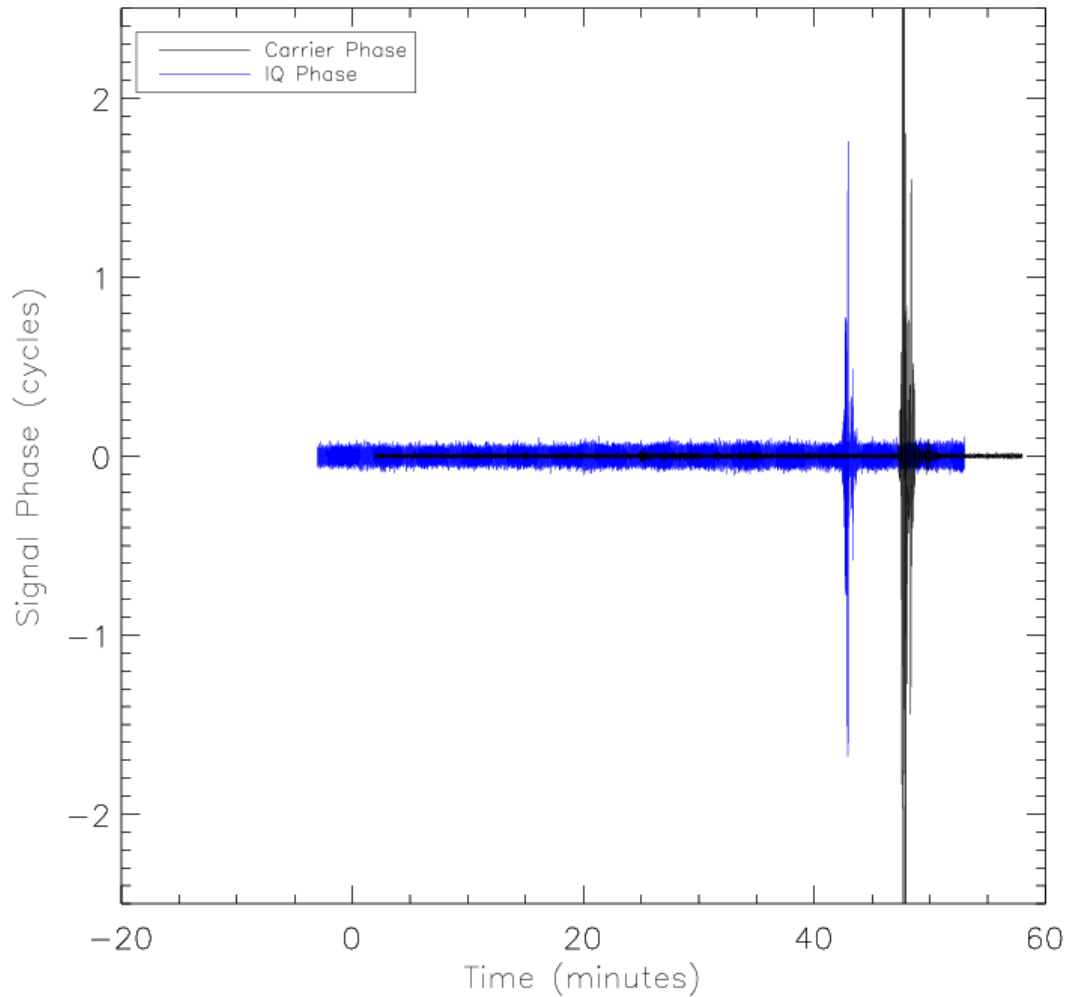


Figure 3.6 An example of the carrier phase observable (black) and the IQ-derived phase (blue). The event has a large portion of quiet time which demonstrates the difference in magnitudes; a significant event is located at roughly 42 minutes (blue) and 47 minutes (black). The IQ-derived phase is shifted negatively by five minutes to better visualize

the magnitudes of the event. The IQ-derived phase overestimates the high-frequency noise and underestimates the magnitude of the event.

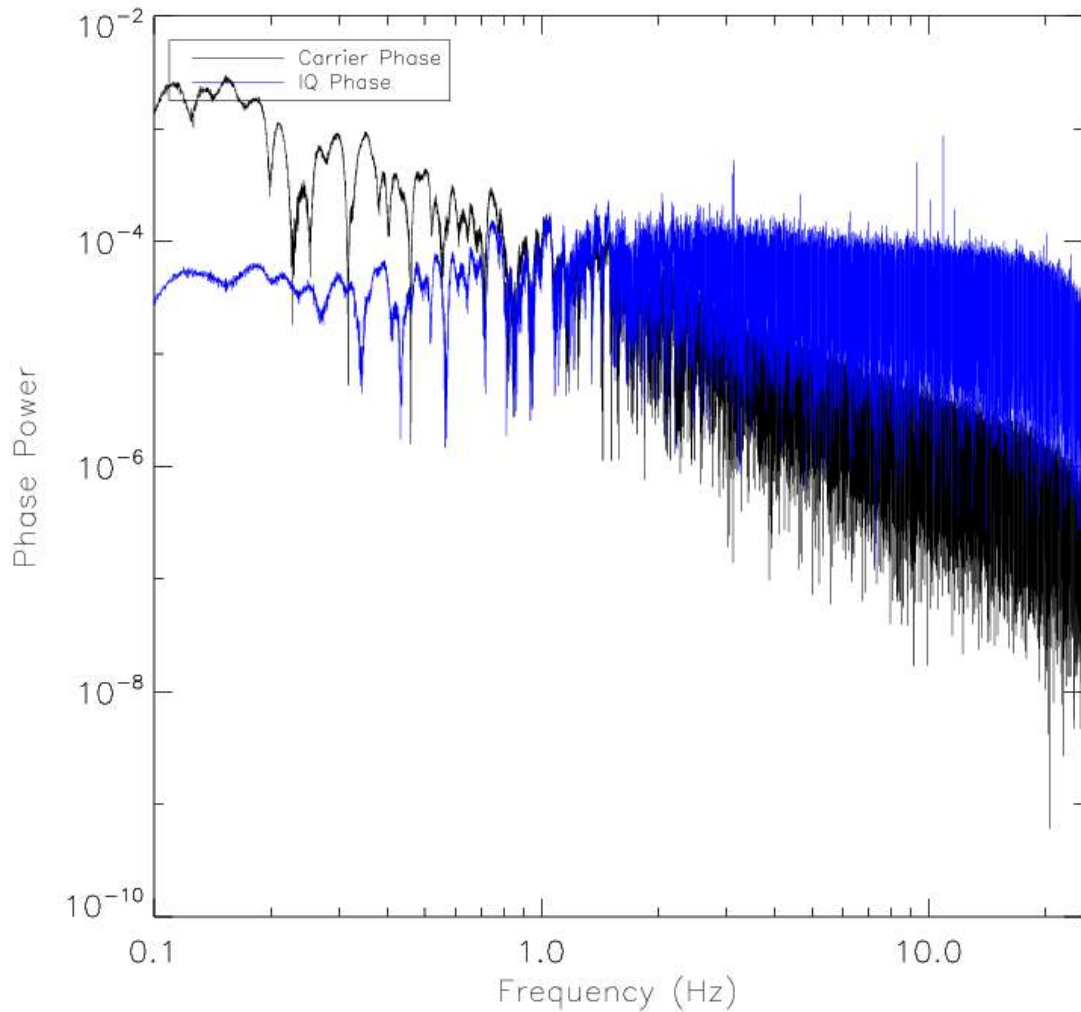


Figure 3.7 The spectrum of the IQ-derived phase (blue) and the carrier phase observable (black). Note that the IQ-derived phase has larger magnitude variations in the high frequencies.

4 Theory

4.1 Introduction

We are interested in the ionosphere's impact on the amplitude and carrier phase of the GPS signals. The impact of the ionosphere on the radio signals can be used to help understand the ionosphere's features. These effects can be split into two categories: low-frequency effects and high-frequency effects. The low-frequency variations are considered purely refractive in nature. Since the ionosphere's refractive index is directly related to the electron density, the refractive variations can be used to study the electron density. Typically, this is a tool used to study the electron density on long timescales and over large areas (Pi et al., 1997; Watson et al., 2016). The high-frequency effects are typically considered scintillation, or, variations due to diffraction of the GPS signal (Rino, 1979). These variations rely on changes in the electron density as well, but due to the stochastic nature of the diffraction-induced variations, the magnitudes of the variations observed on the ground cannot be mapped directly to a change in the density.

The presented work will focus on the determination and analysis of dominantly refractive variations which are associated with high-frequency fluctuations in the GPS signal. Since the high-frequency portion of the signal is typically assumed to be caused by diffractive effects, these variations are very often misclassified. In this chapter, we discuss the relevant theory behind the refractive and diffractive effects of the ionosphere on the GPS carrier phase.

4.2 GPS Scintillation

The theory behind scintillation on the amplitude and phase of trans-ionospheric radio waves, such as those transmitted by GPS, has been a topic of interest for decades (see Yeh and Liu, 1982; Kintner et al. 2007 and references therein). Early interest in scintillation began with works like Hey et al. (1946) and Mills and Thomas (1951) who discovered rapid variations in radio frequency emission from the Cygnus constellation. It was discovered that these variations were not correlated well if the distance between the ground-based observations was large, eliminating the possibility of the variations in the signal originating from the source. As the baseline between the ground-based observations decreased, the correlation between the observed variations increased. From this, it was concluded that the variations were caused by the ionosphere.

Through the years its been shown that these rapid variations in the amplitude and phase of trans-ionospheric radio waves are caused by the changes in phase induced by variations in the refractive index along the signal's ray path. When a radio wavefront encounters a variation in the refractive index, the wavefront exiting the variation will be phase shifted relative to the wavefront which has not encountered the change in refractive index. From the Huygens-Fresnel principle, each point of the wavefront acts as a source of smaller wavelets. It can be thought that the exit point of the change in refractive index acts like a source for the same wave as that which did not enter the

change in refractive index, however, this wave will be phase shifted. As both the background wave and the phase-shifted wave propagate further, they can interact with one another, causing constructive and destructive interference. This interference is viewed at the receiver as high-frequency variations in both the amplitude and phase time series. An illustration of this phenomenon is presented in Figure 4.1. The wavefront from the satellite is presented as the black dashed lines. The ionosphere is displayed as a two-dimensional plane, with phase-changing irregularities scattered throughout. These irregularities alter the phase of the initial wavefront as it passes through them. This is indicated by the red portions of the wavefront. Using a simplified illustration of Huygens principle, the inhomogeneities are thought of as sources of new wavefronts, with a phase shift relative to the original wavefront. These are represented by the red dashed lines below the layer. As the original wavefront and the new wavefronts propagate and spread they will constructively and destructively interfere with one another, creating a diffraction pattern. The diffraction pattern is observed as rapid variations in the amplitude and phase of the signal over time. Note that in this illustration that the scattering of the wavefront due to the homogeneous parts of the layer are ignored for clarity.

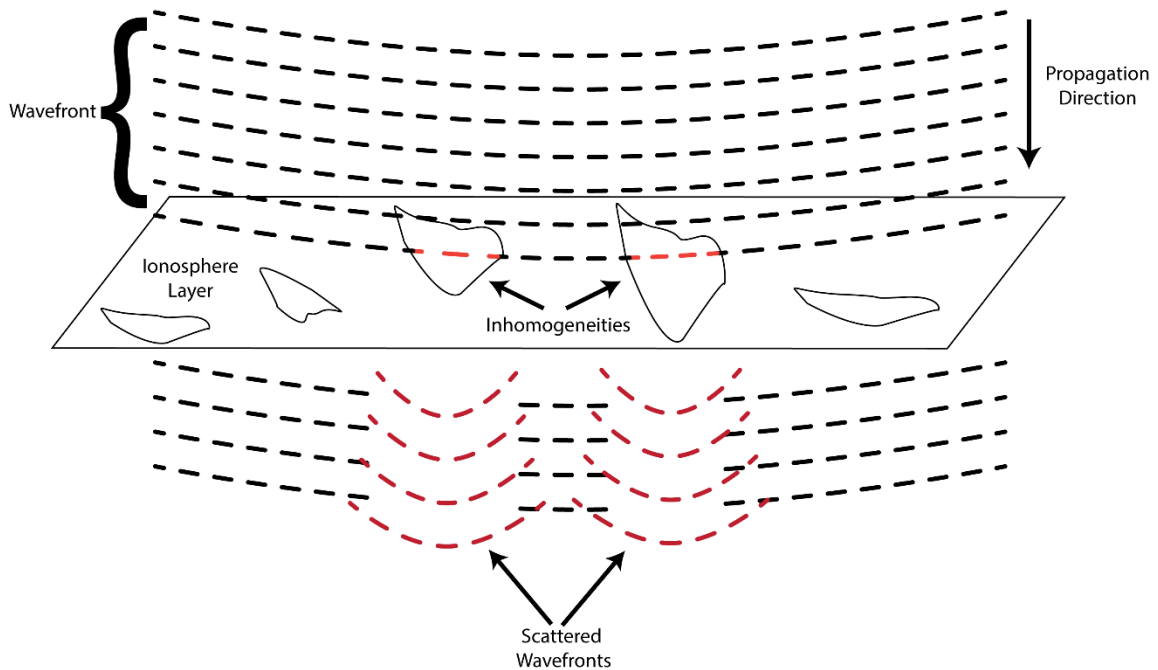


Figure 4.1 Simple illustration of a two-dimensional ionospheric layer, with irregularities scattering a wavefront. The scattered and non-scattered wavefronts will interfere constructively and destructively; this will result in diffractive effects referred to as scintillation. Note that scattering due to the homogeneous part of the layer is ignored for simplicity.

Diffraction induced by irregularities in the ionosphere can be described using Fresnel diffraction principles. Thus, for the diffraction pattern to be observed at a given receiver, two complementary conditions must be fulfilled; the spatial scale of the inhomogeneity must be sufficiently small and the height of the inhomogeneity, relative to the receiver, must be sufficiently large. These conditions are summarized in the equation for the Fresnel scale:

$$d_f = \sqrt{2\lambda z} \quad 4.1$$

where λ represents the wavelength of the trans-ionospheric wave, and z is the height of the inhomogeneity, relative to the receiver. The Fresnel scale d_f defines the largest scale size, at a height z , that can cause diffractive variations in amplitude and phase that will be visible at the receiver. With this maximum spatial scale, we can define a minimum frequency at which these diffractive variations can occur, known as the Fresnel frequency

$$f_f = \frac{v_d}{d_f} \quad 4.2$$

where v_d represents the drift speed between the wave source (GPS satellite for example) and the irregularity, relative to the receiver. Therefore, the frequencies at which diffractive scintillation should be present in the GPS carrier phase and amplitude for a given event will be greater than f_f .

Theoretical and experimental results have concluded that the spectral characteristics of both amplitude and phase scintillation are expected to follow a power law behaviour with a negative slope for weak scintillation cases (Yeh and Liu, 1982 and references

therein). Early observations of this behaviour include Jones (1960) and Rufenach (1971). Weak scintillation is defined by the magnitude of the amplitude variations during the scintillation event. As long as these variations are of low to moderate magnitude, the scintillation should follow the power law behaviour. An illustration of this behaviour is presented in Figure 4.2. The amplitude behaves as we would expect based on the discussion thus far. The amplitude spectrum follows a zero-slope up to the Fresnel frequency. After the Fresnel frequency, the expected power law with a negative slope is observed. This continues through all frequencies until the noise floor is reached; note that the noise floor is not pictured in Figure 4.2. The phase spectrum, on the other hand, does not exhibit the zero-slope in the frequencies below the Fresnel frequency. This is due to refractive variations in the carrier phase. These refractive variations are expected to follow a similar power law behaviour to the scintillation variations. So, the Fresnel frequency, and therefore the frequency at which the diffractive variations begin, is not easily observed in the phase spectrum. As a signal encounters changes in the refractive index, the amplitude of the signal may decrease a small amount, due to reflection, but will never increase due to these changes in refractive index. Therefore, variations in the amplitude below the Fresnel frequency are not present.

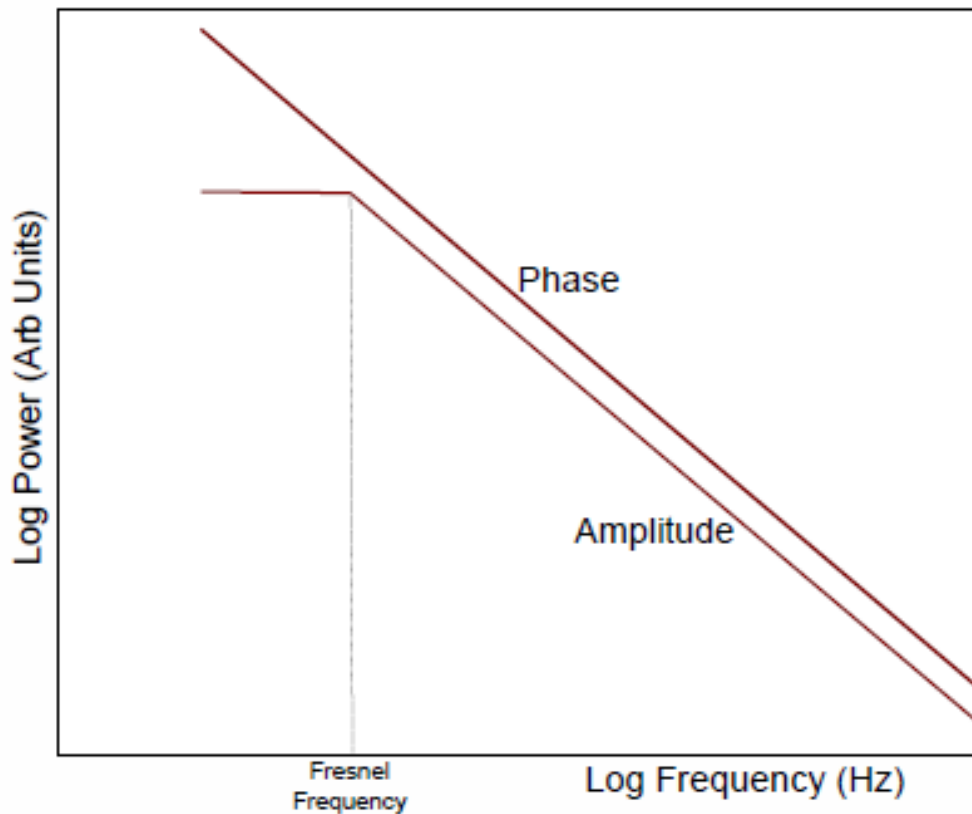


Figure 4.2 Illustration of the expected spectral behaviour for GPS amplitude and phase scintillation.

Note that these refractive variations in the carrier phase, at frequencies near the Fresnel frequency, may also be referred to as scintillation. This is more often the case in the earlier works (Booker, 1958; Crane, 1977; Cordes et al., 1986), but is considered and discussed much less often in more recent publications. For the sake of consistency with these more recent works, we will refer to scintillation only as diffractive scintillation, and refractive variations will be clearly specified as refractive variations. Regarding the more recent scintillation publications, these refractive variations are often ignored

(Mitchell et al., 2005; Mushini, 2012; McCaffrey et al., 2017a). This implies that the high-frequency variations may be wrongly assumed as diffractive. This will be discussed in more detail in Chapter 7.

4.3 Rapid Refractive Variations in Phase

We can model the GPS carrier phase using a simplified version of the carrier phase equation presented in equation 3.3:

$$\Phi_L^{s,r} = \alpha_L^{s,r} + I_L^{s,r} + \epsilon_L^{s,r} \quad 4.3$$

where all the constant and low-frequency terms have been grouped into the $\alpha_L^{s,r}$ term, such as the geometric distance between the receiver and satellite, hardware clock errors, the tropospheric term, etc. $I_L^{s,r}$ and $\epsilon_L^{s,r}$ are the ionospheric term, and the high frequency low magnitude noise, respectively, just like they were presented in equation 3.3. We define the low frequency terms as anything less than 0.1 Hz. This is the convention used in the field, where it is assumed that a cut-off frequency of 0.1 Hz will remove the unwanted terms (the α term) but leave the scintillation effects (Forte and Radicella, 2002).

The ionospheric term can be split into two main components:

$$I_L^{s,r} = \eta_L^{s,r} + d_L^{s,r} \quad 4.4$$

where $\eta_L^{s,r}$ represents the refractive contribution to the ionospheric effects, and $d_L^{s,r}$ represents the scintillation, or diffractive, effects. Typically, the refractive contribution is assumed to be at frequencies below the 0.1 Hz cut-off; this assumes that the Fresnel frequency is very near or below 0.1 Hz in all cases. This assumption originates with work in the low latitude ionosphere, where the assumption is more valid (Forte and Radicella, 2002). Recalling equation 4.2, the Fresnel frequency is directly proportional to the relative drift speed between the GPS satellite and the ionospheric irregularity. In the high latitude ionosphere, drift speeds are much greater than those present in the low latitudes (Chandra et al., 1971; Davies, 1990). This will correspond to greater Fresnel frequencies in the high latitudes. Regardless, a cut-off of 0.1 Hz is still commonly used in most scintillation work. The cut-off is used in the detrending methods, where the raw GPS carrier phase is high pass filtered. This will be discussed in more detail in the later chapters.

The refractive contribution to the ionospheric term is related to the phase refractive index of the ionosphere. We start with the Appleton-Hartree equation, the refractive index for a cold magnetized plasma. The Appleton-Hartree equation is derived by describing the movement of the plasma (electrons and ions) in a uniform magnetic field as an electromagnetic wave travels through it. In deriving the equation, two major

assumptions are made: 1) The ions are too heavy to be significantly impacted by the high frequency wave and thus their motion is ignored. 2) The plasma is assumed to be cold, thus eliminating the pressure force in the initial equation of motion. The Appleton-Hartree equation is, as expressed by Hernández-Pajares (2010):

$$n^2 = 1 - \frac{X}{1 - \frac{Y_T^2}{2(1-X)} \pm \left[\frac{Y_T^4}{4(1-x)^2} + Y_L^2 \right]^{\frac{1}{2}}} \quad 4.5$$

$$X = \frac{\omega_p^2}{\omega^2}, \quad Y_L = -\frac{\omega_g}{\omega} \cos\theta, \quad Y_T = -\frac{\omega_g}{\omega} \sin\theta \quad 4.6$$

where ω_p is the plasma frequency of the electrons, ω_g is the electron gyro frequency, ω is the angular frequency of the wave, and θ is the angle between the propagation direction of the wave and the magnetic field. The plasma and gyro frequency can be expressed more fundamentally as:

$$\omega_p^2 = \frac{N_e q^2}{m_e \epsilon_0}, \quad \omega_g = \frac{Bq}{m_e} \quad 4.7$$

where N_e is the electron density, q is the electron charge ($=1.6022 \times 10^{-19}$ C), m_e is the electron mass ($=9.1094 \times 10^{-31}$ kg), ϵ_0 is the permittivity of free space ($=8.8542 \times 10^{-12}$ F/m), and B is the absolute value of the magnetic field. By expanding equation 4.5 using

a second order Taylor approximation, up to f^{-4} , the Appleton-Hartree equation can be represented like:

$$n = 1 - \frac{1}{2}X \pm \frac{1}{2}XY_L - \frac{1}{8}X^2 - \frac{1}{4}XY^2(1 + \cos^2 \theta) \quad 4.8$$

$$Y^2 = Y_L^2 + Y_T^2 = \left(\frac{\omega_g}{\omega}\right)^2 \quad 4.9$$

By substituting the relationships in equation 4.6 into equation 4.7, we get:

$$n = 1 - \frac{q^2}{8\pi^2 m_e \epsilon_0} \frac{N_e}{f^2} - \frac{q^3}{16\pi^3 m_e^2 \epsilon_0} \frac{N_e B \cos \theta}{f^3} - \frac{q^4}{128\pi^4 m_e^2 \epsilon_0^2} \frac{N_e^2}{f^4} - \frac{q^4}{64\pi^4 m_e^3 \epsilon_0} \frac{N_e B^2 (1 + \cos \theta)}{f^4} \quad 4.10$$

The refractive contribution to the ionospheric term in the carrier phase observable is defined as:

$$\eta = \int_r^s \frac{c}{v} dl - \rho = \int_r^s (n - 1) dl \quad 4.11$$

which is the integral of the refractive index (minus one) along the ray path from the satellite to the receiver. Substituting equation 4.10 into equation 4.11 and evaluating the constants results in:

$$\eta = -\frac{s_1}{f^2} - \frac{s_2}{f^3} - \frac{s_3}{f^4} \quad 4.12$$

$$s_1 = 40.309 \int_r^s N_e dl \quad 4.13$$

$$s_2 = 1.1284 \times 10^{12} \int_r^s N_e B \cos \theta dl \quad 4.14$$

$$s_3 = 812.42 \int_r^s N_e^2 dl + 1.5793 \times 10^{22} \int_r^s N_e B^2 (1 + \cos^2 \theta) dl \quad 4.15$$

The higher order terms, shown here as s_2 and s_3 , have been estimated to represent less than 1% of the overall refractive effects (Datta-Barua et al., 2008). Therefore, the higher order terms are truncated in most analyses. The higher order terms and their possible impact on the presented analysis are discussed in more detail in Chapter 8.

We truncate the refractive contribution to the ionospheric portion of the carrier phase to the first term (equations 4.12 and 4.13) and substitute the refractive index into equation 4.11; this results in the refractive effect on the carrier phase:

$$\eta = -\frac{40.309}{f^2} \int_r^s N_e dl \quad 4.16$$

Clearly, the refractive contribution to the GPS carrier phase is deterministic, where any change in the electron density along the ray path will result directly in changes in the carrier phase.

4.3.1 Total Electron Content

An important parameter in ionosphere monitoring and research is the TEC, defined as:

$$TEC = \int_r^s N_e dl \quad 4.17$$

Which is the integral number of electrons along the ray path between the satellite and receiver, within a meter-squared column. The units for TEC are TEC units (TECU), defined as 10^{16} electrons/m². An illustration of the TEC measurement is shown in Figure 4.3. The TEC is used for monitoring the electron density of the ionosphere, typically through long timescales. For example, global TEC maps are created by a few groups using predominantly GPS data to observe and study the formation, climatology, and

morphology of density enhancements and depletions in the ionosphere (Hernández-Pajares et al., 2009). The GPS-based calculation of TEC assumes that two carriers, most popularly the L1 and L2 carriers, follow nearly identical ray paths through the ionosphere. It also assumes that all terms other than the ionospheric term in the carrier phase equation are frequency independent, and thus are the same for both L1 and L2. By differencing the L1 and L2 carrier phase observables, these terms will be removed leaving only the ionospheric term. This results in the following linear combination:

$$\begin{aligned}\Phi_{L1} - \Phi_{L2} &= -\frac{40.3}{f_{L1}^2} \int_{rx}^{sx} N_e ds + \frac{40.3}{f_{L2}^2} \int_{rx}^{sx} N_e ds \\ \Delta\Phi &= 40.3 \frac{(f_{L1}^2 - f_{L2}^2)}{f_{L1}^2 f_{L2}^2} \int_{rx}^{sx} N_e ds\end{aligned}\quad 4.18$$

We can substitute equation 4.17 into equation 4.18, and rearrange for TEC:

$$TEC = \frac{f_{L1}^2 f_{L2}^2}{40.3(f_{L1}^2 - f_{L2}^2)} \Delta\Phi\quad 4.19$$

Note that a few assumptions have been made, which results in neglecting a few terms. The integer ambiguity terms are not carrier independent and will result in a constant offset in the TEC result. This is an issue for absolute TEC measurements, where the true TEC value is desired. A nearly constant offset, which is not presented in the earlier

equations, but should be noted, is the hardware biases. These biases, stemming from hardware delays between the carriers in both the satellites and receivers, will have an impact like the integer ambiguity; the bias will DC offset the TEC from its true absolute value. The extent as to how long the hardware biases are constant is debated, the lowest assumption comes from Zhang et al. (2017), estimating that the biases can vary within approximately three hours. The work presented here focuses on very high sampling rates, and will not be affected by these possible changes in the biases. We are also not interested in the absolute TEC; we are interested only in the relative variations in TEC. For this reason, we can drop the integer ambiguity terms from equation 4.19 and ignore the hardware biases. The noise, or ϵ , terms are also assumed to be negligible in the above equation. The validity of this assumption will be addressed in Chapter 8. Lastly, the diffraction portion of the ionospheric term is dropped. This is typical in TEC analysis because the diffractive contribution is high frequency, and too low in magnitude to have an impact on the long-term trends typically analyzed in TEC works. As was mentioned, we are interested in the high frequency changes in TEC, thus the diffractive contribution is likely not negligible for the presented work. This will be addressed in more detail in Chapter 7.

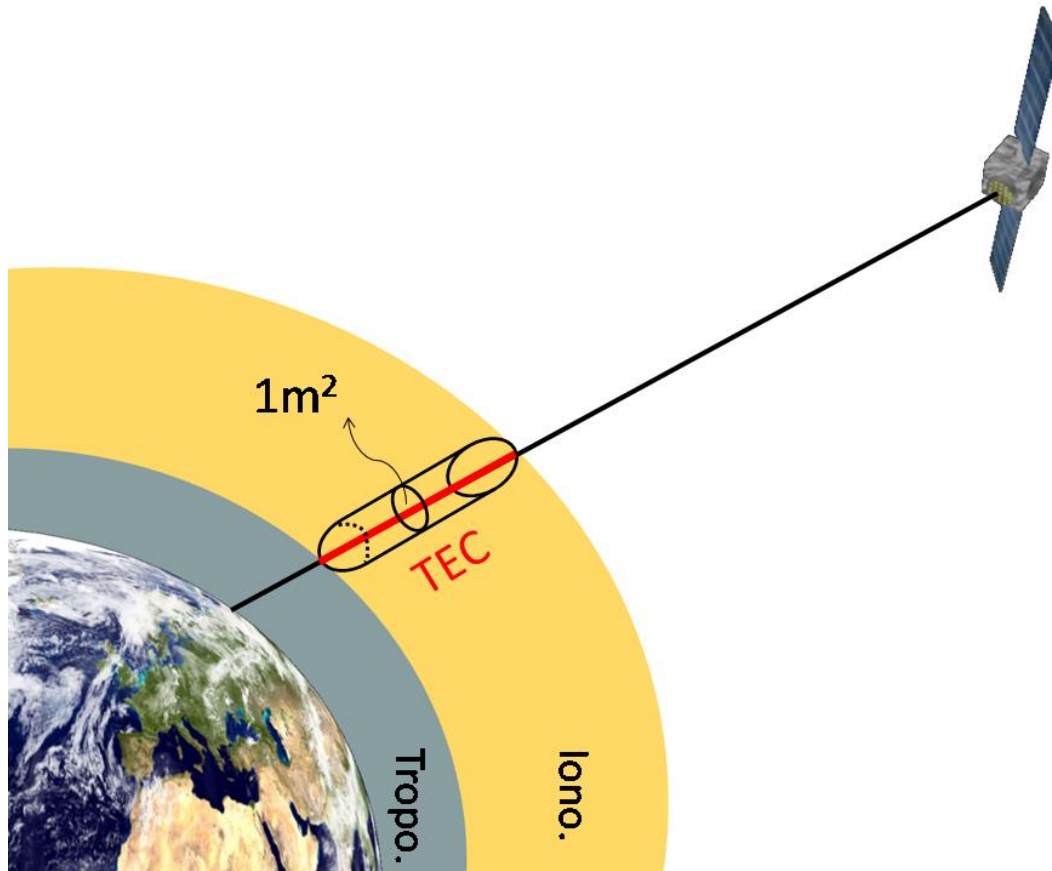


Figure 4.3 Illustration of the TEC measurement.

Note that many TEC works will use what is referred to as the vertical TEC (vTEC). This is a vertical projection of the TEC defined in equation 4.19. This is used when the absolute TEC taken from multiple ray paths at varying elevation angles are compared; since the length of the ray path through the ionosphere will vary with elevation, this projection attempts to remove the elevation dependence, giving an estimate of the TEC through a vertical slice of the ionosphere. The vTEC projection is based on a single, thin shell model of the ionosphere, at a given height. The thin shell model assumes the ionosphere as an infinitesimally thin layer, with a uniform density. The height of the

layer is taken near the peak density height. An illustrative example of the sTEC and vTEC is presented in Figure 4.4. The red slant line along the ray path represents the sTEC; the blue line represents the vertical projection of the sTEC to vTEC. For all results presented in this study, TEC refers to the sTEC. The vertical projection of TEC is used for a single step in the methods used in Chapter 8, where the vertical projection is required in calculating the magnitude of the higher order terms in the ionospheric delay. The projection function is defined as:

$$M(z) = \sqrt{1 - \left(\frac{R_E \cos(z)}{R_E + h}\right)^2} \quad 4.20$$

where h is the chosen height of the layer, z is the complement to the elevation angle of the satellite, and R_E is the radius of the Earth. Thus, the vTEC is defined as:

$$vTEC = sTEC \cdot M(z) \quad 4.21$$

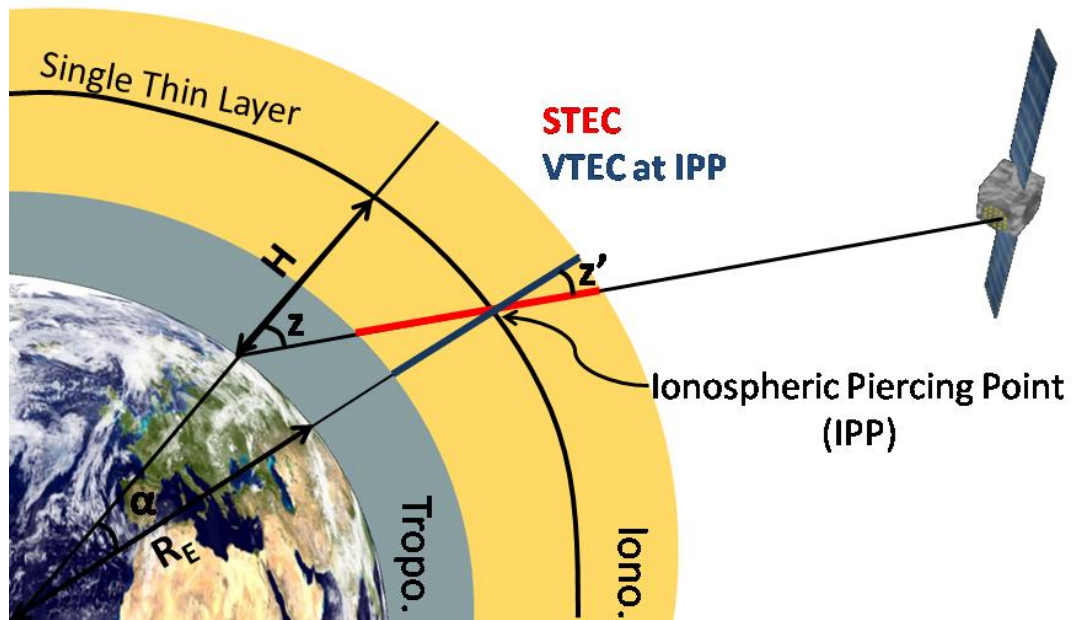


Figure 4.4 An illustrative example of the projection from sTEC to vTEC, using a single thin shell model of the ionosphere. The pierce point of the ray is taken at the assumed height of the shell (h). Retrieved from http://gnss.be/ionosphere_tutorial.php.

5 Data and Methods

5.1 Introduction

The GPS data for this study, as was previously mentioned, comes almost exclusively from the Septentrio PolaRxS Pro receiver. This chapter discusses the raw data files provided by the receiver and some of the processing required to get the raw observables necessary for the presented results. Many processing techniques are employed to get from the raw observables to the desired form. These techniques are common in GPS scintillation research and are discussed in detail. Septentrio provides software with the receiver to retrieve certain aspects of the data, including providing an Ionospheric Scintillation Monitoring Record (ISMR) file. This file consists of, among other things, the typical scintillation indices (these are discussed in detail later in the chapter), as well as some information about the TEC.

Although some relevant data is available in the ISMR files, not everything required for the study is provided. More importantly, the processing techniques used by the software is not publicly available, therefore, we would be forced to use it as a black box which is undesirable. With this in mind, we decode the raw data files directly from the Septentrio receiver, allowing for all techniques and methods to be fully known. This also gives more control over determining which effects may be due to receiver configurations or receiver noise sources, rather than artifacts of the analysis methods.

5.2 Septentrio Binary Format Files

The Septentrio receiver provides data in a binary format, called the Septentrio Binary Format (SBF). These SBF files require decoding before the raw observables can be obtained. As discussed, the utilities provided by Septentrio to automatically decode the files are black boxes, and the options within these utilities are lacking. Therefore, custom utilities have been written and used exclusively for the presented results. The Septentrio provided utilities were used initially only to verify some of the output of the custom utilities.

The SBF files are logged as one-hour long files, aligned to Coordinated Universal Time (UTC). The data is categorized into blocks, known as SBF blocks, containing subsets of data falling under a specific category or set of categories. A couple examples are the *GPSNAV* block, which provides data regarding the GPS navigation message. This includes the health of the satellite and the eccentricity of the orbit. Another is the *MeasEpoch* block, which provides the main GPS observables and is necessary for the work presented here. It contains data like the carrier phase observable, the signal to noise ratio, and the lock-time of the satellite. The blocks all contain a header with information about the block, including the ID number associated with the block type, the length of the block, and time information including the GPS time of week and week number. The time of week is a measurement of time, in seconds, starting at 0 hours every Sunday. The week number counts the number of weeks since 6 January 1980. The SBF blocks may also contain subblocks; these include a subset of the same information

as the main block but for a different satellite or signal. The sampling rates of the blocks can be chosen by the user, allowing desired data to be sampled at higher rates than others. The two most important blocks for this study are the *MeasEpoch* block, which is logged at 1 Hz, and the *IQCorr* block, which is logged at the desired high frequency (50 Hz or 100 Hz, depending on the station). The *IQCorr* block is the block which provides the in-phase and quadrature components necessary for the calculation of the amplitude (see equation 3.1). It also provides the information necessary to get the high-frequency carrier phase observable.

The entire format for the SBF files and the SBF blocks is provided in the Septentrio SBF reference manual (Septentrio, 2015). This provides the necessary info to create the custom utilities used for this study. To compress the files, many observables and data required from the SBF files are encoded into smaller pieces, typically a so-called least or most significant byte (LSB and MSB). An example of this is in the case of the high-frequency carrier phase. As was previously mentioned, the *MeasEpoch* block provides the carrier phase observable but is logged at only 1 Hz. The *IQCorr* block provides the so-called LSB of the carrier phase at the higher sampling rate. This can be done because the carrier phase observable will likely not change significantly over the 0.01 s – 0.02 s intervals, allowing only a 16-bit number to be stored rather than the full carrier phase observable, which would require 32 bits to 64 bits to store. The LSB of the carrier phase is the result of the full carrier phase modulo 65.536 cycles. Thus, this operation must be reversed to reconstruct the full carrier phase at the higher sampling rate. This can be done in the following way:

$$\phi_{t_i} = \phi_{r_{i-1}} - f_d \delta \quad 5.1$$

$$j = \left\lfloor \frac{\phi_{t_i} - \phi_{LSB_i}}{65.536} \right\rfloor \quad 5.2$$

$$\phi_{r_i} = 65.536j + \phi_{LSB_i} \quad 5.3$$

where ϕ_r represents the reconstructed carrier phase observable, i indicated the epoch, f_d is the doppler frequency, δ is the time interval between samples, ϕ_{LSB} is the LSB of the carrier phase, and the vertical lines represent rounding to the nearest integer. Note that the doppler frequency and the reconstructed phase is updated whenever they are updated in the *MeasEpoch* block, or every one second in our chosen configuration.

5.3 Phase Jumps

The carrier phase observable can occasionally be ‘interrupted’, causing large jumps in the raw result. If the jumps are not corrected, they may appear as ionospheric in nature after the initial processing is complete. Therefore, these jumps must be corrected or discarded before processing begins. Two types of artificial jumps are common in the carrier phase, clock jumps and cycle slips. Clock jumps occur in the phase when a large change in the receiver clock occurs. This is due to the intimate relationship between the receiver’s calculation of the carrier phase observable and time. As discussed in Chapter

3, and outlined in equation 3.3, the carrier phase is a measure of the distance between the satellite and the receiver and relies on an accurate estimation of the travel time of the signal. If an abrupt change in the clock occurs, a corresponding jump in the carrier phase will occur. Ideally, jumps in the clock would not occur, however, the clocks used in GPS receivers are not as sophisticated as those aboard GPS satellites. The receiver clocks will drift over time relative to the satellite clocks, thus giving less and less accurate ranging measurements. In a typical receiver setup, the clock will be driven, meaning it is continuously being adjusted to agree with the satellite clocks. These small adjustments in the clock can appear as ionospheric variations, and make the carrier phase nearly useless for ionospheric research. Therefore, when using GPS receivers for ionospheric monitoring, the receiver clock is left to drift freely. This is the best situation for ionospheric monitoring as it will not cause continuous changes in the phase and positioning accuracy is not important. However, the clock is occasionally corrected in this configuration. In the case of the Septentrio PolaRxS Pro, the clock is corrected after it drifts to $500 \mu s$, shifting the clock 1 ms towards to true value. Since the carrier phase observable is dependent on the time, if the clock jumps 1 ms, the phase will jump the corresponding number of cycles, in this case

$$\phi_{jump} = 0.001f_c \quad 5.4$$

where f_c is the carrier frequency. Thus, to repair the phase after a clock jump, we can use the following equation:

$$\phi_i = \phi_{i-1} - \phi_{jump} \quad 5.5$$

An example of the effect of a clock jump of the carrier phase observable is presented in Figure 5.1. The raw, uncorrected, phase is represented by the black line while the corrected phase is represented by the dashed green line. The clock jump occurs at roughly 30 minutes.

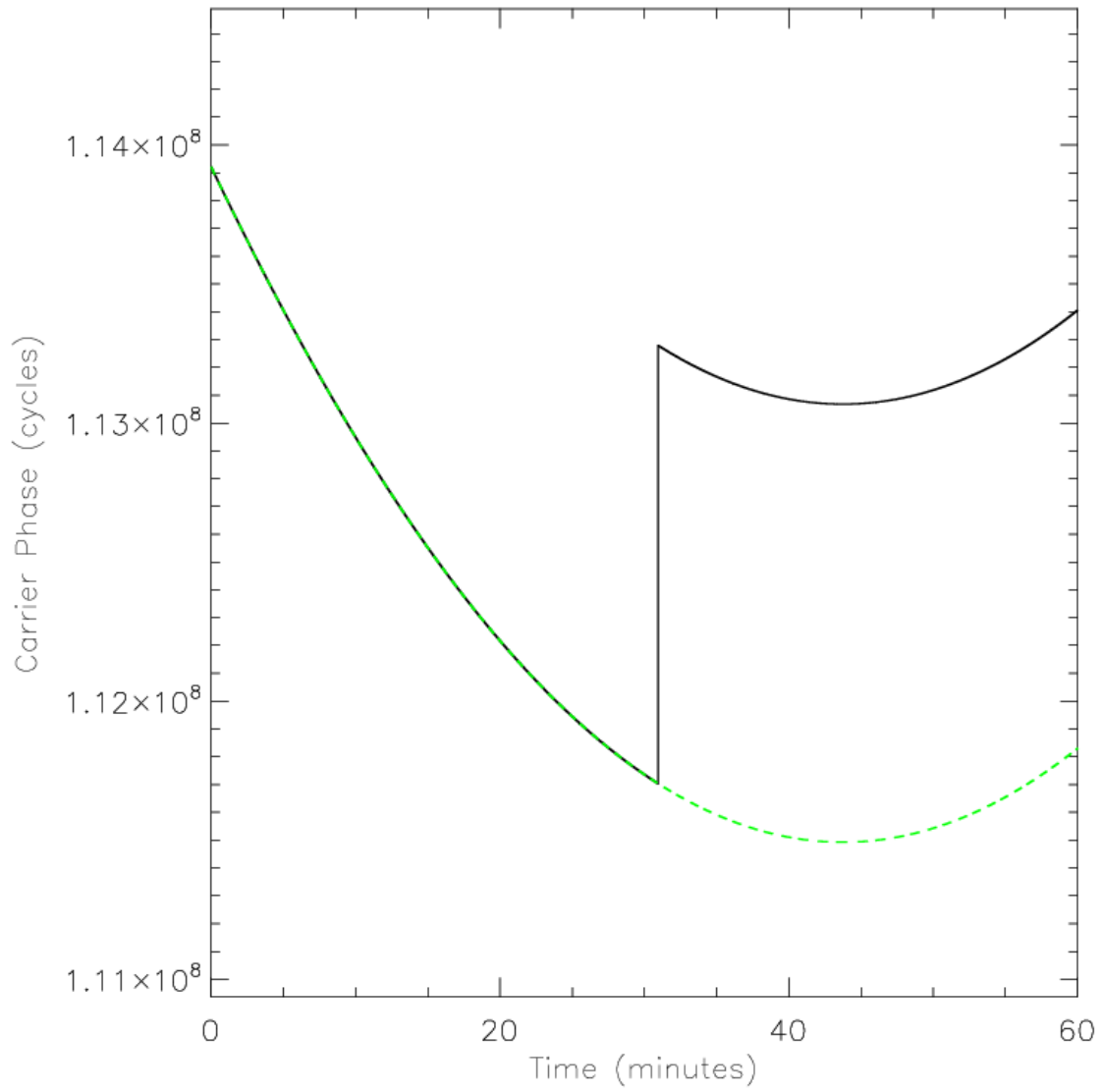


Figure 5.1 Example of a clock jump in the raw carrier phase observable. The uncorrected carrier phase, with the clock jump, is represented by the black curve. The corrected carrier phase observable is represented by the dashed green line.

The second cause of a jump in the carrier phase observable is known as a cycle slip. When the receiver initially begins tracking a signal, it estimates the total number of cycles the signal has undergone while travelling from the satellite to the receiver. This

estimate is usually incorrect; this is the cause of the integer ambiguity, discussed in Chapter 3. The estimate remains constant through the pass of the satellite under most circumstances and is thus not an issue for ionospheric research purposes. However, if the receiver loses lock on the signal and must reacquire it, the receiver will re-estimate the integer ambiguity, and the guess will likely vary from the original guess, thus a jump in the carrier phase observable occurs. There are many methods available to correct for these jumps and to correct for the integer ambiguity itself. An example method developed to correct for the cycle slips can be seen in Blewitt (1990). These methods, although getting better, are rarely perfect. Since the work presented here focuses on the high-frequency variations in the carrier phase observable, small artifacts due to inaccurate corrections to the cycle slips can have a significant impact on the results. For this reason, we do not attempt to correct cycle slips but rather remove them from the analysis. The main contributor to cycle slips is large decreases in the signal to noise ratio induced by large magnitude variations in the amplitude of the signal. Fortunately, these situations are rare in the high latitude region, thus, the number of cycle slips observed throughout the study was very small.

5.4 Standard Scintillation Analysis Methods

As discussed in Chapter 3, the GPS carrier phase observable is a combination of many terms, most of which are not important to the study. To remove these terms, which are mostly constant or low frequency, the signal is high pass filtered using a 0.1 Hz cut-off. The method of high pass filtering the raw signal is referred to as detrending. We note

that we have previously discussed issues with using a 0.1 Hz detrending cut-off frequency in the high latitude regions; we continue to use this cut-off frequency because it is widely used in the field and we aim to further show the impact it can have on the high latitude results.

The most common filters used in detrending are a sixth-order Butterworth filter (Van Dierendonck et al., 1993) and a wavelet filter (Mushini et al., 2012). We use the wavelet filter since it is designed to allow for bandpass filtering as well; bandpass filtering will be necessary for later analyses. Detrending the phase can be illustrated using the carrier phase equation, previously outlined in equation 3.3:

$$\Phi_L^{s,r}(t) = \rho^{s,r}(t) + c(dt^s(t) - dt^r(t)) + T^{s,r}(t) - I_L^{s,r}(t) + \lambda_L N_L^{s,r} + \epsilon_L^{s,r}(t) \quad 5.6$$

After detrending, the resulting phase equation is:

$$\Phi_L^{s,r}(t) = -I_L^{s,r}(t) + \epsilon_L^{s,r}(t) \quad 5.7$$

The geometric range and tropospheric delay (Misra and Enge, 2006) are both removed due to their very low period. Both are dependent on the satellite elevation and vary smoothly through a sweep of the satellite. The hardware clock errors are also very low frequency; in Figure 5.2 a representative example of the rate of the clock drift is shown

in blue. It takes roughly six hours for the clock to drift 1 ms. For the receivers within CHAIN, drift rates of four to eight hours are common. Therefore, all these terms are removed when using the high pass filter with the 0.1 Hz cut-off.

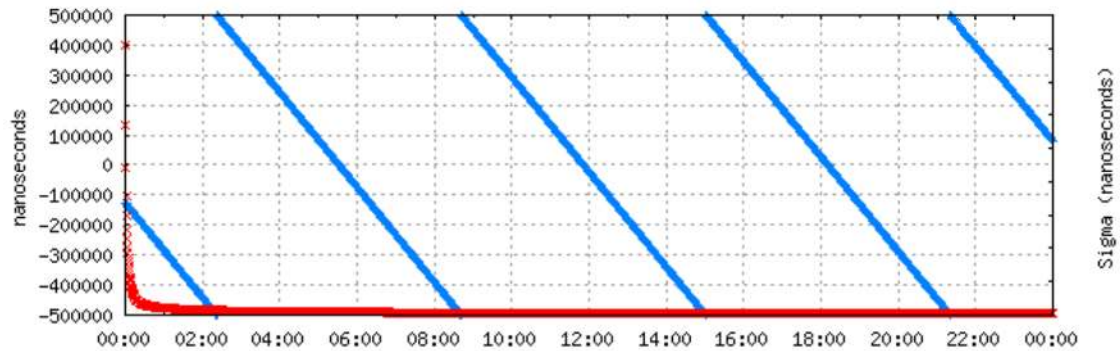


Figure 5.2 Representation of the receiver clock drift (blue). After the clock drifts $500 \mu\text{s}$, it is shifted 1 ms towards the correct value.

Unlike the phase, which is provided as part of a linear combination of terms, the amplitude of the signal is provided more directly from the receiver. We can think of the amplitude more simply as having low and high-frequency components. The low-frequency components consist mainly of satellite motion and the slow rate of change of the ionosphere, the high-frequency components, which are left after detrending, contain the ionospheric-induced variations and noise. Thus, after detrending, both the amplitude and the phase are left with an ionospheric part and a noise part. The noise term is composed of two main sources of error, hardware noise, and multipath. Hardware noise is typically considered very low in magnitude and therefore considered negligible, however, this assumption will be addressed as necessary throughout the presented

results. The multipath can be trickier, as it can appear very much like ionospheric-induced variations, and therefore events must be tested to ensure they are not multipath.

5.4.1 Multipath

Multipath is variations in the GPS signal induced by the signal interfering with a reflected part of itself. The GPS signal may reflect off geological or man-made features which lie around the receiver's antenna. The reflected signal will then reach the antenna after travelling a longer distance than the direct path to the antenna; this means the multipath and direct path signals will be out of phase. The direct path signal and the multipath signal will then form a composite signal which is received at the antenna, leading to possibly significant variations in the amplitude and carrier phase observable. An illustrative example of a multipath situation is presented in Figure 5.3.

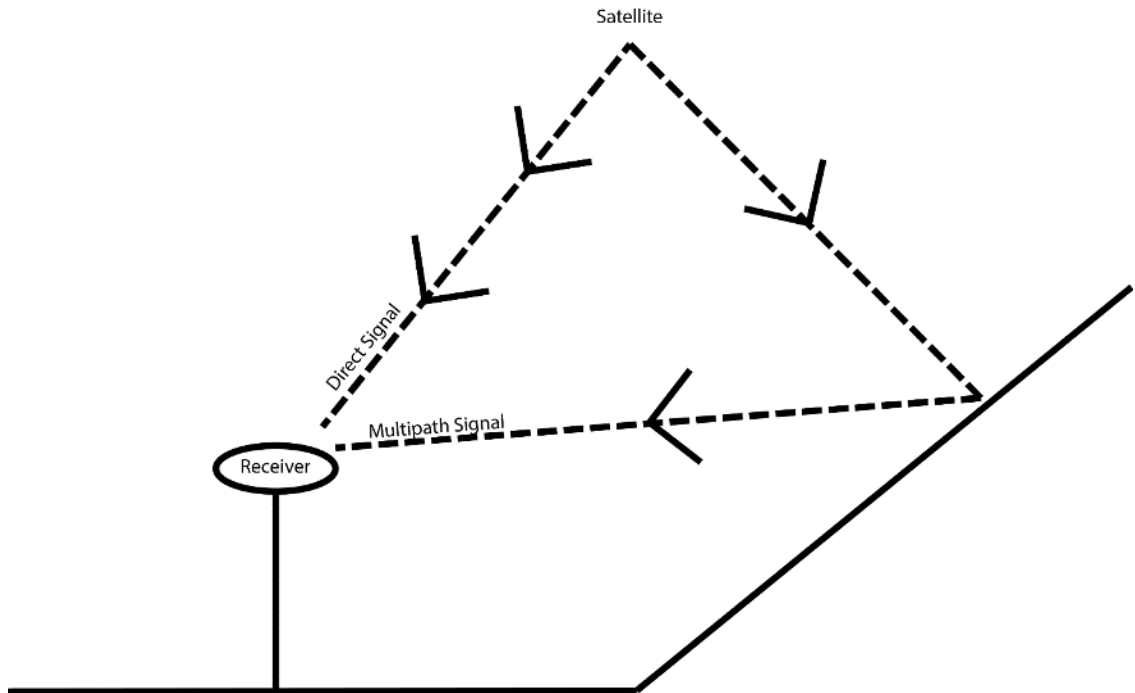


Figure 5.3 A simple illustration describing multipath. Multiple signals from the same satellite arrive at the antenna with varying path lengths, leading to an inference of the signals.

To distinguish multipath from ionospheric-induced variations, we exploit the GPS satellites' orbital period and the likely permanent nature of the multipath reflectors. The satellites have an orbital period of one half a sidereal day, thus, looking at the satellite data in half sidereal day increments should show the same ray path for the same GPS satellite. If multipath is present, it should then be seen to repeat in these half sidereal day increments. To simplify, when analyzing a variation event which may be ionospheric in nature, we analyze the same satellite exactly one sidereal day before and after the event. If similar variations are not observed on either of the other days, this suggests that the event is not caused by repeatable multipath. A visualization of this

technique is presented in Figure 5.4. The panels, from top to bottom, present the signal intensity (left) and the normalized standard deviation taken over one-minute intervals (right) for three consecutive days. The first day is presented in the top panel. The panels are exactly one solar day apart, thus any features repeated on sidereal day intervals should be shift roughly four minutes earlier each consecutive day. In the amplitude data and the standard deviations, there are clear features that are repeated each solar day, with a roughly four-minute shift. The most prominent is the feature located at roughly 42 minutes on the first day.

The method used in removing multipath events from our analysis is similar to the one presented in McCaffrey and Jayachandran (2017a). In short, an event of interest in a given time series (amplitude, carrier phase, or TEC) is compared to the same time series taken one sidereal day prior to, and one sidereal day subsequent to, the event. If a similar event is present in these days, then the event is assumed to be multipath.

It is less likely, but still possible, for multipath to be caused by non-permanent structures, like large snow banks for example. For this reason, checking the sidereal days does not guarantee an event is free of multipath. Another tool in determining multipath in carrier phase variation events relies on the theoretical limit of the effect of multipath on the carrier phase observable; this limit is a one-quarter cycle, or 0.06 m (El-Rabbany, 2002). If the variations in the carrier phase are greater than a quarter cycle, then it cannot be a multipath event.

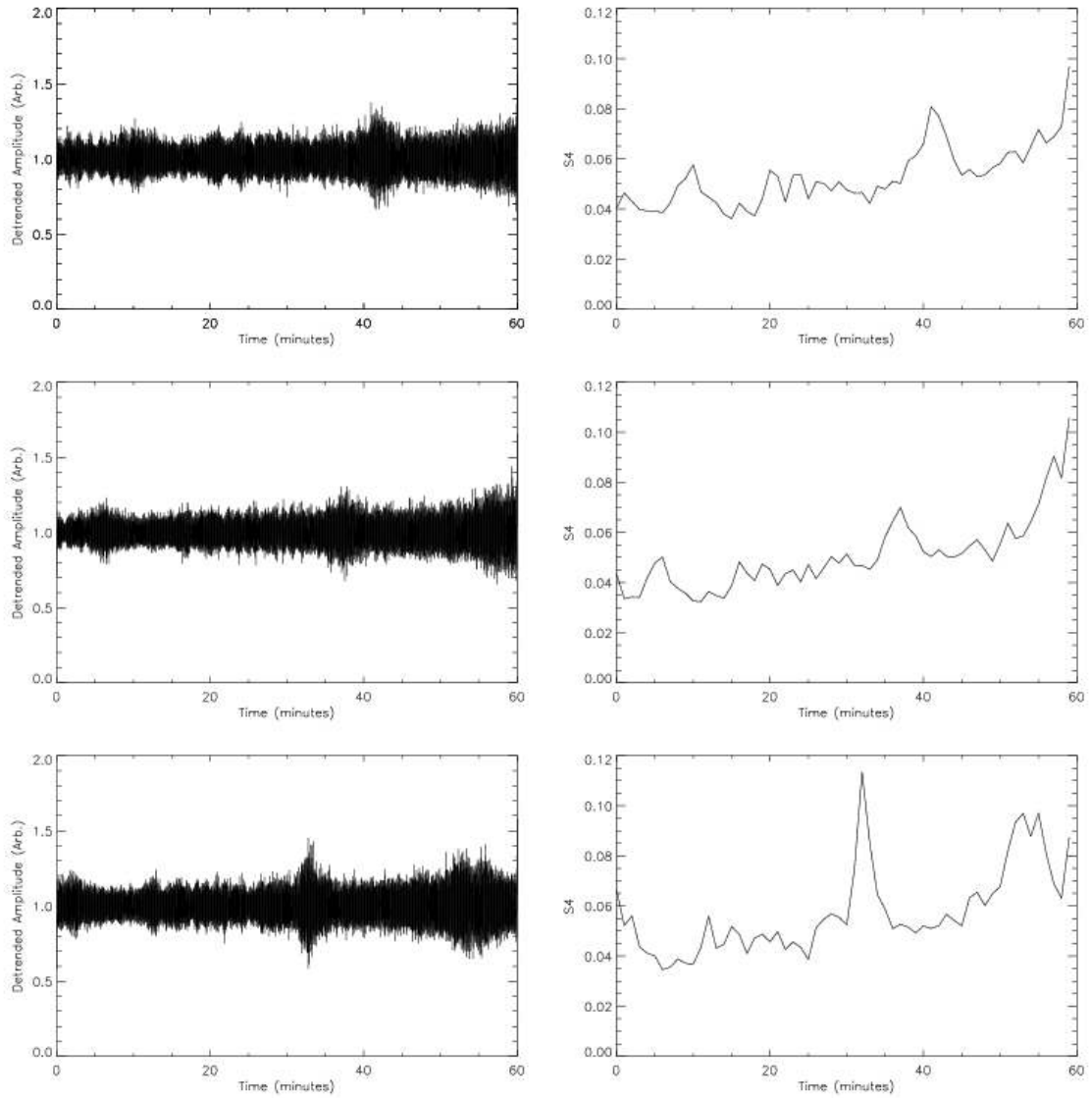


Figure 5.4 An example of the repetitive nature of multipath. The amplitude (left) and normalized standard deviations over one-minute intervals (right) are presented for three consecutive solar days. Features like the one present at roughly 42 minutes on the first day are seen to repeat each day, shifted negatively by approximately four minutes. This indicates the features repeats on sidereal day intervals.

5.4.2 Scintillation Indices

After obtaining the detrended signals, the common method of determining scintillation events in the amplitude and carrier phase makes use of the scintillation indices. The scintillation indices, S_4 for the amplitude and σ_ϕ for the carrier phase, are defined as follows:

$$S_4 = \sqrt{\frac{\langle I^2 \rangle - \langle I \rangle^2}{\langle I^2 \rangle}} \quad 5.8$$

$$\sigma_\phi = \sqrt{\langle \phi^2 \rangle - \langle \phi \rangle^2} \quad 5.9$$

Note that S_4 is a unitless quantity while σ_ϕ is typically presented in radians. Historically, scintillation events are chosen based on the value of these indices, using a common cut-off of 0.1 (Fremouw et al., 1978). Any variation events in which the S_4 or σ_ϕ exceed 0.1 are taken as scintillation events and analyzed according.

An illustrative example of the raw carrier phase (top), the detrended carrier phase using the wavelet detrending technique with a 0.1 Hz cut-off (middle), and the corresponding σ_ϕ is presented in Figure 5.5. The high frequency residuals in the signal become apparent in the detrended phase, making it easier to pinpoint and analyze likely ionospheric-induced events. The magnitude of these variation events is then clearly

quantified with the scintillation index. For the presented example, using the typical 0.1 radians cut-off, three events of interest are contained in the presented hour of carrier phase data; the events are located near 2 minutes, 23 minutes, and 37 minutes. A similar example for the amplitude is presented in Figure 5.6. The raw amplitude is presented in the top panel, the wavelet detrended amplitude, using a cut-off of 0.1 Hz, is presented in the middle panel, and the corresponding scintillation index (S_4) is presented in the bottom panel. For this example, we can see a few peaks in S_4 , however, only the event near 45 minutes would be considered a scintillation event since it is the only event in which the S_4 exceeds 0.1.

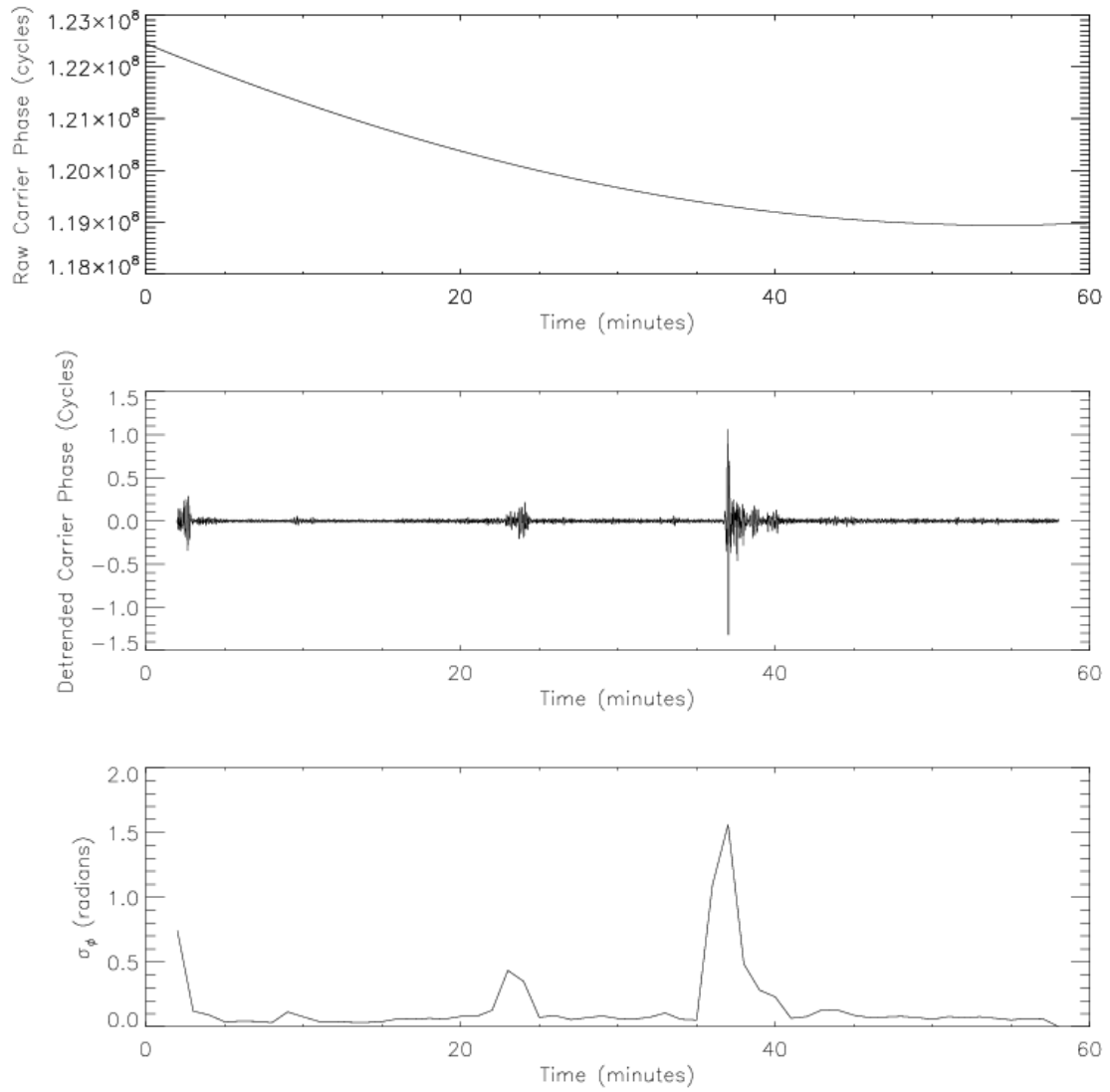


Figure 5.5 An example of the raw carrier phase observable (top), detrended carrier phase using wavelet detrending and a 0.1 Hz cut-off (middle), and the corresponding scintillation index σ_ϕ .

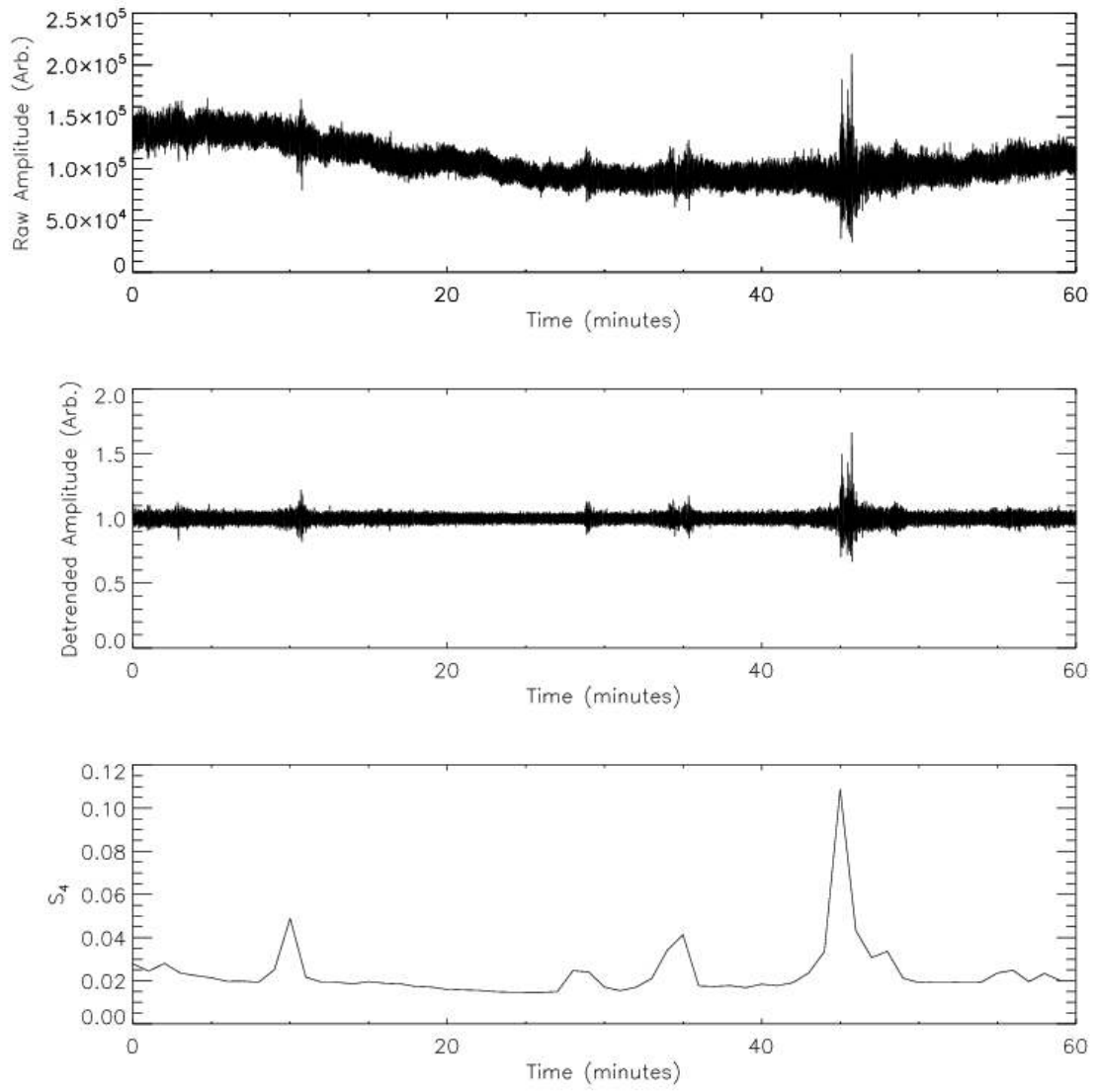


Figure 5.6 An example of the raw amplitude (top), detrended amplitude using wavelet detrending with a 0.1 Hz cut-off (middle), and the scintillation index S_4 corresponding to the detrended amplitude.

Although the detrending methods and the scintillation indices are used nearly ubiquitously in modern scintillation research, these methods have some issues. For example, the detrending technique may not fully remove everything from the phase

equation, thus leaving variations in the carrier phase which are not scintillation. A problem with the scintillation indices is that they only quantify variations in the amplitude and phase; the scintillation indices do not give information about the cause of the variations themselves. If the previously discussed methods of multipath detection were not employed, for example, then many multipath variations would be classified as scintillation using the outlined approach.

6 Independent L2 Tracking

6.1 Introduction

The changes being made as part of the GPS modernization program have the potential to be of great benefit to the ionospheric research and monitoring community. As was discussed in Chapter 3, an open code has been added to the L2 carrier (L2C), which previously transmitted only the encrypted P(Y) code. An open code on the L2 carrier will allow receivers the option of more robust tracking of the carrier; including the ability to track at higher sampling rates, and use tracking techniques which induce less noise and allow for more accurate tracking of the high-frequency dynamics (McCaffrey et al., 2018a). These improvements in the L2 carrier tracking may open new possibilities in the research being performed in the ionospheric monitoring community. For example, the high-frequency dynamics of the L2 carrier are very important for TEC studies (Bhattacharyya et al., 2000; Mitchell et al., 2005; Prikryl et al., 2011), specifically those looking at the high frequency changes in TEC (Yang and Liu, 2017; McCaffrey and Jayachandran, 2017b). However, with the addition of the new L2 open code, and its use in recent studies, it is important that the community understands the opportunities and limitations of the L2C and L2P(Y) observables, and how the tracking techniques used among the available receivers also impact these observables. Understanding the limitations of the different codes and tracking techniques for the observables will help eliminate possible misinterpretations of the data.

The L2C signal is not yet considered to be in full operational capacity, however, with 19 available satellites transmitting the open code as of April 2017, it is at a stage where it can and is being used for ionospheric studies and monitoring (Yang and Liu, 2017; McCaffrey and Jayachandran, 2017b; McCaffrey et al., 2018a; McCaffrey et al., 2018b). The most recent version of the Receiver Independent Exchange (RINEX) format (v3.03), the format used by IGS to distribute its GPS data, incorporates adding both the L2P(Y) and L2C carrier phase observables. The IGS makes its RINEX 3.03 data available through its IGS Multi-GNSS Experiment (MGEX) (Montenbruck et al., 2017). This provides many more researchers access to the modern GPS observables, allowing for more work to be done to either study the L2C observables themselves, or to begin comparing the legacy and modern observables' reliability.

The work by Yang and Liu (2017) is an example of those beginning to compare the legacy L2P(Y)-derived and L2C-derived carrier phase observables. They performed this comparison through the Rate of Change of TEC index (ROTI), an index used routinely in the field (Cherniak et al., 2015; Prikryl et al., 2016, and references therein). The ROTI is defined as the standard deviation of the Rate of change in TEC (ROT), taken over a given interval of time. The ROT is defined as the rate of change in TEC, from epoch to epoch, normalized by the time interval between the epochs (Pi et al. 1997):

$$ROT = \frac{TEC_i - TEC_{i-1}}{t_i - t_{i-1}} \quad 6.1$$

$$ROTI = \sqrt{\langle ROT^2 \rangle - \langle ROT \rangle^2} \quad 6.2$$

where i represents a given epoch, and t represents the time. The angle brackets represent a time average, typically chosen to be five minutes. Any differences observed between the L2P(Y) and L2C-derived ROTI values must originate with the difference in the L2P(Y) and L2C-derived TEC. Recalling the derivation of TEC in Chapter 4, the difference in the L2P(Y) and L2C-derived TEC will come from differences in the L2P(Y) and L2C carrier phase observables.

Yang and Liu (2017) observed significant differences between the L2P(Y) and L2C-derived ROTI, with the magnitude of the differences depending on the receiver used. Therefore, differences in the L2P(Y) and L2C carrier phase observable must be present, and these differences appear to depend on the receiver. Since the L2P(Y) and the L2C carrier will follow the same ray path through the ionosphere and must encounter the same changes in the electron density, the changes in the carrier phase should be identical, thus leading to identical carrier phase observables, TEC, and ROTI. This eliminates the possibility of these differences being ionospheric in nature. Yang and Liu (2017) also performed the analysis between a zero-baseline receiver pair and near zero-baseline receiver pair. The differences were still observed, thus also eliminating multipath and antenna issues as the cause. Based on the results, Yang and Liu (2017) concluded that the receivers are the likely cause of the carrier phase differences. As we will discuss in the next section, we propose the issue is with the tracking techniques

employed by the receivers. We also suggest that the L2P(Y)-derived carrier phase observable, despite its ubiquitous use in past and current research, is the less accurate of the two carrier phase observables.

6.2 L2 Tracking

Tracking techniques employed by GPS receivers are mostly proprietary. This is unfortunate for the ionospheric research community as it forces the receivers to be black boxes to a certain extent. Through tracking techniques used in the past (Woo, 2000), as well as results of GPS observables compared between receiver models (Yang and Liu, 2017), appropriate conclusions about these proprietary tracking techniques can be made. For this work, we focus on the difference in the tracking techniques employed for the L2P(Y) and L2C carrier phase observables.

As was previously discussed, the L2P(Y) carrier is encrypted with an unknown code. This forces the receivers to employ techniques which can bypass the encryption and allow the necessary observables to be obtained. These techniques typically fall into the category of either codeless or semi-codeless. Both techniques rely heavily on the L1C/A signal, using it to aid in the acquisition and tracking of the L2P(Y) signal. This ensures that the tracking of the L2P(Y) signal is more resilient to high-frequency phase dynamics, loss of lock during deep signal fades and decreases the signal acquisition times (Lim et al., 2006). However, this is assuming that the high-frequency dynamics on

the L1 carrier phase are identical, or nearly so, to the L2P(Y) dynamics. This typically results in the true L2P(Y) carrier phase being smoothed and altered to better resemble the L1 dynamics, creating inaccuracies in the high-frequency dynamics of the observable. For example, in the Septentrio PolaRxS Pro receivers of the CHAIN, the L1C/A and L2P(Y) high-frequency phase dynamics are nearly identical. This can be seen in the example presented in Figure 6.1. The example is taken from the Repulse Bay station (REPC), 11 December 2016, UTC hour 0, using GPS satellite PRN 31. The station is located at geographic coordinates 66.52°N, 273.77°E. The detrended L1C/A (top panels) and L2P(Y) (middle left panel) carrier phases present very similar variations, in time and magnitude. The linear correlation between the two is performed and presented in the bottom left panel. The solid line represents the best fit, with the equation $y=1.023x (\pm 5 \times 10^{-3}) - 1 \times 10^{-6} (\pm 4.8 \times 10^{-5})$ and has a correlation coefficient of 0.967. Clearly, the correlation between the L1C/A and L2P(Y) is very strong temporally, as is shown with the very high correlation coefficient, and the magnitudes are nearly identical, as shown by the near unity slope. A similar analysis can be done with the L2C carrier phase observable, presented on the right-hand side of Figure 6.1. The detrended L2C is presented in the middle right panel, and the linear fit presented in the bottom right panel. The fit equation is $y=1.540x (\pm 5 \times 10^{-3}) - 3 \times 10^{-5} (\pm 5 \times 10^{-5})$, with a correlation coefficient of 0.985. Again, the temporal correlation is strong between the phase dynamics, however, the magnitudes of the L2C variations are much larger than those present on the L1C/A carrier. This is more like the expected behaviour for ionospheric-induced phase variations, where the magnitude of the phase variations on a signal with lower frequency magnitude should be larger. This is due to the inverse frequency-squared dependence on the ionospheric delay, see equation 4.16.

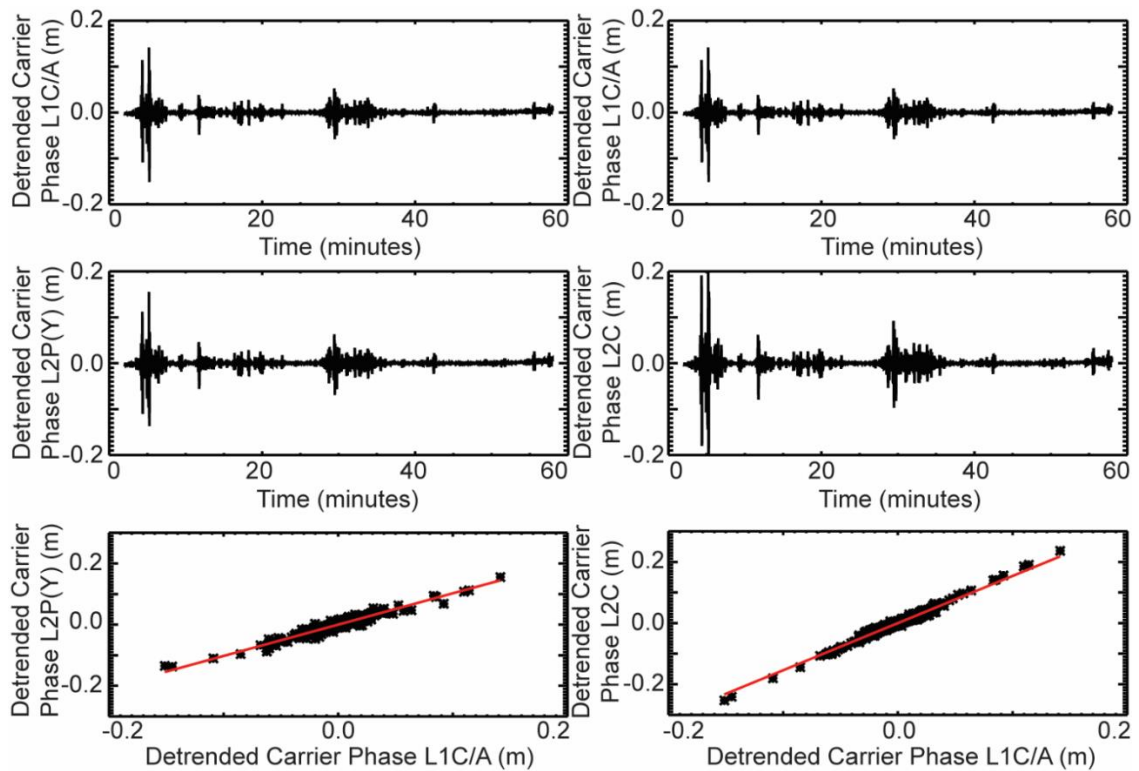


Figure 6.1 An example of the detrended L1C/A carrier phase (top), detrended L2P(Y) carrier phase (middle left), and detrended L2C carrier phase (middle right) taken from a Septentrio PolaRxS Pro receiver. The linear fit between the L1C/A-L2P(Y) carrier phase pair and the L1C/A-L2C carrier phase pair are presented in the bottom left and right panels respectively.

Although the Septentrio PolaRxS Pro clearly exhibits smoothing on the L2P(Y) phase dynamics, causing the magnitude of the variations to match well with the L1C/A dynamics, we cannot assume that other receiver models' L1-aided tracking techniques

will react the same way. We can suggest that the L1-aided tracking will likely influence the L2 carrier phase dynamics in some undesirable way.

From the example presented in Figure 6.1, the Septentrio PolaRxS Pro clearly tracks the L2C carrier differently than the L2P(Y) carrier. We have confirmed with Septentrio that the receiver tracks L2C independent of L1C/A (McCaffrey et al., 2018a). This ensures that the L2C high-frequency phase dynamics are more accurate than those observed on L2P(Y) since the L2C dynamics are recorded as they are observed and are not forced to follow the dynamics observed on the L1C/A carrier. This is possible since the L2C carrier is an open code, which can be known to the receiver, allowing for simplified tracking without the need for the codeless or semi-codeless techniques like those which are necessary for L2P(Y) tracking. However, based on the work by Lim et al. (2006) and Al-Fanek et al. (2007) it is likely that other receivers are not making use of the open L2C code and tracking L2C independent of the L1C/A carrier. This would provide tracking of L2C with the same benefits as discussed for L2P(Y) when L1-aided tracking is used. These benefits are useful for positioning measurements, where long acquisition times and loss of lock are detrimental, but these benefits are not worth the inaccuracy induced in the high-frequency phase dynamics for the ionospheric research community.

6.3 Results

Using a pair of zero-baseline receivers we can investigate the effects of the different tracking methods on the L2P(Y) and L2C carrier phase observable. We use a Septentrio PolaRxS Pro and a Trimble NetR9, each located at the Repulse Bay station of CHAIN. In comparing the carrier phase observables provided by these two receivers, we discuss the results presented in Yang and Liu (2017) and show how they can be explained by the effects of L1-aided tracking. The following results are taken from GPS satellite PRN 31 during UTC hour 0, on 11 December 2016. These results are representative of a larger sample size analyzed in preparation for the study.

We begin by comparing the L2P(Y) to the L2C carrier phase observable for each receiver. Figure 6.2 presents the detrended L2C carrier phase (top), L2P(Y) carrier phase (middle) and the difference between the carrier phases (bottom), with the Trimble examples presented in the left panels and the Septentrio examples presented on the right. The differences in the phase residuals between the Trimble-derived carrier phases is very nearly zero, suggesting the L2P(Y) and L2C carrier phase dynamics are identical. On the other hand, there are clear differences in the Septentrio-derived carrier phases, with differences of over 0.05 m present. We expect these differences for the Septentrio receiver since the tracking methods used for the L2P(Y) and L2C carrier are not the same. The identical residuals observed between the Trimble-derived carrier phases suggest that the tracking methods used for both L2P(Y) and L2C are very likely the same. Since the L2P(Y) carrier tracking is likely to be L1-aided, this implies that the L2C tracking in the Trimble receiver is likely L1-aided as well.

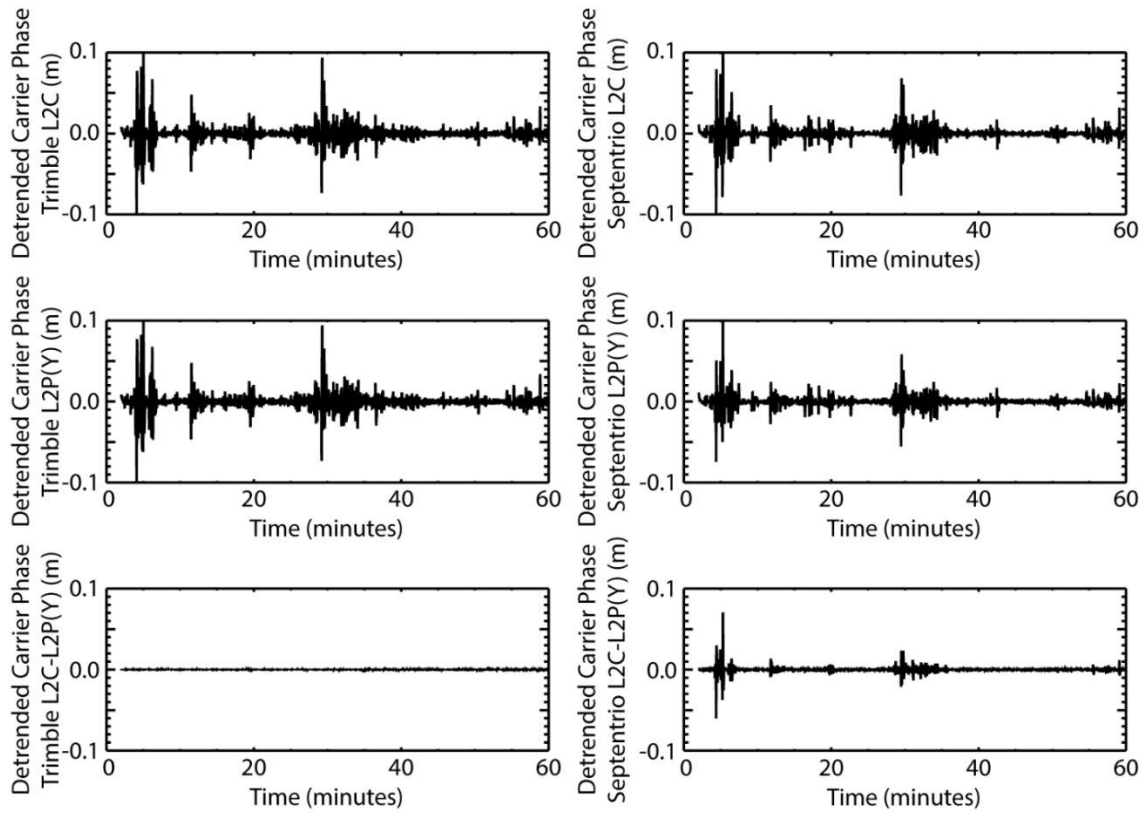


Figure 6.2 An example of the detrended L2C carrier phase (top) and the detrended L2P(Y) carrier phase (middle) for the Trimble NetR9 (left) and Septentrio PolaRxS Pro (right) receivers. The difference between the L2P(Y)-L2C carrier phase pair for each receiver are presented in the bottom panels (Trimble on the left, Septentrio on the right).

In the work presented by Yang and Liu (2017), differences in the L2P(Y) and L2C-derived ROTI were examined; receivers used in the study included a Septentrio PolaRxS Pro, Septentrio PolaRx4, Leica GR10, Trimble NetR9, and a Javad TRE-G3TH DELTA. Our results suggest that the Trimble NetR9 receivers use the same tracking techniques for L2P(Y) and L2C, which agrees with the nearly identical L2P(Y) and L2C-derived

ROTI taken from the Trimble receiver in Yang and Liu (2017) results. The Leica receiver also exhibited nearly identical L2P(Y) and L2C-derived ROTI, suggesting the Leica receiver also uses L1-aided tracking for its L2C carrier phase observable.

Both Septentrio models used in the Yang and Liu (2017) had the largest differences in the L2P(Y) and L2C-derived ROTI. This agrees with the previously presented results; since significant differences are observed between the L1-aided L2P(Y) carrier phase residuals and the independently tracked L2C carrier phase residuals, significant differences in the L2P(Y) and L2C-derived ROTI is expected.

The last receiver analyzed in the Yang and Liu (2017) study is the Javad receiver. The Javad receiver was observed to have moderate differences in the L2P(Y) and L2C-derived ROTI, larger than those observed by the Trimble receivers. We cannot conclude from this result alone whether the Javad receiver tracks L2C independently of L1. However, Yang and Liu (2017) compared the L2P(Y) and L2C-derived ROTI between the Javad receiver and with the Septentrio PolaRx4, which form a very short baseline. Therefore, the ROTI derived by these two receivers, assuming the variations have not been contaminated by the tracking techniques, should be nearly identical. Yang and Liu (2017) compared the ROTI between the receivers, by differencing the L2P(Y) and L2C-derived ROTI between the receivers in the pair. The average differences between the L2P(Y)-derived ROTI is very small, which is not surprising since both the Septentrio and the Javad receivers are expected to track L2P(Y) using an L1-aided technique.

However, significant average differences are observed between the two receivers' L2C-derived ROTI. This result alone does not wholly confirm that the Javad receiver is logging L2C using an L1-aided technique, however, it is likely. We would expect L2C-derived ROTI using independent tracking of L2C to be nearly identical for both receivers. Based on this result, we suggest the Javad receiver is using an L1-aided tracking technique to track the L2C carrier, however, the effects of the Javad receiver's tracking technique on the magnitude of the L2C dynamics are less than those seen on the Trimble and Leica receivers.

Differences in the L2P(Y) and L2C carrier phase dynamics have been clearly shown here, and strongly suggested by the work presented by Yang and Liu (2017). We now attempt to show that the accuracy of the independently tracked L2C carrier phase residuals is better than its L1-aided counterpart. This will be shown in two ways, first by analyzing the L2P(Y) and L2C-derived Ionosphere Free Linear Combination (IFLC), and second, by examining the effects of phase wind-up on the L2P(Y) and L2C carriers.

Work by Carrano et al. (2013) has shown that the high-frequency carrier phase variations, when not accompanied by significant fades in the signal intensity, will likely be refractive in nature. Therefore, these variations will be removed in the IFLC; the IFLC exploits the deterministic nature of the refractive effects of the ionosphere on the phase of the signal and the dispersive nature of the ionosphere. Ignoring the higher-order

effects of the refractive index, a linear combination can be defined which removes the refractive components from the carrier phase observable:

$$\Phi_{IFLC} = \frac{\Phi_1 f_1^2 - \Phi_2 f_2^2}{f_1^2 - f_2^2} \quad (6.3)$$

where Φ is the carrier phase observable on a given carrier, and f is the frequency of a given carrier, with 1 and 2 representing the two carriers L1 and L2. Equation 6.3 assumes the variations in the carrier phase is accurate, any inaccuracy in the variations will cause the refractive variations to not be removed in the IFLC since they will not properly follow the expected inverse-frequency-squared relationship. Using the techniques employed in Carrano et al. (2013) we will use the detrended carrier phase to better examine the high-frequency dynamics of the signals. By calculating the IFLC using both the L2P(Y) and L2C carrier phase separately, and examining how well the refractive variations are removed, we can determine the relative accuracy of each of the L2 carrier phase dynamics.

As we mentioned, Carrano et al. (2013) showed that large variations in the IFLC are present when significant fades in the signal intensity are also present. In Figure 6.3 we present an example of the IFLCs derived using both the L2P(Y) and L2C carrier phase separately, for the zero-baseline Septentrio and Trimble receivers discussed earlier. The top plot shows the detrended signal strength for the Septentrio L2C carrier. Clearly,

there are no significant fades in the signal strength, so significant variations in the IFLC are not expected. In the L2P(Y)-derived IFLCs, shown in the middle panels (the Trimble receiver example on the left, the Septentrio receiver example on the right) we observe significant variations in the IFLC from both receivers. Very similar variations are observed in the L2C-derived IFLC from the Trimble receiver (bottom left). Since the L2P(Y) (and Trimble L2C) carriers are tracked using L1-aided tracking, which we expect to decrease the L2P(Y) dynamics' accuracy, this is not surprising. For the Septentrio L2C-derived IFLC (bottom right), in which we know the L2C carrier to be tracked independently, the variations in the IFLC are minimal compared to those observed in the other IFLCs. In fact, some portions of the variations observed in the other IFLCs are removed nearly completely. This strongly indicates that the independently tracked L2C carrier phase dynamics are more accurate than both the L2P(Y) and L2C carrier which are tracked using L1-aided tracking techniques. We again note that these results are representative of a large sample size which was analyzed for this study.

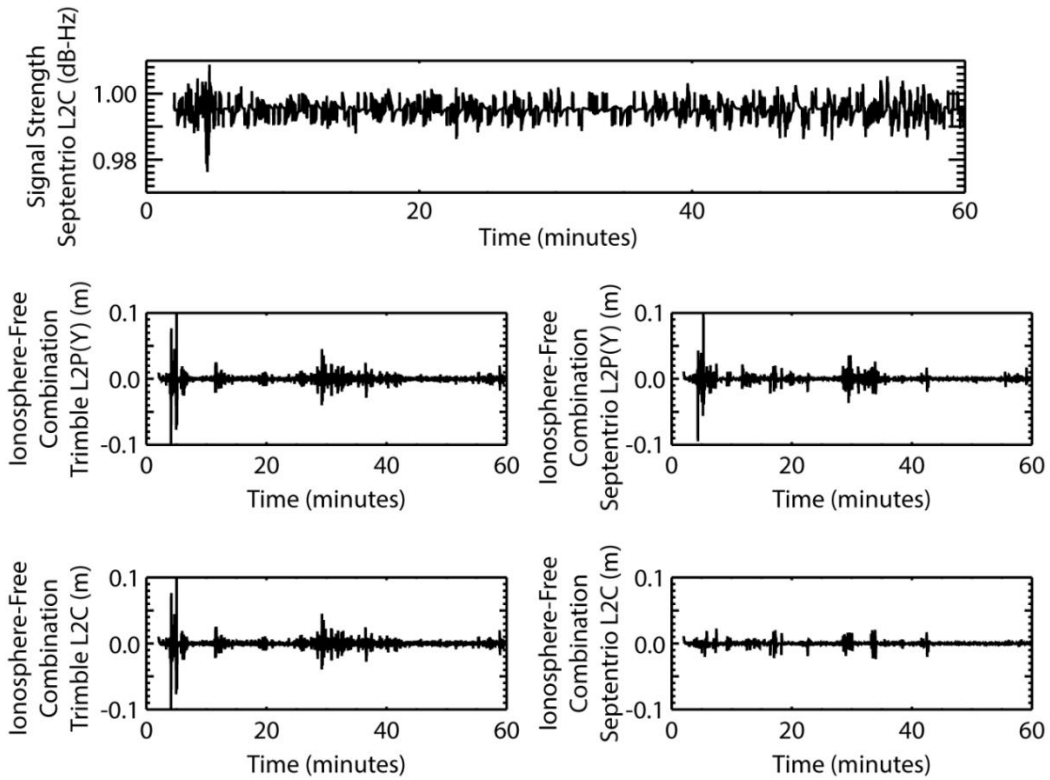


Figure 6.3 The detrended signal intensity for the L2C carrier from the Septentrio receiver is presented in the top panel. The L2P(Y)-derived IFLC (middle) and the L2C-derived IFLC (bottom) are presented for each receiver (Trimble on the left, Septentrio on the right).

By exploiting the effects of phase wind-up on the antenna, we can further show the effects of L1-aided tracking on the accuracy of the L2 carrier phase observable. By quickly rotating the antenna connected to the GPS receiver about its vertical axis, wind-up in the phase can be induced. This wind-up will manifest itself as a divergence between the L1 and L2 carrier phase observable (Kim et al., 2006). At the receiver, a quick rotation of the antenna is comparable to the phase scintillation induced by the ionosphere. A full 360° rotation of the antenna will induce a change in the carrier phase

equal to a full wavelength; 19.0 cm for the L1 carrier and 24.4 cm for the L2 carrier. Taking the difference of the L1 and L2 carrier phase during the full rotation of the antenna should result in a $24.4 \text{ cm} - 19.0 \text{ cm} = 5.4 \text{ cm}$ change.

A Septentrio PolaRx5S and a Trimble BD982 receiver were connected to a single geodetic antenna, mounted on a tripod, which allowed for the antenna to be manually rotated on its vertical axis. The L1C/A, L2P(Y), and L2C carrier phase observables were tracked for both receivers during this rotation. Figure 6.4 shows the L2P(Y)-L1C/A and L2C-L1C/A combination from both receivers. The rotation of the antenna was performed over only a fraction of a second. Note that in the figure the combinations were artificially set to zero for an easier interpretation of the results. The Septentrio L2C-L1C/A combination accurately displays the effects of the antenna rotation. The combination increases, within the fraction of a second taken to rotate the antenna, to the expected 5.4 cm value. This is expected for the independently tracked L2C carrier phase observable. Alternatively, the L2P(Y) combination for the Septentrio receiver takes nearly 8 seconds to converge to the expected 5.4 cm value. This clearly shows the smoothing effect of the L1-aided tracking technique (McCaffrey et al., 2018a).

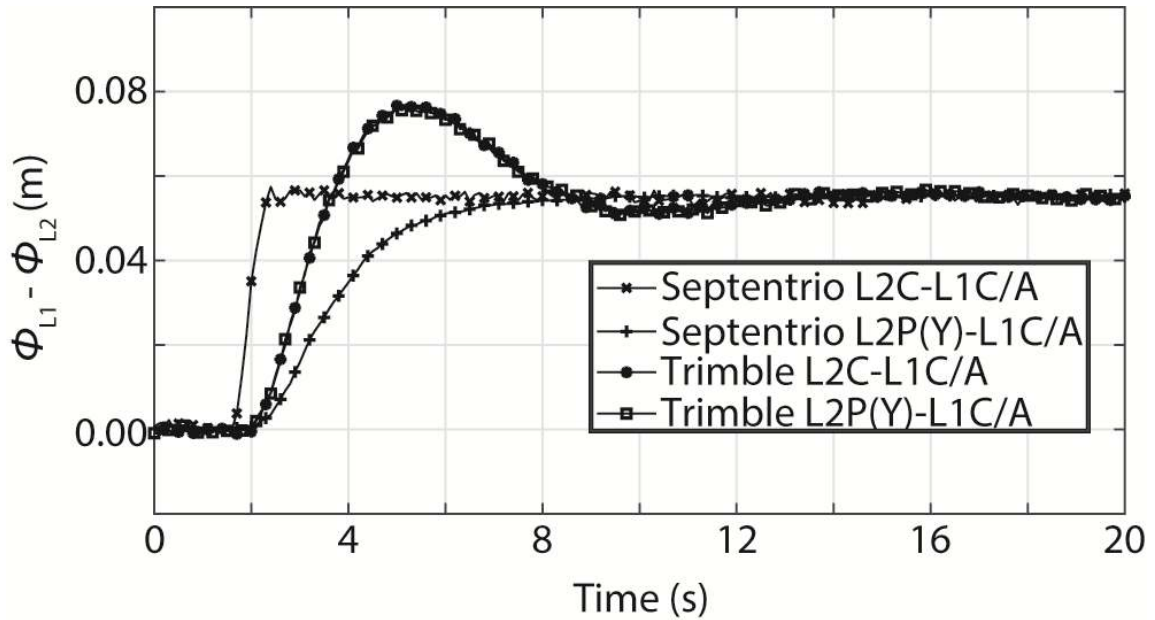


Figure 6.4 The L2C-L1C/A and L2P(Y)-L1C/A combination of the carrier phase observables for the Trimble and the Septentrio receivers, where a full-turn rotation of the antenna occurs about 2 seconds into the time series'. This is the effect of phase wind-up incurred by the antenna rotation.

For the Trimble combinations, both take nearly 10 seconds to converge to the expected value and with no significant difference between the L2P(Y) or an L2C-derived combination. This result further confirms that the Trimble receiver is using L1-aided tracking techniques to track the L2C carrier and shows the effects these techniques have on the carrier phase observable (McCaffrey et al., 2018a).

We note as well the significant difference in the effects of the Septentrio and Trimble tracking. The Trimble tracking technique reacts quicker to the abrupt change in phase

but overestimates the true change, followed by a ringing effect. On the other hand, the Septentrio technique is slower to react to the abrupt phase change, but is more accurate in the magnitude and settles to the true value slightly quicker. We stress that this result suggests that when large abrupt changes in phase occur in the carrier phase of the signal, such as those induced by ionospheric effects, the L1-aided observables tell us more about the receiver than the actual ionospheric phenomenon.

6.4 Conclusion

L1-aided tracking techniques are beneficial to the intended use of navigation and positioning with GPS receivers. However, when using GPS receivers for ionospheric research we have shown that the use of L1-aided tracking techniques reduces the accuracy desired for many ionospheric research techniques. This refers specifically to areas of research where the high-frequency dynamics of the GPS carrier phase observable is required, such as scintillation research, ROT/ROTI analysis, and studies of TEC dynamics. The L1-aided tracking techniques have been shown to smooth the magnitude of the L2 carrier phase dynamics, making them more like the L1 dynamics. In these research areas, the difference between the L1 and L2 carrier phase dynamics is an important factor, which can lead to insights into the formation and morphology of the irregularities being studied. Thus, accuracy in the magnitudes of both carrier phase dynamics is important.

Although many previous works were limited to the L2P(Y) carrier and produced important results using the L1-aided observable, it does not mean it is the most accurate option. With the L2C carrier becoming more prominent and transmitting on more than half of the GPS satellites, it is important that the ionospheric research community moves towards using the L2C carrier phase observable, in conjunction with receivers using L2 independent tracking techniques, in the areas of research which depend heavily on the L2 carrier phase. At the very least, future works must be mindful of their use of the L2 carrier phase observable, making note of which tracking methods are being used with the receivers they have access to, and making that information clear in any conclusions derived from the results. This is very important in products such as the proposed global ROTI maps, which will be provided by IGS (Krankowski et al., 2017). These maps will provide global ROTI indices, like the global TEC maps currently provided, using ROTI data derived from the receivers in the IGS network. As was shown in Yang and Liu (2017) the magnitudes of the ROTI will differ between receivers, since each receiver's L1-aided tracking will likely affect the L2 carrier phase observable differently. This will lead to significant errors in the accuracy of the ROTI maps. Also, if independently tracked L2C carrier phase is used for the receivers in the network that it is available, artificial enhancements in the ROTI maps may be created at these receiver locations.

7 Refractive Phase Variations

7.1 Introduction

The electron density dependence in the refractive index of the ionosphere can have significant impacts on trans-ionospheric signals. The ionosphere is rarely homogeneous, with small and large-scale irregularities in the density existing both spatially and temporally. Both scale size regimes will lead to purely refractive variations in the signal; irregularities of small enough spatial scales can lead to diffractive variations or scintillations, as well. The diffractive effects exhibit themselves as rapid variations in the amplitude and phase as observed by stationary ground-based receivers. The study of these rapid variations is of ongoing interest in the field of ionospheric research and monitoring and has been for decades. The study of these variations has proven vital in helping understand the formation, and morphology of these small-scale irregularities. Relating the signal's features as observed on the ground to the ionospheric phenomenon responsible for the variations has shown to be very useful, with early works by Gruber (1961) and Jespersen and Kamas (1964), and more recent works including Cervera and Thomas (2006), Béniguel et al. (2009), Akala et al. (2012), Paznukhov et al., (2012), and Mezaoui et al. (2014) as examples. These works have shown that many important characteristics of the small-scale irregularities can be deduced from the diffractive variations in the signal's amplitude and phase time series.

In practical applications, such as space-based navigation systems like GPS, the effects of scintillation are detrimental to their intended use. Rapid variations in the amplitude and/or phase of the GPS signal can lead to ranging and positioning errors, and in the most extreme cases lead to loss of lock of the signal entirely (Carrano et al., 2005; Seo et al., 2009; Akala et al., 2012). For these types of applications, it is important that our understanding of the effects of the ionosphere on these signals is as robust as possible, as changes and developments in our understanding may lead to advances and mitigation techniques for practical applications.

The refractive effects of the ionosphere are better understood. The refractive index has a clear relationship with the frequency of the wave and the electron density along the ray path (Papas, 1965). These refractive changes to the signal are typically considered to be of low frequency, caused by large-scale irregularities in the ionosphere. Since these refractive variations are assumed to be of low frequency, they are typically ignored in the discussion of scintillation; this is more common in the modern publications (Mitchell et al., 2005; Jiao et al., 2013; Mushini, 2012; McCaffrey and Jayachandran, 2017a).

Most scintillation works detrend the raw GPS signal using a 0.1 Hz cut-off. The assumption is that only diffractive variations will occur above 0.1 Hz, thus the refractive variations are not present. More accurately, it is assumed that the Fresnel frequency for the events will be very near 0.1 Hz. This cut-off originates with the large body of work performed in the mid to low latitude ionosphere, where the assumption may be more accurate (Fremouw et al., 1978; Forte and Radicella, 2002). However, in the high

latitudes, drift speeds are much larger and will contribute to larger Fresnel frequencies, which may cause the assumption to fail (Forte and Radicella, 2002).

We propose that rapid variations in the GPS carrier phase at frequencies greater than 0.1 Hz can be predominantly refractive. This is more likely an issue in the high latitudes due to the increased drift speeds, therefore, the presented results will focus on this region. We suggest that these rapid refractive variations are being misclassified as diffractive scintillation. We present some examples of these refractive variations and outline the methods used to demonstrate their refractive nature.

7.2 Methods

Two methods will be used in determining refractive variations in the detrended carrier phase examples. The first is a modification on the IFLC. The IFLC is commonly used in positioning techniques (see for example Zumberge et al., 1997), which exploits the frequency dependence of the ionosphere and the closeness of the GPS carrier frequencies. Recalling the refractive effects of the ionosphere on the carrier phase observable, as outlined in equation 4.16, if the frequency dependence is removed, then the effect should be nearly identical between the carriers. Thus, a linear combination of two carriers can be created which removes the refractive effects of the ionosphere. This is the basis of the IFLC, as was previously outlined in equation 6.3.

In the positioning techniques, the entire carrier phase observable would be used, leaving the ranging terms in the IFLC. For our purposes, we detrend the carrier phase before applying the IFLC, removing the constant and low-frequency terms (Carrano et al., 2013). In Equation 5.7 the carrier phase observable after detrending was outlined, showing that only the ionospheric term and the noise term is left. Thus, in using the detrended carrier phases in the calculation of the IFLC, only the diffractive contribution to the ionospheric term and noise will be left; recalling that the ionospheric term can be split into the refractive and diffraction contributions.

The second method of determining the refractive variations in the carrier phase observable starts with the same assumptions as the IFLC but provides a more quantitative approach. Again, recalling the refractive contribution to the carrier phase observable, as outlined in equation 4.16, and assuming the integral electron density for both the L1 and L2 carrier phase are identical, we can perform the following ratio of the L1 and L2 carrier phases:

$$\frac{\Phi_{L2}}{\Phi_{L1}} = \frac{\frac{-40.3}{f_{L2}^2} \int_r^s N_e dl}{\frac{-40.3}{f_{L1}^2} \int_r^s N_e dl} = \frac{f_{L1}^2}{f_{L2}^2} \approx 1.64 \quad 7.1$$

This also assumes that the diffractive variations are either negligible or removed, leaving only the refractive variations. Therefore, we will attempt to remove the diffractive

contribution to the carrier phase observable and use this method to test the remaining variations.

7.3 Results and discussion

7.3.1 Determining Refractive Variations

We focus on two representative phase variation event examples. Both events are taken from the Churchill CHAIN station. The first event is from DOY 186, during hour 0 UTC, using GPS satellite PRN 12; the second from DOY 218, during hour 11 UTC, using GPS satellite PRN 26, both during the year 2015. We present the detrended L1C/A and L2C carrier phase for both events in Figure 7.1 and Figure 7.2, Figure 7.1 presents the DOY 186 example, and Figure 7.2 presents the DOY 218 example. For both figures, the top left panel shows the detrended L1C/A carrier phase for the hour of interest and the middle left panel shows the detrended L2C carrier phase for the same hour. In both examples, we observe significant variations in the carrier phase, with a red horizontal line indicating the chosen event. In the DOY 218 example, there are clearly multiple events which could have been chosen, the event of interest was chosen from the others because it has the highest magnitude variations. The two examples presented here are representative of a large set of examples which have been analyzed.

As discussed, the IFLC can be used to create a time series which should be free of refractive variations present in the carrier phase observables. The IFLC for both events

is presented in their respective bottom left panel. In both examples, we observe that most of the variations observed during the event have been eliminated, suggesting that these variations are dominantly refractive. We compare the spectra for these events, to better observe the variations which have been removed using the IFLC. For both examples, the spectrum for each data set, L1C/A phase, L2C phase, and the IFLC, are presented in the right panels, next to the time series. The red lines in the time series which represents the event of interest also represent the time window used for the FFT calculation. The L1C/A and L2C spectra for both examples present the expected power law behaviour for ionospheric-induced variations (refractive and/or diffractive). The IFLC spectra show a nearly flat spectrum for the lower frequencies, then breaking to the expected power law behaviour. The flat portion of the IFLC spectrum is a considerable difference compared to the L1C/A and L2C spectra. This suggests that most of the low frequencies have been removed by using the IFLC, specifically those less than approximately 2-3 Hz.

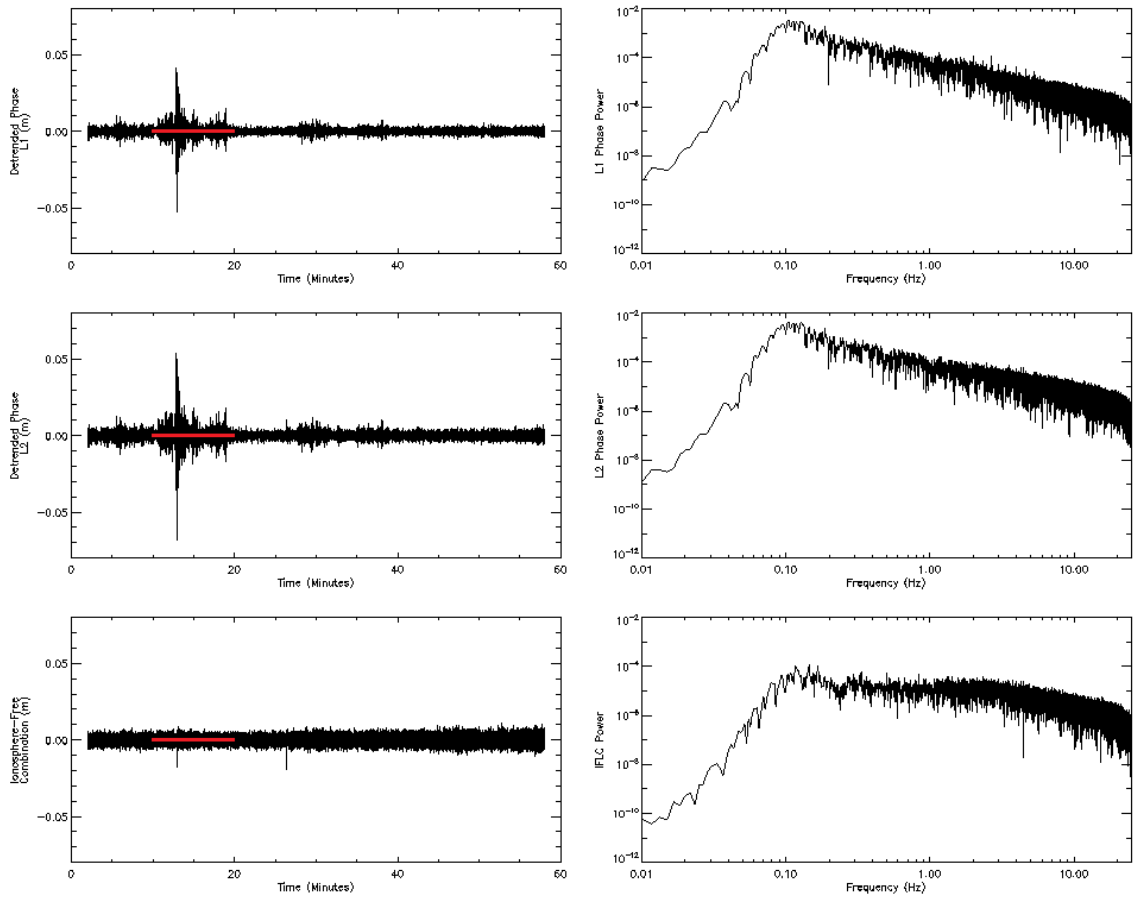


Figure 7.1 Example carrier phase variation events during DOY 186, 2015. The detrended L1 carrier phase (top left), L2 carrier phase (middle left), and the corresponding IFLC (bottom left) are presented. The red lines indicate the event of interest, as well as the time window used in calculating the corresponding spectra (panels to the right of the respective datasets).

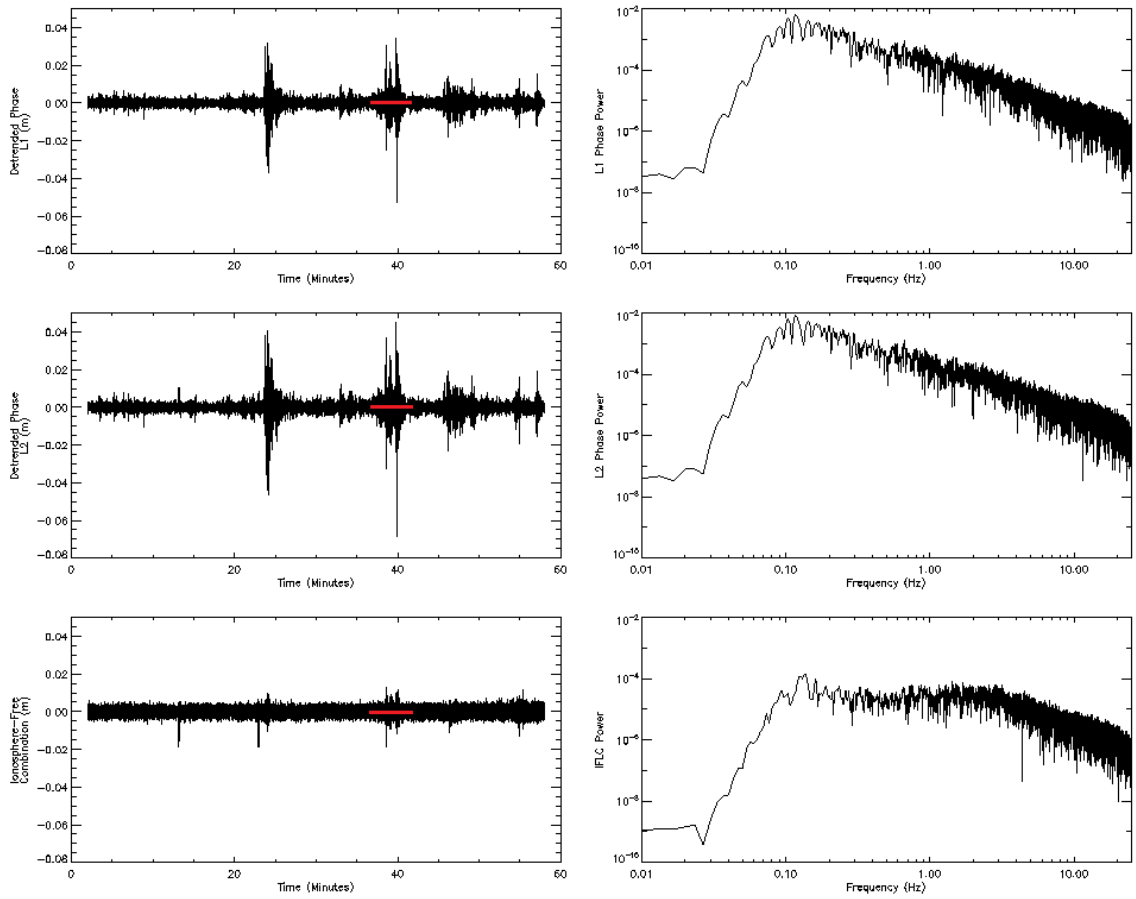


Figure 7.2 Example carrier phase variations event during DOY 218, 2015. The detrended L1 carrier phase (top left), L2 carrier phase (middle left), and the corresponding IFLC (bottom left) are presented. The red lines indicate the event of interest, as well as the time window used in calculating the corresponding spectra (panels to the right of the respective datasets).

To compare these spectra more appropriately, the L1C/A carrier phase spectrum, the L2C carrier phase spectrum, and the IFLC spectrum are presented together, for each example, in Figure 7.3 and Figure 7.4, with Figure 7.3 representing the DOY 186 example and Figure 7.4 representing the DOY 218 example. The L1C/A spectrum is

presented in black, the L2C spectrum in blue, and the IFLC in red. It is very clear in these figures that the IFLC disagrees with the L1C/A and L2C spectra in the low frequencies. For the DOY 186 example, it appears to disagree from 0.1 Hz (the detrending cut-off frequency) to approximately 2 Hz, and 0.1 Hz to approximately 3 Hz for the DOY 218 example. This would suggest that the refractive variations are contained within those respective ranges, and any variations above the 2 Hz or 3 Hz are non-refractive, likely either diffractive variations or noise. However, we must discuss the main assumption used in the IFLC technique.

As is described in the IFLC derivation in Chapter 6, the IFLC assumes all variations which follow the inverse-frequency-squared relationship are refractive, however, this may not be the case. Since the diffractive variations on the carrier phase observable are expected to be stochastic it is possible for some of these effects to follow this relationship. Another possibility that must be considered is that, as we saw in Chapter 4, the diffractive variations will be at higher frequencies than the purely refractive, and due to the expected power law behaviour of these variations, the diffractive variations will inherently have much lower magnitudes. In creating the IFLC, which is a linear combination of the L1C/A and L2C carrier phase observables, we create a data set with a larger noise floor than either the L1C/A or L2C separately. Therefore, it is possible that some diffractive variations are lost in the IFLC noise which would otherwise be visible in the L1C/A or L2C carrier phase alone. With these ideas in mind, we mustn't assume that all the variations removed by the IFLC are refractive in nature and that the

0.1 to 2 or 3 Hz range is purely refractive. However, we can say that it is very likely that purely refractive variations are contained within those frequency ranges.

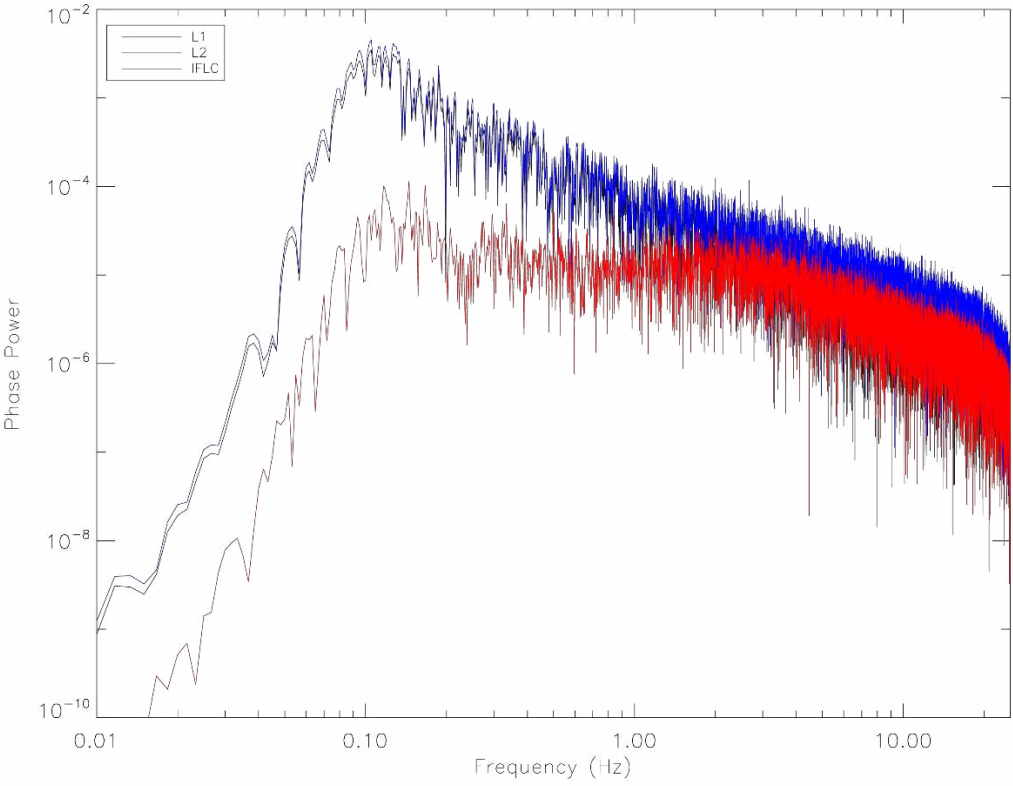


Figure 7.3 The three spectra presented in Figure 7.1. The L1 spectrum is presented in black, L2 in blue, and the IFLC spectrum in red.

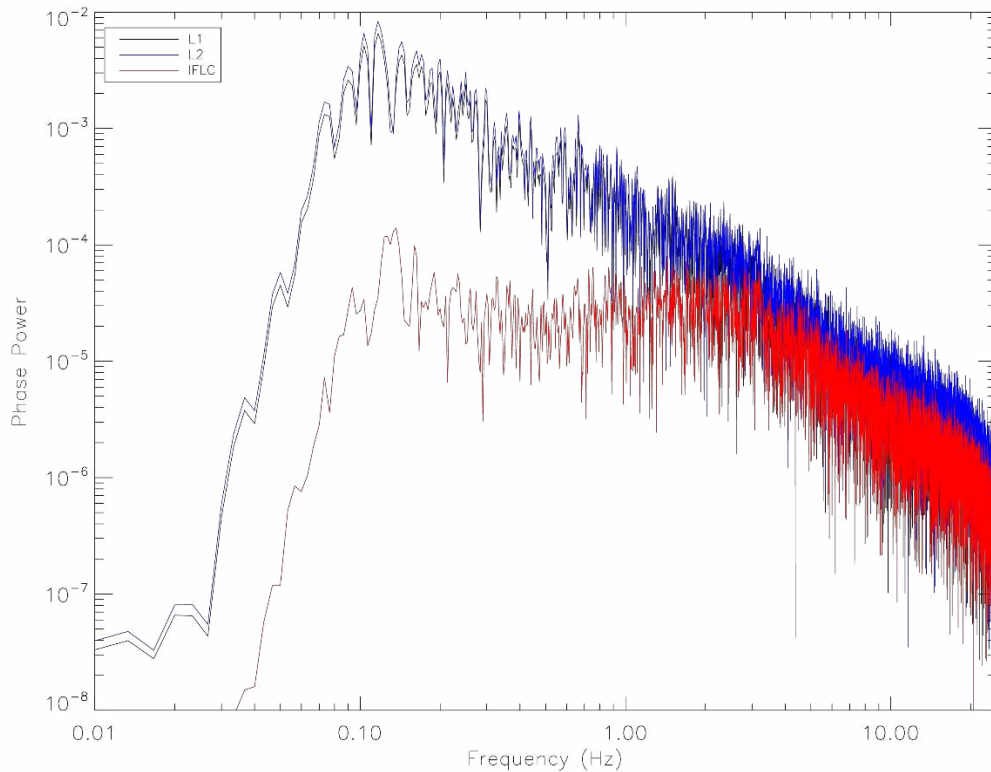


Figure 7.4 The three spectra presented in Figure 7.2. The L1 spectrum is presented in black, L2 in blue, and the IFLC spectrum in red.

Recalling the discussion in Chapter 4, we expect fluctuations in the amplitude of the signal associated with diffractive effects, but not for refractive. Assuming diffractive amplitude variations are present above the noise floor, we can determine a cut off frequency at which the diffractive variations should begin. We examine the amplitude corresponding to the presented phase examples. The detrended amplitudes are presented in Figure 7.5 and Figure 7.6 for the DOY 186 example and in Figure 7.7 and Figure 7.8 for the DOY 218 example. The top panels of the figures Figure 7.5 present the detrended

amplitude corresponding to the same hours presented earlier. There are clear, significant, amplitude variations during the phase variations events we have been examining. This means there are diffractive variations associated with these events, and we can use the amplitude variations to define the cut off frequencies using the spectra. The bottom panel of each figure presents the respective amplitude spectrum. Note that the red line in the detrended amplitude plots represents the time interval used for the spectrum calculation. Recall that we expect a zero-slope spectrum for the amplitude up to the cut off frequency, followed by the expected power law behaviour associated with scintillation. We also expect a flat spectrum in the high frequencies, associated with the white noise floor. We use these assumptions to determine the cut off frequency for the spectra.

Linear fits are performed in the low frequencies, using windows beginning at 0.1 Hz (the detrending cut-off frequency) and increasing in increments of 0.01 Hz. The slopes of these linear fits are examined; the fit with the slope nearest zero is taken and the frequency range over which the fit was calculated is recorded. The highest frequency included in the fit is taken as the “preliminary cut off frequency”, which is used later in the calculation. This fit is represented by the solid blue line in the bottom panels of Figure 7.5 through Figure 7.8. A similar method is performed in the high-frequency noise, where a window ending at 15 Hz is used, with the start of the window decreasing in frequency in increments of 0.01 Hz. The fit with the slope nearest zero is again taken, with the lowest frequency for over which the linear fit is performed is taken as the “preliminary noise floor frequency”. We choose 15 Hz because it should be well into the

noise for most scintillation events (McCaffrey and Jayachandran, 2017a) but before any roll-off associated with the bandpass filtering used for these events. This fit is represented by the solid red line in the bottom panels of Figure 7.5 through Figure 7.8.

To fit the scintillation portion of the spectrum, the power associated with the so-called “preliminary cut off frequency” and the “preliminary noise floor frequency” is obtained. The geometric mean of these two power values is calculated, and the corresponding frequency is then taken as approximately equal to the centre of the scintillation portion of the spectrum. Linear fits are performed in windows centred on this mean frequency, increasing in intervals of 0.01 Hz (0.005 Hz to either side). The fit with the highest correlation coefficient is taken as the fit to the scintillation spectrum. The solid green line represents these fits in the bottom panels of Figure 7.5 through Figure 7.8.

After obtaining the low frequency, high frequency, and scintillation spectral fits, the intersection points between each are calculated. These intersection points give the cut off and noise floor frequencies for the spectrum. In the bottom panels of Figure 7.5 through Figure 7.8 the dashed green lines show the intersection points between these fits, corresponding to the cut off and noise floor frequencies.

For the DOY 186 example, cut off frequencies of 1.00 Hz (L1 carrier) and 0.78 Hz (L2 carrier), and noise floor frequencies of 4.59 Hz (L1 carrier) and 3.71 Hz (L2 carrier) are obtained. For the DOY 218 example, cut off frequencies of 1.49 Hz (L1 carrier) and

1.23 Hz (L2 carrier), and noise floor frequencies of 6.83 Hz (L1 carrier) and 6.49 Hz (L2 carrier) are found. Therefore, for the L1 carrier, diffractive variations should be greater than 1.00 Hz and 1.49 Hz for the respective examples. Recalling the earlier IFLC analysis, it appeared that variations were removed using the IFLC, upwards of 2 Hz to 3 Hz. This would suggest dominantly refractive variations lower than those frequencies. However, the cut off frequencies is much lower than those initial estimates, suggesting the IFLC did, in fact, remove variations from the carrier phase observable which were not purely refractive.

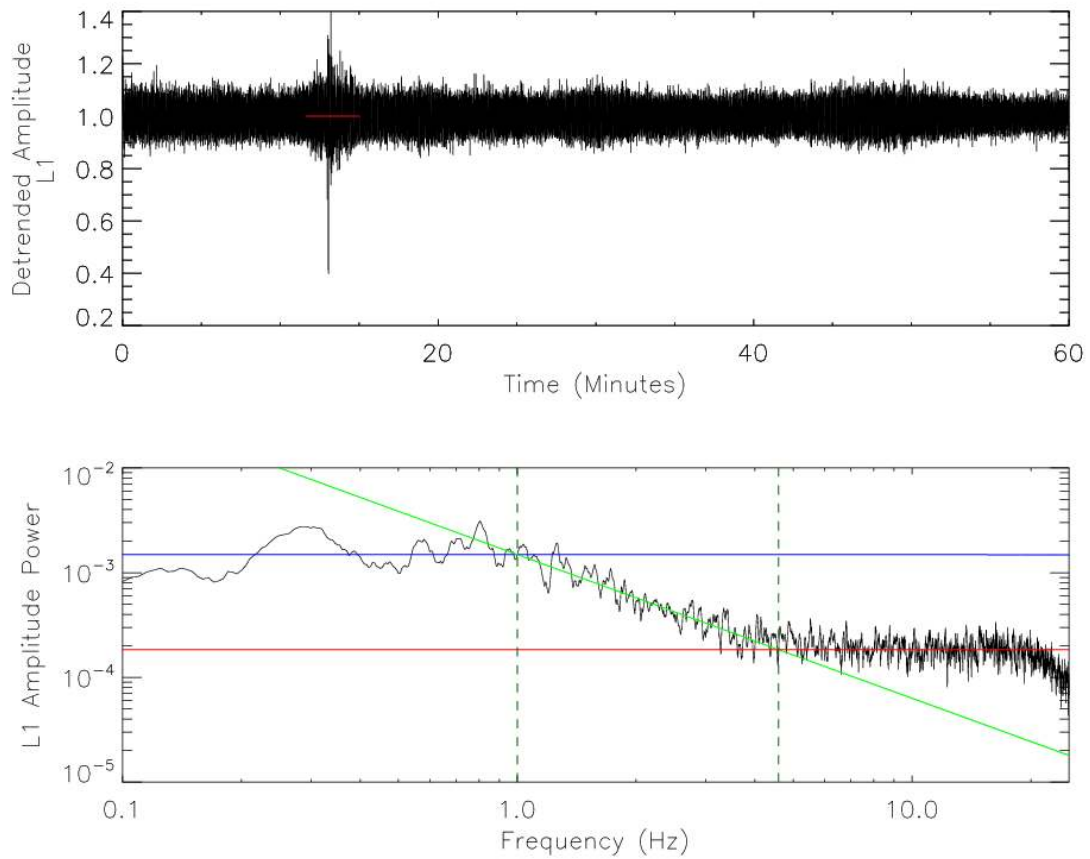


Figure 7.5 L1 amplitude variations for the DOY 186 example. The detrended amplitude is presented in the top panel, with the spectrum, taken over the time interval indicated with the red line, presented in the bottom panel. The fits obtained for the low frequencies, the scintillation frequencies, and the high-frequency noise, are represented by the blue, green, and red lines respectively. The intersection points are indicated by the dashed green lines.

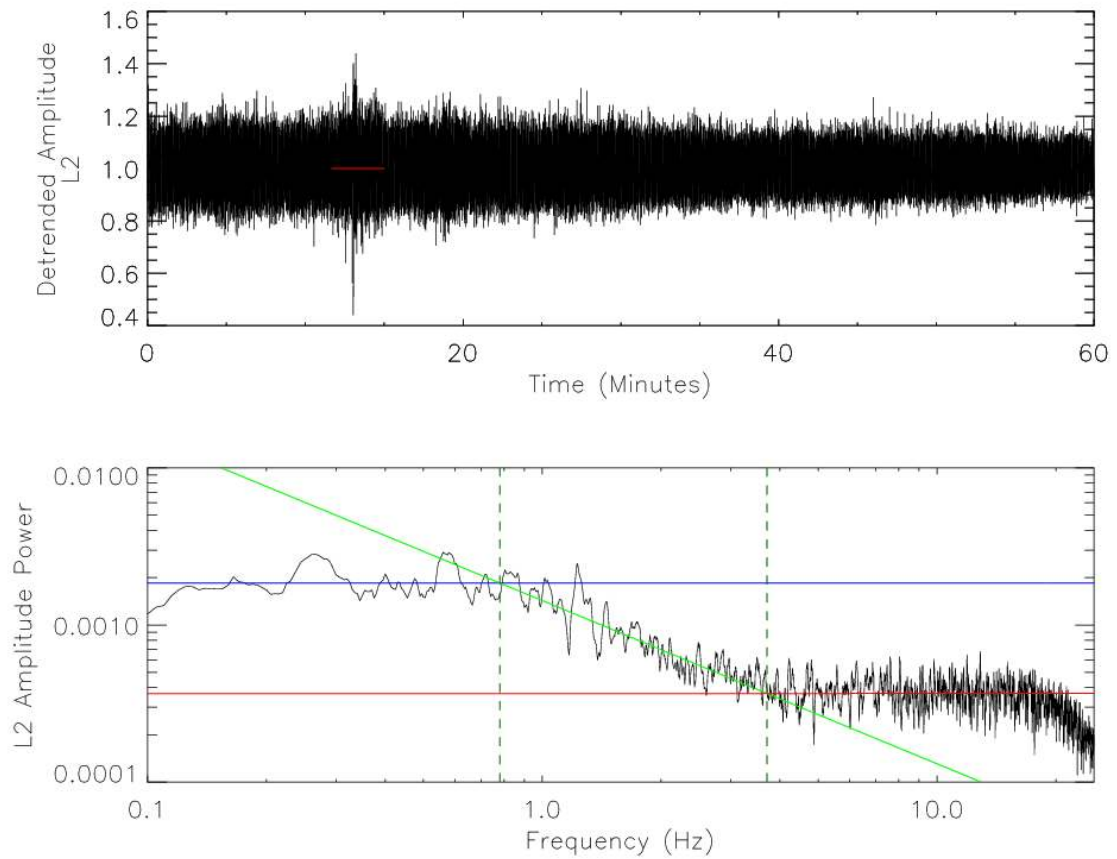


Figure 7.6 L2 amplitude variations for the DOY 186 example. The detrended amplitude is presented in the top panel, with the spectrum, taken over the time interval indicated with the red line, presented in the bottom panel. The fits obtained for the low frequencies, the scintillation frequencies, and the high-frequency noise, are represented by the blue, green, and red lines respectively. The intersection points are indicated by the dashed green lines.

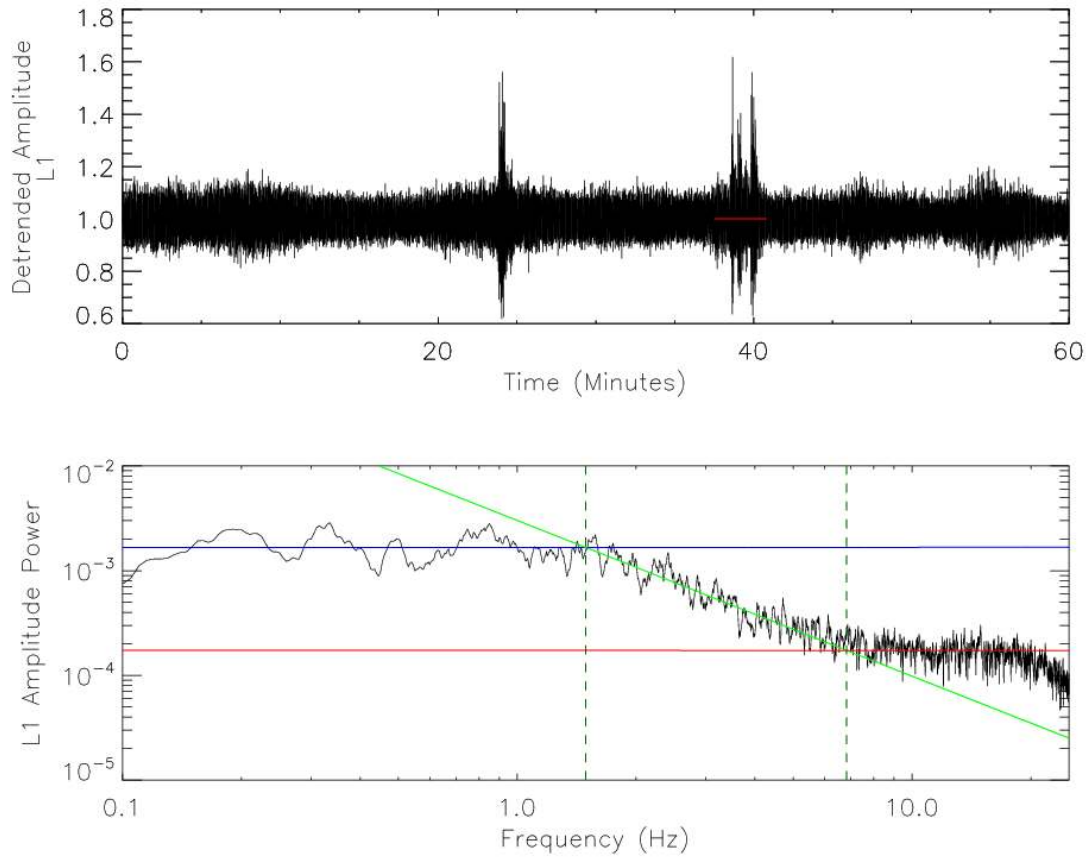


Figure 7.7 L1 amplitude variations for the DOY 218 example. The detrended amplitude is presented in the top panel, with the spectrum, taken over the time interval indicated with the red line, presented in the bottom panel. The fits obtained for the low frequencies, the scintillation frequencies, and the high-frequency noise, are represented by the blue, green, and red lines respectively. The intersection points are indicated by the dashed green lines.

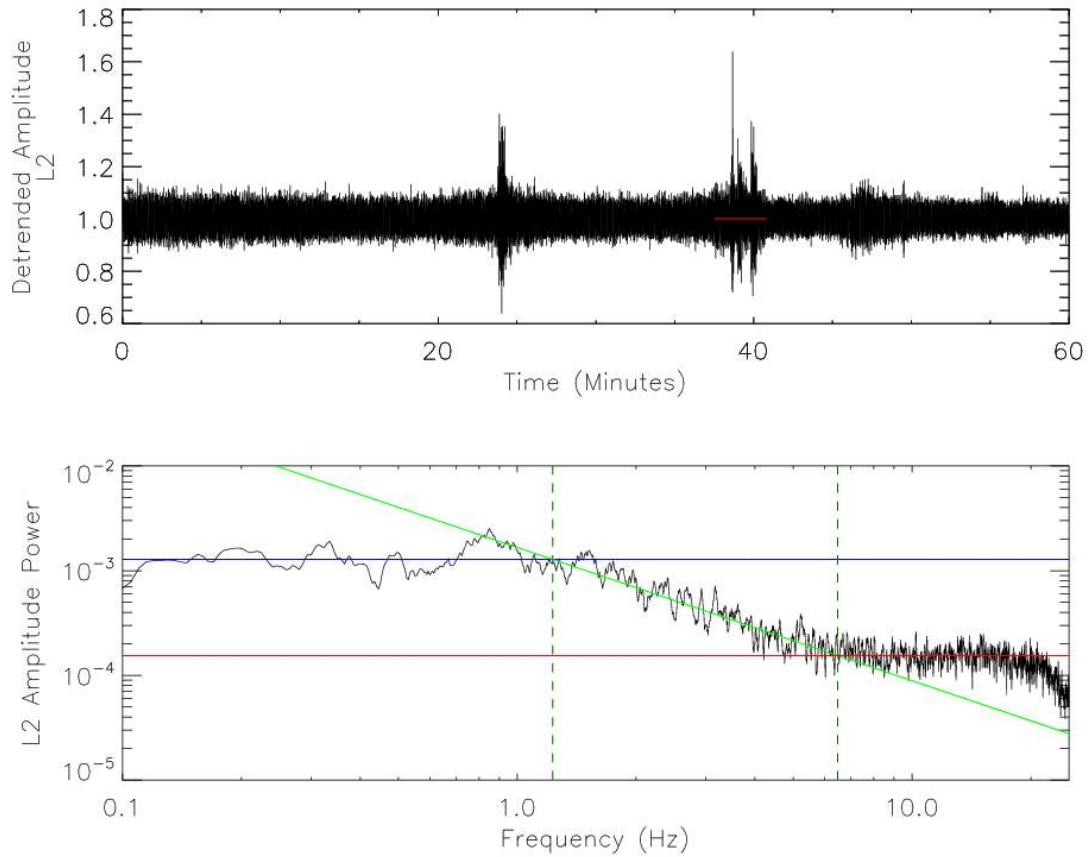


Figure 7.8 L2 amplitude variations for the DOY 218 example. The detrended amplitude is presented in the top panel, with the spectrum, taken over the time interval indicated with the red line, presented in the bottom panel. The fits obtained for the low frequencies, the scintillation frequencies, and the high-frequency noise, are represented by the blue, green, and red lines respectively. The intersection points are indicated by the dashed green lines.

The noise floor frequencies obtained from the amplitude spectra are expected to be lower in frequency (greater in power) than the noise floor we would observe in the carrier phase (McCaffrey and Jayachandran, 2017a). Since we are only concerned with

capturing the refractive variations in their entirety, and not worried about accurately separating the diffractive variations from the noise floor, we will use the noise floor frequencies from the amplitude for use in the carrier phase analysis. With that, we now have three frequency windows to separate the variations types in the carrier phase. The first window is from the detrending frequency (0.1 Hz) to the cut off frequency; this is the purely refractive variations. From the cut off frequency to the noise floor frequency is the diffractive variations. Lastly, from the noise floor frequency to the high-frequency bandpass cut-off is mostly noise. These frequencies are summarized for the L1 and L2 carriers for both examples in Table 7.1.

Table 7.1 The cut off and noise floor frequencies obtained for both the L1 and L2 carriers for the two presented examples.

DOY 186	Cut Off Frequency	Noise Floor Frequency
L1 Carrier	1.00 Hz	4.59 Hz
L2 Carrier	0.78 Hz	3.71 Hz
DOY 218		
L1 Carrier	1.49 Hz	6.83 Hz
L2 Carrier	1.23 Hz	6.48 Hz

Using these frequency windows, we can bandpass filter the carrier phase observables to within these frequencies to examine the suspected refractive, diffractive, and noise

variations separately. This is done to further confirm that the variations within these given frequencies have characteristics we would expect. To begin, we qualitatively compare the three frequency windows. Figure 7.9 and Figure 7.10 presents a sample of the variations associated with each frequency window. Samples from the DOY 186 example are presented in Figure 7.9, and samples from the DOY 218 example in Figure 7.10. The first minute of the event, bandpass filtered to show the refractive variations, is presented in the top panel of each example figure. For both examples, we observe the L1 carrier phase variations, represented by the black lines, appear to correlate very well in time with the L2 carrier phase variations, represented by the blue lines. This is what we expect for purely refractive variations; since the L1 and L2 carrier are expected to follow very nearly the same path through the ionosphere, they should encounter the same changes in electron density and thus refractive index. Due to the inverse frequency-squared dependence in the refractive index, the L2 carrier phase variations should be greater in magnitude than the L1 variations for refractive variations; this is what we observe in both examples.

The middle panels present the suspected diffractive variations for the first ten seconds of the example events. We observe that, for much of the example, the L1 and L2 carrier phase variations do not agree well in time. This is as expected for diffractive variations due to their stochastic nature. Lastly, the bottom panel presents the expected high-frequency noise, also for the first ten seconds of the events. A lack of correlation in time is also observed for both examples but appears much more pronounced in the high-frequency noise when compared to the diffractive variations. For the high-frequency

phase noise induced by the receiver, we do not expect a correlation between the L1 and L2 carrier. This is shown in more detail in Chapter 8.

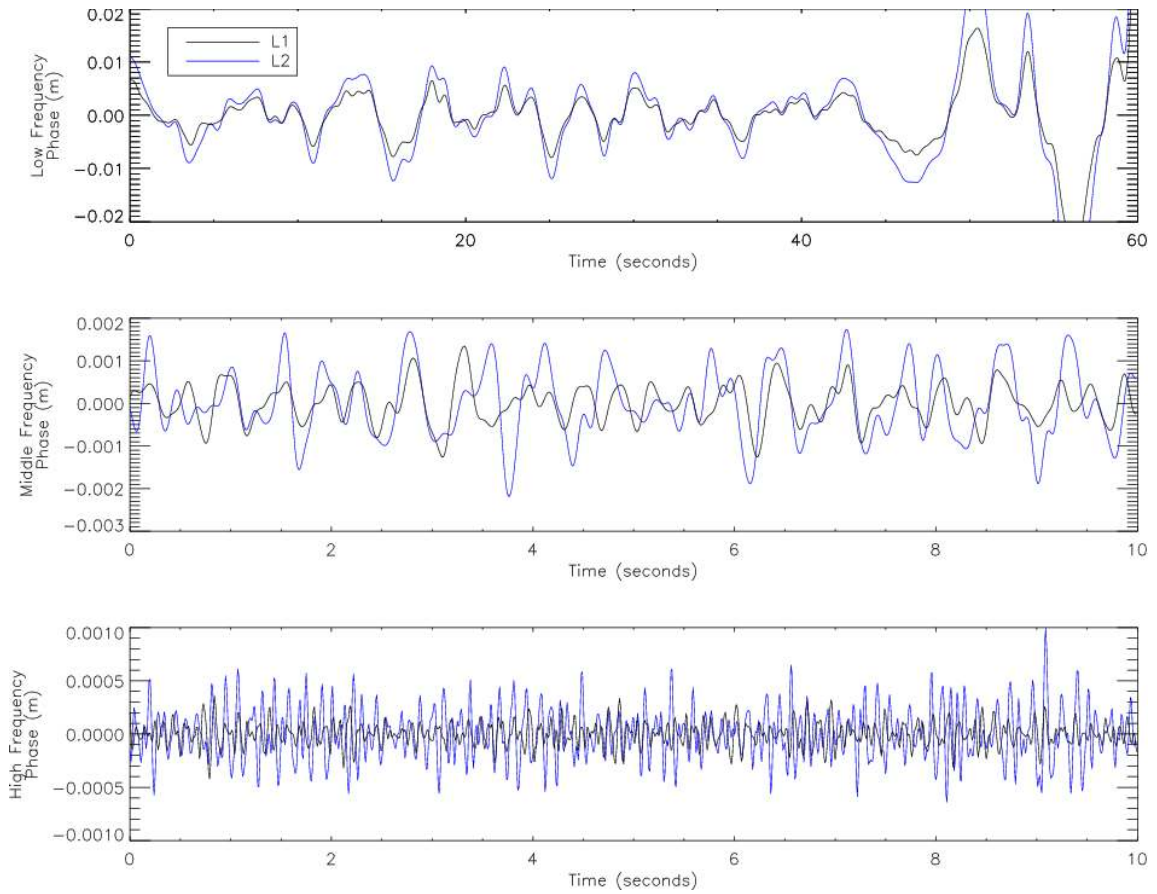


Figure 7.9 An example of the refractive variations (top), diffractive variations (middle), and high-frequency noise (bottom) during the DOY 186 example. The L1 carrier phase variations are presented in black, the L2 carrier phase variations are presented in blue.

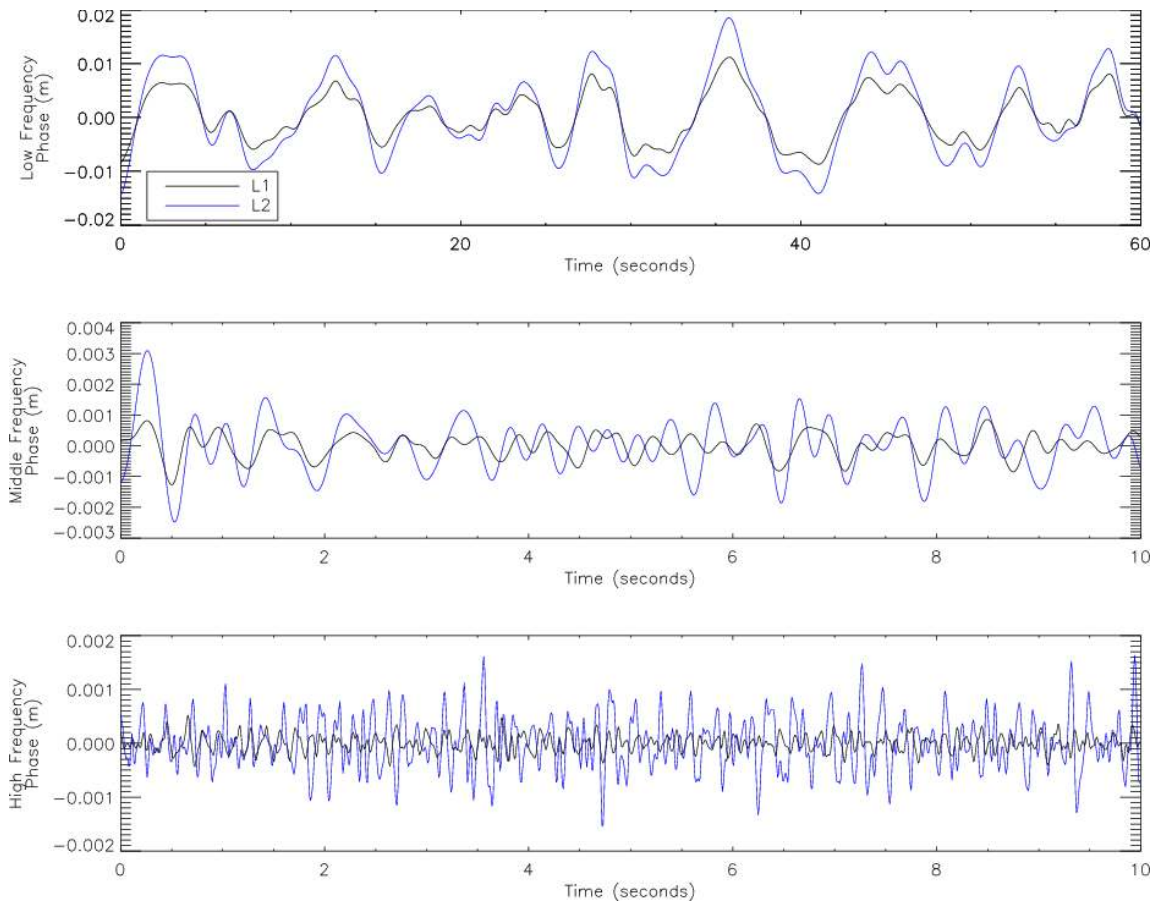


Figure 7.10 An example of the refractive variations (top), diffractive variations (middle), and high-frequency noise (bottom) during the DOY 218 example. The L1 carrier phase variations are presented in black, the L2 carrier phase variations are presented in blue.

To better visualize, and quantify, the correlations (or lack thereof), we perform the linear fits between the L1 and L2 carrier phase variations, bandpass filtered to the three variation types, using the frequencies presented in Table 7.1. In these results, we use the entire event; recall Figure 7.1 and Figure 7.2 which present the time over which the event takes place using the red lines plotted with the detrended carrier phases. These linear fits are presented in Figure 7.11 and Figure 7.12. The DOY 186 example is

presented in Figure 7.11 and the DOY 218 example is presented in Figure 7.12. In both examples, we observe near perfect correlation between the L1 and L2 carrier phase variations, bandpass filtered to the frequencies below the cut off frequencies. The correlation coefficients in both examples are 0.997. The linear fits are presented in the top panels of Figure 7.11 and Figure 7.12. Note as well that the slopes are nearly identical for both examples: 1.64 for the DOY 186 example, and 1.63 for the DOY 218 example. Recalling equation 4.16, the effects of changes in the refractive index is inversely proportional to the frequency of the carrier and proportional to the changes in electron density along the path. As we mentioned earlier, the L1 and L2 carriers are expected to follow very nearly the same path and will, therefore, see the same changes in electron density. If the ratio of the L2 to L1 carrier phase changes is taken, which is the case in calculating the slope of the linear fit, the value for the refractive variations should be the ratio of the frequencies squared. This works out to a value of 1.65, very nearly the value we observe for the slopes. This further suggests that these variations are purely refractive.

The middle panel presents the diffractive variations for both examples. We see in both examples a decrease in both the correlation coefficient and the slope. The correlation coefficients are 0.580 for the DOY 186 example and 0.620 for the DOY 218 example. We would expect a lower correlation between the diffractive variations due to their stochastic nature. The same goes for the slope, an introduction of low magnitude, stochastic variations should cause the slope to vary significantly from the nearly 1.64 value observed with the refractive variations. We observe slope values of 1.19 for the

DOY 186 example and 1.13 for the DOY 218 example. We note that the correlation between the diffractive variations is still somewhat significant. This is likely due to a few factors. First off, our method of determining the cut off frequency cannot be perfect, there is an error associated with the technique and the measurements. The cut off frequency can also vary throughout the event, thus making it impossible to get a perfect cut off frequency from the data. This means that in using this frequency to bandpass filter the carrier phase observable, a small number of refractive variations may be included with the diffractive variations. Since these variations will be at the lowest frequencies, they will have the largest magnitudes, and may then significantly affect the linear fit, both the correlation coefficient and the slope. Secondly, since the L1 and L2 carrier is expected to follow the same path through the ionosphere, and since their frequencies are rather close, the diffractive variations observed on the L1 and L2 carrier phase may be similar enough to induce some correlation. Lastly, these variations are not purely diffractive; changes in electron density with very small spatial scale will still induce refractive variations. In this case, they will be modulated by the diffractive variations; it is likely that these modulated fluctuations will still hold some of the refractive characteristics, thus causing higher correlations and slopes nearer to 1.65 than typically expected for diffractive variations.

Lastly, the linear fit between the L1 and L2 carrier high-frequency noise is presented in the bottom panels of Figure 7.11 and Figure 7.12. We observe very little correlation for both examples; a value of 0.027 for the DOY 186 example and 0.087 for the DOY 218 example. Slopes near zero are also observed, a value of 0.08 for the DOY 186 example

and 0.08 for the DOY 218 example. As we mentioned, we expect no correlation between the L1 and L2 carrier high-frequency noise, just as we observe in the linear fits.

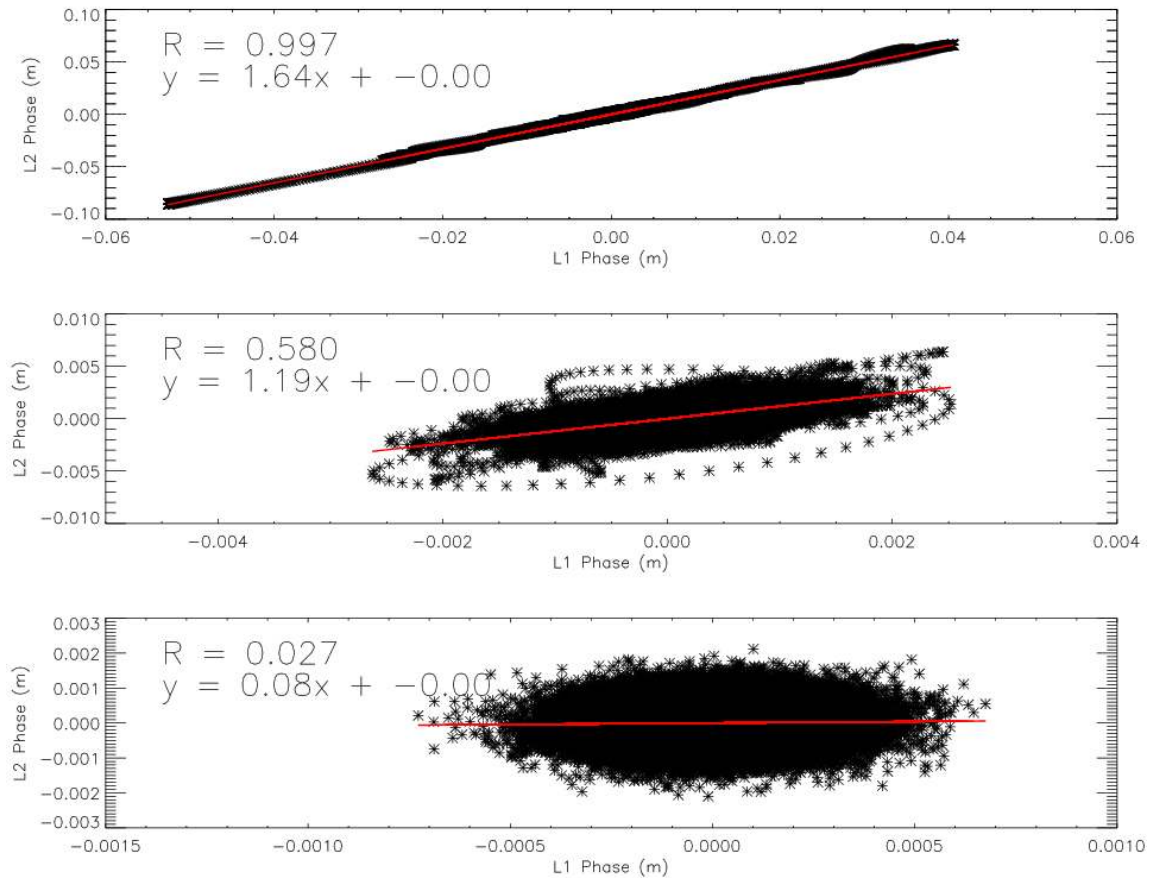


Figure 7.11 The linear fit between the L1 and L2 carrier phase variations, for the DOY 186 example. The carrier phases' have been bandpass filtered to contain only the refractive variations (top), diffractive variations (middle), and high-frequency noise (bottom). The linear fits are represented by the red lines.

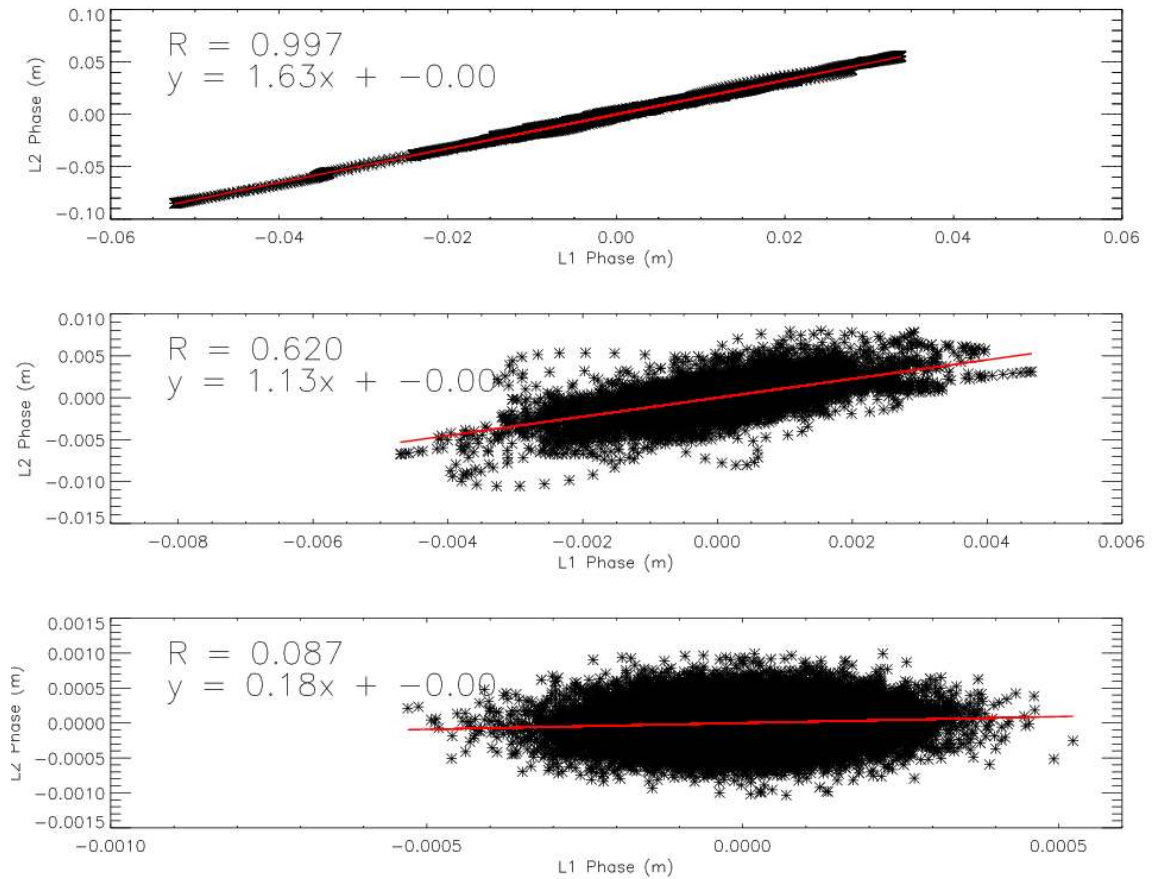


Figure 7.12 The linear fit between the L1 and L2 carrier phase variations, for the DOY 218 example. The carrier phases have been bandpass filtered to contain only the refractive variations (top), diffractive variations (middle), and high-frequency noise (bottom). The linear fits are represented by the red lines.

To further verify the validity of these cut off frequencies, we recall the discussion in Chapter 4 regarding the Fresnel frequency. The Fresnel frequency can be defined as the lowest frequency associated with diffractive variations in the amplitude and phase of the signal for a given event. The frequency is based on the Fresnel scale size and the relative drift velocity. Thus, to verify the predetermined cut off frequencies as the cut off

between the refractive and diffractive variations, they must represent valid Fresnel scale sizes.

We begin the validation by determining the possible relative drift velocities and irregularity height pairs which could be responsible for cut off frequencies like the ones obtained for the presented examples. To outline the method, we present examples using the L1 carrier for both the DOY 186 and DOY 218 events. Recalling the Fresnel scale is defined as $d_F = \sqrt{2\lambda z}$, and the corresponding Fresnel frequency can then be defined as $f_F = v_d/r_F$, we examine a range of possible irregularity heights and calculate the corresponding Fresnel scales. A range of possible drift velocities are then used to calculate the corresponding Fresnel frequencies. We can plot these quantities, represented by the blue curves presented in Figure 7.13 and Figure 7.14. A plane corresponding to the cut off frequencies determined for each example event are presented in red. The intersection between the Fresnel frequency-irregularity height-drift velocity surface and the cut off frequency plane represents a curve corresponding to the range of possible drift velocity and irregularity height pairs responsible for Fresnel frequencies equal to the cut off frequencies. These curves are presented in Figure 7.15 and Figure 7.16 for the DOY 186 and DOY 218 examples respectively.

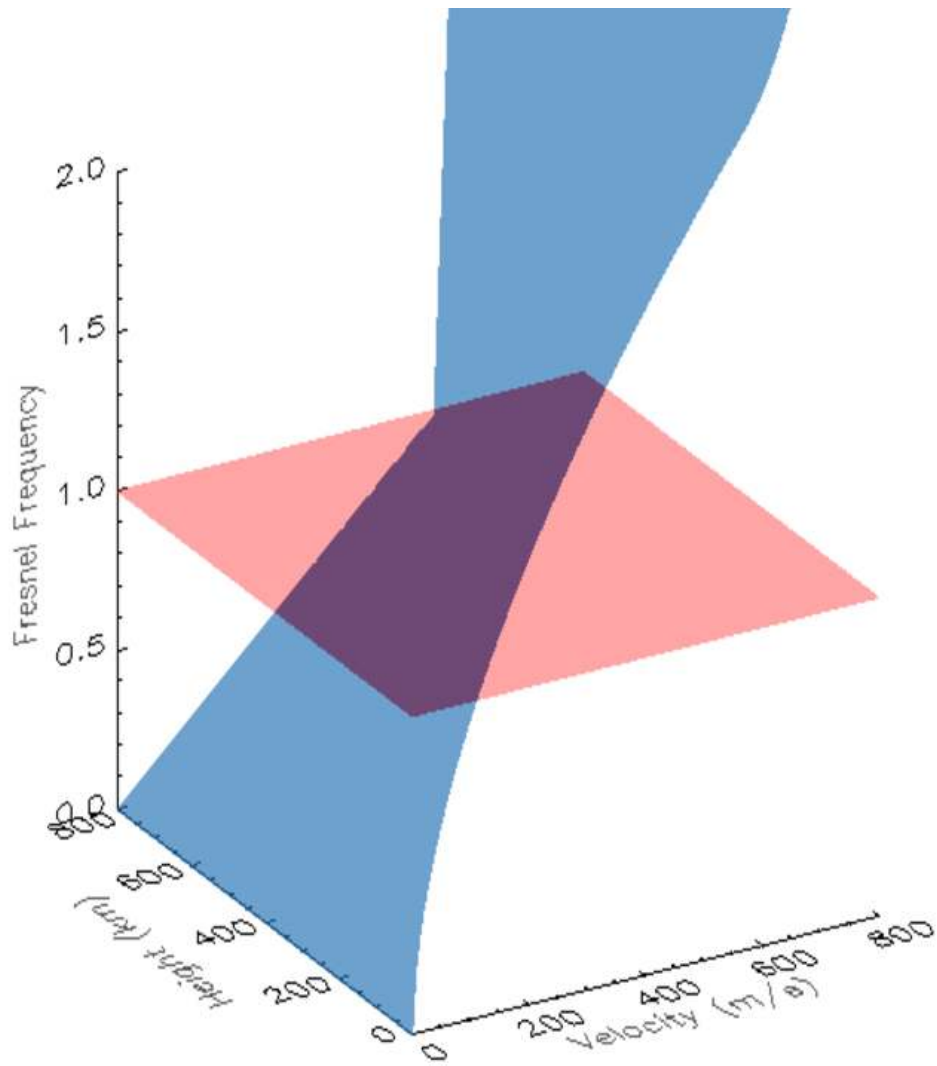


Figure 7.13 The surface representing the Fresnel frequency corresponding to given irregularity height and drift velocity pairs (blue) and the place corresponding to the cut off frequency between refractive and diffractive variations determined for the DOY 186 event (red).

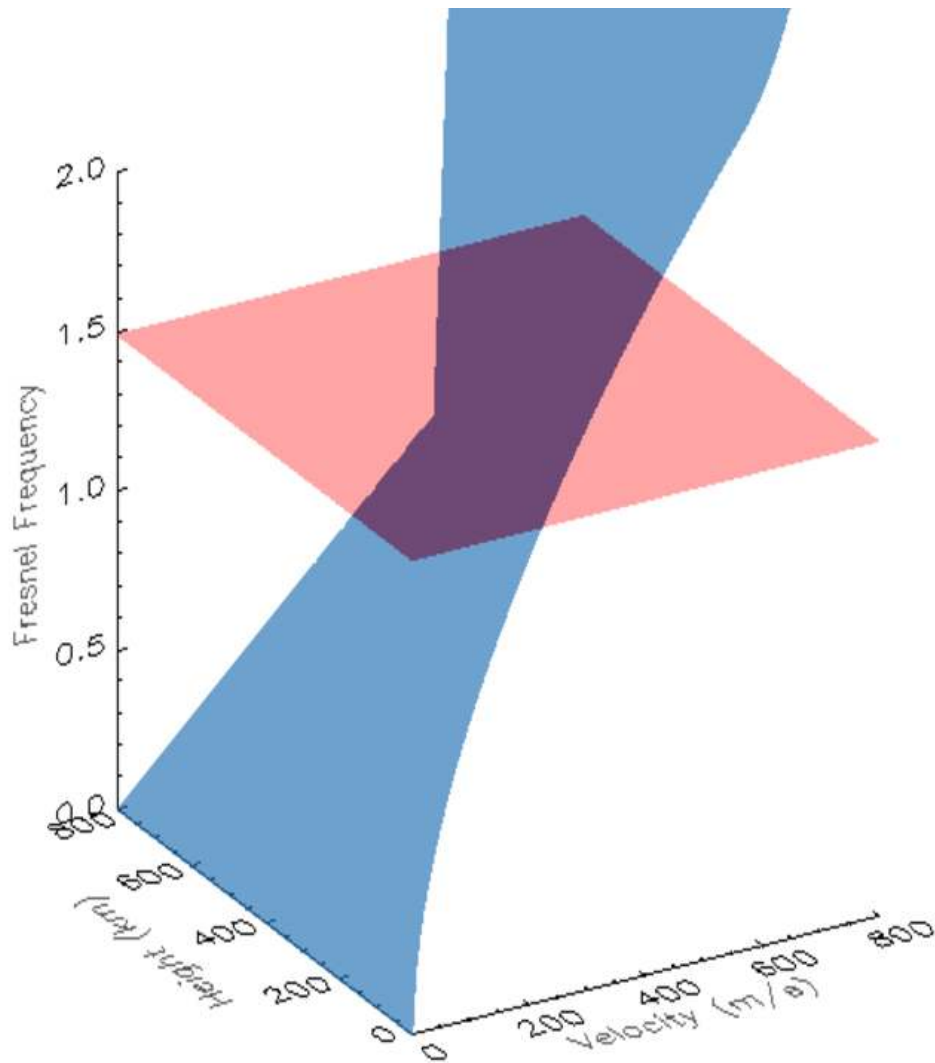


Figure 7.14 The surface representing the Fresnel frequency corresponding to given irregularity height and drift velocity pairs (blue) and the place corresponding to the cut off frequency between refractive and diffractive variations determined for the DOY 218 event (red).

Assuming reasonable irregularity heights on the order of 200 km to 600 km, which would likely contain the F-layer peak (Magdaleno et al., 2011, and references therein),

drift velocities on the order of 300 m/s to 450 m/s are necessary for the DOY 186 example, and drift velocities ranging from 400 m/s to 700 m/s are necessary for the DOY 218 example. Drift velocities on the order of 300 m/s to 700 m/s are reasonable for the auroral region (Aarons, 1982; Basu et al., 1999).

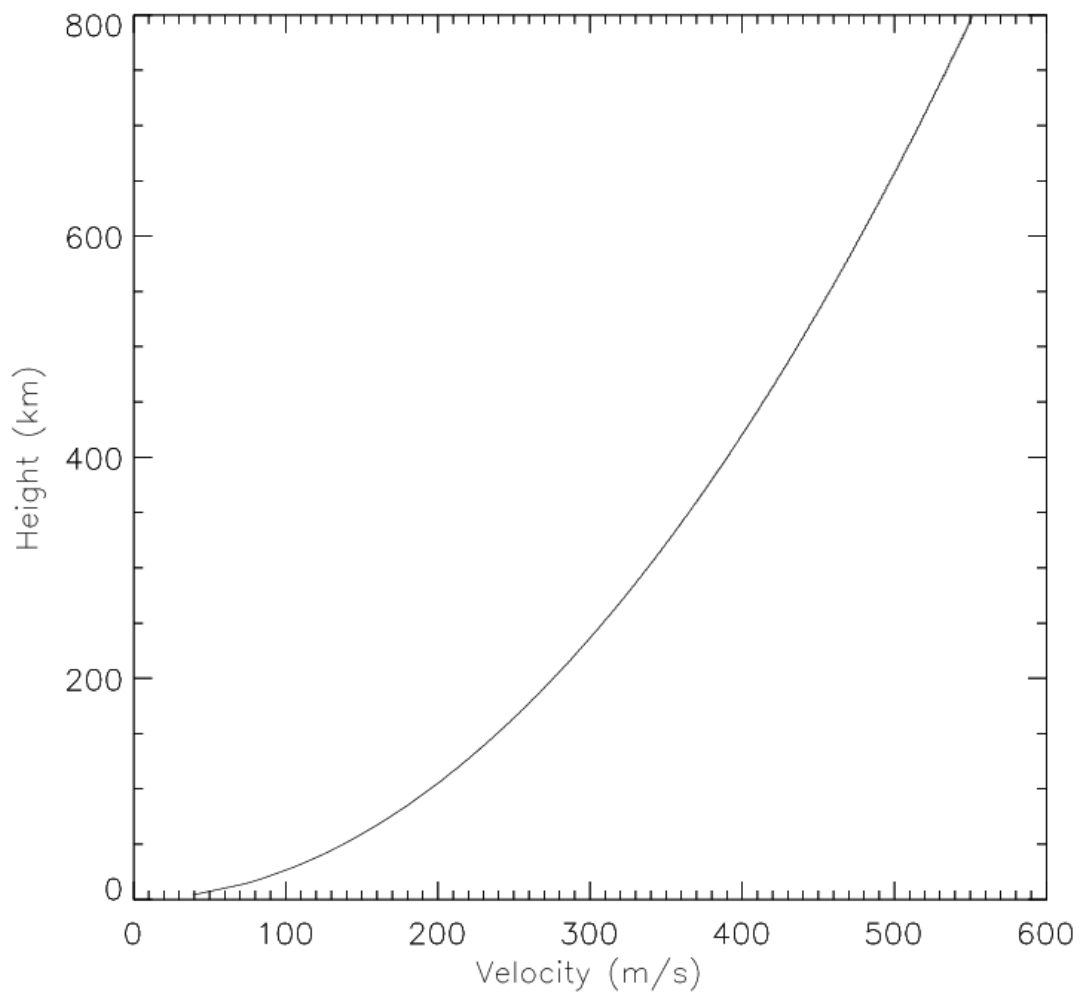


Figure 7.15 The curve representing the intersection between the Fresnel frequency surface and the cut off frequency plane presented in Figure 7.13, corresponding to the

DOY 186 example. This presents the irregularity height and drift velocity pairs necessary for a Fresnel frequency equal to the cut off frequency.

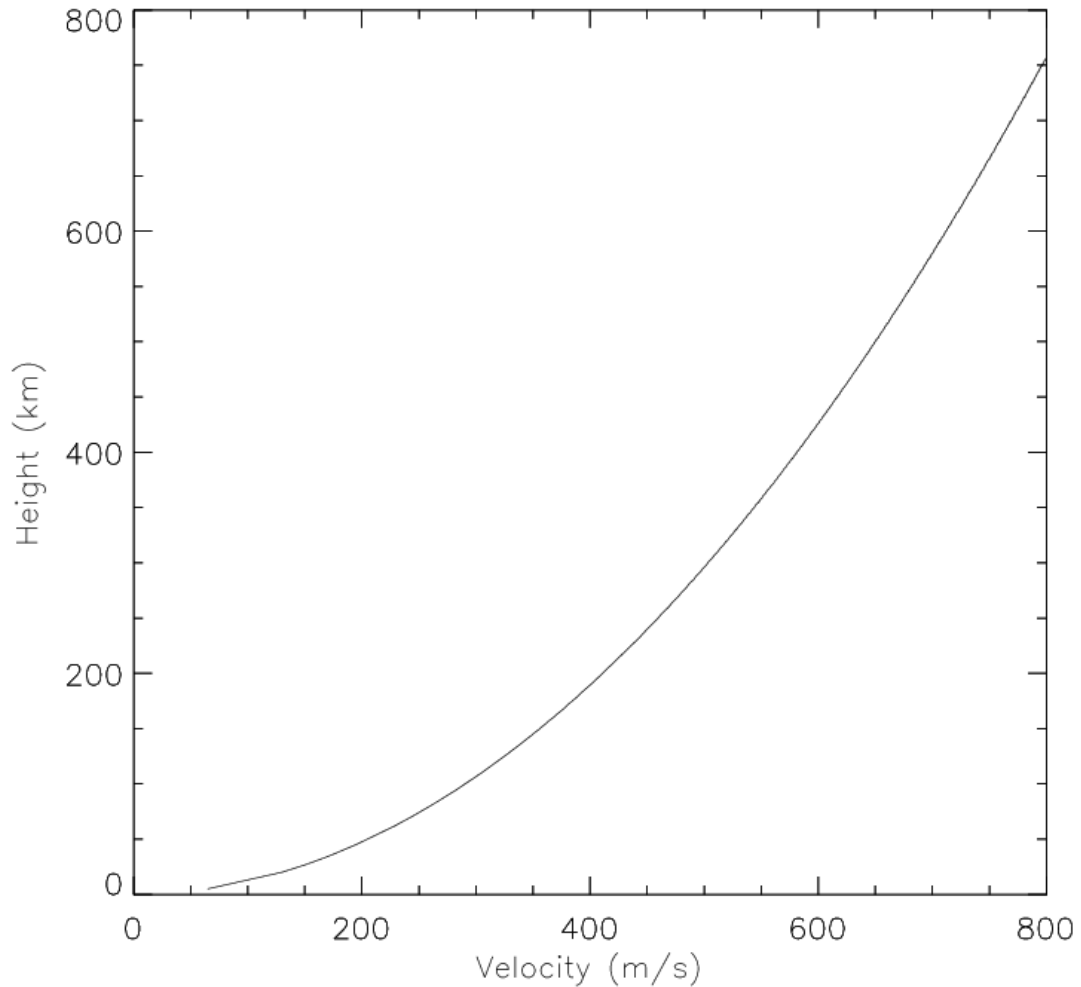


Figure 7.16 The curve representing the intersection between the Fresnel frequency surface and the cut off frequency plane presented in Figure 7.14, corresponding to the DOY 218 example. This presents the irregularity height and drift velocity pairs necessary for a Fresnel frequency equal to the cut off frequency.

To further address the validity of the cut off frequencies as representing likely Fresnel scale sizes, we can obtain rough drift velocity measurements for the example events using the SuperDARN network (Greenwald et al., 1995; Chisham et al., 2007). We obtain the Ionospheric Pierce Point (IPP) for the ray paths of the example events' satellites. We take the IPP at a height of 350 km, corresponding to an approximate peak density height (Magdaleno et al., 2011, Mushini, 2012). Drift data is obtained within a 3° (in geographic latitude and longitude) window surrounding the IPP at the time of the phase fluctuation event. The Christmas Valley East radar is the only radar reporting data in the region of interest for the DOY 186 event, and the Kapuskasing radar provided the data for the DOY 218 event. With the minimal data available from SuperDARN during the events, a rough estimation of the drift speeds is obtained.

For the DOY 186 event, 77 velocity measurements are available within the time and location of interest. A mean drift velocity of 441 m/s with a standard deviation of 76 m/s is obtained. Within 1σ this corresponds to Fresnel scales ranging from 366 m to 518 m, and corresponding irregularity heights of 352 km to 706 km. For the DOY 218 example, 33 velocity measurements are available. A mean of 385 m/s with a standard deviation of 115 m/s is obtained. This corresponds to Fresnel scales on the order of 152 m to 359 m, and irregularity heights of 60 km to 339 km.

Due to the lack of available data, the error in the mean drift velocities are moderately large and are responsible for large ranges in the irregularity heights and Fresnel scales. However, these ranges do correspond to valid values for the region, and the mean drift velocities obtained from SuperDARN agree with the theoretically determined drift velocity ranges to within 1σ . This further validates the cut off frequencies determined using the methods outlined in this section as likely Fresnel frequencies.

We note that determining the Fresnel frequency through these methods ignores a few subtleties, including possible changes in the drift velocity during the length of the event, multiple irregularities along the ray path, and the integrated nature of the carrier phase measurement. With these subtleties in mind, we suggest that the results show that these cut off frequencies are good approximations of the Fresnel frequency for the presented events. For clarity, the cut off frequencies will be referred to as the Fresnel frequency for the remainder of the study.

7.3.2 A Case Study Using Three Carrier Frequencies

Using the same methods outlined in the previous section, we present an example to determine the refractive variations of a GPS carrier phase event where three carrier frequencies are available. We use the same L1 and L2 carrier as was used previously while including the L5 carrier as well. This gives three carrier pairs to do the final linear

fit analysis, where the slopes of the three pairs can be shown to follow their respective frequency-squared ratio. This will help solidify the performance of the method.

The event was found at the Sach's Harbour location of the CHAIN (SACC), located at geographic coordinates 71.99 °N and 234.74 °E. The detrended carrier phases are presented in Figure 7.17, with the L1 carrier phase in the top panel, the L2 carrier phase in the middle panel, and the L5 carrier phase in the bottom panel. Like the previous examples, the red lines indicate the event and time interval over which we perform the analysis. Using the same approach as the previous section, the approximate Fresnel frequencies are obtained using the amplitude spectra for each carrier. The corresponding spectra are presented in Figure 7.18. The L1 amplitude spectrum is presented in the top left panel, the L2 amplitude spectrum in the top right panel, and the L5 amplitude spectrum in the bottom left panel. The blue line, green line, and red lines represent the fits obtained for the low frequency (prior to the Fresnel frequency), the scintillation, and the high-frequency noise portions of the spectrum, respectively. As with the previous analysis, the intersection points of these fits are taken as the Fresnel and noise floor frequencies. These values are presented in Table 7.2.

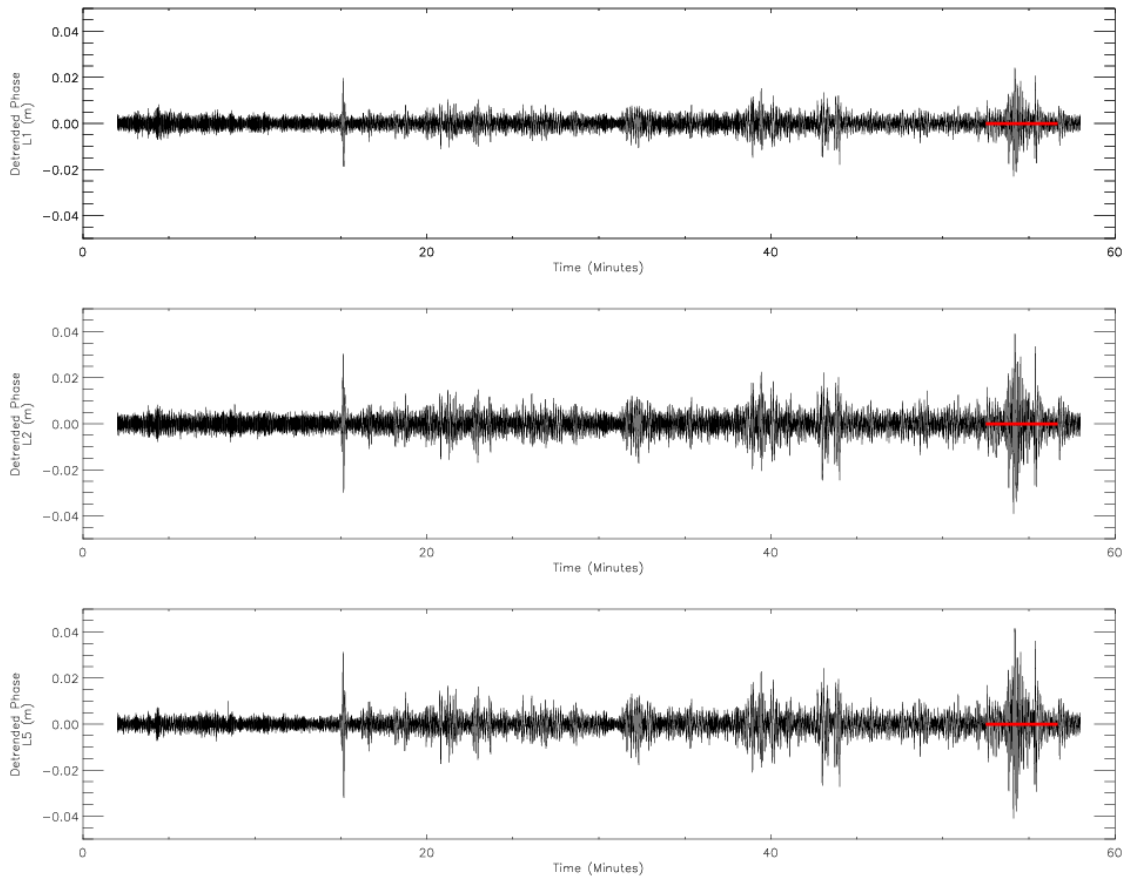


Figure 7.17 The phase variation event for the three carrier frequency example. The detrended L1 carrier phase is presented in the top panel, the L2 carrier in the middle panel, and the L5 carrier in the bottom panel. The red line indicates the event being analyzed.

Table 7.2 The Fresnel and noise floor frequencies for the L1, L2, and L5 carriers.

	Fresnel Frequency	Noise Floor Frequency
L1 Carrier	1.00 Hz	6.01 Hz
L2 Carrier	0.96 Hz	5.78 Hz
L5 Carrier	0.91 Hz	7.35 Hz

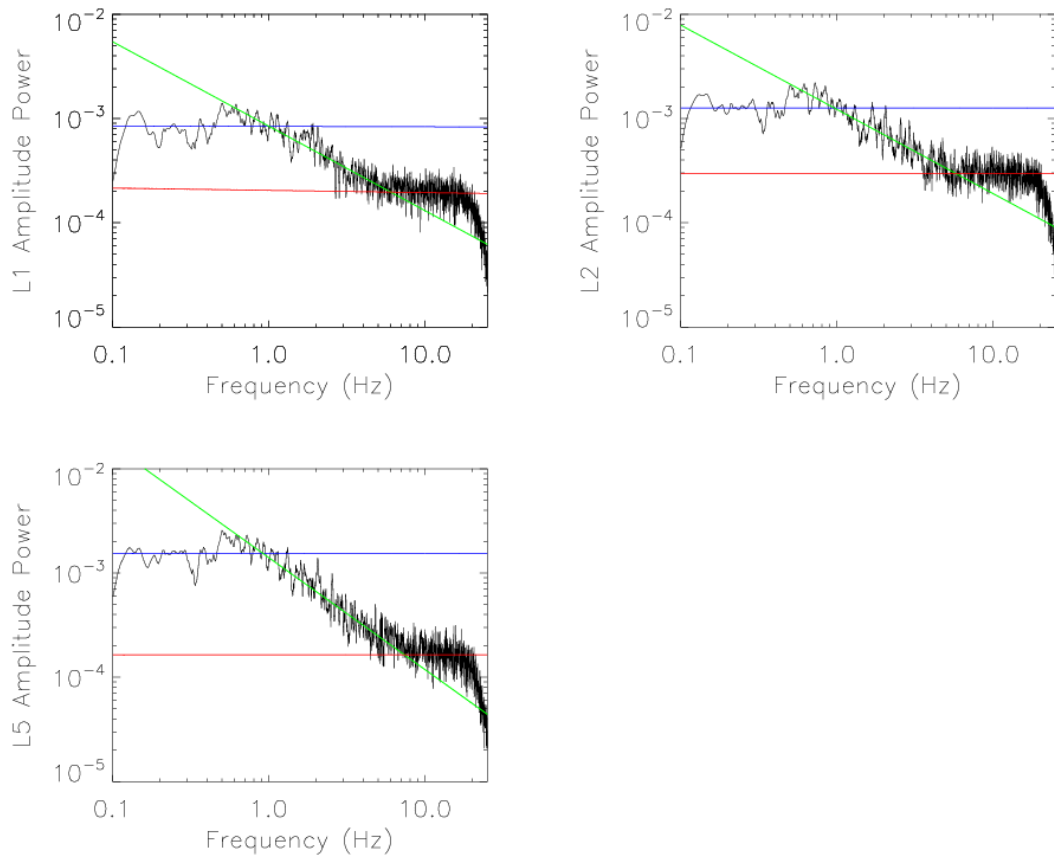


Figure 7.18 The amplitude spectra corresponding to the phase event. The L1 carrier amplitude spectrum is presented in the top left panel, the L2 carrier spectrum in the top right panel, and the L5 carrier spectrum in the bottom left panel. The blue, green, and

red line represent the fits for the zero-slope, low-frequency portion of the spectrum, the scintillation portion, and the high-frequency noise portion, respectively.

We use the frequencies presented in Table 7.2 to bandpass filter each of the carrier phase observables into frequency windows corresponding to the refractive variations, the diffractive variations, and the high-frequency noise. Recall that we use a low-frequency cut-off of 0.1 Hz and a high-frequency cut-off of 25 Hz. The linear fits are performed between each carrier pair for each frequency window. These are presented in Figure 7.19, Figure 7.20, and Figure 7.21. Figure 7.19 presents the L1-L2 carrier pair, Figure 7.20 presents the L1-L5 carrier pair, and Figure 7.21 presents the L2-L5 carrier pair. In the L1-L2 carrier pair example, we observe a correlation coefficient of 0.989 and a slope of 1.60 for the refractive variations linear fit. As was discussed in the previous section this is as we expect for the L1-L2 refractive variations. The diffractive variations have a correlation coefficient of 0.782 and a slope of 0.91. The high-frequency noise has a correlation coefficient of 0.077 and a slope of 0.11. Both correlations act similarly to those presented in the previous examples. For the L1-L5 carrier pair, we observe a correlation coefficient of 0.993 and a slope of 1.72. The frequency-squared ratio for the L1-L5 pair is 1.79, near what we observe for the slope. Expected results for the diffractive and high-frequency noise variations are observed, with a decrease in correlations and slope for the diffractive variations (correlation of 0.841 and slope of 0.87) and more so for the noise (correlation of 0.069 and slope of 0.04). The L2-L5 carrier pair has a correlation of 0.996 with a slope of 1.07. The expected slope for this pair is 1.09, again very near the observed slope. The diffractive and high-frequency

noise variations behave as expected as well. The diffractive variation's correlation coefficient is 0.844 and slope are 0.75, both lower than that observed for the refractive variations. The high-frequency noise has a correlation coefficient of 0.065 and a slope of 0.03; these are very low, as we expect.

We note that in this example we observe that the agreement of the slope with the expected frequency-squared ratios varies between the pairs. The L2-L5 carrier pair agrees the best, while the L1-L5 carrier pair has the worst agreement of the set. We suspect this is due to the closeness of the carrier frequencies, since the L2-L5 carrier pair has the closest carrier frequencies, and the L1-L5 carrier pair have the largest difference in carrier frequencies. We suggest that as the gap between the carrier frequencies increases, differences in the higher order effects, especially ray bending, becomes more prominent. This would lead to slight differences in the refractive variations, causing the correlation to drop slightly.

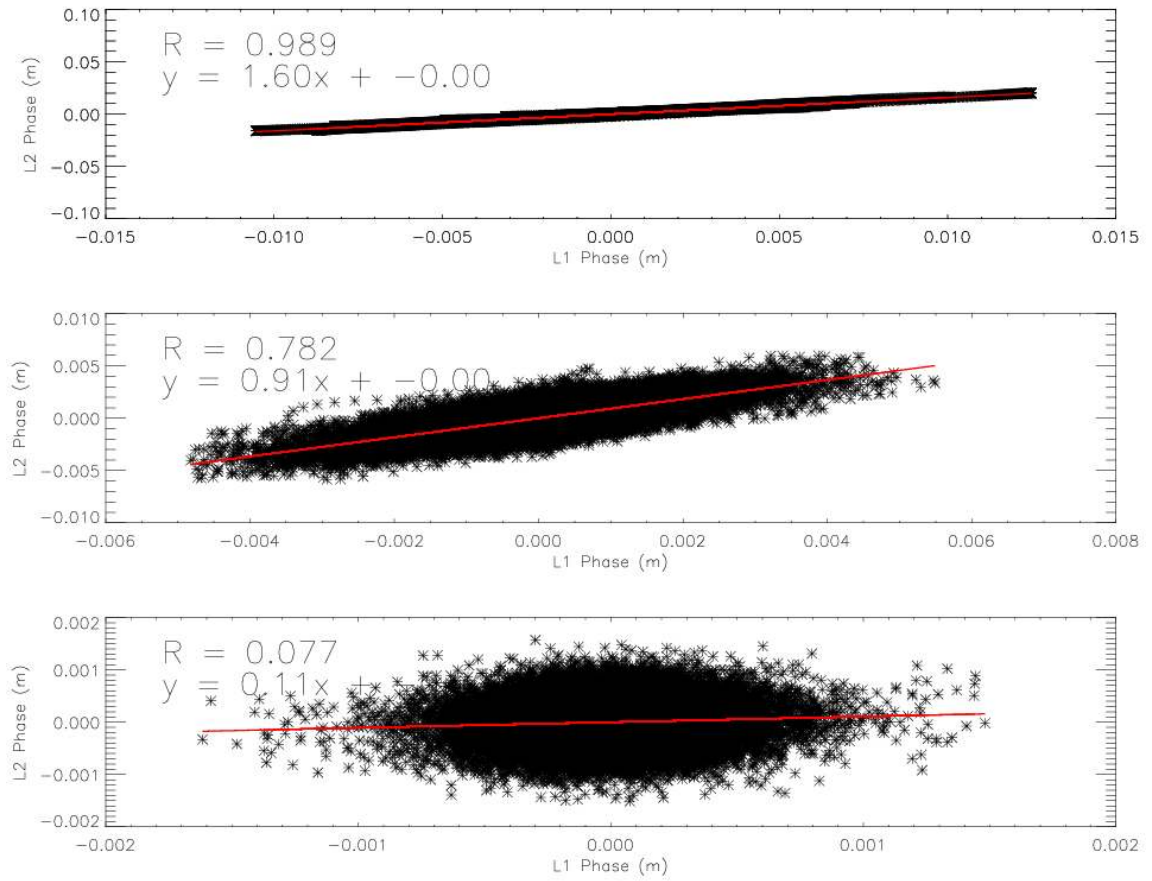


Figure 7.19 The linear fits between the refractive variations (top panel), diffractive variations (middle panel), and the high-frequency noise (bottom panel) for the L1-L2 carrier phase pair.

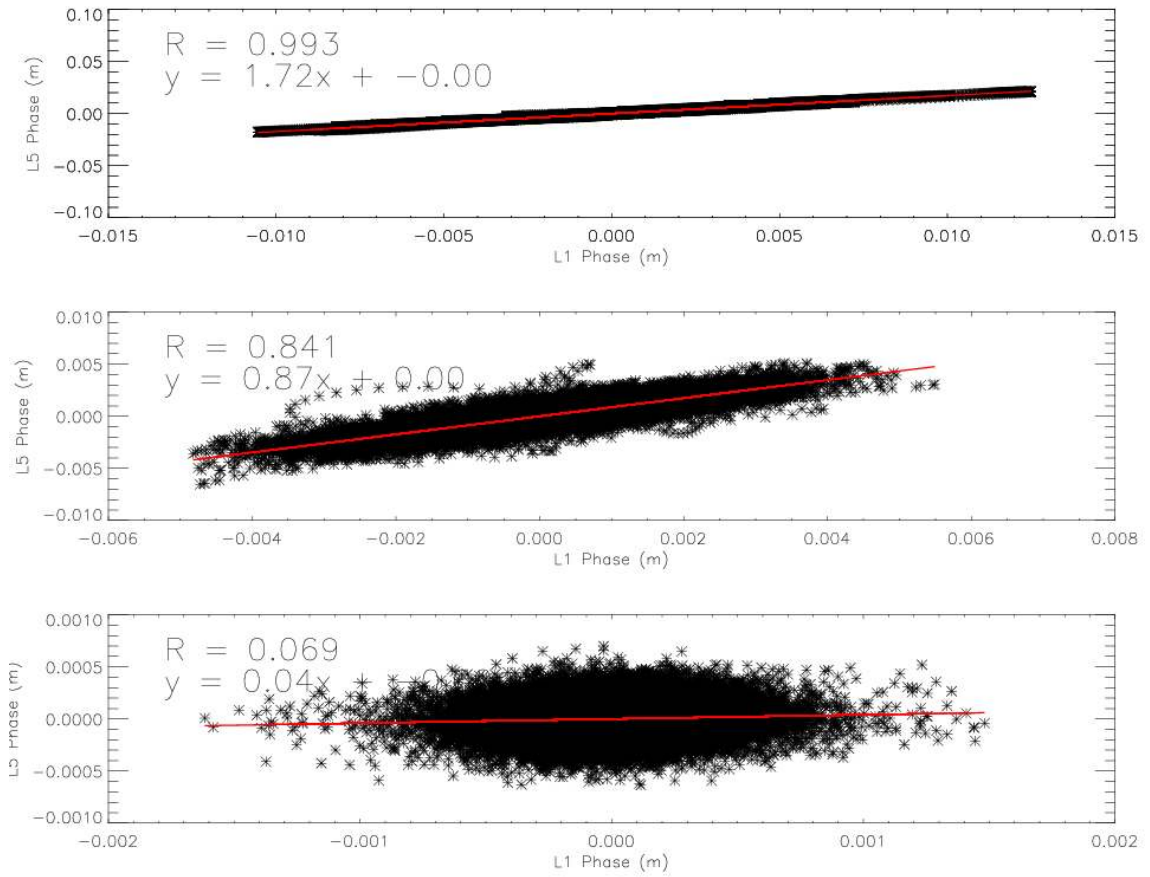


Figure 7.20 The linear fits between the refractive variations (top panel), diffractive variations (middle panel), and the high-frequency noise (bottom panel) for the L1-L5 carrier phase pair.

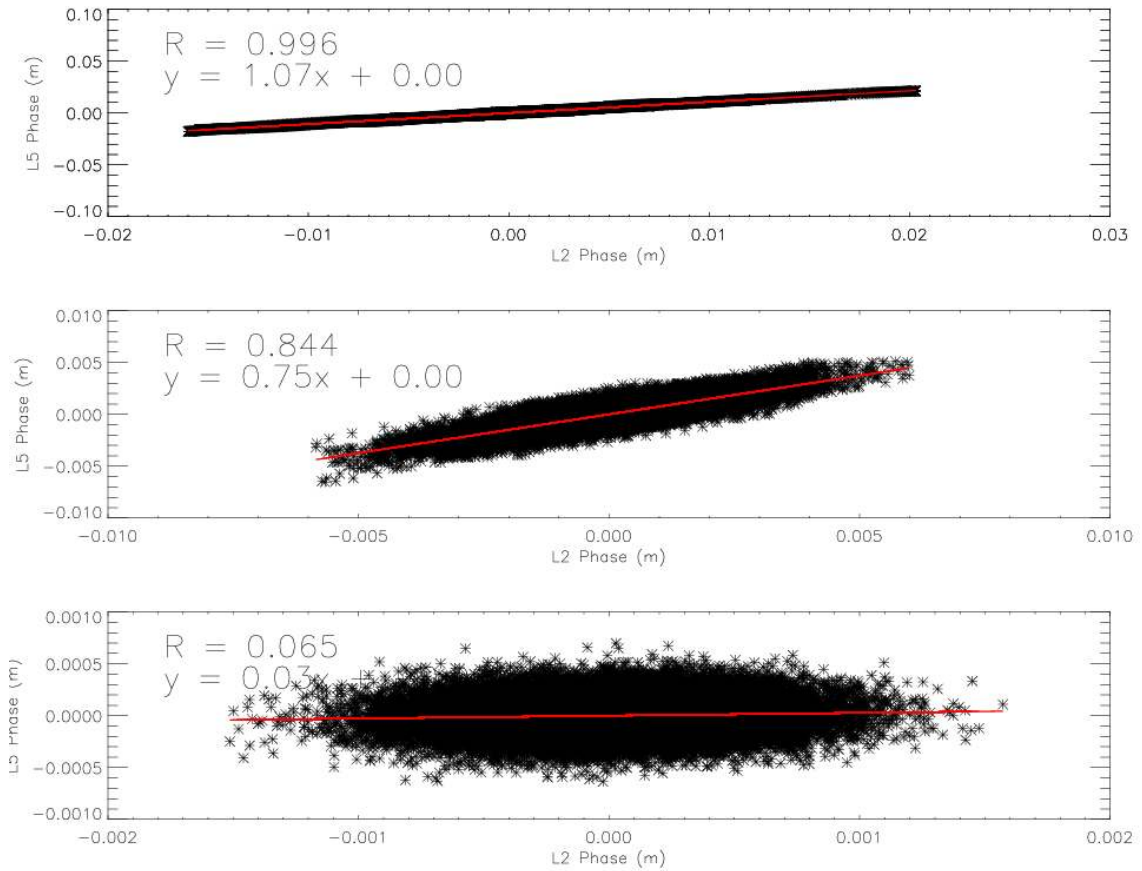


Figure 7.21 The linear fits between the refractive variations (top panel), diffractive variations (middle panel), and the high-frequency noise (bottom panel) for the L2-L5 carrier phase pair.

Having shown that we can differentiate the purely refractive variations from the diffractive variations, we can now ensure that high-frequency variations in the TEC are not contaminated by diffractive variations. This will ensure that a more accurate analysis of the high-frequency TEC can be done. We may also use the TEC as a further check of the high-frequency refractive variations in the carrier phase observable.

7.3.3 Total Electron Content Analysis

Knowing the lower frequency section of the high-frequency variations are purely refractive in nature, we can begin to more accurately analyze the sTEC obtained for the DOY 186 and DOY 218 examples we previously discussed. Note that the presented sTEC has not been corrected for hardware biases and integer ambiguities; only the variations in the sTEC is of interest. We can also use the sTEC as a final check to confirm that the variations in the carrier phase observable, in the 0.1 Hz to Fresnel frequency range, are in fact refractive in nature. First off, we look at the sTEC during these phase variations events. Figure 7.22 and Figure 7.23 present the detrended L1 carrier phase observable, same as observed previously, in the top panels. The bottom panels present the raw sTEC during the same hour. As before, the red line indicates where the event of interest takes place. Figure 7.22 presents this data for the DOY 186 example, and Figure 7.23 presents the data for the DOY 218 example. For both examples, we observed significant variability in the sTEC during the time of the carrier phase variations. The peak variability of the sTEC is on the order of 2 – 4 TECU for the examples, both observed during the largest peak in the detrended carrier phase. We expect the refractive variations in the phase to be directly related to the variations in the sTEC, meaning the frequency of these variations should be identical. We can better view the variations in the sTEC by filtering the sTEC to the frequencies which we have previously determined are refractive in the carrier phase. This is the lower cut-off frequency used in the carrier phase detrending procedure (0.1 Hz) and the Fresnel frequency we determined previously. We present the filtered sTECs in Figure 7.24 and

Figure 7.25; Figure 7.24 representing the DOY 186 example, and Figure 7.25 representing the DOY 218 example. The top panels present the same raw sTEC as the previous figure, while the bottom panels present the corresponding filtered sTEC. We observe large variations in the filtered sTEC which are also associated with the large variations in the carrier phase. This is expected, assuming these are the real variations in the TEC along the ray path responsible for the refractive variations in the carrier phase.

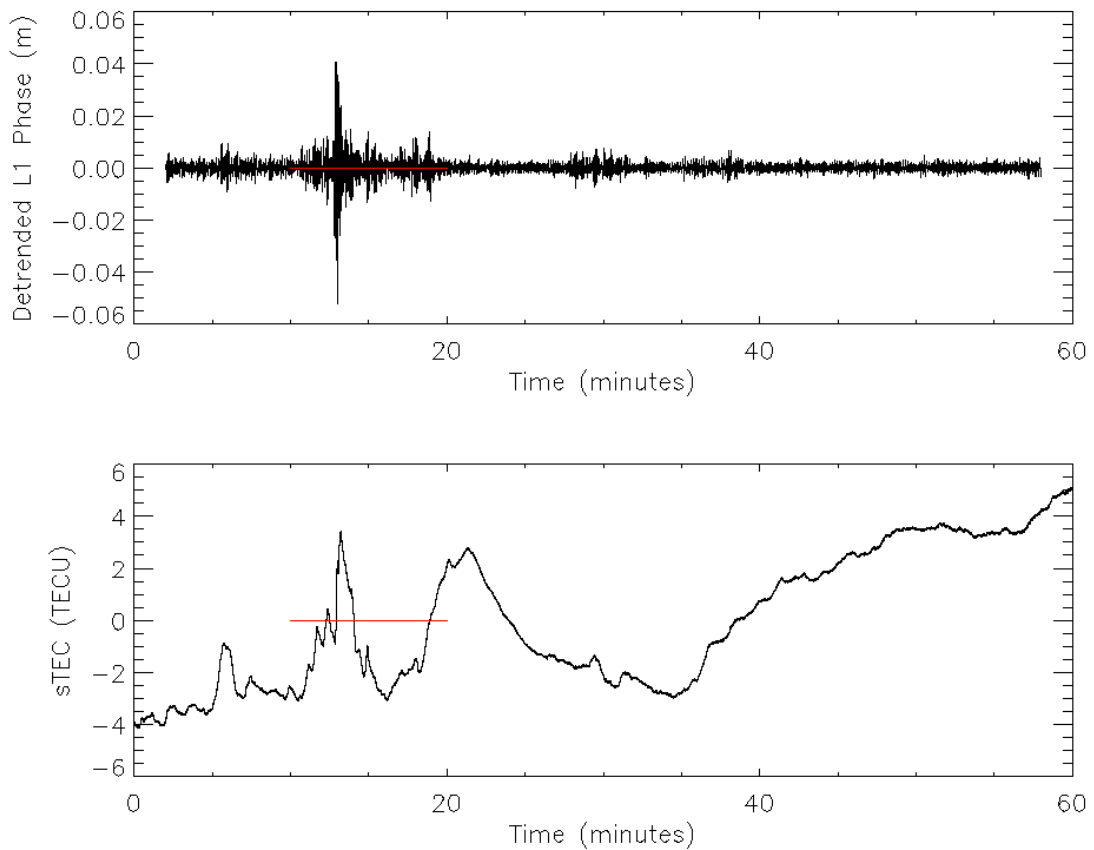


Figure 7.22 The detrended L1 carrier phase observable (top) and the corresponding raw sTEC (bottom) for the DOY 186 example.

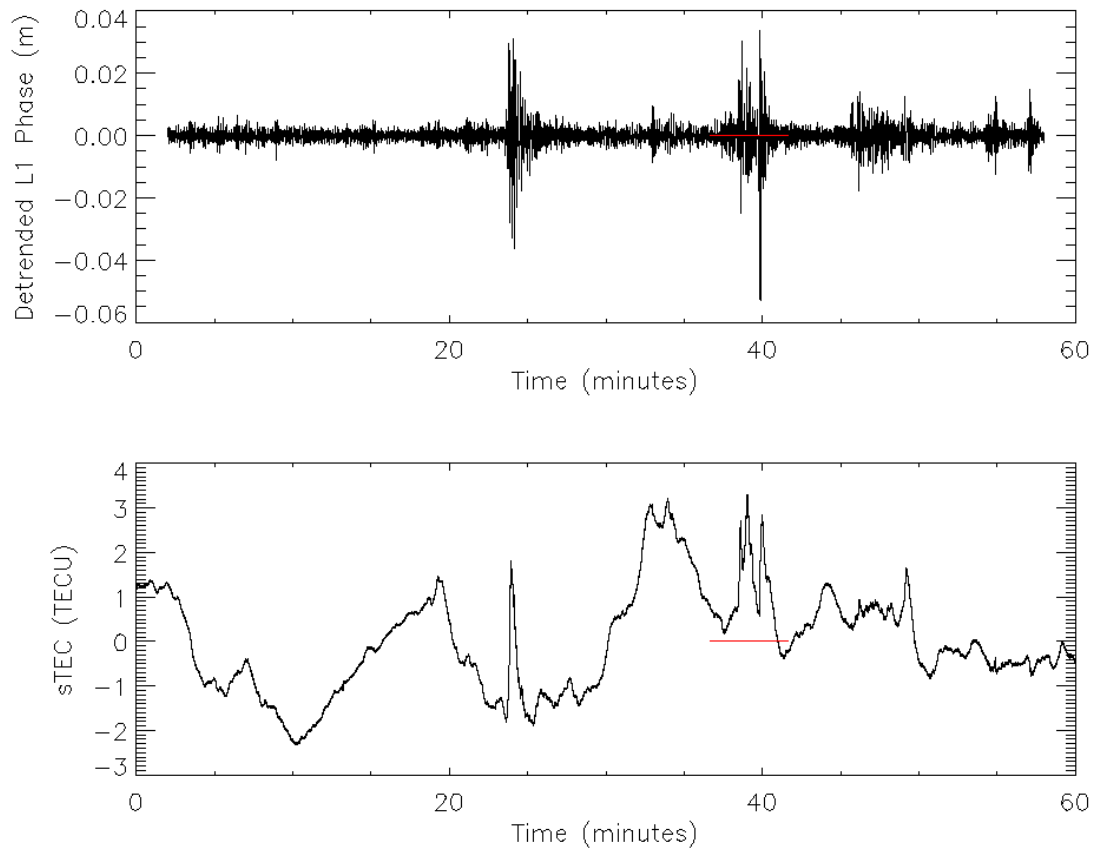


Figure 7.23 The detrended L1 carrier phase observable (top) and the corresponding raw sTEC (bottom) for the DOY 218 example.

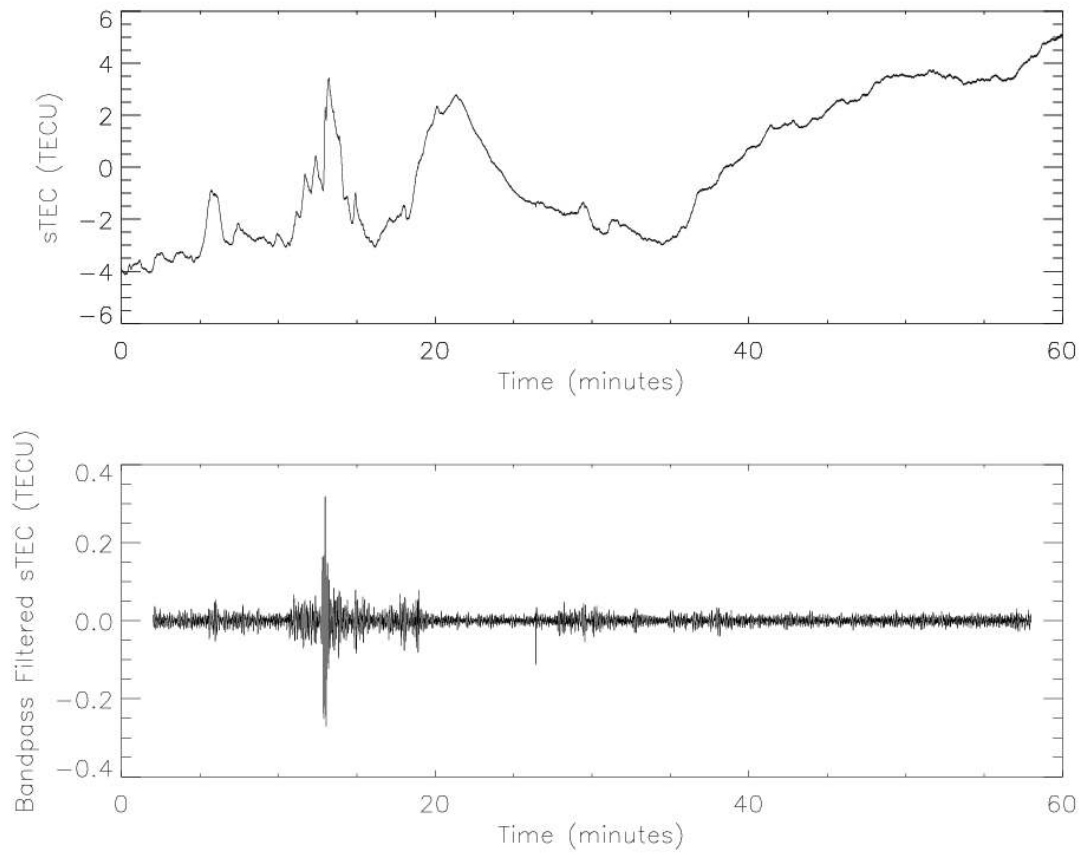


Figure 7.24 The raw sTEC (top) and the filtered sTEC (bottom), which is filtered from the 0.1 Hz low-frequency cut-off to the Fresnel frequency, corresponding to the DOY 186 example.

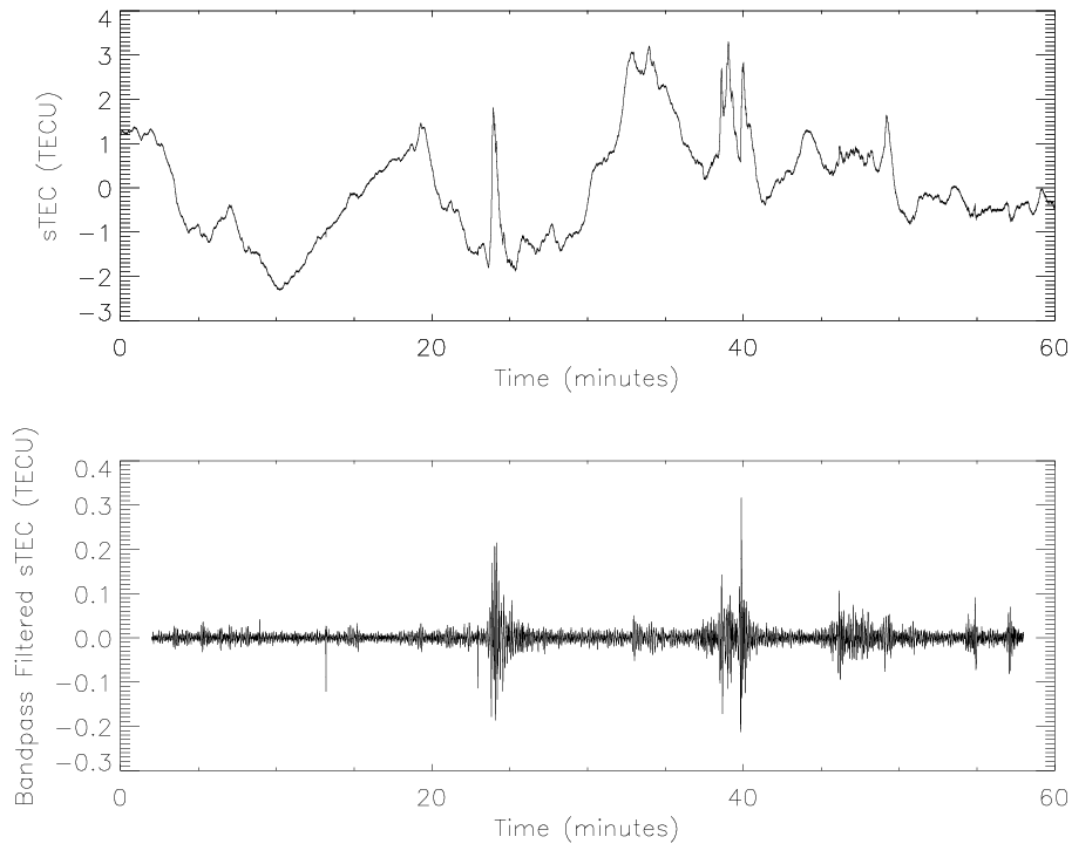


Figure 7.25 The raw sTEC (top) and the filtered sTEC (bottom), which is filtered from the 0.1 Hz low-frequency cut-off to the Fresnel frequency, corresponding to the DOY 218 example.

Using the relationships in equation 4.12, we can estimate the effect the changes in sTEC should have on the carrier phase observables. We use the filtered sTEC, filtered from the 0.1 Hz low-frequency cut-off to the appropriate Fresnel frequencies, to create the estimated effects on the carrier phase at those same frequencies. The detrended L1 and L2 carrier phase are presented in the top left and top right panels, respectively, of Figure 7.26 and Figure 7.27. The estimated effects on the respective carrier phase are presented

below, in the middle panels. In the bottom panels are the difference between the real L1 and L2 detrended carrier phase observable, and the estimated effects calculated using the filtered sTEC. In both the DOY 186 example (presented in Figure 7.26), and the DOY 218 example (presented in Figure 7.27), we observe that nearly all variations are removed in the differences. This shows that the variations in the sTEC, observed at the frequencies associated with refractive variations in the carrier phase observables, properly account for the refractive variations in the carrier phase results. This also shows that these variations in the carrier phase are in fact refractive, due to changes in the electron density along the satellite ray path.

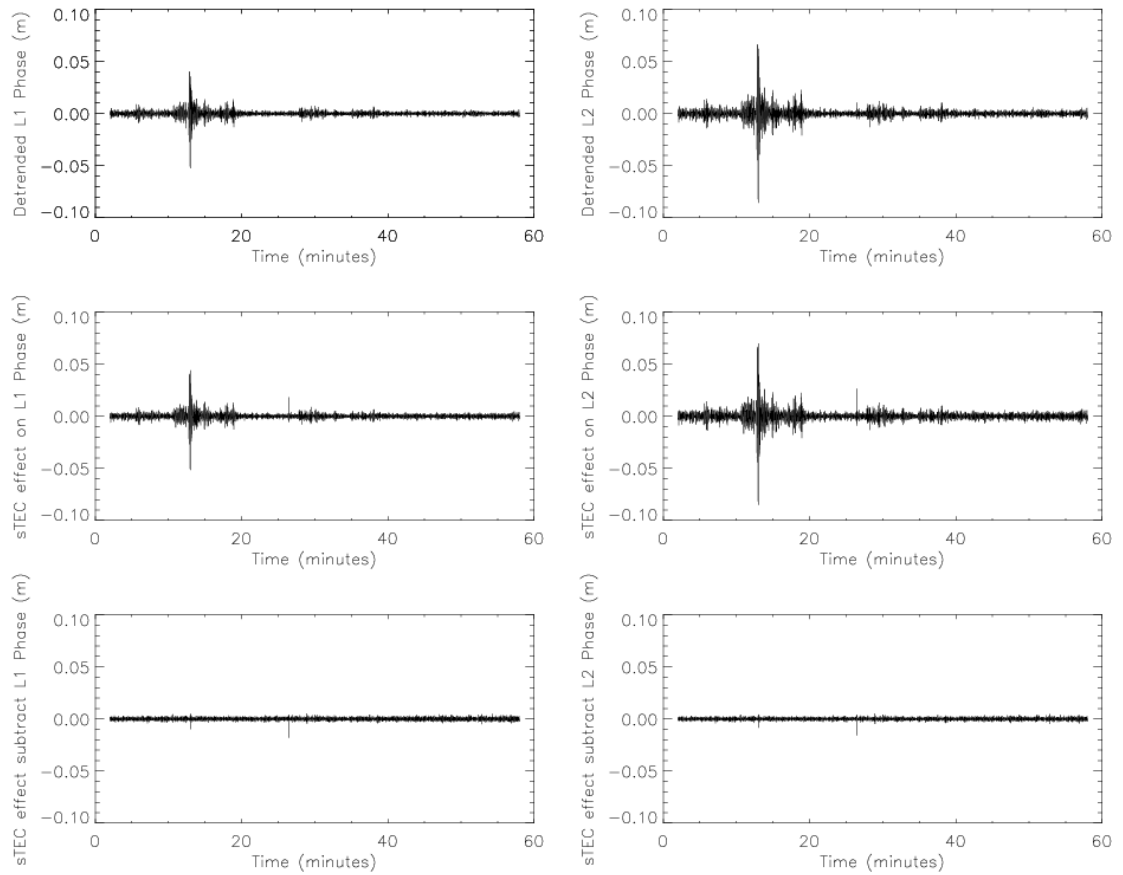


Figure 7.26 The L1 (top left panel) and L2 (top right panel) bandpass filtered carrier phase, filtered from 0.1 Hz to the appropriate Fresnel frequency, the estimated effects of the sTEC (middle panels) on the carrier phase, bandpass filtered to the same frequencies, and the differences between them (bottom panels) corresponding to the DOY 186 example.

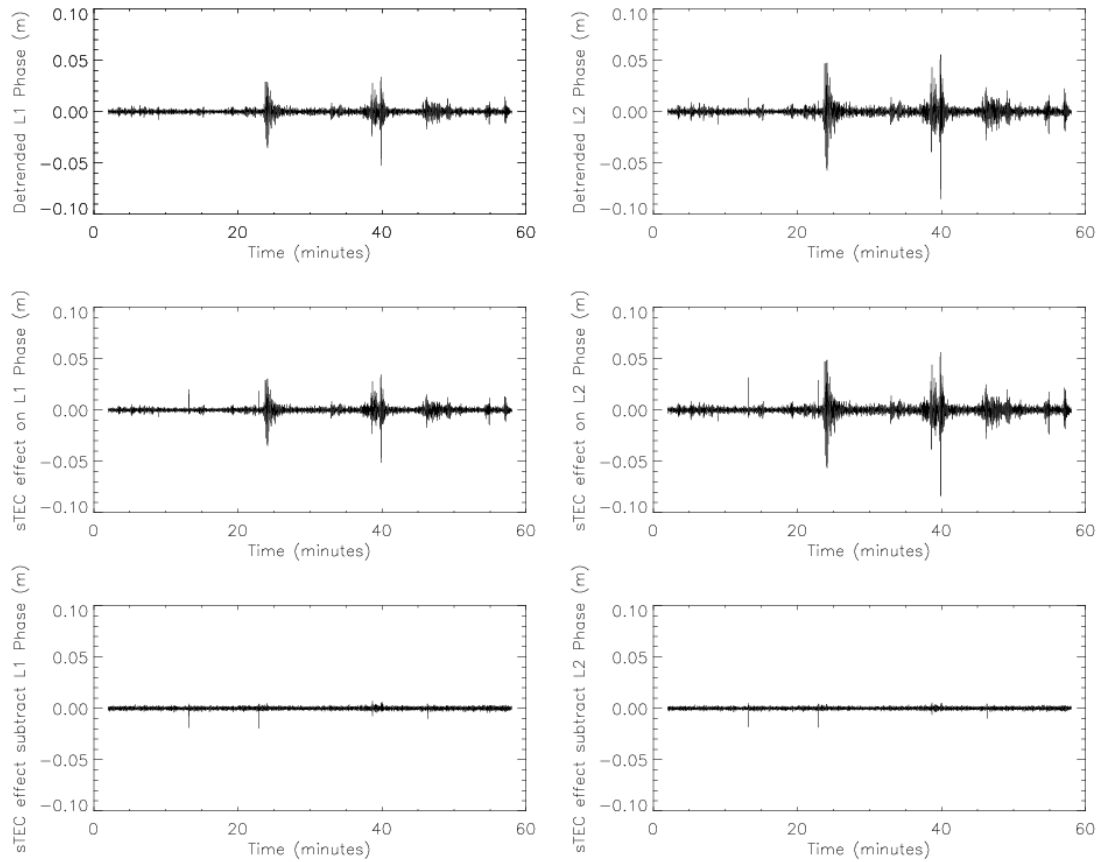


Figure 7.27 The L1 (top left panel) and L2 (top right panel) bandpass filtered carrier phase, filtered from 0.1 Hz to the appropriate Fresnel frequency, the estimated effects of the sTEC (middle panels) on the carrier phase, bandpass filtered to the same frequencies, and the differences between them (bottom panels) corresponding to the DOY 218 example.

7.3.4 Preliminary Determination of the Noise Floor

In the previous results, specifically sections 7.3.1 and 7.3.2, we use a noise floor frequency as determined by the amplitude scintillation events. It was argued that the noise floor frequency associated with the amplitude variations should be an underestimation of the noise floor frequency for the carrier phase. This is acceptable since we were most interested in only separating the refractive variations from everything else. For future works, specifically those interested in the scintillation portion of the carrier phase variations, it will become more important to accurately determine the noise floor frequency, and thus the full frequency range associated with the diffraction-induced phase variations. Work towards determining the noise floor of the GPS carrier phase during scintillation is uncommon. However, it is important that this work is done to more accurately determine this noise floor.

Scintillation is a unique source of stress on the PLL and thus may lead to an increase in the noise floor. Rebeyrol et al. (2006), although not focused on scintillation, have presented work on the noise associated directly with the receiver oscillator; this is the main source of GPS phase noise, as is discussed in more detail in Chapter 8. A combination of sources is shown to be factors in the overall noise, each with exhibiting a spectral power law with slopes ranging from 0 to -4. This is an extremely important result for ionospheric-induced variations in the carrier phase; previously determined scintillation spectral slopes falls directly in this range of noise source slopes. For example, the high latitude climatological work presented by Mushini (2012) shows a mean value of -1.75 for the spectral slopes. Methods of determining the noise floor for

the ionospheric-induced variations is thus very important to ensure parameters such as the spectral slope are not contaminated by this noise.

More recent work by Rougerie et al. (2016) has attempted to demonstrate the properties of the noise floor frequency, specifically during ionospheric-induced variations, and how changes in the receiver configuration may affect this noise floor. The work presented was performed using a GPS receiver simulator, which was provided with a clean signal and a signal affected by scintillation alternatively. With this method, Rougerie et al. (2016) can compare the spectrum of the output of the receiver simulator with the spectrum of the provided input. This can give an insight into the noise floor of the signal and see how changes in the receiver configuration or changes in the signal to noise ratio affect the receiver's output.

Two important results are demonstrated in this work. First, variations observed at frequencies greater than the PLL bandwidth frequency are inaccurate, and must be ignored; the bandwidth frequency can be described as the modulation frequency at which the PLL begins to lose its lock on the reference frequency. The second result is that the noise floor frequency decreases with the signal to noise ratio. Therefore, at lower signal to noise ratios, it is likely that the highest usable frequency for the event is less than the PLL bandwidth frequency. This is shown graphically in Figure 7.28 and Figure 7.29. In the figures, the curve labelled *input* (red) is the scintillation spectrum, as provided by a scintillation model, the curve labelled *no iono* (blue) is the spectrum of the

phase variations outputted by the receiver simulator when no scintillation is applied to the signal, and the curve labelled *iono* (green) is the spectrum of the carrier phase output from the receiver simulator during the times when the scintillation is present. The other curves are not relevant to this discussion. The difference between the two figures is that Figure 7.28 has an unrealistically high signal to noise ratio of 200 dBHz, while Figure 7.29 has a more reasonable value of 45 dBHz. Figure 7.28 also used a PLL bandwidth frequency of 5 Hz while Figure 7.29 uses 10 Hz.

Focusing first on the effect of the PLL bandwidth frequency, its effects can be observed in both Figure 7.28 and Figure 7.29. The *iono* curve should follow the *input* curve until any receiver effects have an impact. Where these curves begin to deviate is an indication of the noise floor frequency, the maximum frequency which can be used for scintillation analysis. In the case of Figure 7.28, the *iono* spectrum agrees very well with the *input* curve until the bandwidth frequency (5 Hz). Beyond the bandwidth frequency, these curves deviate. This behaviour illustrates the effect of the PLL bandwidth frequency on the outputted carrier phase variations. For visual reference, the *input* curve agrees well with the *input (no filter)* curve.

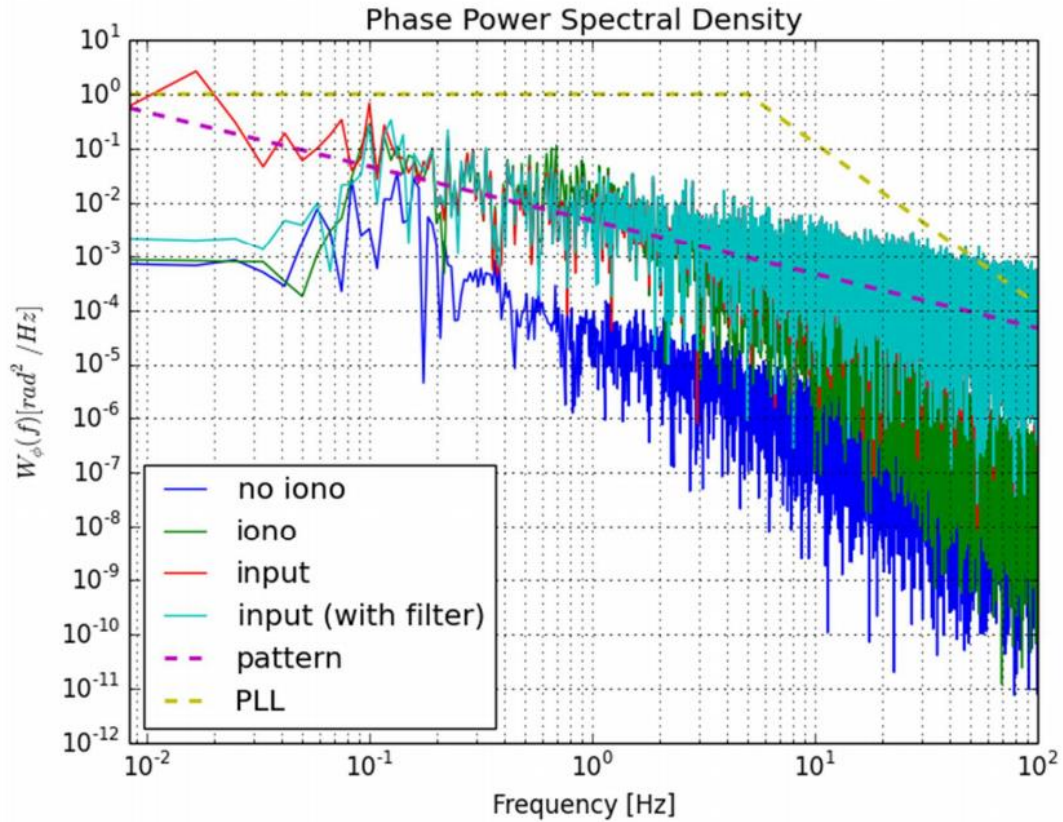


Figure 7.28 The comparison of the input modelled scintillation spectrum (*input*, red) to a GPS receiver simulator, the output from the simulator during the modelled scintillation (*iono*, green) and during no scintillation (*no iono*, blue). The simulator uses a 5 Hz bandwidth and a signal to noise ratio of 200 dBHz for this example (Rougerie et al., 2016).

For Figure 7.29, recall the bandwidth frequency has been increased to 10 Hz; thus, we would expect the receiver simulator output to begin to fail at 10 Hz. However, this is not the case. Rougerie et al. (2016) observed the *iono* spectrum deviates from the *input* spectrum at roughly 0.5 Hz. This suggests that the impact of decreasing the signal to noise ratio has a more severe impact on the carrier phase variations than the PLL

bandwidth and that the PLL bandwidth frequency is more like a theoretical maximum noise floor. The possible combinations of noise sources, as presented by Rebeyrol et al. (2006), are evident in this example, showing a roughly zero slope at the beginning of the deviation, followed by a slope of approximately the same value as the *input* curve (-2.5). Therefore, as suggested by Rougerie et al. (2016), works must determine where their spectra would deviate from the ‘input’.

The *no iono* spectrum during the realistic signal to noise example can be thought of as the noise spectrum; that is to say that this spectrum represents the noise sources of the receiver. We note that the *no iono* spectrum begins to deviate from the *input* spectrum at roughly the same frequency as the *iono* spectrum. This suggests that the effects of the receiver noise on a clean signal and a scintillation signal will be similar and further suggests that these higher frequencies represent the noise of the receiver. We suggest that the effects of the GPS receivers should be like the effects of the receiver simulator, and thus the noise spectra should share similar characteristics. These observations are used as the basis for determining the noise floor frequency for GPS scintillation events.

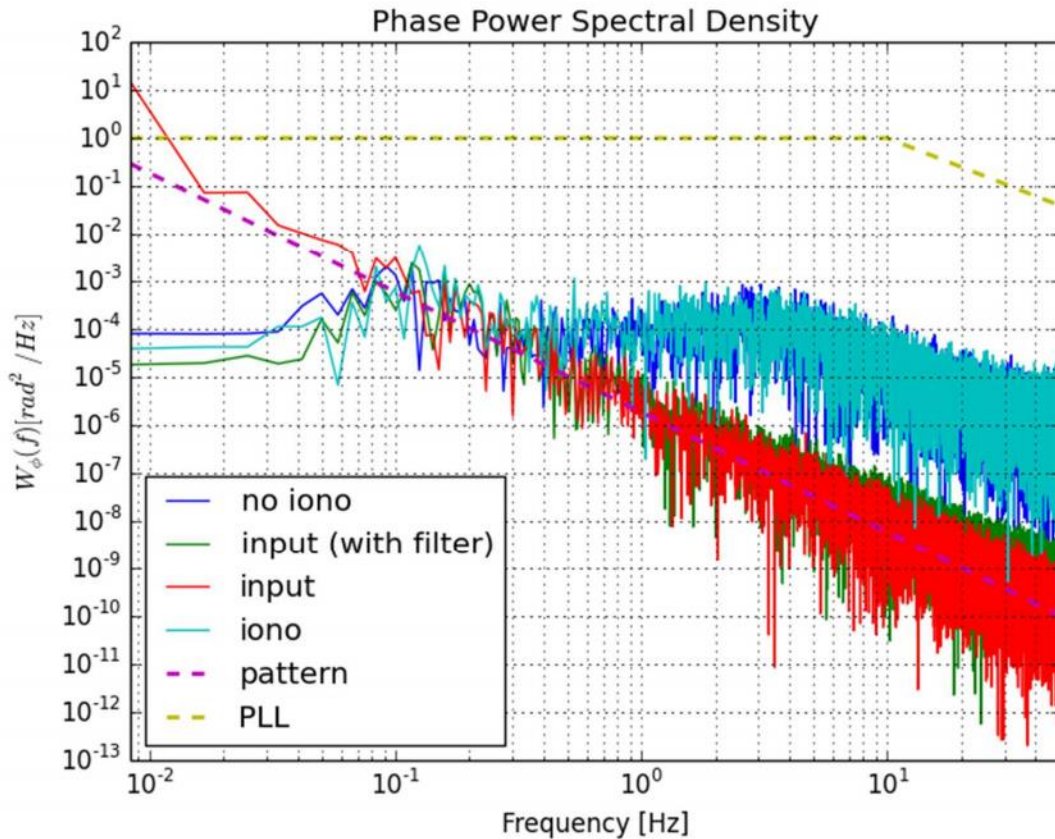


Figure 7.29 The comparison of the modelled scintillation spectrum (*input*, red) input provided to a GPS receiver simulator, the output from the simulator during the scintillation variations (*iono*, green) and when no scintillation occurs (*no iono*, blue). In this example, the simulator uses a 10 Hz bandwidth and a signal to noise ratio of 45 dBHz (Rougerie et al., 2016).

We compare the spectra of quiet time carrier phase to one another to observe this hypothesized noise floor spectrum. We define ‘quiet time’ phase as a time series of phase values with σ_ϕ less than 0.1; this assumes that these carrier phase time series are free of any rapid variations induced by anything other than the receiver. As an example,

we present four spectra taken during different times and different satellites at the same receiver; the data is taken from the receiver at the CHAIN Churchill station during DOY 70, 2015. The four spectra are presented in the top panel of Figure 7.30. The times and satellites used for the four spectra are presented in Table 7.3. The spectra all agree very well with one another, suggesting the source of the high frequency quiet time variations are of a common source. Since the spectra are taken from different satellites, different elevation angles, and at different times of the day (thus viewing different ionospheric conditions) it is likely that the common source is the receiver or antenna hardware. We note that these spectra qualitatively agree with the *no iono* spectrum presented in Figure 7.23, displaying the white noise floor followed by a power law behaviour with a negative slope.

Table 7.3 Colors, satellites, and time ranges for the quiet time carrier phase observable spectra presented in Figure 7.30.

Color	Satellite PRN	Time Interval (UTC HR:MM:SS)
Blue	1	04:05:00 – 04:08:20
Red	3	04:33:20 – 04:36:40
Green	30	00:13:20 – 00:16:40
Orange	17	02:13:20 – 02:16:40

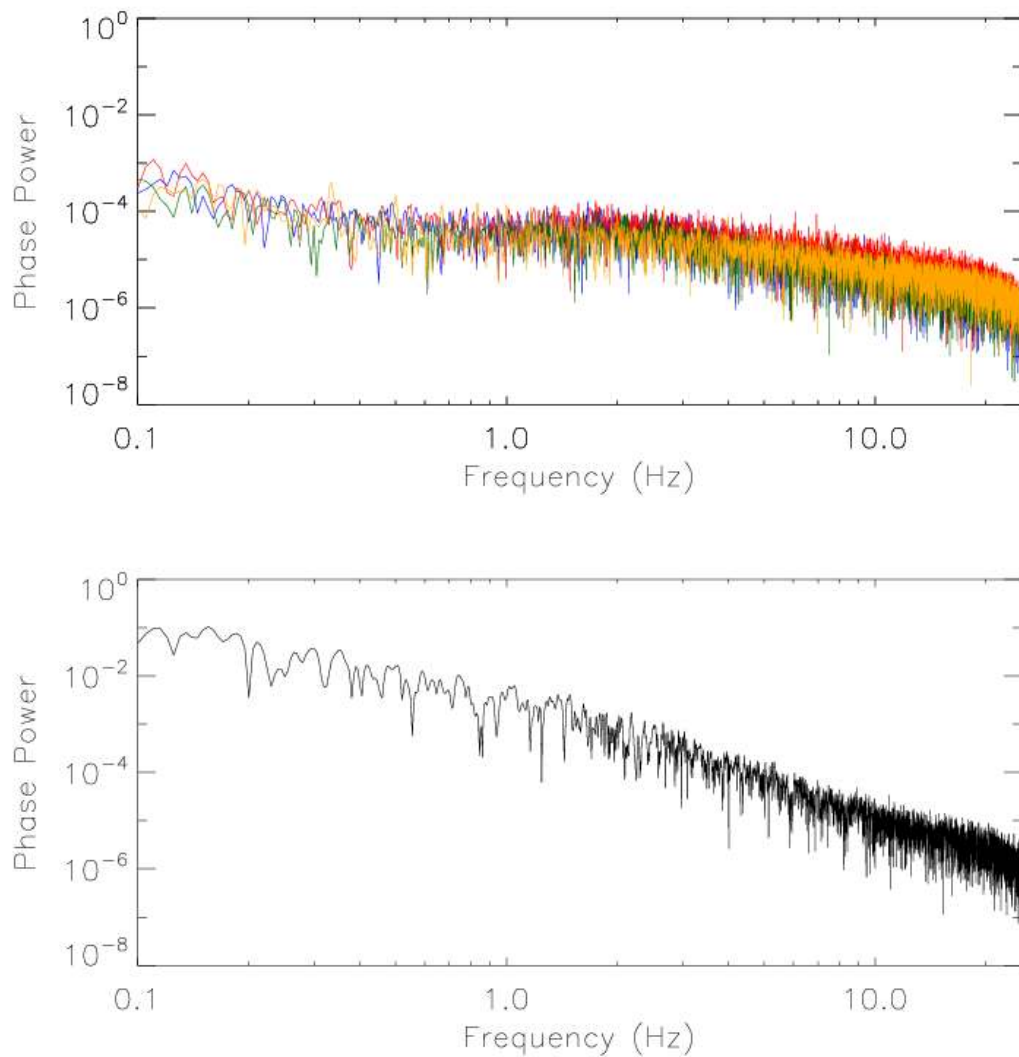


Figure 7.30 Comparison of four quiet time carrier phase spectra (top) and an ionospheric carrier phase variation event (bottom). The four quiet time spectra are taken from four different satellite, at different times throughout DOY 70. All data is taken from the CHAIN Churchill station.

We compare these quiet time spectra with an example ionospheric event. The event spectrum is presented in the bottom panel of Figure 7.30. This event was also taken from

the Churchill station, during DOY 70, using satellite PRN 1. It takes place from 04:46:40 – 04:50:00 UTC. It is clearly higher power through the lower frequencies as we would expect for an ionospheric variations event when compared to a likely noise floor spectrum. To better visualize the comparison between the quiet time spectra and the event spectra, they are plotted together in Figure 7.31. From roughly 0.1 Hz to 2 Hz the event spectrum displays a constant power law behaviour typical of what we expect for scintillation. At roughly 2 Hz there is a break in the spectrum, resulting in a steeper slope. If using this technique as a method of determining the noise floor frequency, the frequency at which the event spectrum and the noise floor spectra begin to agree would be the obvious choice. For this example, the noise floor frequency would be roughly 7 Hz. This is less than typically thought for ionospheric-induced GPS phase variation events (Mushini, 2012; McCaffrey and Jayachandran, 2017a). However, we note that the frequency at which the break in the event spectrum occurs agrees well with the break in the noise floor spectra. This break in the noise floor spectra shows a deviation from a near-zero slope to a negative slope. This agreement in the break frequency suggests that care must be taken in works focusing on ionospheric-induced breaks in the event spectra, like those discussed in Elkins and Papagiannis (1969), Franke and Liu (1983), and Carrano and Rino (2016) and references therein.

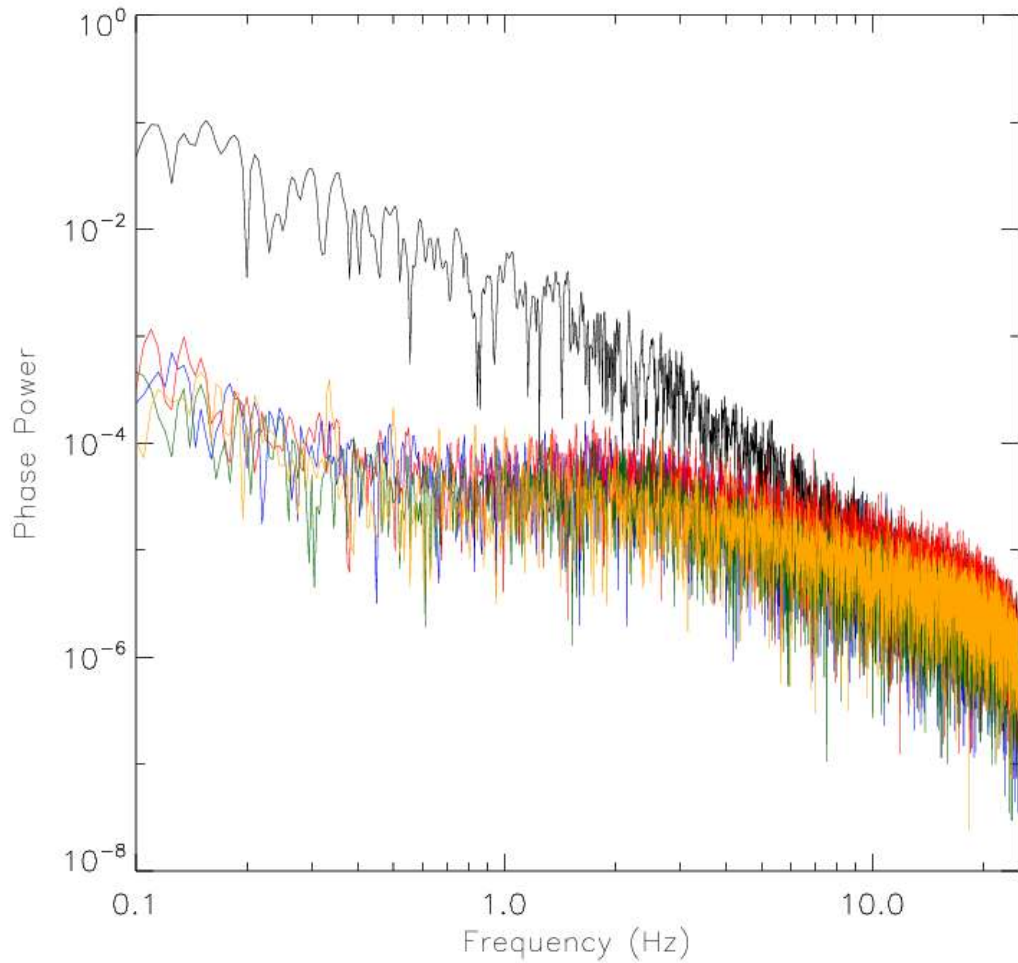


Figure 7.31 The noise floor spectra and event spectrum from Figure 7.30, plotted together to better visualize the comparison.

We note that although different satellites and times were used in the comparison of the quiet time spectra in the previous example, the same day and location were used. This leads to questions about persistent low magnitude variations induced by the ionosphere which may be responsible for the spectral shape we observe. This is further suggested by

the carrier phase observable being an integrated quantity. Although the qualitative shape of the quiet time spectra is like the shape presented by Rougerie et al. (2016), which uses modelled and simulated data containing no real ionosphere; it is still an issue that should be addressed.

A Septentrio PolaRxS receiver was initially installed at the CHAIN GRIC station in 2015 and was later relocated to the CHAIN lab on the University of New Brunswick Campus in Fredericton, New Brunswick (FRSC). Using data obtained from this receiver, once in the GRIC location and once in the FRSC location, we examine the quiet time spectra of two very different ionosphere configurations. Since the FRSC location is located at roughly 45.9 °N, 293.4 °E, it can be considered in the mid-latitudes. An example of quiet time GRIC carrier phase data, FRSC carrier phase data, and the PRN 3 quiet time example from Figure 7.30 are presented in Figure 7.32. The PRN 3 example from CHUC is represented by the blue curve, the GRIC spectrum, taken during UTC hour 0, on DOY 200 of 2015, is represented by the red curve, and the FRSC spectrum, taken on DOY 138, UTC hour 3, in 2017, is represented by the green curve. The qualitative shape of the quiet time spectra for GRIS and FRSC agree very well and agree well with the CHUC example as well. Note that the CHUC example was not the same receiver as the GRIC and FRSC example. The GRIC and FSRC curves do appear to be slightly lower in power than the CHUC curve; we attribute this to the hardware noise levels itself, suggesting the magnitude of the noise associated with that specific receiver may be marginally lower than the CHUC configuration.

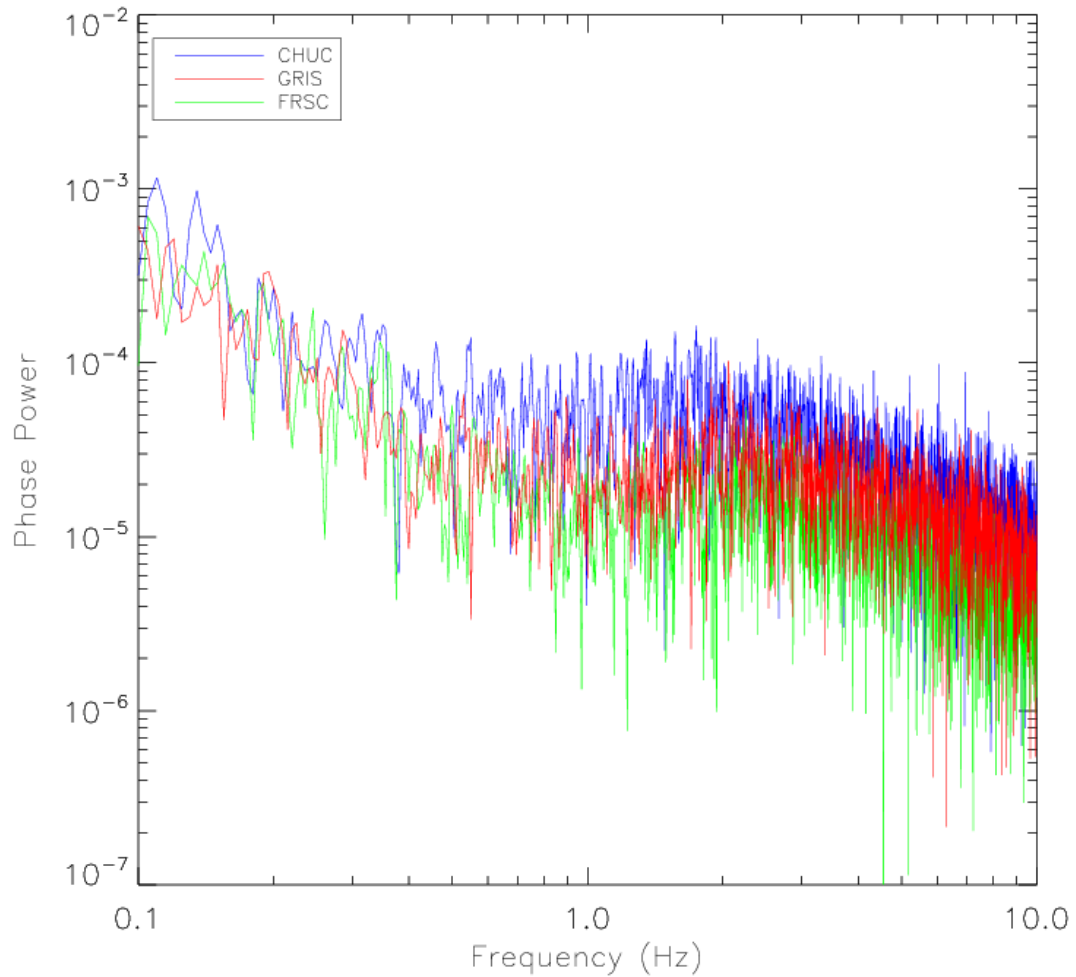


Figure 7.32 Comparison of the quiet time spectra were taken from the CHUC station (blue), the GRIS station (red) and the FRSC station (green). The CHUC station represents the examples presented in Figure 7.30. The GRIS and FRSC station use the same receiver, relocated from the GRSC station (2015) to the FRSC (2017).

In these comparisons, we see that the quiet time curves with varying time, year, satellites, locations, antennas, and receivers (same receiver model) all agree very well,

and present the same qualitative spectral shape; the same spectral shape observed by the simulations presented by Rougerie et al. (2016). This suggests that the quiet time spectra reveal information about the receiver noise levels and that the receiver noise levels are dominating the other possible sources or carrier phase variations at these quiet times.

Work towards determining a valid method of obtaining the noise floor frequency during ionospheric-induced carrier phase variations events is ongoing. Further work is needed to determine if the quiet time spectra are an appropriate view of the receiver noise floor. The presented preliminary analyses suggest this is an appropriate method, but further work is needed. Investigations into the relationship between these quiet time spectra and the break in some scintillation event spectra must also be considered.

7.4 Conclusion

Using independently tracked L1 and L2 carrier phase, we outlined methods to isolate the purely refractive contribution to ionospheric-induced GPS carrier phase events. Rapid variations in the presented frequencies are very often assumed to be diffractive in nature, due to Fresnel-scale and smaller irregularities in the electron density leading to diffractive variations in phase. These variations were shown to be refractive first by using the IFLC, showing a large portion of the variations followed the inverse-frequency-squared dependence we expect from refractive variations.

Using corresponding variations in the amplitude, an approximate Fresnel frequency was obtained for the presented events. This gave a lower frequency limit to the diffractive variations. This validated the IFLC result, showing many of the lower frequency variations were not diffractive. Using the Fresnel frequency to bandpass filter the carrier phase observable to only the suspected refractive variations, we showed that the variations followed the expected inverse-frequency-squared relationship very well. This was performed by calculating the linear fit between the L1 carrier and L2 carrier phase variations. The correlations revealed a high correlation coefficient, indicative of refractive variations, and a slope very near 1.64, the square of the ratio of the carrier frequencies. This same analysis was performed using an example event where the L5 carrier phase was available as well as the L1 and L2 carriers. This provided three carrier pairs to perform the linear fit, each with their own expected slope value. All three pairs performed well, returning values near what was expected.

Lastly, the purely refractive portion of the sTEC was analyzed, bandpass filtered up to the previously obtained Fresnel frequencies. The variations observed at these frequencies in the sTEC were shown to be very nearly identical to the variations in the carrier phase. The expected effect of these sTEC variations on the carrier phase observables was calculated, and differenced from the real carrier phase data. A near zero difference was observed, further indicating that the variations are purely refractive; thus, these variations are caused purely by changes in the electron density along the ray path and are not artifacts due to diffraction.

Understanding that these high-rate variations on the GPS carrier phase can be purely refractive may have implications on trans-ionospheric radio wave error mitigation, as refractive variations are coherent and follow a well-defined relationship with the electron density. This should make for simpler modelling, prediction, and removal of these variations from the carrier-phase observable. The coherent nature of the variations also means that with knowledge of the variations on only one of the carrier frequencies, one can accurately estimate the effects on other carrier frequencies as well; this cannot be easily done with diffractive variations.

A preliminary analysis of the determination of the noise floor frequency for phase variations events is also presented. The high-frequency noise of the GPS carrier phase observable was shown to be coloured, exhibiting a power law behaviour. This is like what is expected for high-frequency ionospheric-induced phase variations, and thus it is important to understand the noise sources to ensure they do not contaminate ionospheric studies. Based on quiet time analysis of the carrier phase observable, a common qualitative spectral shape was observed which was suggested to be reminiscent of the receiver noise floor spectrum. This spectral shape consisted of a white noise portion followed by the coloured noise. Comparing this noise spectrum with a typical event spectrum suggested that the noise floor frequency for ionospheric-induced phase variations events may be much lower than originally thought. We also note a break in the event spectrum corresponding to the break in the noise spectrum. This may suggest that breaks in the carrier phase spectrum during ionospheric-induced events may not be

due to effects of the ionosphere, but rather due to the effects of the receiver hardware on the high frequencies of the signal.

8 High-Frequency TEC

8.1 Introduction

The dispersive nature of the ionosphere can be exploited in conjunction with the multiple carrier frequencies transmitted by the GPS; the multiple GPS frequencies can be manipulated to obtain an integral measure of the electron density along the signals' ray paths. The resulting measurement is referred to as the TEC. The spatial and temporal resolution of the GPS constellation allows for monitoring the TEC in most areas of the globe, including the dynamic high latitude region. The auroral ionosphere specifically is very dynamic, with structures in electron density varying dramatically in both spatial and temporal scale sizes (Trondsen and Cogger, 1998; Knudsen et al., 2001). The modernization of GPS and its introduction of the open L2C code allows for higher sampling rates of the L2 carrier phase observable and in turn the TEC. The use of independent tracking by the Septentrio receivers, which are used in the CHAIN, ensures the most accurate high-frequency dynamics of the L2C, and therefore TEC, measurements. The more accurate and higher sampling rate of TEC allows for monitoring of these very small-scale structures in electron density in the auroral region. Studying these small-scale structures is critical in furthering our understanding of the mechanisms which generate them as well as the underlying dynamics which drive them.

Previous TEC analysis, both in and out of the auroral region, were performed primarily using 30 second or 1-second sampling rates. With CHAIN's recent expansion and the

introduction of the Septentrio PolaRxS Pro receiver into its network, auroral region TEC at a maximum sampling rate of 100 Hz is now possible. This major increase in the sampling rate allows for the first look at sub-second features in TEC and thus the auroral region electron density. This is used to attempt to explain the underlying mechanisms which cause these small-scale structures to form.

8.2 Data and Methods of Analysis

The presented GPS-derived TEC data originates entirely from Septentrio PolaRxS Pro receivers located within the CHAIN. The L1C/A and L2C carrier phase observables are tracked at sampling rates of either 50 Hz or 100 Hz, depending on the location. This allows for the calculation of TEC at a maximum rate of 100 Hz. Note that since only L2C can be used, only satellites transmitting L2C are available for this study. Therefore, when we mention ‘all available satellites’, we refer to only block IIR-M or newer satellites.

The standard method of calculating sTEC, as is outlined in Chapter 4, is used. We recall the effect of the changes in refractive index on the GPS carrier phase observable,

$$\eta = -\frac{s_1}{f^2} - \frac{s_2}{f^3} - \frac{s_3}{f^4} \quad 8.1$$

$$s_1 = 40.309 \int_r^S N_e dl \quad 8.2$$

$$s_2 = 1.1284 \times 10^{12} \int_r^S N_e B \cos \theta dl \quad 8.3$$

$$s_3 = 812.42 \int_r^S N_e^2 dl + 1.5793 \times 10^{22} \int_r^S N_e B^2 (1 + \cos^2 \theta) dl \quad 8.4$$

where N_e is the electron density, B is the geomagnetic field, and θ is the angle between the GPS ray path and the geomagnetic field vector; we define TEC as

$$TEC = \int_r^S N_e dl \quad 8.5$$

Thus, truncating the higher order terms in ionosphere delay, we can calculate TEC in the following way:

$$TEC = \frac{f_{L1}^2 f_{L2}^2}{40.3(f_{L1}^2 - f_{L2}^2)} \Delta\Phi \quad 8.6$$

where f is the carrier frequency, and $\Delta\Phi$ is the difference between the L1 and L2 carrier phase observables.

In our analysis, we must ensure the variations we observe are not caused by artifacts due to the higher order terms which are truncated in the TEC derivation or due to diffractive effects. We must also ensure the variations are significant, meaning they are above the receiver noise floor. We describe the methods used in estimating the magnitudes of the higher order terms in the ionospheric delay and the receiver noise in the following subsections.

8.2.1 Bounding the Higher Order Terms

A portion of the analysis will focus on the higher order terms in the TEC equation, derived from the Appleton-Hartree equation. These terms are presented in equations 8.1 through 8.4. We are interested in the possible magnitudes of these higher order terms and their impact on the high-frequency TEC dynamics. To estimate these magnitudes, we use the methods outlined in Datta-Barua et al. (2008), modified for the auroral region where necessary. They use methods of estimating the upper bounds of the magnitudes of these higher order terms. To begin, we note that both the second and third order terms (equations 8.3 and 8.4) both depend on the magnetic field. To simplify and bound these equations, the magnitude of the magnetic field at an IPP corresponding to a height of 350 km is chosen. This height is meant to represent the peak height for the density and is the height typically used when performing thin shell approximations (Lanyi and Roth, 1988; Wilson et al., 1995). This height also agrees well with peak density height measurements performed in the Canadian high latitude region (Mushini et al., 2009). The magnetic field term will have the most impact at the peak density, therefore, taking

the magnitude of the magnetic field at this height and using it as an average height along the entire ray path creates an upper bound. This then allows the magnetic field term to be removed from the integrals. According to Campbell (1996), the geomagnetic field has been shown to decrease during times associated with an active ionosphere, and Mannucci et al. (2005) have shown that the peak electron density increases in height, where the geomagnetic field is weaker, during active ionospheric times. Therefore, choosing the magnitude of the B field at a quiet time peak height will act as an upper bound for active ionospheric times as well.

In both terms, the angle between the GPS ray path and geomagnetic field vector are present. This angle will inherently get shallower as we increase in geographic latitude, due to the fixed inclination angle of the GPS orbital planes. To upper bound the cosine of the angle at high latitudes, we choose a fixed angle of zero.

Lastly, in the third order term, there is the square of the electron density. We simplify and bound this term again using the methods outlined in Datta-Barua et al. (2008):

$$\int_r^s N_e^2 dl \approx N_m \nu \int_r^s N_e dl \quad 8.7$$

where N_m is the maximum density, and ν is the shape factor. The maximum density is estimated by

$$N_m = \frac{I_v}{100 \text{ km}} \quad 8.8$$

where I_v is the absolute first order ionospheric delay term, mapped to vertical. The maximum density is then the total density spread over a 100 km band. Bilitz (2001) showed that the maximum density is usually spread over a 150 km to 200 km band, thus, using a thickness of 100 km here, and a shape factor of 1, we ensure an upper bound estimate.

Substituting these upper bound approximations into equations 8.3 and 8.4 gives the following:

$$s_2 \leq s'_2 \int_r^s N_e dl; \quad s'_2 = 1.1284 \times 10^{12} B \cos(0)|_{IPP} \quad 8.9$$

$$s_3 \leq (s'_3 + s''_3) \int_r^s N_e dl; \quad s'_3 = 812.42 N_m \nu; \quad s''_3 = 1.5793 \times 10^{22} (2B^2)|_{IPP} \quad 8.10$$

These equations will be used in estimating the upper bounds of the second and third order terms in the ionospheric delay.

8.2.2 Receiver Phase Noise

The dominant noise observed in the carrier phase observable, and thus the TEC, originates from the receiver Phase Lock Loop (PLL). Therefore, we can estimate the magnitude of the TEC noise by modelling the PLL jitter effects. The total PLL jitter can be expressed as (Irsigler and Eissfeller, 2002):

$$\sigma_{PLL} = \sqrt{\sigma_T^2 + \sigma_A^2 + \sigma_V^2} + \frac{e(t)}{3} \quad 8.11$$

where σ_T is the thermal phase noise, σ_A is the Allen deviation noise, σ_V is the vibration induced noise, and $e(t)$ is the dynamic stress tensor. The thermal noise term is modelled as:

$$\sigma_T = \sqrt{\frac{B_L}{c/n_0} \left(1 + \frac{1}{2T \cdot c/n_0}\right)} \quad 8.12$$

where B_L is the receiver loop bandwidth frequency, c/n_0 is the carrier to noise ratio, and T is the predetection integration time. For the setup of the Septentrio PolaRxS Pro receivers in CHAIN, the receiver loop bandwidth frequency is 15 Hz, and the predetection integration time is 0.01 s. The carrier to noise ratio is logged at a 1 Hz

sampling rate in this setup, allowing the thermal noise to be calculated at a maximum 1 Hz sampling rate as well.

The Allen deviation noise is dependent on the order of the PLL used in the receiver. For the Septentrio PolaRxS Pro, this is third order. This results in the following representation for the Allen deviation noise:

$$\sigma_A^2 = 2\pi^2 f_0^2 \left(\frac{\pi^2 h_{-2}}{3\omega_L^3} + \frac{\pi h_{-1}}{3\sqrt{3}\omega_L^2} + \frac{h_0}{6\omega_L} \right) \quad 8.13$$

where f_0 is the carrier frequency, $\omega_L = 1.2B_L$, and the h values are clock parameters dependent on the oscillator used in the receiver. For the Septentrio PolaRxS Pro an Oven Controller Crystal Oscillator (OXCO) is used. This results in values of $h_0 = 2.51 \times 10^{-26} \text{ s}$, $h_{-1} = 2.51 \times 10^{-23} \text{ s}$, and $h_{-2} = 2.51 \times 10^{-22} \text{ s}$.

The vibration induced noise is, as the name suggests, dependent on external sources of vibration felt by the oscillator. For the CHAIN Septentrio receivers, most are in remote locations with little to no external vibration-inducers in proximity to the receiver. If vibrations are felt by the receiver, they should be short-lived and of small enough magnitude that they will be negligible. However, in an effort to ensure the magnitudes are an upper bound of those likely encountered in the real data, we include the vibration

induced jitter term using common values for a vibration spectrum as presented in Kaplen and Hegarty (2005). For a third-order PLL the vibration induced phase jitter can be modelled like:

$$\phi_V^2 = 2\pi f_0^2 \int_{f_i}^{f_f} \frac{k_g^2(\omega) G_g(\omega) \omega^4}{\omega_L^6 + \omega^6} d\omega \quad 8.14$$

where k_g is the oscillators g-sensitivity, and G_g is the single-sided vibration spectral density. The integral is taken over the vibration spectral density, ranging from the frequencies f_i to f_f . Using constant g-sensitivity of 1×10^{-9} 1/g and a constant spectral density of 0.005 g²/Hz (one-tenth the strength of a typical aircraft vibration spectrum, (Irsigler and Eissfeller, 2002)), and setting the frequency spectrum from 0 Hz to infinity we can calculate the expected magnitude. Taking these assumptions into account, the above equations can be simplified to:

$$\phi_V^2 = 2\pi f_0^2 k_g^2(\omega) G_g(\omega) \int_{f_i=0}^{f_f=\infty} \frac{\omega^4}{\omega_L^6 + \omega^6} d\omega = \frac{2\pi f_0^2 k_g^2(\omega) G_g(\omega)}{3\omega_L} \quad 8.15$$

Evaluating the expression results in a magnitude of approximately 0.03 rad for the L1 carrier.

The dynamic stress tensor is dependent on the motion of the receiver, as felt by the oscillator. More precisely, it is dependent on the derivative of position to the same order as the PLL order. As was previously mentioned, the PLL order for the Septentrio PolaRxS Pro is third order, meaning the stress tensor is sensitive to the third order derivative of position, or the first order derivative of acceleration. The equation for the dynamic stress tensor, for a third-order PLL, is:

$$e(t) = \frac{d^2x(t)}{dt^2} \cdot \frac{1}{(1.2B_L)^2} \quad 8.16$$

Note that the dynamic stress tensor equation is in units of meters. Since the CHAIN stations are set up in remote locations and left stationary after they have been set up, there should be no effect from the dynamic stress tensor term. Therefore, we choose to ignore this term in the final PLL jitter estimation.

8.2.3 Constraining to Refractive Variations

As was discussed in Chapter 7, ionospheric-induced high-frequency variations in the carrier phase can come from both refractive and diffractive mechanisms. Here we are focusing on only sub-second variations in the TEC. Recall that TEC is directly proportional to the difference between the L1 and L2 carrier phase observables, as is described in equation 4.19. If these sub-second variations are diffractive in nature, they

are not representative of the true changes in electron density and are thus considered artifacts in the TEC. To ensure the results do not contain these artifacts, we develop criteria to eliminate these diffractive events. These are based on the work presented in Chapter 7.

First, we define significant variations in TEC. The data, as it is provided by the Septentrio receiver, is in one-hour increments, aligning with UTC time. Thus, results are processed in these one-hour increments. We examine the TEC using the standard deviations taken over one-second intervals. This is described in more detail in the following section. If these one-second standard deviations exceed the two-sigma threshold then they are considered significant. The two-sigma threshold is defined as

$$\sigma_2 = \langle \bar{x} \rangle + 2\langle \sigma_x \rangle \quad 8.17$$

where x is the data set of interest, and the square brackets indicate an interval of time of one UTC hour, aligning with the provided data files unless otherwise stated.

Two conditions must be met for the sTEC variations to be considered real refractive variations and not diffractive artifacts. First, there must be no significant variations in the amplitude of the signal during the same time as the significant TEC variations.

Variations in the amplitude imply diffractive variations are present, as the amplitude will

not vary due to pure refractive variations. We note that amplitude variations do not rule out the possibility of refractive variations in the sub-second range; this is seen in the examples presented in Chapter 7. However, it does indicate that diffractive variations are present in the high frequencies, therefore, to ensure we are dealing with only purely refractive variations, TEC variations with significant corresponding amplitude variations are chosen to be ignored. Significant variations are determined using the scintillation index S_4 , described in equation 5.8. For a significant TEC variation event, we calculate the S_4 for both the L1 and L2 amplitudes. If the S_4 for either carrier exceeds the two-sigma threshold during the hour in which the event takes place, then the variations in the amplitude are considered significant at that time. TEC variations corresponding to these amplitude variations are then removed from the analysis.

The second criterion for determining the purely refractive variations is based on the inverse frequency-squared dependence discussed in equation 4.16 and the results presented in Chapter 7. If variations in the L1 and L2 carrier phase are refractive then they will be deterministic, following an inverse-frequency squared relationship. If the ratio of the two variations are taken, or the slope of the linear fit between the two is determined, the result should be approximately equal to the ratio of squared frequencies. For the L1 and L2 carriers, this is roughly 1.646. When significant variations are found in the TEC, the slope of the fit between the L1 and L2 carrier phase is obtained. Based on the results presented in Chapter 7, we bandpass filter the L1 and L2 carrier phase observable from 0.1 Hz to 2 Hz before performing the fit. If the slope of the fit lies between 1.62 and 1.66, then the event is considered refractive, otherwise, the TEC

variations are removed from the analysis. The slope and frequency ranges were chosen based on heuristic analysis, comparing the slopes of established refractive events with events which were not dominantly refractive.

An example of a refractive phase variations event determined using the above criteria, is presented in Figure 8.1 and Figure 8.2. This example was taken from the Churchill station (CHUC) within the CHAIN, using satellite PRN 1 during UTC hour 4. In Figure 8.1, the detrended L1 and L2 carrier phase observables are presented in the top left and top right panels respectively. The event of interest is clearly visible centred roughly on 47 minutes. The L1 and L2 detrended amplitude are presented in the middle left and middle right panel respectively. From the detrended amplitude alone it is clear that no significant variations occur with the phase variations event. In the bottom panels, the corresponding S_4 is presented, L1 on the left and L2 on the right. The red line indicates the two-sigma threshold. The L1 and L2 S_4 do not exceed the threshold during the phase variation event, and this meets the first criterion. The linear fit between the L1 and L2 carrier phase variations during the event is presented in Figure 8.2. The slope is 1.65, lying within the 1.62 – 1.66 range. Thus, this example event is a refractive variation event based on the established criteria.

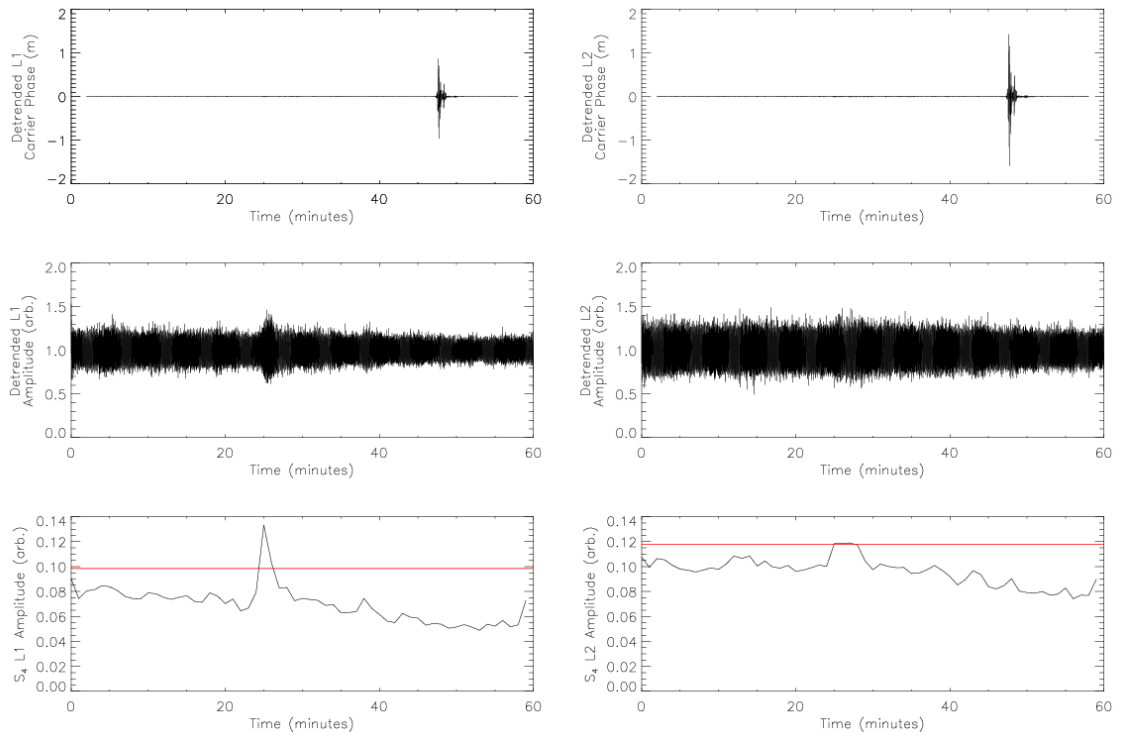


Figure 8.1 Example phase variations induced by purely refractive variations based on the established criteria. Data was taken from the CHUC station using satellite PRN 1 during UTC hour 4. The detrended L1 (top left) and L2 (top right) carrier phase observables are presented with the corresponding detrended L1 (middle left) and L2 (middle right) amplitude data. The event takes place at roughly 47 minutes. The corresponding S_4 for each amplitude data set is presented in the bottom panels with the two-sigma rule threshold in red. The S_4 does not exceed the threshold during the phase variation event.

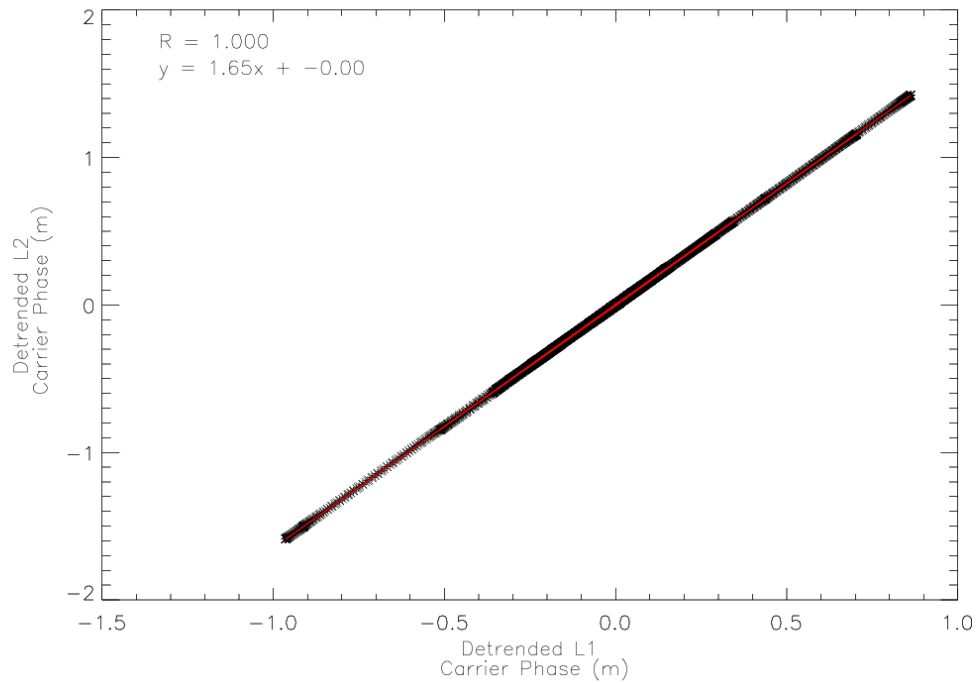


Figure 8.2 The linear fit between the detrended L1 and L2 carrier phase observables during the example event. The slope is 1.65, falling within the 1.62 – 1.66 range chosen for the refractive variations criteria.

8.3 Results and Discussion

To begin the analysis of the sub-second signatures in the high-frequency TEC, we qualitatively examine the high-frequency variations in an example sTEC data set. One minute of representative sTEC data is presented in the top panel of Figure 8.3. To better visualize the sub-second variations in the sTEC, a two-second subset of the data is presented in the bottom panel. Clear variability is observed in the sub-second regime,

with very small magnitudes, on the order of 0.01 TECU. These variations are representative of the low magnitude sTEC we observed for this study. More active sTEC examples will be presented later. Due to the very small magnitude and consistent nature of these variations, we suggest two possible causes for them; artifacts due to the neglected higher order terms in the ionospheric delay equation, or high-frequency receiver noise.

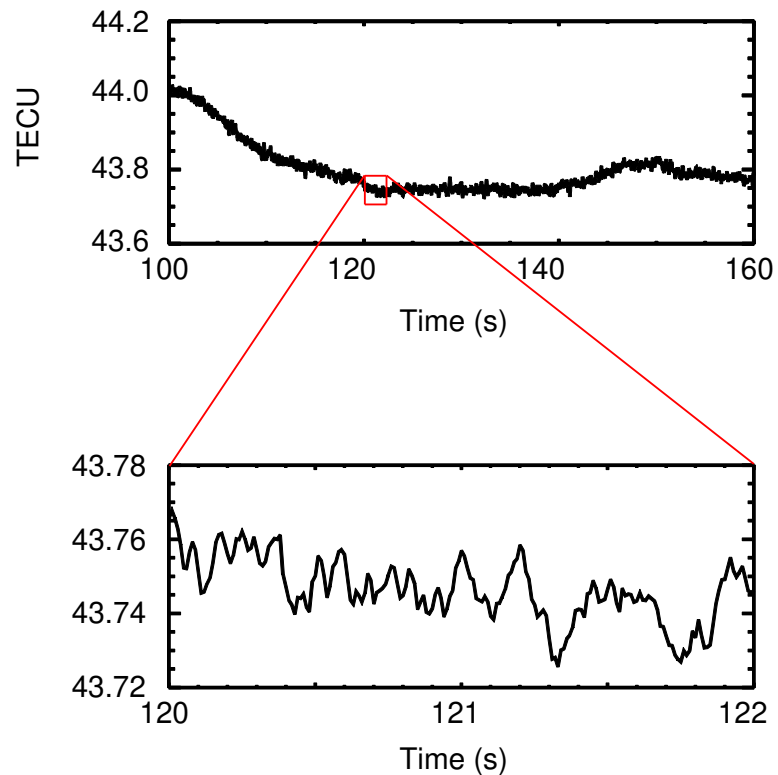


Figure 8.3 A qualitative example of the small amplitude, high-frequency variations in the inactive high-frequency sTEC. The top panel shows a representative example of the 100 Hz sTEC, for one minute. The bottom panel shows a two-second subset of the above sTEC.

To better quantify the sub-second sTEC variations, we calculate the standard deviation of the time series, using a one-second window. This will give a method of quantifying the magnitude of the sub-second variations. The one-second standard deviations were calculated for all available satellites at the Churchill and Fort Simpson stations for 50 full days worth of data. The median of the standard deviations was found to be 0.012 TECU with a standard deviation of 0.001 TECU. An example of the one-second standard deviation for an inactive two and a half hours of sTEC data is presented in Figure 8.4.

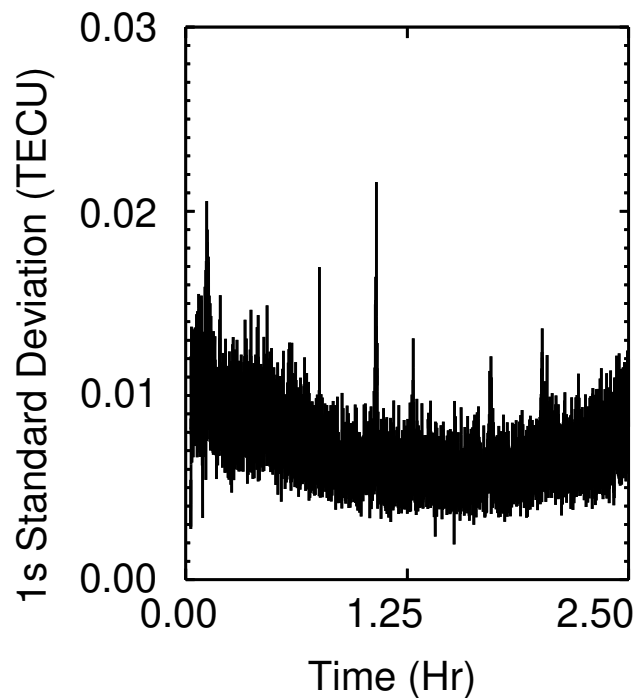


Figure 8.4 A representative example of the one-second standard deviations of sTEC used to quantify the sub-second variations in the high-frequency TEC.

Recall in Chapter 4, where it was discussed that the GPS-derived sTEC is directly proportional to the delay induced on the GPS carrier phase observable and that the refractive index of the ionosphere is derived from the Appleton-Hartree equation. In deriving the refractive index, the Appleton-Hartree equation is Taylor expanded in frequency and truncated to the first term. The first term accounts for most of the effects, making the higher order terms negligible in most cases. However, the sub-second variations we observe are very low magnitude. Therefore, the higher order terms must be examined further. Many works have been done to estimate the effects of the higher order terms on the TEC (for example, see Kedar et al. (2003) and Hoque and Jakowsky (2007)), however, these works focus on the mid- and low-latitude regions. The assumptions and data used in these studies for these regions may not be acceptable for the high latitudes, so we perform a more appropriate analysis here. We use equation 8.1 with equations 8.9 and 8.10 outlined in the previous section, to obtain the expected magnitudes of the second and third order terms in the ionospheric delay. This was done for all available satellites, visible to either the Churchill or Fort Simpson stations, for the same 50 days used for the one-second standard deviation result. The median of the expected magnitudes for the higher order terms was 0.042 TECU with a standard deviation of 0.023 TECU. Note that this is an upper bound on the magnitudes. Therefore, although the median of these magnitudes is larger than the median of the one-second standard deviations in sTEC, we cannot conclude with certainty that these variations are an artifact of the higher order effects. However, it is likely that the higher order terms are contributing to these sTEC variations.

We also mentioned that these small magnitude variations in sTEC may be caused by receiver noise. Again, the method of estimating the magnitude of the receiver phase noise, or jitter, is outlined in the previous section. The jitter was obtained for each available satellite at the Churchill and Fort Simpson station, for the same 50 days used in the previous results. The median jitter was found to be 0.022 TECU with a standard deviation of 0.001 TECU. This is also significantly larger than the magnitude of the variations being observed in the sTEC. This estimation of the jitter is likely also an overestimation due to the inclusion of the vibration induced jitter term. However, with both the jitter and the higher order term magnitudes being significantly larger than the TEC variations, we must conclude that these variations are caused by a combination of these sources. This means that these low magnitude, consistently observed variations are not ionospheric in nature.

As was mentioned near the beginning of this section, larger magnitude sub-second variations were observed as well. These were less frequent, but with magnitudes occasionally greater than 2 TECU. The one-second standard deviations in sTEC, for an example two-hour active period, is presented in Figure 8.5. Large magnitude variations are observed, beginning most prominently at approximately 4.8 hours, with a few less intense events observed at 5.1 hours, 5.4 hours, and 5.7 hours. Note that the expected phase jitter for the two hours is presented as the green line and the expected magnitude of the higher order effects in the ionospheric delay is represented by the blue line. Both the higher order effects and the phase jitter are much too small to account for the first

and fourth events. This suggests that these events are more than likely ionospheric-induced variations in the sTEC. Recall, however, in the previous section, the estimate of the magnitude of the higher order terms in the ionospheric delay is dependent on an estimate of the magnitude of the geomagnetic field. For the analysis thus far, the International Geomagnetic Reference Frame (2008) model has been used. This model will not produce high-frequency variations in the field which may, in fact, be present during these active times in the sTEC. If these high-frequency variations in the geomagnetic field are of a large enough magnitude, it could induce large variations in the ionospheric delay stemming from the higher order terms. We present the magnitude of the geomagnetic field variations necessary to cause variations in the sTEC ranging from 0.1 TECU up to 3 TECU. This is presented in Figure 8.6. To cause variations of just 0.1 TECU, the geomagnetic field must vary with magnitudes on the order of 100 μT ; this is unrealistically large. Therefore, it is very unlikely that any variations in the geomagnetic field are responsible for the large magnitude variations in sTEC.

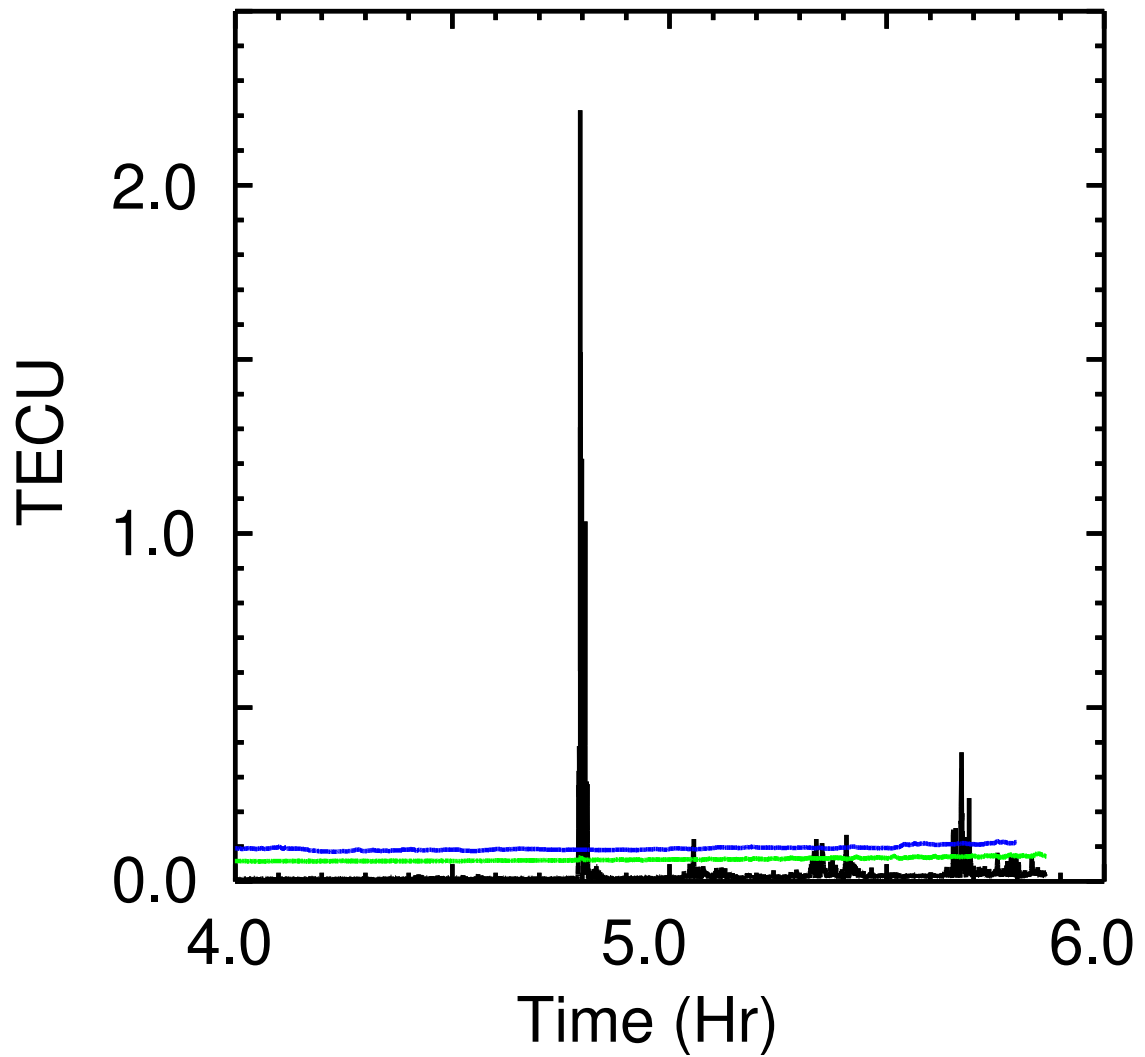


Figure 8.5 An example of active sTEC, where larger magnitude sub-second variations are present. The one-second standard deviations in TEC are presented in black, the expected magnitude of the receiver phase jitter in green, and the expected magnitude of the higher order delay terms are in blue.

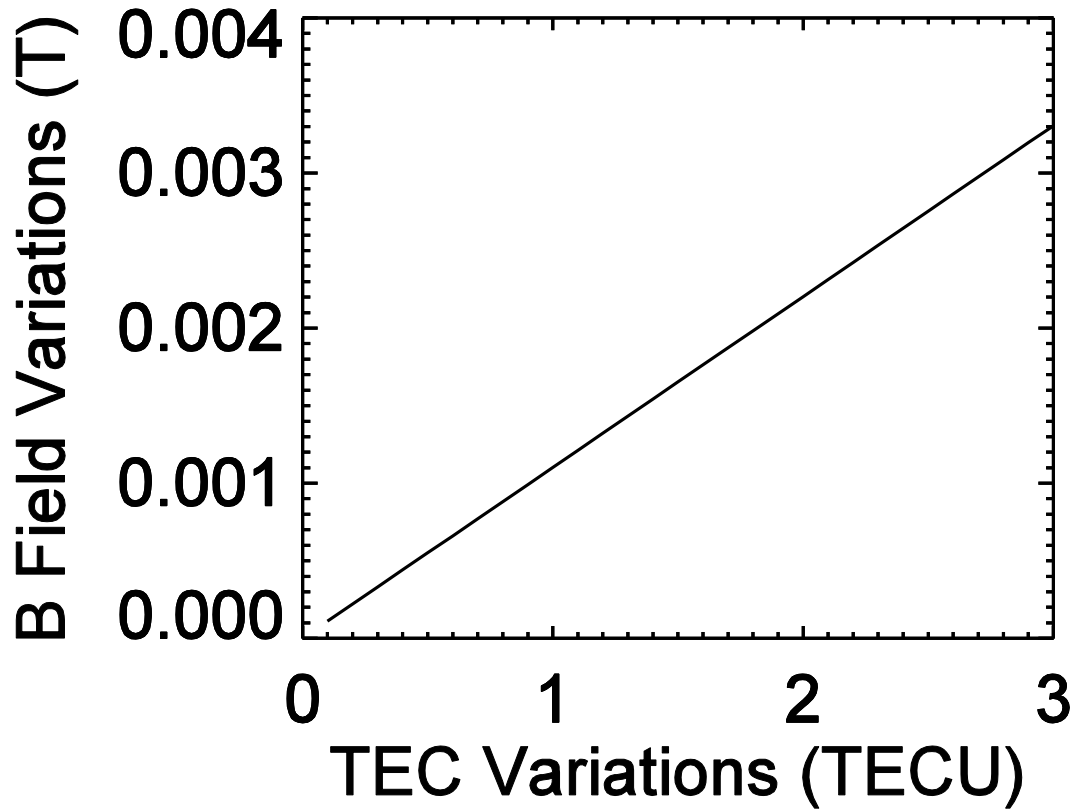


Figure 8.6 The magnitude of the variations in the geomagnetic field necessary to induce variations in TEC from 0.1 to 3 TECU.

8.3.1 Generation Mechanisms

To further show that these sub-second variations in TEC are of ionospheric origin, and to determine the generation mechanisms of these small-scale structures, we attempt to correlate them with other geophysical phenomena. The CARISMA network (Mann et al., 2008) has an induction coil magnetometer, sampling at 20 Hz resolution, located in Fort Churchill, near the Churchill station in the CHAIN. Analysis of the significant sub-

second TEC events shows a qualitative correlation with sub-second variations observed in the geomagnetic field. An example event is presented in Figure 8.7, with the one-second standard deviations in sTEC presented in the top panel, and the one-second standard deviations in the horizontal component of the geomagnetic field in the bottom panel. Four prominent events are observed in the sTEC variations, occurring near 0.7 hours, 1.1 hours, 1.4 hours, and 1.6 hours. We observe significant variations at approximately these times in the geomagnetic field data as well. As with all events analyzed, various degrees of correlation is observed between the sub-second geomagnetic field variations and the sub-second sTEC variations; for all events there is a significant qualitative correlation, suggesting a relationship between the two.

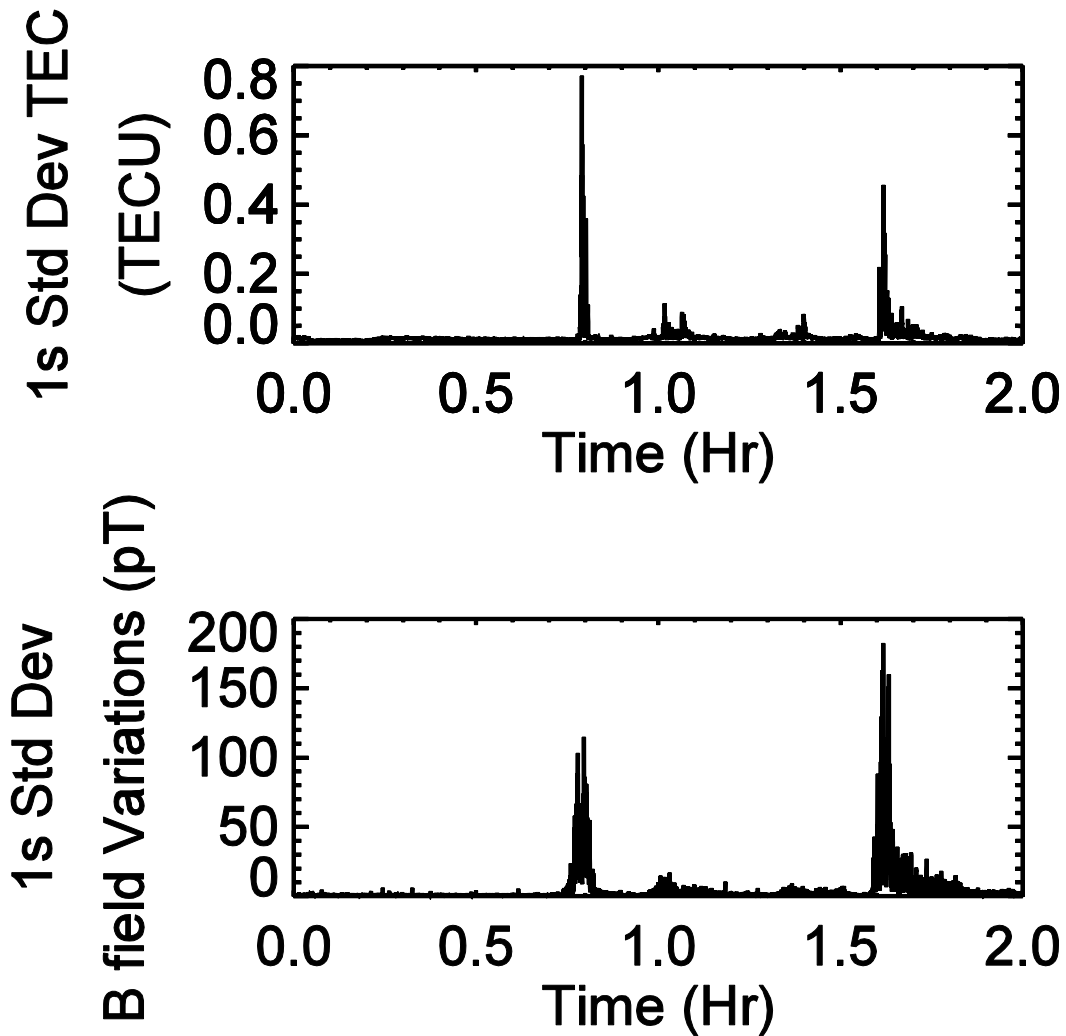


Figure 8.7 An example of significant sub-second sTEC (top) and visually correlating sub-second variations in the geomagnetic field variations (bottom).

This correlation between the sub-second geomagnetic field variations and sub-second sTEC variations is further corroborated by examining the time of day in which the variations are most likely to occur. The distribution of all sub-second sTEC events, from DOY 91 through DOY 365, 2015, at the Churchill station (when data is available) is

presented in Figure 8.8. We observe that sub-second sTEC events are most likely to occur around hour 0, hour 9, and hour 15 local time, with the peaks being approximately 4 hours wide. For the geomagnetic field data, the distribution of times when these events occur is presented in Figure 8.9. We observe peaks in the distributions near local midnight, hour 7, hour 11, and hour 16. These peaks in the geomagnetic field data occur well within the times where the sTEC events are most prominent. This further suggests the correlation between the sub-second sTEC variations and the geomagnetic field activity.

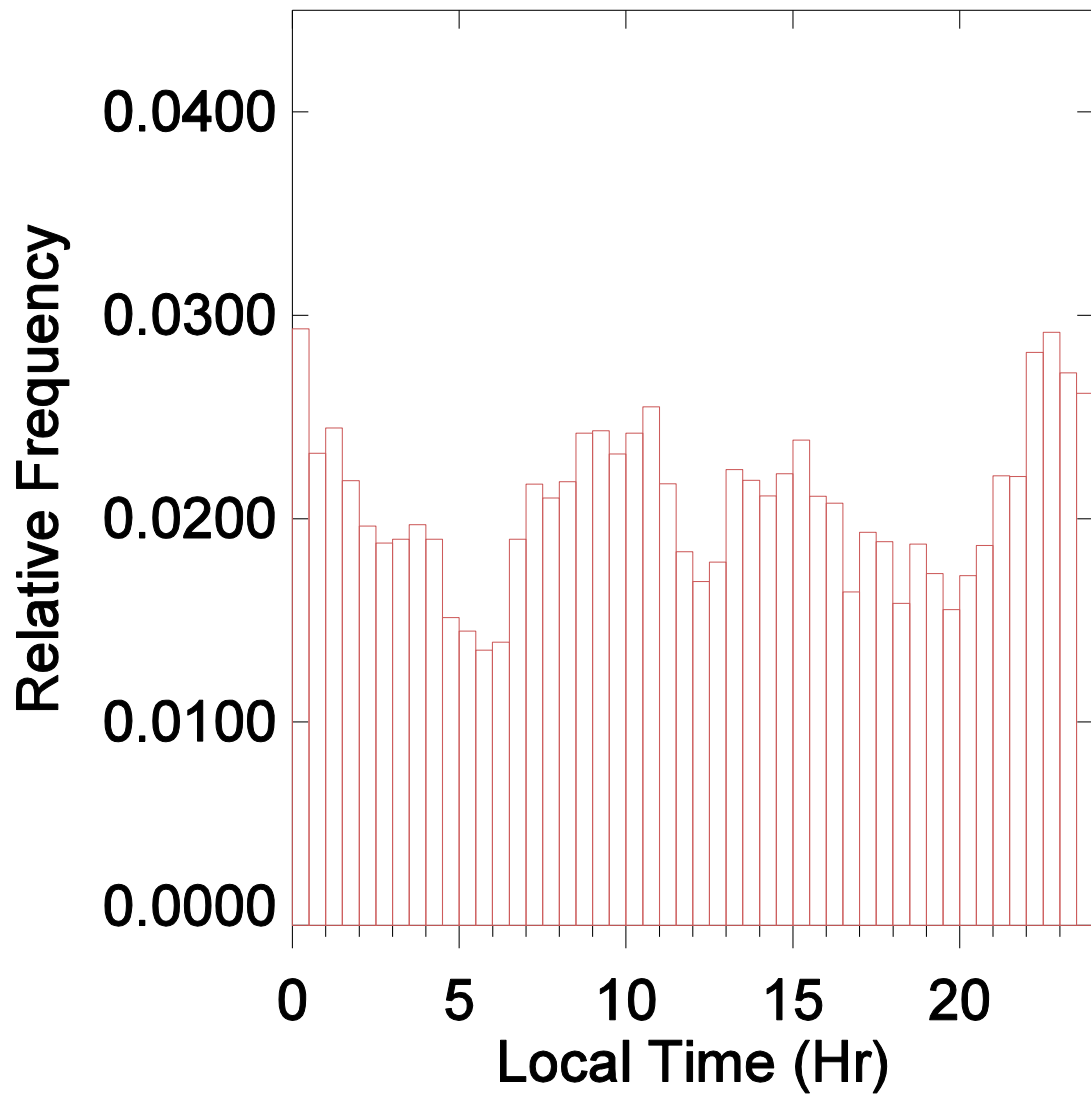


Figure 8.8 Distribution of the local times corresponding to TEC events, for DOY 91 – 365, 2015.

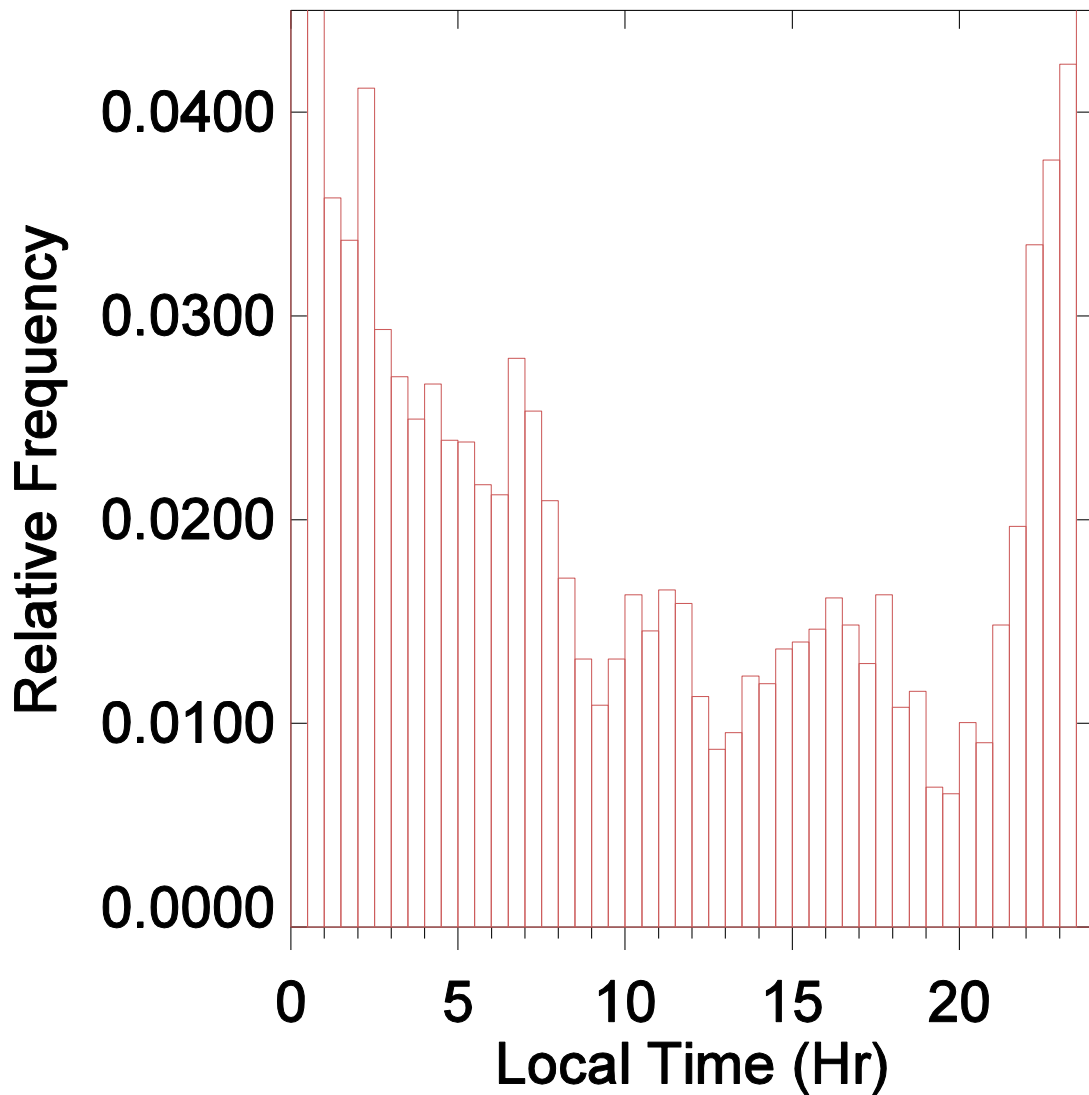


Figure 8.9 Distribution of local times corresponding to geomagnetic field variations events for DOY 91 – 365, 2015.

As we discussed, it is unlikely that the variations in the magnetic field themselves are the cause of these rapid variations in sTEC. This can be further observed by a closer examination of an example event of the geomagnetic field variations and the variations in the sTEC, presented in Figure 8.10. To better visualize the comparison between the

sTEC variations and the geomagnetic field variations both are high pass filtered to remove the low-frequency components. The geomagnetic field data is detrended with a cut-off of 0.01 Hz, to remove the low-frequency trend and focus only on the rapid variations of the geomagnetic field. As was discussed, we do not expect the magnetic field variations to be the cause of the TEC variations; therefore, a lower detrending cut-off is used with the magnetic field data to better visualize when the activity occurs. The sTEC is filtered using a 1 Hz cut-off since we focus on the variations greater than 1 Hz. The example is again taken from the Churchill location, during DOY 73, UTC hour 5. We see that the significant variations in the geomagnetic field (top panel) range from approximately 0.45 hr to 0.6 hr. For the three example sTEC arcs (second through fourth panels) the variations in the sTEC vary in time, the first example (PRN 17) is seen just before the geomagnetic field variations, the second example (PRN 3) is seen in the middle of the geomagnetic field variations, and the last sTEC event (PRN 1) is seen at the end of the geomagnetic field variations. This further suggests that the geomagnetic field variations are likely not the cause of variations in sTEC. It is more likely that some geophysical phenomenon is the cause of both the geomagnetic field variations and the variations in the sTEC.

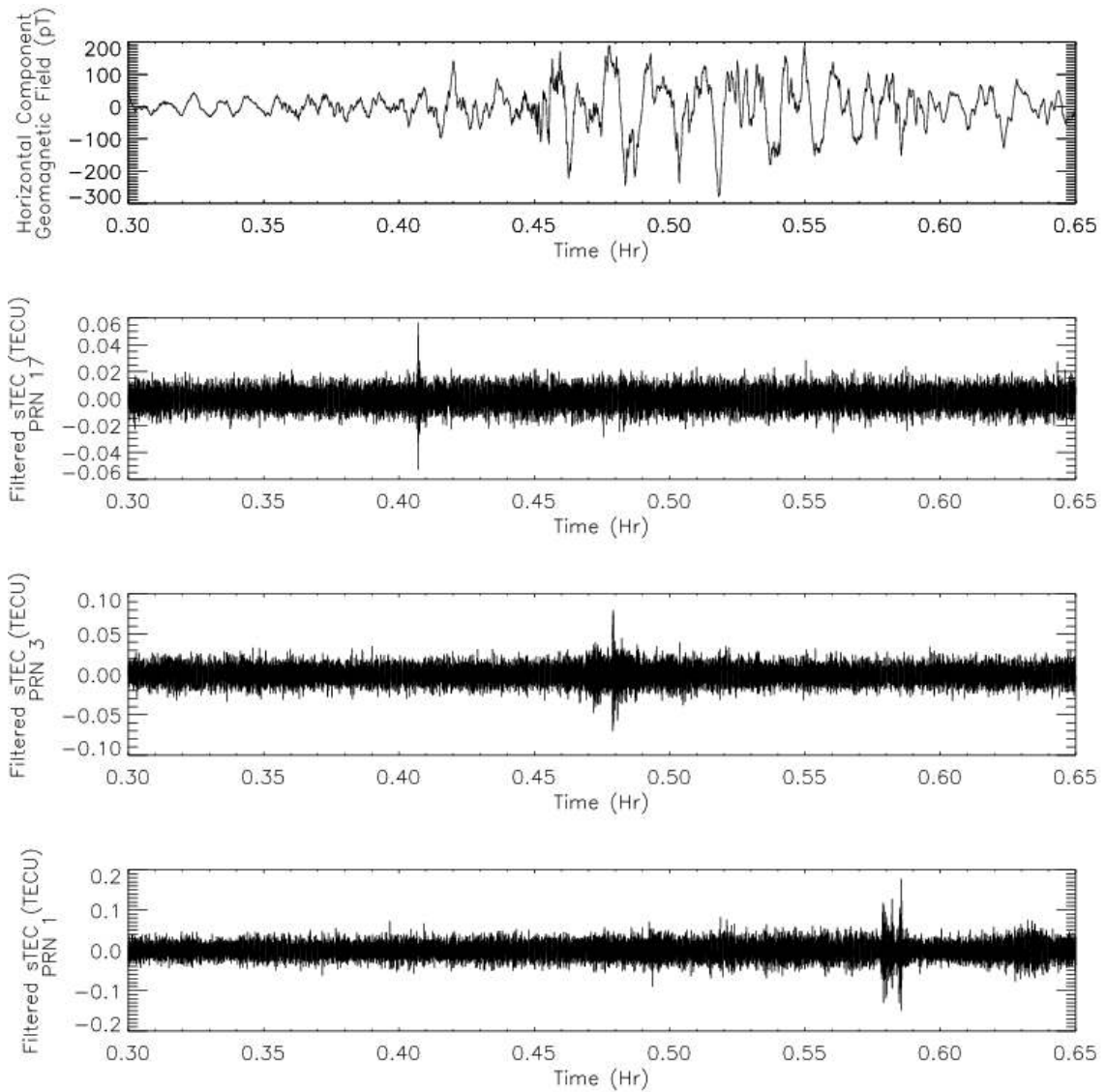


Figure 8.10 Comparison of the geomagnetic field variations (top panel) and variations in the sTEC, as seen from three separate GPS satellites (second through fourth panels). The geomagnetic field and sTEC data have been high pass filtered to better visualize to higher frequency variations.

Using the data available from the Defence Meteorological Satellite Program (DMSP) satellites, we investigate the effects, and possible correlation, of high latitude participle

precipitation with the geomagnetic field and sTEC variations, presented thus far. We examine an example on March 17, 2015, using a pass of the DMSP satellite 16 from 11 hours 23 minutes to 11 hours 30 minutes UTC. We compare this event with a quiet time the day before, March 16, 2015, with a pass from 11 hours 37 minutes to 11 hours 44 minutes UTC. A selection of satellites, PRNs 5, 7, 15, and 29, as observed by the CHAIN stations Arviat, Gjoa Haven, Rankin Inlet, and Repulse Bay, are used. The pass of the DMSP satellite for the time intervals is presented in Figure 8.11. March 16 is presented on the left, and March 17 on the right. The DMSP satellite track is represented by the red line, the four CHAIN stations represented by the black diamonds, and the IPPs for the GPS satellites, at a height of 350 km, are represented by the blue lines. We examine the total electron flux from the DMSP satellite during these passes. These are presented in Figure 8.12. The left panel represents the pass during March 16, the right panels represent the pass during March 17. We observe a significant increase in the electron energy flux, with the total energy increasing nearly two-fold during the March 17 pass. Note that the total energy flux is an integral measurement of the electron flux over all monitored energy levels. For the DMSP satellite, the energies range from 30 eV to 30 KeV.

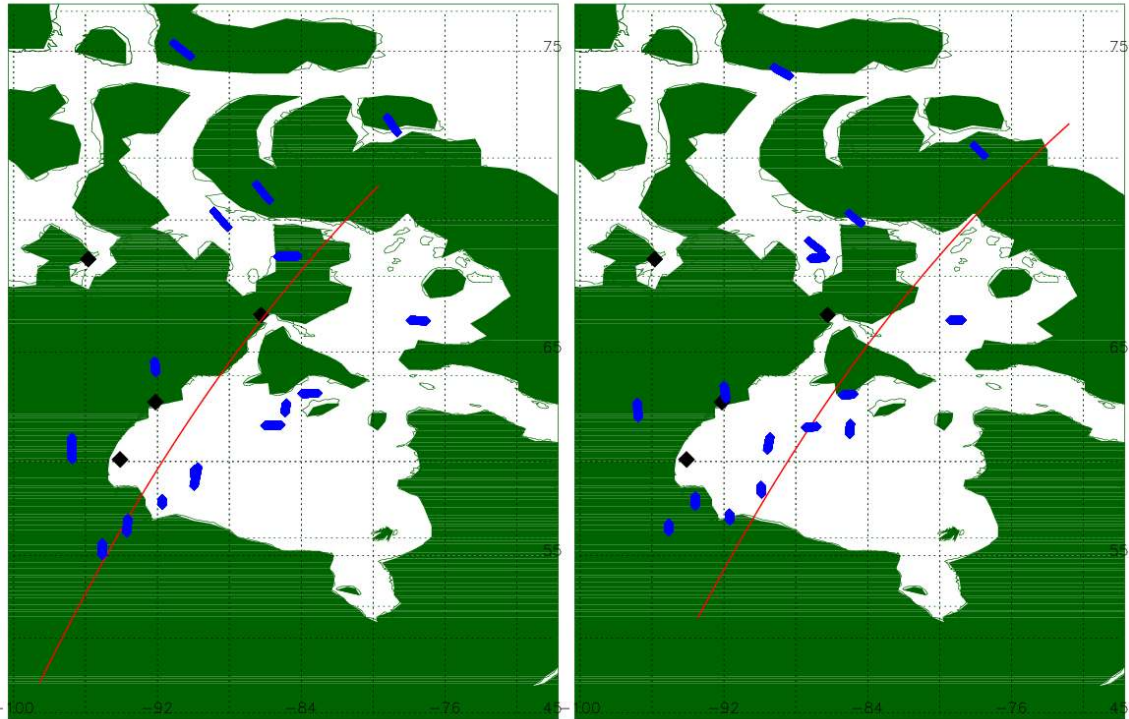


Figure 8.11 The track of the DMSP 16 satellite for March 16, 2015 (left) and March 17, 2015 (right), represented by the red line. The Arviat, Gjoa Haven, Rankin Inlet, and Repulse Bay CHAIN station are represented by the black diamonds, with the IPPs of a few satellites of interest represented by the blue lines.

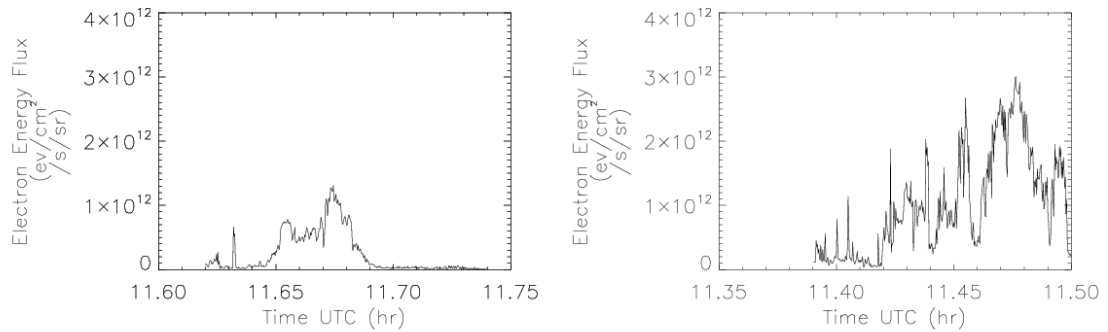


Figure 8.12 Electron energy flux for the DMSP 16 satellite pass over the Canadian high latitudes. The passes occur during hour 11 UTC, on March 16, 2015 (left) and March 17, 2015 (right).

The one-second standard deviations in sTEC during these times are presented in Figure 8.13. Each colour represents a separate arc. There is a clear increase in the high-frequency variations in the sTEC when comparing the March 16 results (left) with the March 17 results (right). This coincides with the increase in particle precipitation observed with the DMSP 16 satellite. Geomagnetic field activity also increases during hour 11 UTC for March 17, 2015, when compared to March 16, 2015. This is seen in the horizontal component of the geomagnetic field, as reported by the Induction Coil Magnetometer (ICM) at the CARISMA Churchill location. The geomagnetic field results are presented in Figure 8.14; the data has been high pass filtered, which a cut-off of 0.01 Hz like the previously presented results.

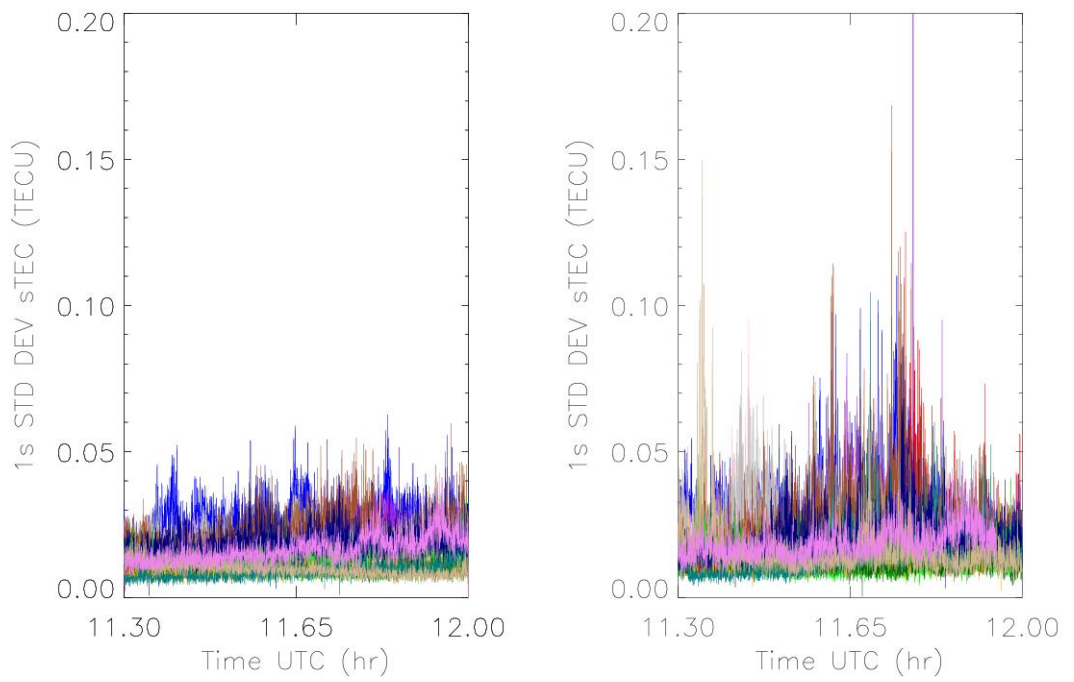


Figure 8.13 The one-second standard deviations for GPS satellite PRNs 5, 7, 15, and 29, as seen from the Arviat, Gjoa Haven, Rankin Inlet, and Repulse Bay stations. Each colour represents a ray path. The left panel shows the data from March 16, 2015, the right panel shows that data from March 17, 2015.

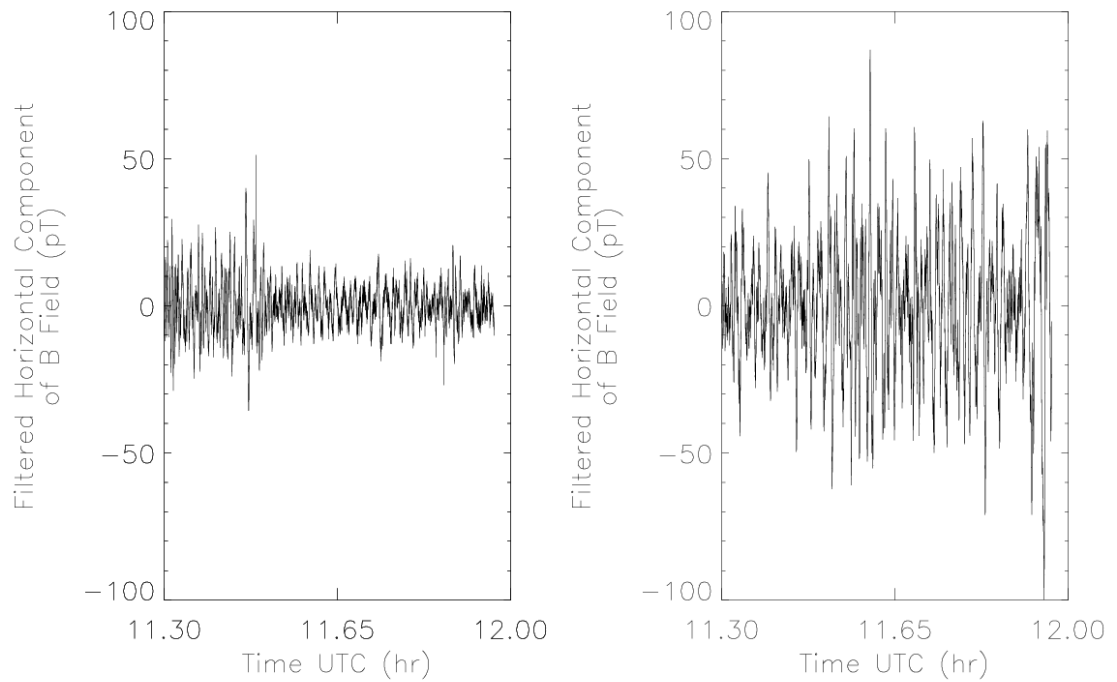


Figure 8.14 The horizontal component of the geomagnetic field, high pass filtered, for March 16, 2015 (left) and March 17, 2015 (right).

These results suggest a correlation between the electron precipitation in the region, the variations in the ground-based magnetic field data, and the sub-second sTEC variations. Before discussing possible physical connections behind this correlation we present two more examples, one in which large magnitude magnetic field and TEC variations are present, and a second in which much lower magnitude variations are present in both the TEC and magnetic field. The events take place during March 10, 2015 (DOY 70). In this example we use ten CHAIN stations to observe the high-frequency TEC variations; these are ARVC, CHUC, CORC, FSIC, FSMC, GILC, MCMC, RABC, RANC, and REPC. This gives a wide coverage of the high latitude and auroral region. The one-

second standard deviations of sTEC, for all satellite paths observed by these receivers, are presented in Figure 8.15. Our analysis suggests that the first of the two events take place from roughly 5 hours UTC to 9 hours UTC, while the second event is from approximately 16.5 hours UTC to 19.5 hours UTC. The large magnitude, sub-second, variations in the sTEC is clearly observed during these times.

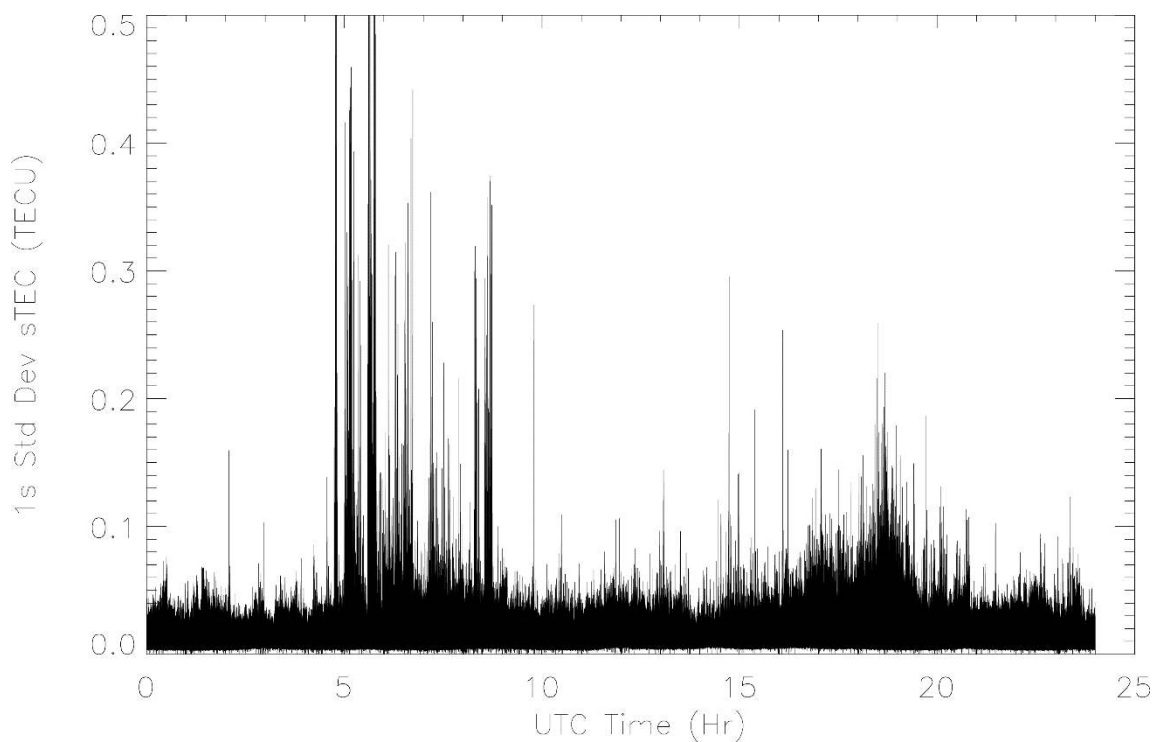


Figure 8.15 The one-second standard deviation in sTEC for all available ray paths during DOY 70, 2015.

The horizontal geomagnetic field component, as measured at the Churchill station in CARISMA during DOY 70, is presented in Figure 8.16. As per the earlier analysis, the

data is high-pass filtered with a 0.01 Hz cut-off. We observe significant activity at times overlapping with the first sTEC event, and very mild activity during the second event.

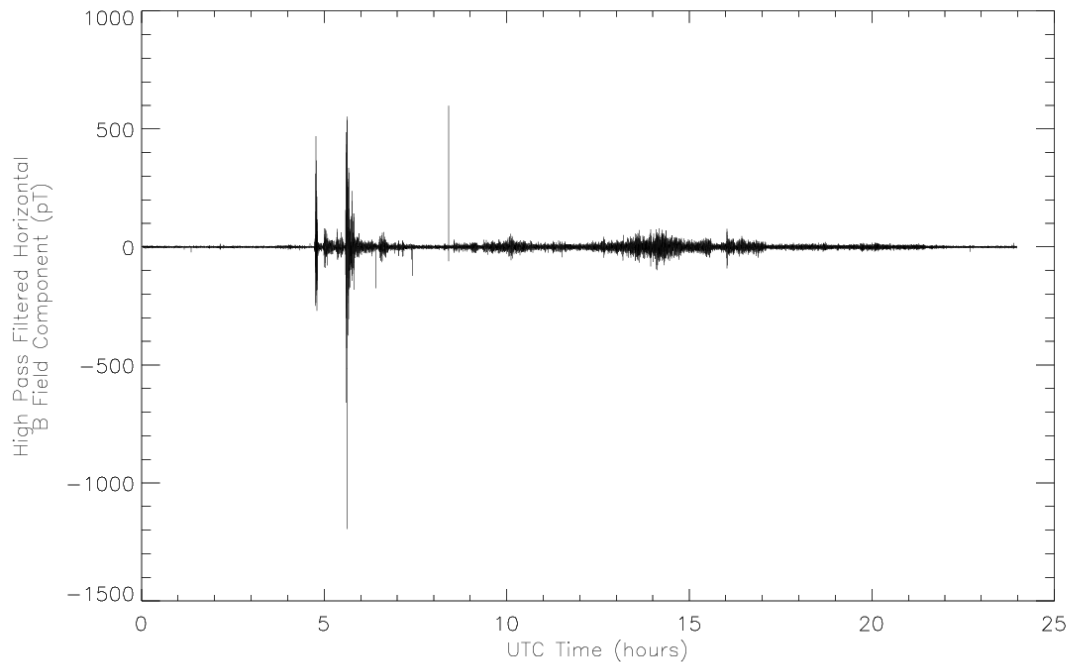


Figure 8.16 The high pass filtered horizontal component of the magnetic field data. The data was taken from the Churchill station ICM in the CARISMA network during DOY 70, 2015. Significant variations in field data are present during roughly 5 hours UTC to 8 hours UTC, which corresponds to the first sTEC event. Much lower magnitude variations are present in the magnetic field data during the 16.5 hours UTC to 19.5 hours UTC sTEC event.

Unfortunately, the DMSP satellites are not located within the area of interest during the time of the events; however, we can use the particle precipitation data provided by the Geostationary Operational Environmental Satellite (GOES). Two GOES satellites are operational, providing overlapping coverage of North and South American regions. The coverage from these two satellites is illustrated in Figure 8.17. GOES-West (GOES-15) provides coverage with a western bias, while GOES-EAST (GOES-13) provides coverage with an eastern bias. Since GOES-13 provides coverage more suitable to the CHAIN network, data provided by GOES-13 is used for this study.

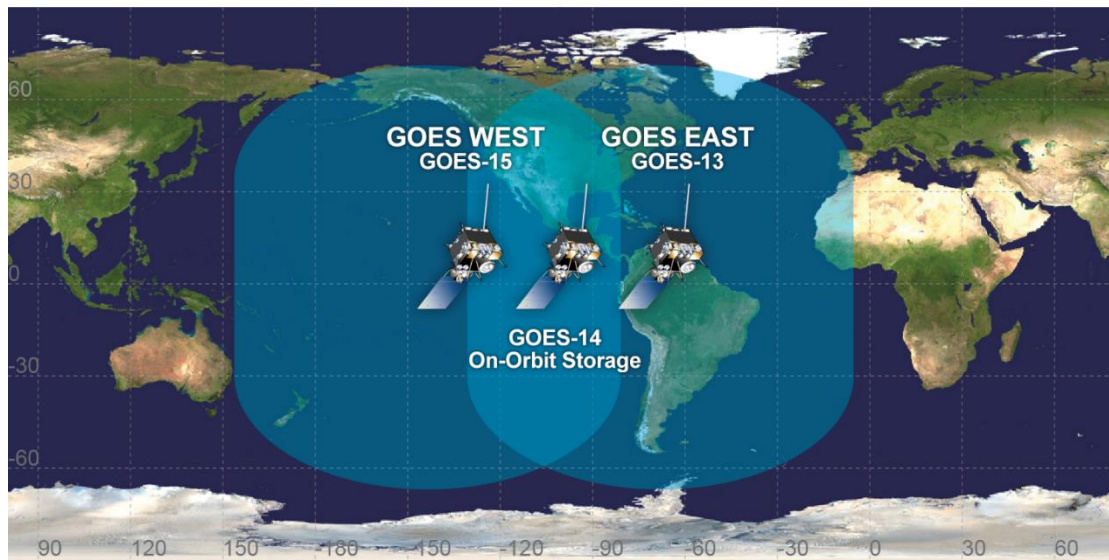


Figure 8.17 Illustration of the coverage provided by the GOES-West and GOES-East geostationary satellites. The GOES-East satellite provides coverage of central and eastern Canada and is, therefore, more relevant to this study. Retrieved from <https://www.nesdis.noaa.gov/content/goes-r-has-become-goes-16>.

The GOES provides electron flux for three energy levels: electrons with energies greater than 0.8 MeV, greater than 2 MeV, and greater than 4 MeV. In Figure 8.18 we present the electron flux for the entire day of March 17, the panels are arranged in increasing order of the energy levels, from top to bottom. The black lines in each panel correspond to the electron flux measured by the eastward facing detector while the blue line represents the westward facing detector. In the 0.8 MeV and 2 MeV minimum energy levels we observe a significant smooth increase in electron flux starting at approximately 5.5 hours UTC. This corresponds well with the first sub-second sTEC variation event. In the 4 MeV minimum energy levels data we also observe a significant increase in flux prior to 18 hours UTC. This corresponds well to the second sTEC variation event.

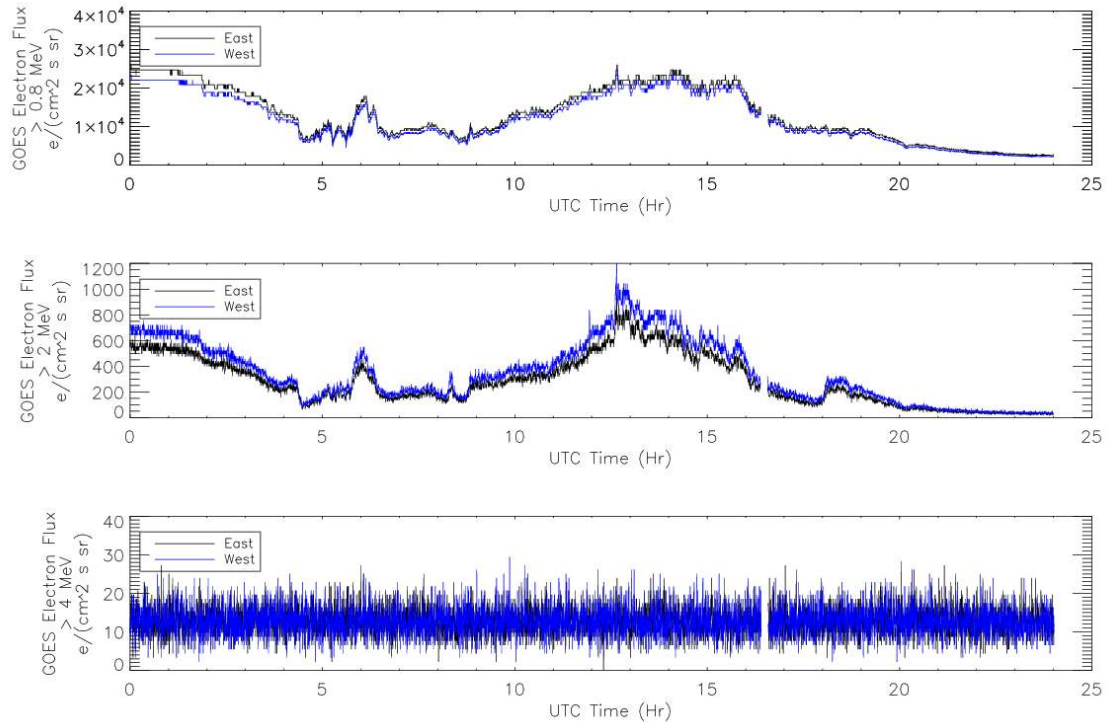


Figure 8.18 The electron flux measurements from the GOES-13 during March 10, 2015. The panels are ordered by energy levels, increasing from top to bottom. The blue lines represent the westward facing detector and the black lines represent the eastward facing detector.

We note that a significant, low frequency, increase in flux is observed between the two events of interest with no corresponding significant sub-second TEC activity. This change in electron flux is still expected to cause variations in the TEC. For completeness, this is shown in Figure 8.19 TEC along various GPS ray paths during UTC hours 10 through 16, DOY 70, 2015, for six CHAIN stations. Each colour represents a different ray. Figure 8.19 which presents the available rays for the GPS satellites for six of the CHAIN stations, during UTC hour 10 through UTC hour 16. The

TEC is presented at a 1 Hz sampling rate; each ray path is represented by a different colour. Clear activity is observed on many of the ray paths; this shows low-frequency activity in the TEC which is likely due to the lower frequency activity in the electron flux.

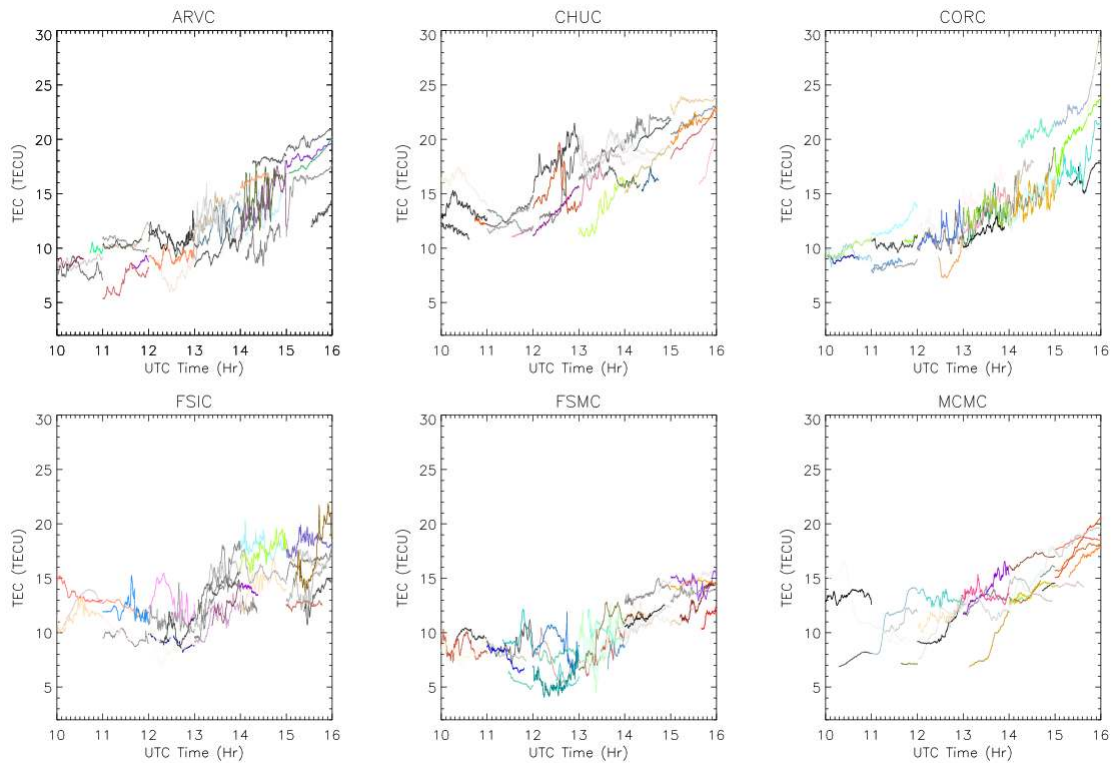


Figure 8.19 TEC along various GPS ray paths during UTC hours 10 through 16, DOY 70, 2015, for six CHAIN stations. Each colour represents a different ray.

These results, corresponding the sub-second TEC events, suggest a couple important points which were observed in the analysis. First, all the sub-second sTEC variations events were observed to correlate with a significant increase in electron precipitation in

the region. Second, the events associated with lower energy electron precipitation corresponding to greater magnetic field activity.

The variations in the magnetic field observed during the presented events are likely related to changes in the ionospheric current. Currents in the ionosphere are caused by the bulk motion of the plasma, which can be due predominately to either the $\mathbf{E} \times \mathbf{B}$ drift or through the neutral wind's impact on the lower layers of the ionosphere. In the ionosphere, the conductivity is directly related to the electron density (Vickrey et al., 1981), so, any changes in the electron density can lead to changes in the ionospheric current and thus changes in the observed magnetic field. Changes in the current may also be due to changes in the electric field, which can be affected by a sudden influx of electrons. These changes in the electron density will also be observed in the sTEC; thus, the electron precipitation is suggested to be the mechanism responsible for both the variations in the magnetic field and the sub-second sTEC variations.

In the cases where significant sub-second sTEC variations are observed with higher energy electron precipitation and less magnetic field activity, we suggest that the quantity of the precipitation electron is responsible. In the presented example, it is clear from the electron flux results that the quantity of higher energy electrons is much less than the electrons of lower energies. In the presented example, the average lower energy electron flux (> 0.8 MeV) is nearly forty times greater than the larger energy flux (> 2 MeV). Since the variations in the magnetic field are related to the changes in electron

density, we suggest that the quantity of higher energy electrons is not sufficient to induce the large magnetic field variations like we observe during the other events. This is further substantiated by the observed magnitude of the sub-second sTEC variations, where the magnitudes of the variations in the higher energy electron event are approximately half the magnitude of the lower energy electron event.

8.4 Conclusion

With the introduction of GPS L2 carrier phase sampled at high frequencies, first-ever observations of sub-second sTEC variations in the Canadian auroral region are presented. Small magnitude variations are observed consistently through the analyzed data set, while large magnitude variations are observed sporadically. The small magnitude variations are shown to be lower in magnitude than the expected receiver phase jitter, thus suggesting these variations are not of ionospheric origin. The larger magnitude variations are not accounted for by the phase jitter, nor by the effects of the higher order terms in the ionospheric delay. These variations were shown to exhibit a qualitative correlation with activity in the horizontal component of the geomagnetic field, as reported by an induction coil magnetometer, nearly co-located with the GPS receiver being used. The large magnitude, sub-second, variations in sTEC are more likely observed during local midnight, morning, and afternoon. Similar peaks in the local time distribution for the geomagnetic field activity is observed, suggesting the sTEC variations are of ionospheric origin, and that a relationship exists between the variations in sTEC and the geomagnetic field.

From the GOES 13 and DMSP 16 satellite, we observe a significant increase in electron flux (30 eV to 30 KeV range for DMSP and > 0.8 MeV for GOES 13) coinciding with an increase in sub-second sTEC activity. We suggest that the precipitating particles may be the cause of the variations in electron density observed at sub-second time scales in the sTEC, suggesting the precipitating particles are inducing small-scale variations in the electron density along the GPS satellite's path. The increase of electrons are also suggested to cause changes in the ionospheric current, and thus changes in the magnetic field observed on the ground. This is why significant magnetic field activity was observed with the sub-second sTEC variation event.

Higher energy electron precipitation (> 2 MeV) was also shown to cause significant sub-second variations in sTEC. These events presented much lower magnitude variations in the sub-second TEC as well as the magnetic field activity. It was suggested that the much lower number of higher energy electrons is responsible for the decrease in the magnitudes of the magnetic field variations. This was further substantiated by the decrease in the magnitudes of the sub-second sTEC variations during the events coinciding with higher energy electron precipitation.

9 Conclusion and Future Work

9.1 Summary

Studies into the high frequency, ionosphere-induced, variations in the GPS carrier phase observable play an interesting and important role in the research and monitoring of the medium. Modern analysis of these variations tends to assume they are scintillation, or diffractive, in nature. This has been based on hard cut-offs, generic indices, sweeping assumptions, and analysis techniques based on low latitude results of the ionosphere. In general, these may not perform well in any region of the ionosphere, but this is especially true of the high latitudes. Due to the unique dynamics of the high latitude ionosphere compared to those observed in the mid and low latitudes, these techniques and assumptions may fail when used in the region. However, these assumptions are used ubiquitously for all regions, including the high latitudes. Recent work has begun to address these issues, but much more is needed. The advances in the GPS hardware is also allowing for more to be done to show the limitations of these assumptions.

A major problem with the assumptions and techniques is the 0.1 Hz cut-off used with the high pass detrending filters. This cut-off was chosen as a generic Fresnel frequency, with an assumption that all scintillation events will have Fresnel frequencies near or less than this value. This is not valid for the high latitude regions due to the very high drift speeds observed there. This is likely to introduce high-frequency refractive effects into the scintillation data, thus including them in the scintillation analyses. By exploiting the

deterministic properties of the refractive variations, we demonstrated the existence of these high-frequency refractive variations and outlined a method to determine and isolate them in future works. The method is based on determining an approximate Fresnel frequency from the variations in the amplitude of the signal, and by observing the slope and correlation of a linear fit between the carrier phase variations in carrier pairs. The deterministic nature of the refractive variations suggests very good correlation in the variations between carrier pairs and predicts specific slope values. The method was demonstrated using a couple dual-frequency examples and further verified using a triple-frequency example. Since the method depends on the inverse frequency-squared dependence on the refractive variations, multiple frequency pairs further confirm the high-frequency refractive variations.

With the outlined techniques, these refractive variations can then be isolated and analyzed, ensuring they are not contaminated with diffractive artifacts. This is used to study the sub-second variations in the auroral region TEC. These variations are observed in two forms: low magnitude and persistent, and large magnitude and sporadic. The GPS receiver phase noise and the higher order terms in the ionospheric delay are analyzed. It was concluded that the magnitude of phase noise was large enough to be the cause of the low magnitude variations but not the sporadic variations; the higher order terms in the ionospheric delay were shown to be too low in magnitude to be the cause of either the low or high magnitude variations. Thus, the larger magnitude variations were deemed ionospheric in nature.

A statistical analysis of these sub-second TEC variations revealed a qualitative correlation with variations in the ground-based magnetic field data obtained in the region. Electron precipitation data was also observed during these times, indicating an increase in the overall electron flux. This suggested that the electron precipitation is the likely cause of both the sub-second TEC variations and the magnetic activity. The precipitation of electrons into the ionosphere will cause direct changes in the current density of the medium, and thus induce magnetic field variations. To produce the sub-second TEC variations, it is likely that the particle precipitation is inducing very small spatial scale irregularities in the electron density.

9.2 Major Results

- Independent tracking of the GPS carriers is necessary for any accurate high-frequency analysis of the GPS carrier phase observable. Works interested in the high frequency carrier phase should use data obtained from independent tracking whenever possible.
- Dominantly refractive variations are present and common in the GPS carrier phase at frequencies greater than 0.1 Hz. Methods of determining and isolating these variations have been presented. These methods may be used in future works to ensure the high frequency variations (refractive or diffractive) are properly isolated.

- Sub-second variations in TEC have been observed in the auroral region and appear to be related to high energy electron precipitation. These variations have been analyzed to be free of diffractive artifacts, thus concluding that these high frequency variations are dominantly refractive.
- Preliminary analysis suggests the carrier phase noise floor is lower in frequency than previously thought. This, combined with the colored nature of the high frequency phase noise, may be represented in scintillation analysis if not treated carefully.

9.3 Future Work

The work presented here takes the first steps towards exploiting the improved accuracy of the independent tracking of the L2C carrier phase and using it to study the high frequency, purely refractive variations observed in the auroral region. The increased accuracy obtained from the independent tracking can be used for many future works. This may include verifying past high-frequency TEC, and ROTI measurements. Works focusing on ROTI or TEC, especially those focused on statistical analysis such as global maps or regional statistics will benefit from knowing whether the receivers used were using dependent tracking techniques, as this would cause varying differences in the magnitudes of the TEC and ROTI variations. For example, if many different receivers are used in these maps located near one another, the variations induced by the tracking

methods may have resulted in increased errors or even artificial variations in the calculated density.

Past works focusing on scintillation will benefit from ensuring independent tracking was used (if L2 was used in the study) and more importantly, ensuring the refractive contribution is removed. Past statistical approaches to scintillation may benefit from removing the refractive contribution to these events, and ensure no purely refractive events were included. This may lead to advances in climatology and morphology results.

Further work on the sub-second TEC variations will be important to further understand the proposed mechanisms behind the small-scale and/or very fast drifting irregularities. Taking advantage of other hardware, which can better present the ionospheric medium during these high-frequency TEC variations, is an important next step for this work. Although this hardware may not have the resolution to see structures of the necessary size for these high-frequency variations, it may be able to rule out possibilities like very fast drifting larger scale irregularities.

Including other satellite constellations (eg the Russian global navigation system and the European Union's global navigation system) could prove useful to further the presented work. These other constellations use different frequencies than those used by the GPS, and thus could be used to further validating the work and in determining accuracy thresholds in larger differences in frequency pairs.

Finally, more robust analysis into the GPS receivers' carrier phase noise floor is a must as increased sampling rates become more readily available. For any work in an ionospheric study where high sampling rates with the GPS carrier phase are used, it is vital to understand the noise sources and noise floor of the data. As we suggest here, it is possible that the effects of the receiver have a more pronounced impact than previously thought, and this impact may induce spectral features like those expected for ionospheric effects. Ensuring receiver effects are not confused with ionospheric effects is vital for the future of the ionospheric research and monitoring community.

Bibliography

- Aarons, J. (1982). Global morphology of ionospheric scintillations. *Proceedings of the IEEE*, 70(4), 360-378. doi:10.1109/proc.1982.12314
- Akala, A. O., Doherty, P. H., Carrano, C. S., Valladares, C. E., & Groves, K. M. (2012). Impacts of ionospheric scintillations on GPS receivers intended for equatorial aviation applications. *Radio Science*, 47(4). doi:10.1029/2012rs004995
- Al-Fanek, O., Skone, S., Lachapelle, G., & Fenton, P. (2007, January). Evaluation of L2C observations and limitations. In *Proceedings of ION GNSS* (pp. 2510-2518).
- Basu, S., Groves, K. M., Quinn, J. M., & Doherty, P. (1999). A comparison of TEC fluctuations and scintillations at Ascension Island. *Journal of Atmospheric and Solar-Terrestrial Physics*, 61(16), 1219-1226. doi:10.1016/s1364-6826(99)00052-8
- Béniguel, Y., Adam, J.-P., Jakowski, N., Noack, T., Wilken, V., Valette, J.-J., ... Arbesser-Rastburg, B. (2009). Analysis of scintillation recorded during the PRIS measurement campaign. *Radio Science*, 44(1), doi:10.1029/2008rs004090

- Bhattacharyya, A., Beach, T. L., Basu, S., & Kintner, P. M. (2000). Nighttime equatorial ionosphere: GPS scintillations and differential carrier phase fluctuations. *Radio Science*, 35(1), 209-224. doi:10.1029/1999rs002213
- Bilitza, D. (2001). International reference ionosphere 2000. *Radio Science*, 36(2), 261-275. doi:10.1029/2000rs002432
- Blewitt, G. (1990). An automatic editing algorithm for GPS data. *Geophysical research letters*, 17(3), 199-202. doi:10.1029/gl017i003p00199
- Booker, H. G. (1958). The use of radio stars to study irregular refraction of radio waves in the ionosphere. *Proceedings of the IRE*, 46(1), 298-314. doi:10.1109/jrproc.1958.286791
- Bruder, J. A., Carlo, J. T., Gurney, J. H., & Gorman, J. (2003). IEEE Standard for Letter Designations for Radar-Frequency Bands. *IEEE Aerospace & Electronic Systems Society*, 1-3. doi:10.1109/ieeestd.1984.81588
- Campbell, W. H. (1996). Geomagnetic storms, the Dst ring-current myth and lognormal distributions. *Journal of Atmospheric and Terrestrial Physics*, 58(10), 1171-1187. doi:10.1016/0021-9169(95)00103-4

- Carrano, C. S., Groves, K. M., & Griffin, J. M. (2005, May). Empirical characterization and modeling of GPS positioning errors due to ionospheric scintillation. In *Ionospheric Effects Symposium* (pp. 1-9).
- Carrano, C. S., Groves, K. M., McNeil, W. J., & Doherty, P. H. (2013, January). Direct measurement of the residual in the ionosphere-free linear combination during scintillation. In *Proceedings of the 2013 Institute of Navigation ION NTM meeting, San Diego, CA*.
- Carrano, C. S., & Rino, C. L. (2016). A theory of scintillation for two-component power law irregularity spectra: Overview and numerical results. *Radio Science*, *51*(6), 789-813. doi:10.1002/2015rs005903
- Cervera, M. A., & Thomas, R. M. (2006, December). Latitudinal and temporal variation of equatorial ionospheric irregularities determined from GPS scintillation observations. In *Annales Geophysicae* (Vol. 24, No. 12, pp. 3329-3341). doi:10.5194/angeo-24-3329-2006
- Chandra, H., Misra, R. K., & Rastogi, R. G. (1971). Equatorial ionospheric drift and the electrojet. *Planetary and Space Science*, *19*(11), 1497-1503. doi:10.1016/0032-0633(71)90009-2
- Cherniak, I., Zakharenkova, I., & Redmon, R. J. (2015). Dynamics of the high-latitude ionospheric irregularities during the 17 March 2015 St. Patrick's Day storm:

Ground-based GPS measurements. *Space Weather*, 13(9), 585-597.

doi:10.1002/2015sw001237

Chisham, G., Lester, M., Milan, S. E., Freeman, M. P., Bristow, W. A., Grocott, A., ... & Greenwald, R. A. (2007). A decade of the Super Dual Auroral Radar Network (SuperDARN): Scientific achievements, new techniques and future directions. *Surveys in Geophysics*, 28(1), 33-109. doi:10.1007/s10712-007-9017-8

Cordes, J. M., Pidwerbetsky, A., & Lovelace, R. V. E. (1986). Refractive and diffractive scattering in the interstellar medium. *The Astrophysical Journal*, 310, 737-767. doi:10.1086/164728

Crane, R. K. (1977). Ionospheric scintillation. *Proceedings of the IEEE*, 65(2), 180-199. doi:10.1109/proc.1977.10456

Datta-Barua, S., Walter, T., Blanch, J., & Enge, P. (2008). Bounding higher-order ionosphere errors for the dual-frequency GPS user. *Radio Science*, 43(5). doi:10.1029/2007rs003772

Davies, K. (1990). *Ionospheric radio* (No. 31). IET.

El-Rabbany, A. (2002). *Introduction to GPS: the global positioning system*. Artech house.

- Elkins, T. J., & Papagiannis, M. D. (1969). Measurement and interpretation of power spectrums of ionospheric scintillation at a sub-auroral location. *Journal of Geophysical Research*, 74(16), 4105-4115. doi:10.1029/ja074i016p04105
- Forte, B., & Radicella, S. M. (2002). Problems in data treatment for ionospheric scintillation measurements. *Radio Science*, 37(6). doi:10.1029/2001RS002508, 2002.
- Franke, S. J., & Liu, C. H. (1983). Observations and modeling of multi-frequency VHF and GHz scintillations in the equatorial region. *Journal of Geophysical Research: Space Physics*, 88(A9), 7075-7085. doi:10.1029/ja088ia09p07075
- Fremouw, E. J., Leadabrand, R. L., Livingston, R. C., Cousins, M. D., Rino, C. L., Fair, B. C., & Long, R. A. (1978). Early results from the DNA Wideband satellite experiment—Complex-signal scintillation. *Radio Science*, 13(1), 167-187. doi:10.1029/rs013i001p00167
- Greenwald, R. A., Bristow, W. A., Sofko, G. J., Senior, C., Cerisier, J. C., & Szabo, A. (1995). Super dual auroral radar network radar imaging of dayside high-latitude convection under northward interplanetary magnetic field: Toward resolving the distorted two-cell versus multicell controversy. *Journal of Geophysical Research: Space Physics*, 100(A10), 19661-19674. doi:10.1029/95JA01215

- Gruber, S. (1961). Statistical analysis of radio star scintillation. *J. Atmos. Terr. Phys.*, 20(1), 59-71. doi:10.1016/0021-9169(61)90098-8
- Heelis, R. A., Lowell, J. K., & Spiro, R. W. (1982). A model of the high-latitude ionospheric convection pattern. *Journal of Geophysical Research: Space Physics*, 87(A8), 6339-6345.
- Hegarty, C. (2013). *Workshop on GNSS Data Application to Low Latitude Ionospheric Research*. Lecture presented in Trieste, Italy.
- Hernández-Pajares, M. (2010). IERS technical note no. 36. Ch. 9. Ionospheric model for radio techniques. *IERS Conventions*, 179.
- Hernández-Pajares, M., Juan, J. M., Sanz, J., Orus, R., Garcia-Rigo, A., Feltens, J., ... & Krankowski, A. (2009). The IGS VTEC maps: a reliable source of ionospheric information since 1998. *Journal of Geodesy*, 83(3), 263-275.
doi:10.1007/s00190-008-0266-1
- Hey, J. S., Parsons, S. J., & Phillips, J. W. (1946). Fluctuations in cosmic radiation at radio-frequencies. *Nature*, 158(4007), 234. doi:10.1007/978-94-009-7752-5_23

- Hoque, M. M., & Jakowski, N. (2007). Higher order ionospheric effects in precise GNSS positioning. *Journal of Geodesy*, 81(4), 259-268. doi:10.1007/s00190-006-0106-0
- Hunsucker, R. D., & Hargreaves, J. K. (2007). *The high-latitude ionosphere and its effects on radio propagation*. Cambridge University Press.
- Irsigler, M., & Eissfeller, B. (2002). PLL tracking performance in the presence of oscillator phase noise. *GPS solutions*, 5(4), 45-57. doi:10.1007/pl00012911
- Jayachandran, P. T., Langley, R. B., MacDougall, J. W., Mushini, S. C., Pokhotelov, D., Hamza, A. M., ... & Kelly, T. (2009). Canadian high arctic ionospheric network (CHAIN). *Radio Science*, 44(1). doi:10.1029/2008rs004046.
- Jespersen, J. L., & Kamas, G. (1964). Satellite scintillation observations at Boulder, Colorado. *J. Atmos. Terr. Phys.*, 26(4), 457-473. doi:10.1016/0021-9169(64)90027-3
- Jiao, Y., Morton, Y. T., Taylor, S., & Pelgrum, W. (2013). Characterization of high-latitude ionospheric scintillation of GPS signals. *Radio Science*, 48(6), 698-708. doi:10.1002/2013rs005259

- Jones, I. L. (1960). Further observations of radio stellar scintillation. *Journal of Atmospheric and Terrestrial Physics*, 19(1), 26-36. doi:10.1016/0021-9169(60)90104-5
- Jursa, A. S. (1985). *Handbook of geophysics and the space environment* (ch. 10).
Springfield, VA: NTIS.
- Kaplan, E., & Hegarty, C. (2005). *Understanding GPS: principles and applications*.
Artech house.
- Kedar, S., Hajj, G. A., Wilson, B. D., & Heflin, M. B. (2003). The effect of the second order GPS ionospheric correction on receiver positions. *Geophysical Research Letters*, 30(16). doi:10.1029/2003gl017639
- Kim, D., Serrano, L., & Langley, R. (2006). INNOVATION-Phase Wind-Up Analysis-Assessing Real-Time Kinematic Performance. *GPS World*, 17(9), 58-64.
- Kintner, P. M., Ledvina, B. M., and De Paula, E. R. (2007). GPS and ionospheric scintillations. *Space weather*, 5(9). doi:10.1029/2006sw000260
- Knudsen, D. J., Donovan, E. F., Cogger, L. L., Jackel, B., & Shaw, W. D. (2001). Width and structure of mesoscale optical auroral arcs. *Geophysical research letters*, 28(4), 705-708. doi:10.1029/2000gl011969

Komjathy, A. (1997). *Global ionospheric total electron content mapping using the Global Positioning System* (Doctoral dissertation, University of New Brunswick).

Krankowski, A., Cherniak, I., & Zakharenkova, I. (2017, April). The new IGS ionospheric product-TEC fluctuation maps and their scientific application. In *EGU General Assembly Conference Abstracts* (Vol. 19, p. 8109).

Lanyi, G. E., & Roth, T. (1988). A comparison of mapped and measured total ionospheric electron content using global positioning system and beacon satellite observations. *Radio Science*, 23(4), 483-492. doi:10.1029/rs023i004p00483

Leick, A., Rapoport, L., & Tatarnikov, D. (2015). *GPS satellite surveying*. John Wiley & Sons.

Lim, D. W., Moon, S. W., Park, C., & Lee, S. J. (2006, April). L1/L2CS GPS receiver implementation with fast acquisition scheme. In *Position, Location, and Navigation Symposium, 2006 IEEE/ION* (pp. 840-844). IEEE. doi:10.1109/plans.2006.1650683

Magdaleno, S., Altadill, D., Herraiz, M., Blanch, E., & de La Morena, B. (2011). Ionospheric peak height behavior for low, middle and high latitudes: A potential

empirical model for quiet conditions—Comparison with the IRI-2007 model. *Journal of Atmospheric and Solar-Terrestrial Physics*, 73(13), 1810-1817. doi:10.1016/j.jastp.2011.04.019

Mann, I. R., Milling, D. K., Rae, I. J., Ozeke, L. G., Kale, A., Kale, Z. C., ... & Lee, E. A. (2008). The upgraded CARISMA magnetometer array in the THEMIS era. *Space Science Reviews*, 141(1-4), 413-451. doi:10.1007/978-0-387-89820-9_18

Mannucci, A. J., Tsurutani, B. T., Iijima, B. A., Komjathy, A., Saito, A., Gonzalez, W. D., ... & Skoug, R. (2005). Dayside global ionospheric response to the major interplanetary events of October 29–30, 2003 “Halloween Storms”. *Geophysical Research Letters*, 32(12). doi:10.1029/2004gl021467

Marconi, G. (1922) Wireless telegraphy. *Proceedings of the IRE*, 10, 215–238.

McCaffrey, A. M., & Jayachandran, P. T. (2017a). Spectral characteristics of auroral region scintillation using 100 Hz sampling. *GPS Solutions*, 21(4), 1883-1894. doi:10.1007/s10291-017-0664-z

McCaffrey, A. M., & Jayachandran, P. T. (2017b). Observation of sub-second variations in auroral region total electron content using 100 Hz sampling of GPS

observables. *Journal of Geophysical Research: Space Physics*.

doi:10.1002/2017ja024255

McCaffrey, A. M., Jayachandran, P. T., Langley, R. B., & Sleewaegen, J. M. (2018a).

On the accuracy of the GPS L2 observable for ionospheric monitoring. *GPS*

Solutions, 22(1), 23. doi:10.1007/s10291-017-0688-4

McCaffrey, A. M., Jayachandran, P. T., Hamza, A. (2018b) Determination and Analysis

of the Refractive Contribution to GPS Phase Variations, Unpublished

manuscript.

Mezaoui, H., Hamza, A. M., & Jayachandran, P. T. (2014). Investigating high-latitude

ionospheric turbulence using global positioning system data. *Geophysical*

Research Letters, 41(19), 6570-6576. doi:10.1002/2014GL061331.

Mills, B. Y., & Thomas, A. B. (1951). Observations of the source of radio-frequency

radiation in the constellation of Cygnus. *Australian Journal of Chemistry*, 4(2),

158-171. doi:10.1071/ch9510158

Misra, P., & Enge, P. (2006). Global positioning system: Signals, measurements and

performance second edition. *Massachusetts: Ganga-Jamuna Press*.

Mitchell, C. N., Alfonsi, L., De Franceschi, G., Lester, M., Romano, V., & Wernik, A. W. (2005). GPS TEC and scintillation measurements from the polar ionosphere during the October 2003 storm. *Geophysical Research Letters*, 32(12). doi:10.1029/2004gl021644.

Montenbruck, O., Steigenberger, P., Prange, L., Deng, Z., Zhao, Q., Perosanz, F., ... & Schmid, R. (2017). The Multi-GNSS Experiment (MGEX) of the International GNSS Service (IGS)—achievements, prospects and challenges. *Advances in space research*, 59(7), 1671-1697. doi:10.1016/j.asr.2017.01.011.

Mushini, S. C., Jayachandran, P. T., Langley, R. B., & MacDougall, J. W. (2009). Use of varying shell heights derived from ionosonde data in calculating vertical total electron content (TEC) using GPS—New method. *Advances in Space Research*, 44(11), 1309-1313. doi:10.1016/j.asr.2009.07.015

Mushini, S. C., Jayachandran, P. T., Langley, R. B., MacDougall, J. W., & Pokhotelov, D. (2012). Improved amplitude-and phase-scintillation indices derived from wavelet detrended high-latitude GPS data. *GPS solutions*, 16(3), 363-373. doi:10.1007/s10291-011-0238-4.

Mushini, S. C. (2012). *Characteristics of scintillating GPS signal at high latitudes during solar minima* (Doctoral dissertation, University of New Brunswick, Department of Physics).

Papas, C. H. (2014). *Theory of electromagnetic wave propagation*. Courier Corporation.

Paznukhov, V. V., Carrano, C. S., Doherty, P. H., Groves, K. M., Caton, R. G., Valladares, C. E., ... Tsidu, G. M. (2012). Equatorial plasma bubbles and L-band scintillations in Africa during solar minimum. *Annales Geophysicae*, 30(4), 675–682. doi:10.5194/angeo-30-675-2012

Pi, X., Mannucci, A. J., Lindqwister, U. J., & Ho, C. M. (1997). Monitoring of global ionospheric irregularities using the worldwide GPS network. *Geophysical Research Letters*, 24(18), 2283-2286. doi:10.1029/97gl02273.

Prikryl, P., Ghoddousi-Fard, R., Weygand, J. M., Viljanen, A., Connors, M., Danskin, D. W., Jayachandran, P. T., Jacobsen, K. S., Andalsvik, Y. L., Thomas, E. G., & Ruohoniemi, J. M. (2016). GPS phase scintillation at high latitudes during the geomagnetic storm of 17–18 March 2015. *Journal of Geophysical Research: Space Physics*, 121(10). doi:10.5194/angeo-33-637-2015

Prikryl, P., Jayachandran, P. T., Mushini, S. C., & Chadwick, R. (2011, February). Climatology of GPS phase scintillation and HF radar backscatter for the high-latitude ionosphere under solar minimum conditions. In *Annales Geophysicae* (Vol. 29, No. 2, p. 377). Copernicus GmbH. doi:10.5194/angeo-29-377-2011

Rees, M. H. (1989). *Physics and chemistry of the upper atmosphere* (Vol. 1). Cambridge University Press.

Rebeyrol, E., Macabiau, C., Ries, L., Issler, J. L., Bousquet, M., & Boucheret, M. L. (2006, January). Phase noise in GNSS transmission/reception system. In *ION NTM 2006, National Technical Meeting of The Institute of Navigation* (pp. pp-698).

Rino, C. L. (1979). A power law phase screen model for ionospheric scintillation: 1. Weak scatter. *Radio Science*, *14*(6), 1135-1145. doi:10.1029/rs014i006p01135

Rougerie, S., Ait-Ighil, M., & Fabbro, V. (2016, September). Impact of GNSS receiver tuning on the estimation of scintillation index. In *ION GNSS 2016*.

Rufenach, C. L. (1971). A radio scintillation method of estimating the small-scale structure in the ionosphere. *Journal of Atmospheric and Terrestrial Physics*, *33*(12), 1941-1951. doi:10.1016/0021-9169(71)90170-x

Seo, J., Walter, T., Chiou, T. Y., & Enge, P. (2009). Characteristics of deep GPS signal fading due to ionospheric scintillation for aviation receiver design. *Radio Science*, *44*(1). doi:10.1029/2008rs004077

Septentrio (2015) PolaRxS SBF Reference Guide v2.9.0

- Trondsen, T. S., & Cogger, L. L. (1998). A survey of small-scale spatially periodic distortions of auroral forms. *Journal of Geophysical Research: Space Physics*, *103*(A5), 9405-9415. doi:10.1029/98ja00619
- Van Dierendonck, A. J., Klobuchar, J., & Hua, Q. (1993, September). Ionospheric scintillation monitoring using commercial single frequency C/A code receivers. In *proceedings of ION GPS* (Vol. 93, pp. 1333-1342).
- Vickrey, J. F., Vondrak, R. R., & Matthews, S. J. (1981). The diurnal and latitudinal variation of auroral zone ionospheric conductivity. *Journal of Geophysical Research: Space Physics*, *86*(A1), 65-75. doi:10.1029/ja086ia01p00065
- Watson, C. (2011). *GPS TEC and riometer techniques for observing absorption events in the high latitude ionosphere* (Doctoral dissertation, University of New Brunswick, Department of Physics).
- Watson, C., Jayachandran, P. T., Singer, H. J., Redmon, R. J., & Danskin, D. (2016). GPS TEC response to Pc4 “giant pulsations”. *Journal of Geophysical Research: Space Physics*, *121*(2), 1722-1735. doi:10.1002/2015ja022253
- Wilson, B. D., Mannucci, A. J., & Edwards, C. D. (1995). Subdaily northern hemisphere ionospheric maps using an extensive network of GPS receivers. *Radio Science*, *30*(3), 639-648. doi:10.1029/94rs03186

- Woo, K. T. (2000). Optimum Semicodeless Carrier-Phase Tracking of L2. *Navigation*, 47(2), 82-99. doi:10.1002/j.2161-4296.2000.tb00204.x.
- Yang, Z., & Liu, Z. (2017). Investigating the inconsistency of ionospheric ROTI indices derived from GPS modernized L2C and legacy L2 P(Y) signals at low-latitude regions. *GPS solutions*, 21(2), 783-796. doi:10.1007/s10291-016-0568-3.
- Yeh, K. C., & Liu, C. H. (1982). Radio wave scintillations in the ionosphere. *Proceedings of the IEEE*, 70(4), 324-360.
doi:10.1109/proc.1982.12313
- Zhang, B., Teunissen, P. J., & Yuan, Y. (2017). On the short-term temporal variations of GNSS receiver differential phase biases. *Journal of Geodesy*, 91(5), 563-572.
doi:10.1007/s00190-016-0983-9
- Zumberge, J. F., Heflin, M. B., Jefferson, D. C., Watkins, M. M., & Webb, F. H. (1997). Precise point positioning for the efficient and robust analysis of GPS data from large networks. *Journal of Geophysical Research: Solid Earth*, 102(B3), 5005-5017. doi:10.1029/96jb03860

Curriculum Vitae

Candidate's full name: Anthony Craig Mark McCaffrey

Universities attended:

University of New Brunswick, Master of Science, 2015

University of Prince Edward Island, Bachelor of Science, 2012

Publications

McCaffrey, A. M., Jayachandran, P. T., Themens, D. R., & Langley, R. B. (2017). GPS receiver CODE bias estimation: A comparison of two methods. *Advances in Space Research*, 59(8), 1984-1991.

McCaffrey, A. M., and P. T. Jayachandran (2017), Observation of Sub-Second Variations in Auroral Region Total Electron Content using 100 Hz sampling of GPS observables, *Journal of Geophysical Research: Space Physics*

McCaffrey, A. M., and P. T. Jayachandran (2017), Spectral characteristics of auroral region scintillation using 100 Hz sampling, *GPS Solutions*

McCaffrey, A. M., Jayachandran, P. T., Langley, R. B., & Sleewaegen, J.-M. (2017), On the accuracy of the GPS L2 observable for ionospheric monitoring. *GPS Solutions*, 22(1)

Conference Presentations:

McCaffrey, A. M., & Jayachandran, P. T. (2014, August). Auroral scintillation characteristics using 100 Hz sampling of global positioning system satellite signals. In *General Assembly and Scientific Symposium (URSI GASS), 2014*.

McCaffrey, A. M., Jayachandran, P. T., Themens, D. R., & Langley, R. B. (2015, December). Analysis of Co-located IGS Network GPS Receiver DCBs Derived by CODE and a Single Station Estimation Method. In *AGU Fall Meeting Abstracts*.

McCaffrey, A. M., & Jayachandran, P. T. (May, 2017). Spectral characteristics of auroral region scintillation using 100 Hz sampling. In *Ionospheric Effects Symposium (IES), 2017*.

McCaffrey, A. M., & Jayachandran, P. T. (August, 2017). Sub-second Variations in Auroral Region Total Electron Content. In *General Assembly and Scientific Symposium (URSI GASS), 2017*.

McCaffrey, A. M., Jayachandran, P. T., Langley, R. B., & Sleewaegen, J.-M. (June. 2018), On the accuracy of the GPS L2 observable for ionospheric monitoring., In *Atlantic Radio Science Meeting (URSI AT-RASC), 2018.*